Mesoscopic transport phenomena in epitaxial graphene nanostructures: A surface science approach

Von der Fakultät für Mathematik und Physik
der Gottfried Wilhelm Leibniz Universität Hannover
zur Erlangung des Grades
Doktor der Naturwissenschaften
Dr. rer. nat.
genehmigte Dissertation

von

M. Sc. Jens Baringhaus
geboren am 14.06.1987 in Hannover

2015

Referent: Prof. Dr. Christoph Tegenkamp
Korreferent: Prof. Dr. Walter de Heer
Korreferent: Prof. Dr. Thomas Seyller

Tag der Promotion: 06.11.2015

ABSTRACT

Since silicon-based electronic devices have already reached the upper physical limits, concerning for example processing speed or heat dissipation, a novel type of electronics is needed. Graphene nanostructures are a major candidate for the realization of carbon-based electronic devices due to their outstanding electronic properties, such as width dependent band gaps or the presence of ballistic transport channels. Unfortunately, conventional lithography methods are known to induce large defect potentials, and are hence detrimental to these peculiar electronic features. To overcome these obstacles, graphene nanostructures were synthesized in this thesis by means of self-organizational growth as well as atomic intercalation of epitaxial graphene on silicon carbide substrates. A 4-tip STM was used to record the local transport characteristics with a spatial resolution of down to 100 nm.

The self-organizational graphene growth on the sidewalls of silicon carbide mesa structures results in the formation of narrow graphene stripes, so called graphene nanoribbons, of extraordinary structural and electronic quality. Single-channel ballistic transport was observed on a lateral scale of several μm, manifesting in a constant conductance of $1\,e^2/h$. The ballistic channel is temperature independent and exists even above room temperature. A second, thermally activated, ballistic channel with a smaller localization length was found. Their distinct characteristics indicate that the transport mechanisms in the two channels are fundamentally different. Such an exceptional transport behavior was not expected by theory and a conclusive explanation for its origin is still missing.

In a second approach, the local doping of epitaxial graphene on silicon carbide was tuned by the intercalation of Germanium. The intercalation of one or two layers leads to the development of symmetrically n-type or p-type doped graphene islands and consequently to the formation of p-n junctions at their interface. Scanning tunneling spectroscopy was used to demonstrate the excellent lateral homogeneity of the doping levels as well as the extremely narrow length of the p-n junctions. The transport characteristics of graphene p-n junctions are dominated by Klein tunneling which manifests in an angular dependent transmission function. The angular dependence was verified indirectly with a serial connection of two p-n junctions in a polarizer-analyzer setup.

These results suggest that graphene nanostructures obtained by atomic intercalation and self-organizational growth are of exceptionally high structural and electronic quality. The observation of mesoscopic transport phenomena at room temperature is of high interest especially with respect to the implementation of graphene nanostructures in future electronic devices.

Keywords
epitaxial graphene, graphene nanoribbons, ballistic transport, Klein tunneling

ZUSAMMENFASSUNG

Die siliziumbasierte Mikroelektronik stößt zunehmend an physikalische Leistungsgrenzen. Aufgrund ihrer besonderen elektronischen Eigenschaften, wie zum Beispiel skalierbare Bandlücken oder robuste ballistische Transportkanäle, könnten die Nanostrukturen des zweidimensionalen Materials Graphen zu essentiellen Bausteinen für kohlenstoffbasierte elektronische Anwendungen werden. Da der Einsatz konventioneller Lithographiemethoden eine hohe Defektdichte zur Folge hat, wurden für die Herstellung von Nanostrukturen in dieser Arbeit alternative Methoden wie selbstorganisiertes Wachstum und atomare Interkalation verwendet. Ein 4-Spitzen-STM erlaubt Messungen der lokalen Leitfähigkeit mit einer Präzision von bis zu 100 nm.

Durch eine gezielte Vorstrukturierung von Siliziumcarbid Substraten kann ein präferentielles Wachstum des Graphens auf den Seitenwänden von Mesa-Strukturen induziert werden. Die so erzeugten Graphen Nanoribbons zeichnen sich durch eine hohe strukturelle Qualität aus und zeigen außergewöhnliche Transporteigenschaften. Ballistischer Transport wurde sowohl bei Raum- als auch Tieftemperatur über Distanzen von einigen Mikrometern beobachtet. Der konstante Leitwert von $1\,e^2/h$ ist charakteristisch für einen vollständig spinpolarisierten Kanal. Ein zweiter ballistischer Transportkanal tritt nur über kurze Distanzen sowie bei erhöhten Temperaturen auf. Die beiden Kanäle unterscheiden sich hinsichtlich Temperatur- und Lokalisierungsverhalten fundamental voneinander. Weder die Existenz zweier unterschiedlicher ballistischer Moden, noch die Beobachtung ballistischer Transportphänomene bei Raumtemperatur wurden durch theoretische Vorhersagen bisher erfasst.

Der zweite Ansatz nutzt die gezielte Interkalation von Germanium zwischen die Graphenschicht und das Siliziumcarbid Substrat. Hierdurch entstehen koexistierende, symmetrisch n- und p-dotierte Bereiche sowie p-n-Übergänge. Die laterale Homogenität der Dotierniveaus sowie die extrem geringe Breite der p-n-Übergänge konnten mit Hilfe von Rastertunnelspektroskopie nachgewiesen werden. Das elektronische Transportverhalten von Graphen p-n-Übergängen wird im Wesentlichen durch das so genannte Klein-Tunneln bestimmt, welches sich in einer Abhängigkeit der Transmissionswahrscheinlichkeit vom Einfallswinkel der Elektronen äußert. Durch die Serienschaltung von zwei p-n-Übergängen konnte diese Winkelabhängigkeit indirekt nachgewiesen werden.

Aus diesen Ergebnissen kann gefolgert werden, dass durch Selbstorganisation sowie Interkalation erzeugte Graphen-Nanostrukturen auf Siliziumcarbid Substraten sich durch eine hohe strukturelle als auch elektronische Qualität auszeichnen. Der Nachweis von mesoskopischen Transportphänomenen bei Raumtemperatur ist vielversprechend im Hinblick auf die Realisierung ballistischer elektronischer Bauteile.

Schlagwörter
epitaktisches Graphen, Graphen Nanoribbons, ballistischer Transport, Klein-Tunneln

ACRONYMS

1d	One dimension, one-dimensional
2d	Two dimensions, two-dimensional
3d	Three dimensions, three-dimensional
2pp	Two-point probe
4pp	Four-point probe
AFM	Atomic force microscopy
AGNR(s)	Armchair graphene nanoribbon(s)
AM – ZZGNR(s)	Antiferromgnetic zigzag graphene nanoribbon(s)
ARPES	Angle-resolved photo emission spectroscopy
CCS	Confined controlled sublimation
EDX	Energy-dispersive X-ray spectroscopy
EFM	Electrostatic force microscopy
FM – ZZGNR(s)	Ferromagnetic zigzag graphene nanoribbon(s)
GNC(s)	Graphene nanoconstriction(s)
GNR(s)	Graphene nanoribbon(s)
(L)DOS	(Local) density of states
LEED	Low energy electron diffraction
LEEM	Low energy electron microscopy
ML	Monolayer
PCC	Perfectly conducting channel
QFSMLG	Quasi-freestanding monolayer graphene
SEM	Scanning electron microscopy
s – SNOM	Scattering-type near field optical microscopy
STM	Scanning tunneling microscopy
STS	Scanning tunneling spectroscopy

TEM	Transmission electron microscopy
UHV	Ultra-high vacuum
VRH	Variable-range hopping
ZZGNR(s)	Zigzag graphene nanoribbon(s)

SYMBOLS

Ψ	Wave function
a	Lattice constant
α	Polarizability
C_i	Electron-phonon coupling constant
C	Capacitance
d	Distance between tip and sample
D_a	Acoustic deformation potential
$D(E)$	Density of states
$D_{n,p}$	Barrier length in n-p-n, p-n-p structures
Δ	Transport gap
E	Energy
E_d	Energetic location of Dirac point
E_f	Fermi level
E_g	Band gap
E_{qf}	Quasi-Fermi level
e	Elementary charge
$\vec{\epsilon}$	Electric field
ϵ_t	Permittivity
$f(E)$	Fermi-Dirac distribution
Φ	Work function
F	Potential slope at p-n interface
$F(E)$	Finesse
$\vec{G}$	Reciprocal lattice vector
G	Conductance
Γ	Terrace width

Γ_d	Dyne's smoothing parameter
h	Planck constant
$\hbar$	$h/2\pi$
I	Current
I_t	Tunneling current
I_D	Intensity of Raman D peak
I_G	Intensity of Raman G peak
$\vec{J}$	Current density
k	Wave vector
k_f	Fermi wave vector
k_B	Boltzmann constant
λ_e, λ_0	Mean free path
λ_Θ	Phase coherence length
λ_L	Laser wavelength
L	Probe spacing, sample length
L_0	Localization length
L_D	Medium distance between defects
M	Number of modes in a ballistic conductor
$M_{\mu\nu}$	Matrix element
m_e	Electron mass
μ	Mobility
n	Charge carrier density, electron density
ν	Frequency
p	Hole density
Π	Spring constant
$\vec{p}$	Momentum
Q	Amount of charge
q	Charge

P	Invasiveness of voltage probes
R	Resistance
R_l	Resistance per unit length
R_s	Sheet resistance
r	Tip radius
ρ	Resistivity
ρ_s	Mass density
$\vec{\sigma}$	Pauli matrices
T	Temperature
T_m	Characteristic Mott temperature
$T_{n,m}$	Transmission between probe n and m
t	Time
t_{np}	Length of a p-n junction
t_h, t_h', t_h''	Hopping energies
τ	Relaxation time
Θ	Phase, phase shift
$\vec{v}_d$	Drift velocity
$\vec{v}_f$	Fermi velocity
V	Voltage
V_b	Bias voltage
V_d	Bias voltage at Dirac point
V_g	Gate voltage
v_s	Sound velocity
W	Device width
Ξ	Diffusion coefficient

CONTENTS

Part I

INTRODUCTION AND PHYSICAL BACKGROUND

1

INTRODUCTION

Silicon technology has dominated electronic applications for more than 60 years now. However, its unbeatable position arises from the immense knowledge about silicon processing techniques as well as the vast amount of control over its properties, e.g. doping. On the other hand Silicon's electronic properties do not back up this status, they are rather good enough than ideal for the purpose of building electronic devices. An ideal future electronic device should feature high operating speed and low heat dissipation together with large range scalability at room temperature. With regards to these demands silicon technology already reaches its limits [1].

This shortcoming can be illustrated by the example of the mean free path, which describes the average distance between randomly distributed electronic scatterers within a material. It is one of the most important parameters to describe the quality of an electronic conductor. If the size of an electronic device is below the mean free path, scattering occurs only at the device boundaries, the transport is referred to as ballistic. Since the electrons are not scattered randomly, ballistic devices should reach extremely high operating speeds as well as fast response times. Silicon, on which most electronic applications are based, has a mean free path of only a few nm. Hence electrons transported through these devices encounter a large number of scattering events and the transport regime is called diffusive. Other compound semiconductors such as GaAs exhibit mean free paths up to 200 nm at room temperature. However, disadvantages such as high processing costs or a low hole mobility (about $400\,\mathrm{cm}^2/\mathrm{Vs}$ in GaAs compared to about $500\,\mathrm{cm}^2/\mathrm{Vs}$ in Si) have prevented the replacement of silicon by compound semiconductors. Despite the fact that their realization is unlikely with silicon technology, a number of ballistic electronic devices have been proposed and realized, e.g. ballistic rectifier [2] or ultra-fast switches [3, 4]. They are synthesized usually by using GaAs/AlGaAs heterostructures which host a two-dimensional electron gas (2DEG) at their interface. Mean free paths exceeding 160 µm have been reported at temperatures as low as 0.1 K [5]. Heterostructures combining AlGaAs and InGaAs have shown ballistic transport properties even at room temperature [6]. Unfortunately, the rather complex device architecture and synthesis make it unlikely that such heterostructures will be used for more than niche applications.

On the other hand, carbon-based electronics might be a viable candidate as replacement for silicon in high performance applications [7]. Carbon is found in diverse structures such as diamond, graphite, buckyballs, carbon nanotubes (CNTs) or graphene. This diversity in structure comes with a corresponding diversity of, partially even unique, electronic properties. Especially CNTs were believed to catalyze the development of carbon-based electronics since their discovery in 1991 [8]. Their 1d nature and the symmetry of the band structure made them a promising candidate for ballistic conduction with large mean free paths due to the absence of backscattering [9, 10]. Indeed, room-temperature ballistic transport over length scales of several µm has been observed [11, 12]. CNTs of specific crystallographic orientations were also predicted to exhibit band gaps scaling with the tube diameter [13, 14] and CNT field-effect transistors were reported early on [15]. Despite all these promising progress, CNTs are of no relevance in the commercial production of electronic devices until now. Mass production of CNTs with precise positioning as well as with suitable quality for device building has not been achieved yet.

Graphene, a single plane of graphite, is a further candidate for future high performance electronics. Its peculiar band structure was first calculated by Wallace in 1947 [16] and the prediction of an effective mass of zero for charge carriers in graphene made its synthesis highly desirable. Experimental research was triggered mainly by the development of relatively easy production methods such as epitaxial growth on silicon carbide (SiC) [17] or mechanical exfoliation from graphite crystals [18]. Early observations of the predicted half-integer quantum Hall effect [19], even at room temperature [20] as well as ultra-high carrier mobilities [21] of about $\mu_e = 200.000\,\mathrm{cm}^2/\mathrm{Vs}$ underlined the tremendous potential of graphene. Further unique phenomena such as a realization of the Klein paradox [22], reflectionless tunneling of a relativistic electron through a potential barrier, were proposed [23, 24] and experimentally realized [25, 26].

Since a graphene sheet is a zero-gap semiconductor possible ways of introducing band gaps into the material came soon in the focus of research. Band gaps are needed in all kinds of electronic devices, especially transistors, where high on-off ratios are essential. The possibility to combine the high electron mobility, already present in pristine graphene, with a band gap seemed promising. One of the most common approaches for band gap engineering is the confinement of electrons in narrow ribbons of graphene, the so called graphene nanoribbons (GNRs). The confinement energy gap arising in such ribbons oriented in the armchair direction (armchair referring to the shape of the edge), was predicted to scale with its width [27]. Hence their use in transistors seemed to be an obvious choice. On the other hand, GNRs oriented in the so called zigzag direction exhibit electronic states localized in their edges [28, 29]. Perfectly conducting channels were predicted for well-ordered zigzag GNRs which allow electron transport over large length scales without backscattering [30]. This makes GNRs a further candidate for realizing room temperature ballistic conduction.

Unfortunately, the synthesis of high quality graphene nanostructures turned out to be difficult by means of conventional lithography [31–34]. Although alternative etching techniques such as nanoparticle assisted hydrogen etching [35] or lithography by means of a scanning tunneling microscope (STM) [36] were shown to create nanostructures with well-ordered edges [37, 38] their relevance is restricted to scientific use. Hence a non-destructive synthesis process, easily adoptable to industrial production scales would be of great benefit. In this thesis two routes towards graphene nanostructures by self-organizational processes will be discussed. Both rely on the epitaxial growth of graphene on SiC which was already reported in 1975 [39] and shown to

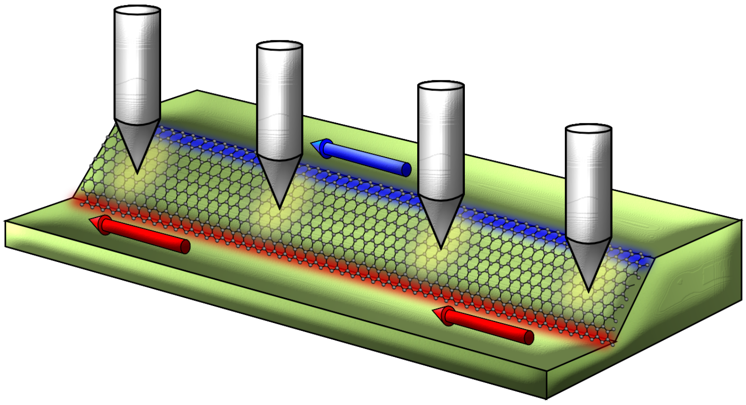

Figure 1.1: Artistic view of four STM tips contacting a graphene nanoribbon grown on a SiC nanofacet.

produce graphene of very high quality [17, 40, 41]. Furthermore, epitaxial growth was proposed early on to be the only viable route towards graphene based electronic applications [42]. One major advantage of this system is that graphene nanostructures can be selectively grown in the desired shape rather than cut from an extended sheet. This is possible via preprocessing of the SiC surface by using AlN caps [43] or by inducing inclined nanofacets which trigger preferential graphene growth [44]. Furthermore, tuning the graphene/SiC interface, e.g. by intercalation of foreign atoms [45–47] gives rise to modifications of the electronic structure of graphene, e.g. doping. Selective intercalation can hence induce nanostructures such as potential barriers [40] on the lattice scale. Both routes, intercalation and growth via self-assembly, shall be explored in this thesis. It will be demonstrated that they are not only viable in order to enter the ballistic transport regime, but furthermore provide electronic nanostructures of exceptional quality.

Despite the quality of the electronic system itself, defining suitable contacts is a serious issue when dealing with high mobility samples. The resist used for the lithographic definition of contacts is known to induce unintentional doping in graphene [48–50]. On the other hand, studying ballistic systems requires a careful analysis of parasitic contact resistances and hence maximum control over the interface between contact and conductor. To avoid lithographic contacts, a multi-tip STM will be used in this thesis. It hosts four independent tips which can be used as current and voltage probes. This ensures a maximum amount of operational freedom concerning probe geometries and provides fast access to the intrinsic transport properties of any kind of material. Multi-tip STMs were shown to be suitable to carry out surface transport investigations on numerous systems such as graphene [51], CNTs [52] or silicide nanowires [53] and even to detect spin signals in Bi films on Si(111) surfaces [54]. However ballistic transport has not been studied so far by means of a multi-tip STM. This thesis will provide evidence for the first time that mesoscopic transport phenomena are indeed accessible with a multi-tip STM.

This thesis is divided into 5 parts. After the introduction, part I continues with chapter 2 which gives a brief overview over the basics of electronic transport. Ballistic as well as diffusive transport will be compared and the main hallmarks of these two transport regimes will be highlighted. Special focus is laid on the characteristics of four-point probe measurements as the main investigation tool used in this thesis. In chapter 3 the electronic properties of graphene and GNRs shall be reviewed, focusing especially on the peculiar bandstructures of these systems as well as their transport properties. The main experimental setup, the multi-tip STM in combination with a high resolution scanning electron microscopy (SEM), will be briefly introduced in chapter 4.

The first experimental results will be presented in part II. Epitaxial ML graphene shall be investigated in detail in chapter 5 as a reference system for the experimental setup as well as for the following investigations of graphene nanostructure. A vast number of techniques, e.g. SEM, Raman, tunneling spectroscopy or local transport, will be introduced and shown to provide reliable access to the electronic properties of graphene based systems. This knowledge will be further deepened in chapter 6 where defective graphene samples shall be investigated. Nanoinhomogeneities as well as substrate step edges will be identified as major sources for electron scattering.

Part III then turns to the nanostructuring of graphene. A self-assembling growth process of epitaxial graphene nanoribbons on pre-processed SiC surfaces will be presented and reviewed in chapter 7. The outstanding quality of these ribbons will be underlined by tunneling spectroscopy and STM. Special focus is laid again on electronic as well as transport characteristics. Evidence will be provided that the ballistic transport regime is indeed accessible in these structures. In order to gain a better understanding of the exceptional ballistic transport characteristics, chapter 8 is devoted to their detailed characterization. Two different ballistic channels will be identified, which exhibit fundamentally different temperature dependence as well as localization behavior. The extreme robustness of one of the channels against temperature and disorder lets it even survive structural modification of the ribbons. This will be demonstrated in chapter 9 where narrow constriction are patterned into the sidewall ribbons by STM lithography. Coherent electronic transport serves as fingerprint for the high electronic and structural quality of these constrictions, and will be evaluated experimentally and theoretically.

In a further approach, the interface of the epitaxial graphene will be locally modified by the intercalation of Germanium. The results will be shown in part IV. The creation of p-n junctions will be demonstrated in chapter 10. Due to the chemical rather than electrostatic nature of gating, the junctions can be made ultra narrow and consequently fully ballistic. The extremely high homogeneity of the intercalated graphene as well as the p-n potential barriers provide easy access to Klein tunneling phenomena. They will be probed by local transport in chapter 11 in single as well as serial connections of multiple p-n interfaces.

In part V, a summary of the content of this thesis will be provided in chapter 12 together with an outlook on future follow-up research projects in chapter 13.

A brief description of all measurement methods which were used during the work on this thesis can be found in the appendix A.

2

ELECTRONIC TRANSPORT

The transport properties of any nanodevice depend critically on characteristic length scales, namely the electronic mean free path λ_e and the phase coherence length λ_Θ. The electronic mean free path is the distance which an electron can travel between scattering events, while the phase coherence length is the distance over which quantum coherence is preserved. For simplicity the nanodevice shall be represented by two ideal contacts (meaning ideally injecting and extracting current) connected by an active region of length L and width W limiting the current flow through the system due to λ_e and λ_Θ. In this simple picture three transport regimes can be identified. First, if the electronic mean free path as well as the phase coherence length are much shorter than the width and length of the active region, a large number of elastic and inelastic scattering events occur while the electron travels through the sample (cf. fig. 2.1(a)). This transport regime is called diffusive and can be described essentially by Boltzmann theory, which will be discussed later on. Increasing the mean free path and the phase coherence length such that $W \ll \lambda_e < L \ll \lambda_\Theta$ leads to the second transport regime called quasi-ballistic. As depicted in fig. 2.1(b) the electron undergoes less elastic and no inelastic scattering. Hence, transport is phase coherent as well as ballistic in one direction. Increasing the mean free path further, finally, $W, L \ll \lambda_e, \lambda_\Theta$ and the system is fully ballistic. The only scattering events that occur are reflections from the boundaries of the active region. This means that the electron trajectories can be controlled by an appropriate shape of the device.

From these first considerations it is clear that the ballistic transport regime can be reached via two ways, increasing the mean free path of the electrons or decreasing the size of the sample. The first approach will be realized later on in part III using sidewall graphene nanoribbons with mean free paths in the order of several µm. On the other hand, in part IV ballistic transport through graphene p-n junctions will be presented which was realized by an extreme narrowing of the lateral dimension of the p-n interface. In the following, basic concepts of electronic transport, which will be needed for the interpretation of the measurements later on, shall be discussed in more detail.

2.1 DIFFUSIVE TRANSPORT

Focusing again on the simple picture of a conductor connected to two ideal contacts (fig. 2.2(a)), the corresponding band diagram under application of an external bias

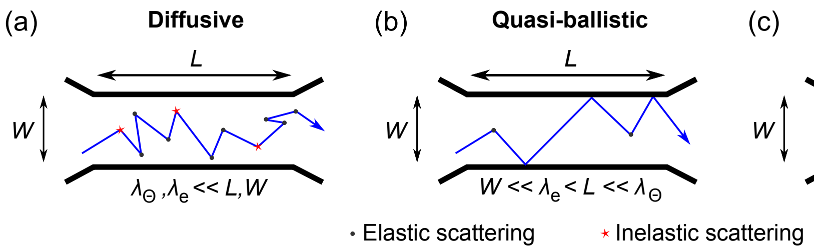

Figure 2.1: Schematic illustration of electron trajectories in the (a) diffusive, (b) quasi-ballistic and (c) ballistic transport regime.

voltage is shown in fig. 2.2(b). The bias voltage V causes an electric field $\vec{\epsilon} = \hat{x}V/L$ which accelerates the electrons in the conductor. In the diffusive transport regime the mean drift velocity is given by

$$\vec{v}_d = \mu\vec{\epsilon} \tag{2.1}$$

with μ being the mobility of charge carriers. A current density $\vec{J}$ can be defined as the amount of charge dQ which flows through the conductor of width W in time dt

$$\vec{J} = \hat{x}\frac{dQ}{dt}W\,. \tag{2.2}$$

It is obvious that $dQ = n\,q\,v_d\,dt\,/\,W$ [55] with a carrier concentration n. Hence, the current density can be written as

$$\vec{J} = n\,q\,\vec{v}_d\,. \tag{2.3}$$

On the other hand, following Ohm's law the current density is related to the electric field via

$$\vec{J} = \sigma\vec{\epsilon}\,. \tag{2.4}$$

This results finally in the well-known expression for the conductivity

$$\sigma = q\,n\,\mu\,. \tag{2.5}$$

Some further remarks are required for the case of a degenerate conductor at low temperatures. The expression of the current density $\vec{J}$ in eq. 2.3 is valid for any homogeneous conductor and implies that all conduction electrons are contributing to the drift current. However at low temperatures ($k_BT \ll E_f - E_0$) the measurable net current is only carried by the electrons energetically close to the Fermi energy [56]. This is depicted in the dispersion relation in fig. 2.2(c). An electric field $\vec{E}$ applied to the system shifts the distribution function of the electrons in direction of the field. This defines quasi-Fermi levels E_{fq}^{+} for electrons moving in the direction of $\vec{E}$ and E_{fq}^{-} for the opposite direction. Electrons in states below E_{fq}^{-} can carry no current because these states are completely filled. For $E_{fq}^{-} < E < E_{fq}^{+}$ the $-k$ states are empty but the

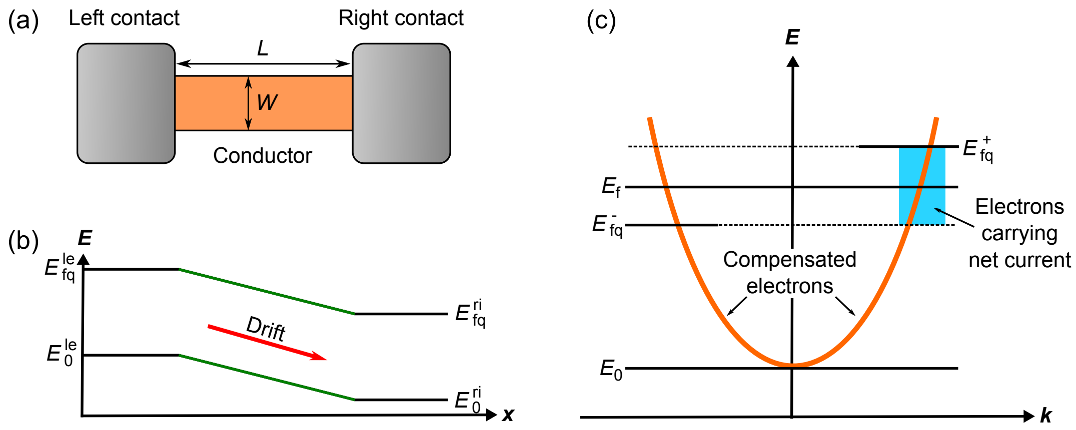

Figure 2.2: (a) Schematic illustration of a conductor with left and right contact. (b) Band diagram under application of a bias voltage between the contacts showing the origin of drift current. E_{fq}^{le} (E_{fq}^{ri}) denotes the quasi-Fermi levels of the left (right) contact and E_0^{le}, E_0^{ri} the bottom of the subband. (c) Dispersion relation $E(k)$. Electrons carrying a net current are indicated in light blue. Adapted from [56].

$+k$ states are filled. Hence, these electrons can carry a net current. The separation of the quasi Fermi levels is related to the electric field by the following expression [56]

$$E_{fq}^{+} - E_{fq}^{-} = 2e\,\epsilon\,\lambda_e\ . \tag{2.6}$$

This result is intuitively clear since it means that the separation of the quasi-Fermi energies is proportional to the energy an electron gains in the electric field while traveling a distance as long as its mean free path. The fact that the current is carried only by electrons close to the Fermi level is a major simplification for the understanding of transport properties at low temperatures, because not all electrons but only those close to the Fermi energy need to be considered [56].

2.1.1 FOUR-POINT PROBE MEASUREMENTS ON DIFFUSIVE CONDUCTORS

Measuring the resistance R of a diffusive conductor is usually done by using a four-point probe (4pp) setup as depicted in fig. 2.4(a). The reason for the usage of four probes becomes immediately clear by comparing it with a two-point probe measurement (2pp). In this case, every probe serves as current (I) source as well as voltage (V) probe. The overall resistance is

$$R = \frac{V}{I} = 2R_{\text{probe}} + 2R_{\text{contact}} + R_{\text{sample}} \tag{2.7}$$

and hence the sum of the resistance of the probes itself R_{probe}, the contact resistance R_{contact} and the resistance of the sample R_{sample}. Thus, the determination of R_{sample} requires knowledge of the exact values of R_{probe} and R_{contact} which is hard to achieve experimentally [57]. In contrast to the 2pp case, in a 4pp setup not all probes serve

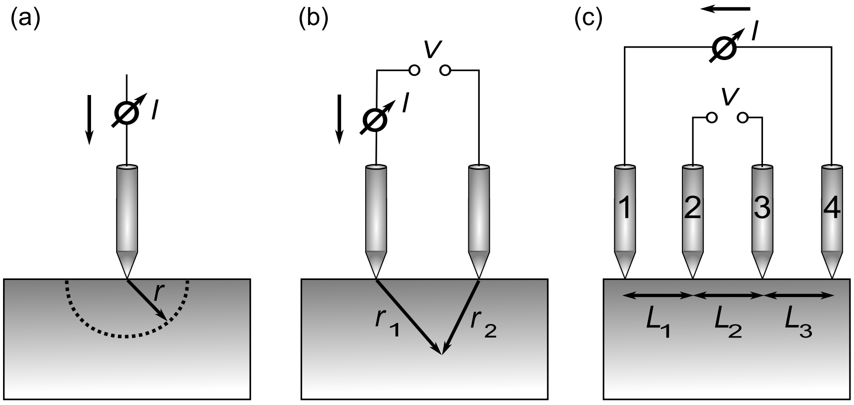

Figure 2.3: Schematic representation of the setup of (a) one (b) two and (c) four probes for the calculation of the resistance in a 4pp measurement (cf. eq. 2.16).

as current and voltage probes. Two of the probes drive a current through the sample while the voltage drop is measured simultaneously with the other two probes as depicted in fig. 2.4(a). The current flowing through the voltage probes is practically zero due to the high input impedance of the voltmeter. Hence, the voltage drop over probes and contacts can be neglected and the measured resistance is equal to R_{sample}. For an actual transport measurement, it is important to keep in mind that this can of course only hold true as long as the input impedance of the voltmeter is large compared to the contact resistance.

To calculate the resistivity in a 4pp measurement, a uniform and infinite sample is assumed. For a single tip the corresponding electric field is given by

$$\vec{\epsilon} = J\rho = -\frac{dV}{dr} \tag{2.8}$$

where ρ is the resistivity of the sample and r the distance to the tip. A corresponding sketch is shown in fig. 2.3(a). The current density can be expressed as

$$J = \frac{I}{2\pi r^2} \ . \tag{2.9}$$

This allows to calculate the voltage in distance r from the tip from

$$\int_0^V dV = -\frac{I\rho}{2\pi}\int_0^r dr \frac{1}{r^2} \ . \tag{2.10}$$

This results in

$$V = \frac{I\rho}{2\pi r} \ . \tag{2.11}$$

In the same manner, the voltage in the 2pp setup shown in fig. 2.3(b) can be calculated to

$$V = \frac{I\rho}{2\pi}\left(\frac{1}{r_1} - \frac{1}{r_2}\right) . \tag{2.12}$$

Hence, in the 4pp setup shown in fig. 2.3(c), the voltage at tip 2 is given by

$$V_2 = \frac{I\rho}{2\pi}\left(\frac{1}{L_1} - \frac{1}{L_2 + L_3}\right) \tag{2.13}$$

and at tip 3 by

$$V_3 = \frac{I\rho}{2\pi}\left(\frac{1}{L_1 + L_2} - \frac{1}{L_3}\right) . \tag{2.14}$$

The overall voltage is then given by

$$V = \frac{I\rho}{2\pi}\left(\frac{1}{L_1} - \frac{1}{L_2 + L_3} - \frac{1}{L_1 + L_2} + \frac{1}{L_3}\right) . \tag{2.15}$$

In the special case of an equidistant probe spacing ($L = L_1 = L_2 = L_3$), the measured resistance simplifies to

$$R = \frac{V}{I} = \frac{\rho}{2\pi}\frac{1}{L} . \tag{2.16}$$

2.1.2 GEOMETRIC CORRECTION FACTORS

It is important to note that eq. 2.16 is only true for an infinitely large sample with a homogeneous conductivity. As soon as L is in the order of the geometric dimensions of the sample, correction factors F_1, F_2, F_3 need to be taken into account ($\rho = R\,F_1 F_2 F_3$). The most important case for the measurements discussed later on, is the consideration of a sample with a thickness $d \ll L$. This corresponds to two-dimensional conductivity. The correction factor F_1 accounting for a small sample thickness is in general given by [57]

$$F_1 = \frac{d/L}{\ln\left(\frac{\sinh\left(\frac{d}{L}\right)}{\sinh\left(\frac{d}{2L}\right)}\right)} . \tag{2.17}$$

In the case of $d \ll L$, eq. 2.17 reduces to

$$F_1 = \frac{d/L}{2\ln(2)} . \tag{2.18}$$

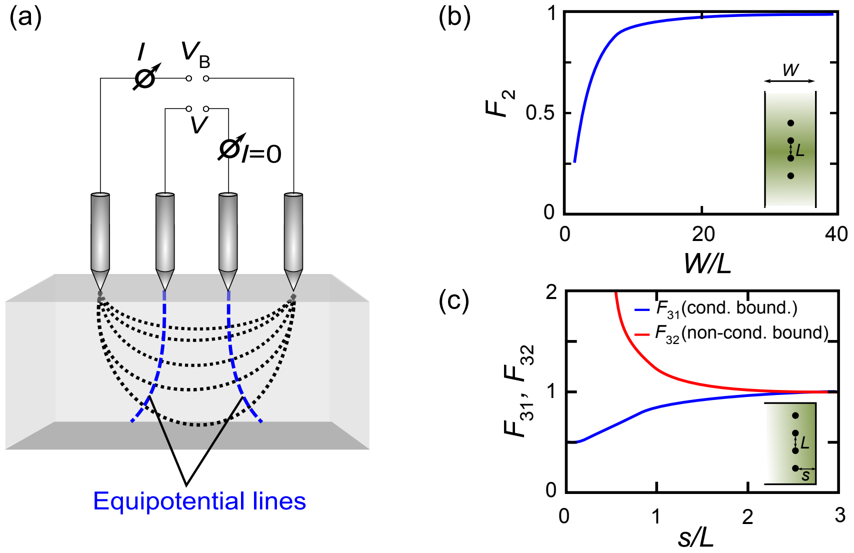

Figure 2.4: (a) Schematic of a 4pp measurement in linear configuration. Current paths are shown as black dotted lines. (b) Correction factor F_2 for a 4pp measurement on a square sample with width W and probe spacing L. (c) Correction factor F_{31} and F_{32} for a finite distance of the probes to a conducting and non-conducting sample boundary. s is the distance of the probes relative to the edge of the sample.

Typically, a two-dimensional sheet is characterized by its sheet resistance $R_s = \rho/d$, the resistivity of the sheet averaged over its thickness. Using eq. 2.18, the following expression for the sheet resistance can be obtained

$$R_s = \frac{\pi}{\ln(2)} R \,. \tag{2.19}$$

Thus in 2d the resistance is independent of the probe spacing. This is in contrast to the three-dimensional case where $R \sim 1/L$ and also to diffusive transport in one dimension where $R \sim L$ [58].

The implementation of additional correction factors F_2 and F_3 is necessary if the lateral sample dimensions are in the order of the probe spacing (F_2) or if the probes are placed close to the boundaries of the sample (F_3). Examples for F_2 and F_3 are plotted in fig. 2.4(b, c). Since finding the exact correction factors can be difficult and error-prone, a widely used alternative approach for the determination of sheet resistances is the so called dual configuration method. It relies on the measurement of current-voltage characteristics in two measurement configurations in which current and voltage probes are interchanged. An example for an appropriate combination of configuration A and B is shown in fig. 2.5. From these measurements, the sheet resistance can be simply calculated solving the expression [59]

$$e^{\frac{2\pi R_A}{R_s}} - e^{\frac{2\pi R_B}{R_s}} = 1 \tag{2.20}$$

where R_A (R_B) is the resistance measured in configuration A (B). Besides an easily accessible sheet resistance, the dual configuration also provides the possibility to

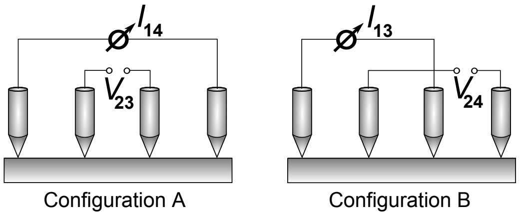

Figure 2.5: Probe configurations A and B used for dual configuration measurements.

discriminate between 2d and 1d conductance. A continuous conductive (2d) sheet yields a resistance ratio $R_A/R_A = \ln(4)/\ln(3)$ while 1d conductance manifests in a resistance ratio $R_A/R_B = 1$ [60].

A final remark shall be made on behalf of anisotropic conductivity in a thin sheet. In case that the conductivity of the sheet is homogeneous, the anisotropy is an intrinsic property of the sheet itself. The measured resistance in a linear 4pp arrangement can be deduced from the Poisson equation and is given by [61]

$$R = \frac{\ln(2)}{\pi\sqrt{\sigma_x \sigma_y}} \tag{2.21}$$

for probe arrangement along the x-axis of the sample. It is independent of the orientation of the sample [62]. The situation is different for an inhomogeneous surface where the anisotropy stems from extrinsic influences such as step edges. Here, the measured conductivity depends on the orientation of the sample relative to the probes [63]. Thus, by means of a linear 4pp measurement the different sources for anisotropy can be distinguished. However, it is not suitable to determine the exact values of the direction dependent conductivities σ_x, σ_y of a homogeneously conductive sheet. Only a geometrical mean value of the conductivities can be obtained. This problem can be solved by arranging the probes in a square rather than linear configuration. Two adjacent probes serve as current source and the voltage is measured with the other two probes. In such a square 4pp setup the measured resistance for alignment of the current probes along the x-axis is given by [62]

$$R = \frac{1}{2\pi\sqrt{\sigma_x \sigma_y}} \ln\left(1 + \frac{\sigma_x}{\sigma_y}\right) . \tag{2.22}$$

Alignment along the y-axis interchanges σ_x and σ_y in the equation. Hence, two different resistance values are measured for different alignment of the probes which allows to obtain the exact values of σ_x and σ_y, in contrast to the linear setup.

2.2 BALLISTIC TRANSPORT

As soon as the mean free path of the electrons is smaller than the dimensions of the samples the electrons start to travel ballistically. This has important consequences on conductance measurements performed in this regime. The same model which was

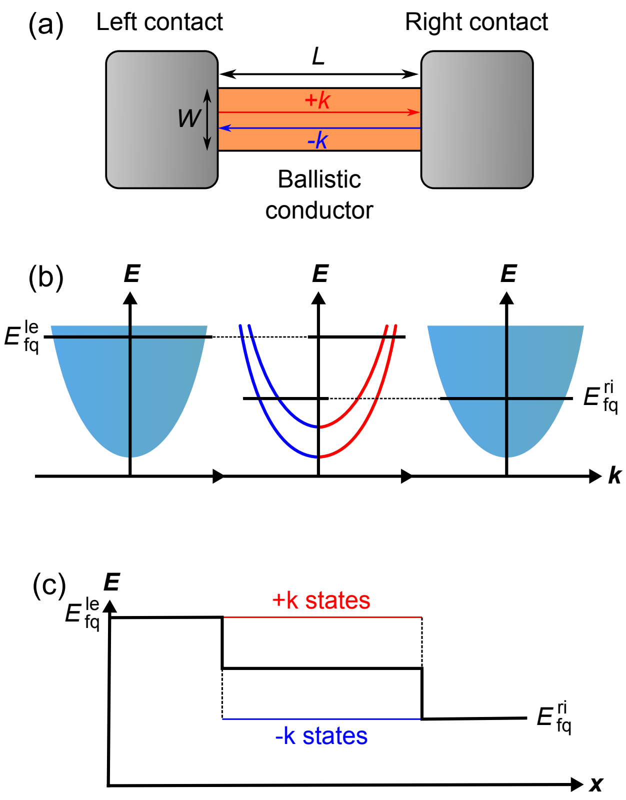

Figure 2.6: (a) Schematic illustration of a ballistic wire with left and right contact. (b) Electron dispersion within the contacts and the ballistic wire. Within the contacts the density of subbands is extremely high such that they appear continuous. The narrow wire exhibits only few subbands. (c) Band diagram showing the variation of the quasi-Fermi level E_{fq} along contacts and wire. Adapted from [56].

used before, a conductor connected to two ideal contacts, is again sufficient for the following considerations. The conductor is now narrow, meaning that the dispersion relation consists of only a few modes and $\lambda_e \gg L, W$. The application of a bias voltage to this conductor results in a splitting of the quasi-Fermi levels of the left and right contact $E_{fq}^{le} - E_{fq}^{ri} > 0$ (cf. fig. 2.6(b)). Since the contacts are assumed to be ideal no reflection occurs when electrons enter the conductor. This has the consequence that $+k$ ($-k$) states in the conductor are occupied only by electrons from the left (right) contact. Hence, an electron coming from the left (right) contact populates a $+k$ ($-k$) state in the conductor and leaves the conductor into the right (left) contact without reflection. Inside the contacts, the subband density is very high resulting in almost equal quasi-Fermi levels for $+k$ and $-k$ states independent of the current flow. Inside the narrow conductor, where only a few subbands are present, an applied bias voltage results in a splitting of the quasi Fermi-levels for $+k$ and $-k$ states $E_{fq}^{+} - E_{fq}^{-} = eV$. Furthermore, the quasi-Fermi level of the $+k$ ($-k$) states in the conductor is equal to the quasi-Fermi level in the left (right) contact [56] as shown in fig. 2.6(c). This is reasonable since a shift of the quasi-Fermi level of the left (right) contact has no effect on the quasi-Fermi level of the $-k$ ($+k$) states in the conductor. Thus, a shift of the quasi-Fermi energy of the left (right) contact has to result in an equal shift of the $+k$ ($-k$) states. Upon these consideration the calculation of the current is straightforward by simply summing up the currents carried by the individual subbands. The net current is the difference between the right moving electrons generating current I_+ and the left moving electrons (I_-)

$$I = I_+ - I_- = \frac{e}{L}\sum_k v\, f_+(E) - \frac{e}{L}\sum_k v\, f_-(E) \tag{2.23}$$

with f_+ (f_-) being the Fermi-Dirac distribution of the $+k$ ($-k$) states. By using

$$v = \frac{1}{\hbar}\frac{\partial E}{\partial k} \tag{2.24}$$

and converting the sum into an integral

$$\sum_k \rightarrow 2\frac{L}{2\pi}\int dk \tag{2.25}$$

eq. 2.23 converts to

$$I = \frac{2e}{h}\int_0^\infty (f_+(E) - f_-(E))\, M(E)\, dE = \frac{2e}{h} M(E_{fq}^{le} - E_{fq}^{ri})\,. \tag{2.26}$$

The factor of 2 in eq. 2.25 accounts for the spin degeneracy. M is the number of modes within the conductor. In the last step, M is assumed to be constant in the energy range $E_{fq}^{le} > E > E_{fq}^{ri}$. The conductance can then be easily calculated to

$$G = \frac{I}{V} = \frac{2e}{h} M \frac{(E_{fq}^{le} - E_{fq}^{ri})}{V} = \frac{2e}{h} M \frac{eV}{V} = \frac{2e^2}{h} M\,. \tag{2.27}$$

Hence the conductance of a ballistic wire is quantized and increases with the number of modes.

So far, only the value of the conductance was considered but not the location of the associated voltage drop. As already discussed, the quasi-Fermi level of the $+k$ ($-k$) states is equal to that of the left (right) contact as shown in fig. 2.6(c). This implies that the average value of the quasi-Fermi level shows an equal drop at the conductor/contact interface. Thus the resistance of a ballistic wire is caused by a voltage drop at the interface. The resistance of a ballistic conductor is solely a contact resistance.

Up to now, perfectly conducting channels were assumed where every electron injected in the left transmits to the right. For imperfect channels eq. 2.27 can be written as a sum over the individual channels with transmission probability T_n [56]

$$G = \frac{2e^2}{h}\sum_{n=1}^{M} T_n\,. \tag{2.28}$$

This formula is known as the Landauer expression.

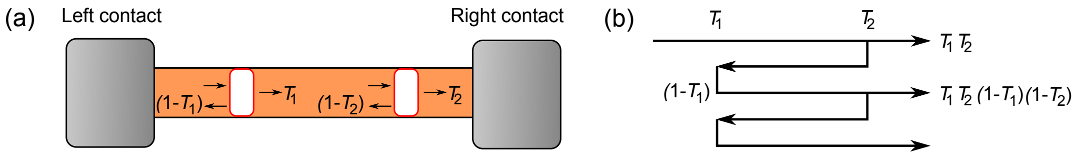

Figure 2.7: (a) Schematic illustration of a ballistic wire with two scattering centers with transmission probabilities T_1 and T_2 in serial connection. (b) The net transmission through the two scattering centers is obtained by summation over the transmission and reflection coefficients. Adapted from [56].

2.2.1 MULTIPLE SCATTERERS

Now, a serial connection of conductors with different transmission probabilities T can be considered. The setup is depicted in fig. 2.7(a) for two scattering centers with transmission probabilities T_1 and T_2. In the trivial case of $T_1 = T_2 = 1$ the measured resistance is the same as in absence of the two scattering centers $R = h/2e^2$. If now $T_1, T_2 < 1$, a simple guess would be to just multiply the transmissions to get the overall transmission. But this would only account for the direct transmission of an electron and completely neglect multiple reflections [56]. It is indeed necessary to sum up all individual transmission probabilities for zero and multiple reflection to get the overall transmission. This is indicated in fig. 2.7(b). Hence, the overall transmission is given by

$$\begin{aligned} T = T_1\,T_2 + T_1\,T_2\,(1-T_1)\,(1-T_2) + T_1\,T_2\,(1-T_1)^2\,(1-T_2)^2 + \ldots \\ = T_1\,T_2 \sum_{n=0} \left((1-T_1)(1-T_2)\right)^n . \end{aligned} \tag{2.29}$$

Since $(1-T_1)(1-T_2) < 1$ the sum is a simple geometric series which yields

$$T = \frac{T_1\,T_2}{1-(1-T_1)(1-T_2)} . \tag{2.30}$$

This expression can be written as

$$\frac{1-T}{T} = \frac{1-T_1}{T_1} + \frac{1-T_2}{T_2} . \tag{2.31}$$

This additive behavior of two scattering centers can be easily expanded to N scattering centers, each having a transmission of T_N. This results in

$$\frac{1-T}{T} = N\frac{1-T_N}{T_N} \tag{2.32}$$

which yields a total transmission of

$$T(N) = \frac{T_N}{N(1-T_N)+T_N} . \tag{2.33}$$

Eq. 2.33 can be rewritten, relating T to the length of the conductor. Defining

$$\lambda_0 \equiv \frac{T_N}{\frac{N}{L}(1-T_N)} , \tag{2.34}$$

T(L) is given by

$$T(L) = \frac{\lambda_0}{L+\lambda_0} . \tag{2.35}$$

The quantity of λ_0 is directly related to the mean free path λ_e. The probability of scattering by an individual scatterer is $(1-T_N)$. Assuming that $T_N \approx 1$ it follows that $(1-T_N)N/L\,\lambda_e \approx 1$. Hence,

$$\lambda_e \approx \frac{1}{\frac{N}{L}(1-T_N)} \approx \lambda_0 . \tag{2.36}$$

This is of course only true as long as the individual scatterers have a transmission probability close to 1.

Using eq. 2.33 the resistance of a ballistic conductor can now be written as

$$R = \frac{h}{2e^2M}\frac{1}{T} = \frac{h}{2e^2M} + \frac{h}{2e^2M}\frac{N(1-T_N)}{T_N} , \tag{2.37}$$

splitting it up into the contact resistance $h/2e^2M$ and the resistance of the conductor itself. Furthermore, with eq. 2.35 the resistance can be written as a function of the conductor length L in the following way

$$R(L) = \frac{h}{2e^2M}\frac{1}{T} = \frac{h}{2e^2M} + \frac{h}{2e^2M}\frac{L}{\lambda_0} = \frac{h}{2e^2M}\left(1+\frac{L}{\lambda_0}\right) . \tag{2.38}$$

Thus, for additional scatterers present in the ballistic conductor, the resistance is expected to linearly increase with the wire length with an offset of $h/2e^2M$ at $L=0$.

2.2.2 LOCALIZATION

So far, the possibility of interference between scatterers was neglected and the electrons were treated as classical particles. However, this is not sufficient in a sample where the phase coherence length exceeds the mean free path. In this case the sample can be treated as series of phase-coherent units each containing many elastic scatterers [56]. The interferences between the scatterers lead to an overall increased resistance of the conductor which is called localization. In the absence of quantum interferences eq. 2.38 was derived to relate the resistance R with the conductor length L, by making use of the incoherent serial connection of scatterers according to eq. 2.30. Such an expression can be found in a similar manner including quantum interference. A coherent serial connection of two scatterers can be described by [56, 64]

$$T = \frac{T_1\,T_2}{1-2\sqrt{(1-T_1)(1-T_2)}\cos(\Theta)+(1-T_1)(1-T_2)} \tag{2.39}$$

where Θ is the phase shift acquired from scattering with both scatterers. The resistance R_Θ can be found by averaging over Θ

$$R_\Theta = \left\langle \frac{1-T}{T} \right\rangle = \int \frac{1}{2\pi} \frac{1-T}{T} d\Theta = \frac{1-T_1}{T_1} + \frac{1-T_2}{T_2} + 2\frac{1-T_1}{T_1}\frac{1-T_2}{T_2} \,. \tag{2.40}$$

R_Θ is normalized to $h/2e^2$. Eq. 2.40 implies that $R_\Theta = R_1 + R_2 + 2R_1R_2$, a combination of the individual resistances of the two scatterers. If now a short section of length ΔL is added to a section of length L, and $R_1 = R(L)$ and $R_2 = \Delta L/\lambda_0$, this results in

$$R(L+\Delta L) = R(L) + \frac{\Delta L}{\lambda_0}(1 + 2R(L)) \tag{2.41}$$

and hence, in the differential equation [56]

$$\frac{dR}{dL} \approx \frac{1+2R}{\lambda_0} \,. \tag{2.42}$$

Its solution is given by [65]

$$R(L) = \frac{1}{2}\left(e^{\frac{2L}{\lambda_0}} - 1\right) . \tag{2.43}$$

The resistance R(L) is still normalized to $h/2e^2$. Eq. 2.43 predicts an exponential increase of the resistance rather than a linear one if the wire is long enough. It should be kept in mind that the averaging over individual scatterers of course only works as long as their scattering behavior is not too different. The scaling law given in eq. 2.43 is a mean resistance value and cannot account for all possible scattering arrangements. Since the resistance varies exponentially with length, adding an additional resistor to a given one can result in large fluctuations of the measured resistance. A detailed discussion concerning these issues can be found in [64, 66].

As long as the length of a phase coherent conductor is much smaller than the localization length $L_0 = M\lambda_0$, where M denotes the number of modes in the wire, the conductor is called weakly localized. In this case, eq. 2.43 can be expanded in a Taylor series [56]

$$R(L) \sim \frac{L}{L_0} + \left(\frac{L}{L_0}\right)^2 = R_{cl} + \Delta R. \tag{2.44}$$

Here, L_0 can be replaced with λ_0 in case of a single mode wire. The first term L/L_0 is the classical resistance $R_{cl} = L/L_0$ which increases linearly following Ohm's law, and the second term $\Delta R = R_{cl}^2$ is the correction due to quantum interference. Consequently, the corresponding correction of the conductance due to quantum interference can be written as

$$\Delta G = \frac{1}{R(L)} - \frac{1}{R_{cl}} = \frac{1}{R_{cl} + \Delta R} - \frac{1}{R_{cl}} \approx \frac{-\Delta R}{R_{cl}^2} = -1 \,. \tag{2.45}$$

Hence quantum interferences will reduce the resistance by $2\,e^2/h$ in the regime of weak localization.

If the phase coherence length exceeds the localization length, the system is called strongly localized. The disorder within the conductor is so strong that no diffusion of the electron waves is present any longer. One important step is now to relate the conductivity of a strongly localized system with its temperature. This can be done using the variable range hopping model by Mott [67]. An electron which is strongly localized close to the Fermi level can hop from one localized site to another when receiving a sufficient activation energy from a phonon or an external electric field. The hopping electron will always try to minimize the hopping distance r and the activation energy ΔE needed. Since these conditions will usually not be satisfied at the same time, an optimum hopping distance can be defined. This leads to a corresponding hopping probability

$$P \sim e^{-\frac{2L}{L_0}-\frac{\Delta E}{k_B T}}\,. \tag{2.46}$$

From here, the relation between conductivity and temperature can be derived to [67]

$$\sigma \sim e^{-\left(\frac{T_m}{T}\right)^{\frac{1}{\mathrm{dim}+1}}} \tag{2.47}$$

where dim denotes the dimension of the system and T_m is the characteristic Mott temperature. The Mott temperature is related to the localization length L_0 and the density of (defect) states at the Fermi energy $D(E_f)$. In 2d for example, this relation is given by [67, 68]

$$T_m = \frac{13.6}{k_B\,L_0^2\,D(E_f)}\,. \tag{2.48}$$

Hence, measuring the temperature dependent conductivity in the regime of strong localization is a possible pathway to deduce the dimensionality and the localization length of an electronic system.

2.2.3 FOUR-POINT PROBE MEASUREMENTS ON BALLISTIC CONDUCTORS

In section 2.1.1 a 4pp setup was identified as essential in order to obtain the exact conductivity of a sample without the parasitic influence of the contact resistances. In contrast, the previous section has shown that for a ballistic conductor the quantized contact resistance is actually the interesting property one wants to obtain. Hence measuring with only two contacts is sufficient to see the quantized conductance stemming from the ballistic nature of transport. Since only a contact resistance is present when measuring an ideal ballistic conductor, no dependency on the contact or probe spacing is expected (ideal referring to a transmission $T = 1$). A length dependence can be present in case of additional scatterers within the conductor (cf. eq. 2.38). But in this case the separation in contact resistance and resistance of the conductor itself is straightforward.

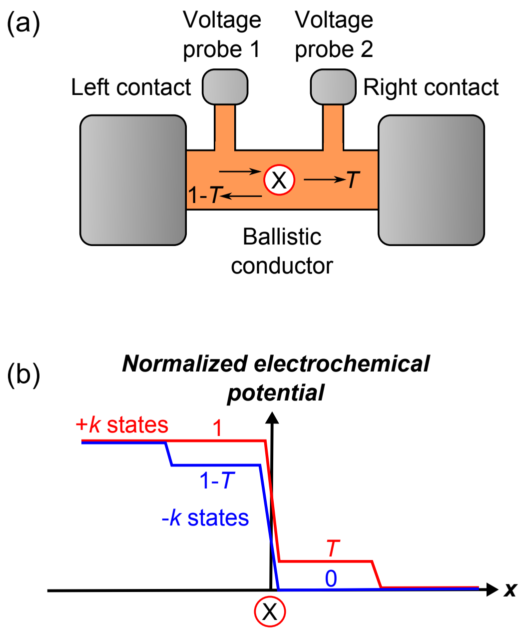

Figure 2.8: (a) Schematic illustration of a ballistic wire with left and right contact and two voltage probes. The scatterer X has the transmission T. (b) Band diagram showing the variation of the electrochemical potential along contacts and wire. For simplicity the electrochemical potential in the left contact is set to 1 and in the right contact to 0. Adapted from [56].

This leaves the question if a 4pp measurement on a ballistic conductor is anyhow necessary or useful. To answer this question, the resistance in a 4pp setup on a ballistic conductor shall be evaluated. The 4pp arrangement is shown in fig. 2.8(a). It consists of a ballistic conductor with a scatterer in the center which has a transmission probability of $T < 1$, the left and right contact and two voltage probes. No current is applied between the voltage probes similar to a 4pp measurement in the diffusive regime. Fig. 2.8(b) shows the variation of the electrochemical potential across the conductor. The situation is essentially the same as the one shown in the beginning of this section in fig. 2.6(c) except for the additional scatterer. For simplicity the electrochemical potential in the left (right) contact is set to 1 (0). The $+k$ states enter the ballistic conductor from the left contact without any change and they leave the ballistic conductor into the right contact with a step-like decrease to the chemical potential present in the right contact (0 here). At the scatterer an additional drop is observed which lowers the electrochemical potential from 1 to T accounting for the limited transmission through the scatterer. The electrochemical potential of the $-k$ states in between the left contact and the scatterer is $1 - T$, due to backscattering. The voltage probes measure the local electrochemical potential of either the $+k$ or the $-k$ states, hence, in both cases a difference of $1 - T$. The current is given by (cf. eq. 2.27)

$$I = \frac{2e}{h} M T \,. \tag{2.49}$$

This leads to the resistance

$$R_{4pp} = \frac{(1-T)}{eI} = \frac{h}{2e^2M}\frac{1-T}{T} \;. \tag{2.50}$$

In the absence of a scatterer ($T = 1$) $R = 0$. This is a reasonable result, since the 4pp measurement is designed for the purpose of measuring voltage drops without the influence of contact resistances. In a fully ballistic conductor with $T = 1$ voltage drops are only present at the contact interface and there is nothing to detect for the 4pp measurement.

So far, the voltage probes were assumed to be identical in the sense that their coupling to the $+k$ states is the same as to the $-k$ states. If voltage probe 1 in fig. 2.8(a) couples only to the $-k$ states and voltage probe 2 only to the $+k$ states, the measured resistance is given by [56]

$$R_{4pp} = \frac{(1-T)-T}{eI} = \frac{h}{2e^2M}\frac{1-2T}{T} \;. \tag{2.51}$$

This would lead to even negative R_{4pp} if $T > 1/2$. As soon as the voltage probes do not couple identically to $+k$ and $-k$ states a measurement will not yield the resistance given by eq. 2.50 but can give any value $\frac{h}{2e^2M}\frac{1-2T}{T} < R_{4pp} < \frac{h}{2e^2M}\frac{1}{T}$ [56].

2.2.4 BÜTTIKER FORMALISM

An easy way to to calculate currents and corresponding resistances in multi-terminal devices was developed by Büttiker [69, 70]. Since there is no qualitative difference between a voltage and a current probe the current at each probe can be expressed as

$$I_m = \frac{2e^2}{h}\sum_n T_{n,m}V_m - T_{m,n}V_n \tag{2.52}$$

where $T_{n,m}$ is the transmission probability from probe n to m. The transmission probabilities need to obey the sum rule

$$\sum_n T_{n,m} = \sum_n T_{m,n} \tag{2.53}$$

to make sure that the current is zero when all potentials at the probes are equal. For a 3pp device this results in the following relation

$$\begin{pmatrix} I_1 \\ I_2 \\ I_3 \end{pmatrix} = \frac{2e^2}{h}\begin{pmatrix} T_{1,2}+T_{1,3} & -T_{1,2} & -T_{1,3} \\ -T_{2,1} & T_{2,1}+T_{2,3} & -T_{2,3} \\ -T_{3,1} & -T_{3,2} & T_{3,1}+T_{3,2} \end{pmatrix}\begin{pmatrix} V_1 \\ V_2 \\ V_3 \end{pmatrix} \;. \tag{2.54}$$

For a 4pp the voltage at one of the terminals can be set to zero (for example $V_4 = 0$), giving the following matrix equation

$$\begin{pmatrix} I_1 \\ I_2 \\ I_3 \end{pmatrix} = \frac{2e^2}{h} \begin{pmatrix} T_{1,2}+T_{1,3}+T_{1,4} & -T_{1,2} & -T_{1,3} \\ -T_{2,1} & T_{2,1}+T_{2,3}+T_{2,4} & -T_{2,3} \\ -T_{3,1} & -T_{3,2} & T_{3,1}+T_{3,2}+T_{3,4} \end{pmatrix} \begin{pmatrix} V_1 \\ V_2 \\ V_3 \end{pmatrix} . \tag{2.55}$$

Every current and thus, also every resistance in a 3pp or 4pp device can be easily obtained from these two equations.

2.2.5 PROBE INVASIVENESS

A final remark concerns the invasiveness of the voltage probes. A probe which is strongly coupled to the conductor may destroy phase coherence. Electrons which enter the probe are injected back into the system losing any information regarding the phase [71, 72]. To avoid this, weakly coupled probes, meaning large resistances between the voltage probes and the conductor, are required. As depicted in fig. 2.9(a) the invasiveness can be understood in general as a transmission probability separating the probe from the ballistic conductor. If electrons now travel from the left to the right contact they have a probability P (the invasiveness) to enter the probe. The phases of the electrons entering the probe are randomized before they are reinjected into the conductor. This means that an invasive voltage probe acts as a phase breaking scatterer [56]. The reinjected electrons can either proceed to travel to the right contact or go back to the left contact. Hence the total transmission from left to right contact has two components, one from the coherent and one from the incoherent transport. This determines the 2pp resistance between the left and right contact in a single mode wire to

$$R_{2pp}^{l,r} = \frac{h}{2e^2} \frac{1}{T_{el} + T_{in}} \tag{2.56}$$

with the elastic transmission probability T_{el} accounting for electrons traveling directly from left to right contact without entering the voltage probe and T_{in} accounting for the inelastic transmission probability of electrons which entered the voltage probe. For a non-invasive probe no electrons enter the voltage probe and $T_{in} = 0$. This corresponds to the case of normal 2pp ballistic conduction given in eq. 2.27. Alternatively, $R_{2pp}^{l,r}$ can be obtained from eq. 2.54 resulting in [69]

$$R_{2pp}^{l,r} = \frac{V_l - V_r}{I} = \frac{h}{2e^2} \frac{T_{v,l} + T_{v,r}}{T_{r,l}\, T_{v,l} + T_{r,l}\, T_{v,r} + T_{v,l}\, T_{r,v}} \tag{2.57}$$

where $T_{n,m}$ indicates the respective transmission coefficients between left contact (l), right contact (r) and voltage probe (v) (note that $T_{n,m} = T_{m,n}$ for symmetric probes).

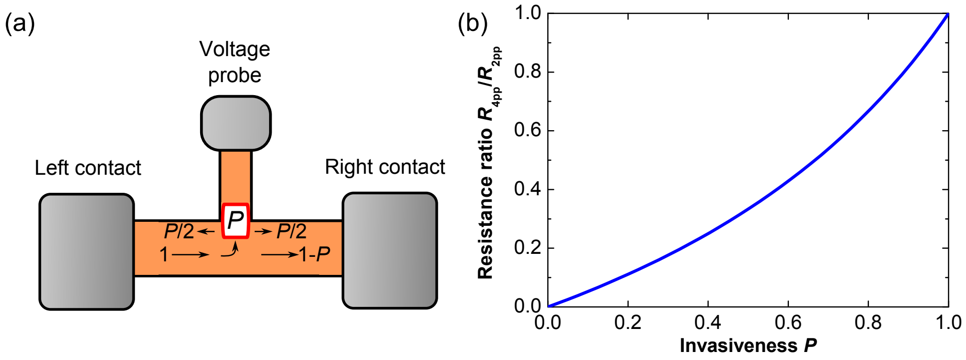

Figure 2.9: (a) Schematic illustration of an invasive voltage probe of invasiveness P in contact with a ballistic conductor. (b) Resistance ratio R_{4pp}/R_{2pp} for a ballistic conductor with $T = 1$ according to eq. 2.64.

Since the elastic transmission is obviously $T_{el} = T_{l,r}$ an expression for T_{in} can be derived from eq. 2.56 to

$$T_{in} = \frac{T_{l,v} T_{r,v}}{T_{v,l} + T_{v,r}} \, . \tag{2.58}$$

This directly implies that the additional voltage probe simply acts as an inelastic scatterer. In the case of a fully invasive probe ($T_{el} = 0$), eq. 2.56 converts to

$$R^{l,r}_{2pp} = \frac{h}{2e^2} \left(\frac{1}{T_{v,l}} + \frac{1}{T_{v,r}} \right) \, . \tag{2.59}$$

For a ballistic conductor with globally perfect transmission $T_{v,l} = T_{v,r} = 1$ eq. 2.59 predicts a doubling of the 2pp resistance in the presence of an additional voltage probe. This is the classical addition of serial resistors. Thus, a fully invasive voltage probe has the same effect on the 2pp resistance as a scattering center with $T = 1/2$.

Eq. 2.56 can also be easily rewritten with respect to the invasiveness P for the case of a perfect ballistic conductor. P is a measure of the probability with which an electron enters the voltage probe. Consequently, the elastic transmission probability is given by $T_{el} = 1 - P$ and $T_{v,l} = T_{v,r} = P$. Inserting this into eq. 2.58 and 2.56 results in

$$R^{l,r}_{2pp} = \frac{h}{2e^2} \frac{1}{(1-P) + \frac{P^2}{2P}} = \frac{h}{2e^2} \frac{2}{2-P} \, . \tag{2.60}$$

An interesting quantity is the resistance ratio between the additional resistance from the invasiveness of the voltage probe R_{inv} and the actual quantized contact resistance $R_0 = h/2e^2$ which is measured when no voltage probes are attached. The contribution of the invasive probe to the overall resistance R_{inv} can be obtained by subtracting the contact resistance $h/2e^2$ from R^{lr}_{2pp} in eq. 2.60. The resistance ratio is then given by

$$\frac{R_{inv}}{R_0} = \frac{R^{lr}_{2pp} - R_0}{R_0} = \frac{2}{2-P} - 1 = \frac{P}{2-P} \, . \tag{2.61}$$

This considerations regarding invasiveness can be done in a similar manner for a 4pp setup. Now the conductor is contacted with a left contact (l), a first voltage probe (v1), a second voltage probe (v2) and the right contact (r). First, the resistance needs to be expressed in terms of the individual transmission coefficients between the probes. Following eq. 2.55 R_{4pp} is given by [70, 73]

$$R_{4pp} = \frac{h}{2e^2} \left(\frac{T_{l,v1}}{T_{l,v1} + T_{v1,r}} - \frac{T_{l,v2}}{T_{l,v2} + T_{v2,r}} \right) . \tag{2.62}$$

Again, the transmission of the wire itself was assumed to be perfect. The transmission between left (right) contact and the first (second) voltage probe is obviously $T_{l,v1} = T_{v2,r} = P$ while for the other two $T_{v1,r} = T_{l,v2} = P(1-P)$. Therefore, R_{4pp} is calculated from eq. 2.62 to

$$R_{4pp} = \frac{h}{2e^2} \frac{P}{2-P} . \tag{2.63}$$

This directly results in the ratio between R_{4pp} and R_{2pp}

$$\frac{R_{4pp}}{R_{2pp}} = \frac{P}{2-P} \tag{2.64}$$

which is the same result as for the case of just one voltage probe which was obtained in eq. 2.61. Eq. 2.64 has important consequences. In the extreme case of fully invasive voltage probes with invasiveness $P = 1$, the probes itself separate the narrow conductor into three equal pieces [74]. Consequently, a 4pp measurement with fully invasive probes yields the same result as a 2pp measurement, $R_{4pp}/R_{2pp} = 1$. In contrast, non-invasive voltage probes ($P = 0$) on a ballistic conductor with $T = 1$ lead to $R_{4pp}/R_{2pp} = 0$ which is consistent with eq. 2.50. Hence, by performing a 4pp measurement on a ballistic conductor, the invasiveness of the probes can be determined.

3

GRAPHENE AND GRAPHENE NANORIBBONS

3.1 GRAPHENE

Graphene is a monoatomic layer of carbon atoms arranged in a honeycomb lattice. Both its structural as well as its electronic properties make it a viable candidate for high-performance applications in almost all technological branches. A short review of the peculiar properties of graphene and graphene nanostructures shall be given in this chapter.

3.1.1 STRUCTURAL AND ELECTRONIC PROPERTIES OF GRAPHENE

The carbon atoms within a graphene sheet are sp^2 hybridized. Every atom features 3 in-plane sp^2 orbitals with an angle of $120°$ relative to each other and a $2p_z$ orbital in perpendicular direction (cf. fig. 3.1(a)). Arranging these atoms in a hexagonal lattice leads to in-plane covalent σ bonds stemming from the sp^2 orbitals as well as out-of-plane π bonds as depicted in fig. 3.1(b). The non-local charge carriers in the π bonds are responsible for most of the unique electronic properties of graphene. The binding energy between carbon atoms within one layer is by far larger than the binding energy in between the layers (4.3 eV compared to 0.07 eV). This is the reason why the mechanical exfoliation of graphene layers from graphite crystals works surprisingly well and produces well-ordered graphene flakes on a µm scale [75]. The crystal structure of graphene is a triangular lattice with a base of two atoms per unit cell [76]. The graphene lattice is shown in fig. 3.1(c). Its unit cell is defined by the two lattice vectors $\vec{a}_1$ and $\vec{a}_2$ which can be expressed as

$$\vec{a}_1 = \frac{a}{2}(3, \sqrt{3}), \ \vec{a}_2 = \frac{a}{2}(3, -\sqrt{3}) \tag{3.1}$$

with a lattice constant $a = |\vec{a}_1| = |\vec{a}_2| \approx 2.46\text{Å}$.

The corresponding reciprocal lattice is shown in fig. 3.2(a). Of particular importance are the corners of the first Brillouin zone. The points K and K' are inequivalent due to the two sublattices of the graphene structure. Their location in reciprocal space can be written as

$$\vec{K} = \left(\frac{2\pi}{3a}, \frac{2\pi}{3\sqrt{a}}\right), \ \vec{K'} = \left(\frac{2\pi}{3a}, -\frac{2\pi}{3\sqrt{a}}\right) . \tag{3.2}$$

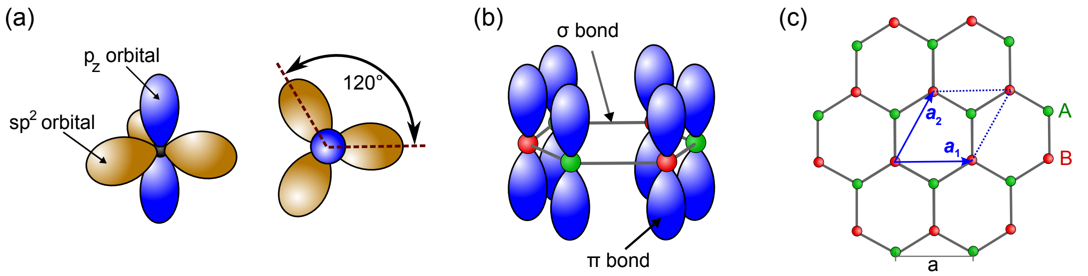

Figure 3.1: (a) Schematic of an sp^2 hybridized carbon atom in side and top view. (b) Single hexagon of a graphene lattice. In-plane σ and out-of-plane π bonds are indicated. (c) Graphene lattice with sublattices A and B indicated by green and red carbon atoms. The unit cell defined by the lattice vectors $\vec{a}_1$ and $\vec{a}_2$ is shown. The lattice constant $a = |\vec{a}_1| = |\vec{a}_2| \approx 2.46\,\text{Å}$.

The band structure of graphene can be calculated in the tight-binding approximation [16]. Since the energy bands arising from the σ bonds are energetically separated by more than 5 eV only the π bands need to be considered. The Hamiltonian is given by [76]

$$H = -t_h \sum_{<i,j>,s} a^\dagger_{s,i} b_{s,j} + \text{h.c.} - t'_h \sum_{<i,j>,s} a^\dagger_{s,i} a_{s,j} + b^\dagger_{s,i} b_{s,j} + \text{h.c.} \tag{3.3}$$

with units chosen such that $\hbar = 1$ for simplicity. Here, $a_{s,i}$ ($a^\dagger_{s,i}$) describes the annihilation (creation) of an electron carrying spin s on site $\vec{R}_i$ on sublattice A. In the same manner, $b_{s,i}$ ($b^\dagger_{s,i}$) describes the annihilation (creation) of an electron carrying spin s on sublattice B. Furthermore, t_h and t'_h are the nearest- and next nearest-neighbor hopping energies. Hopping between nearest-neighbors requires the electron to change the sublattice while for next nearest-neighbour hopping it can stay in its original sublattice. Hence it is intuitively clear that $t_h > t'_h$ with $t_h \approx 2.8\,\text{eV}$ and $-0.02\,\text{eV} \leqslant t'_h \leqslant 0.02\,\text{eV}$. This results in the energy bands [16]

$$\begin{aligned} E(\vec{k}) = \pm t_h &\sqrt{3 + 2\cos\left(\sqrt{3}k_y a\right) + 4\cos\left(\frac{\sqrt{3}}{2}k_y a\right)\cos\left(\frac{3}{2}k_x a\right)} \\ &- t'_h\left(2\cos\left(\sqrt{3}k_y a\right) + 4\cos\left(\frac{\sqrt{3}}{2}k_y a\right)\cos\left(\frac{3}{2}k_x a\right)\right) . \end{aligned} \tag{3.4}$$

The band structure is shown in fig. 3.2(b). At each of the corners of the first-order Brillouin zone (K, K′) the valence and conduction bands touch in exactly one point. Away from the Dirac points valence and conduction band are well separated energetically. Due to this unique band structure, graphene is often referred to as a "zero-gap semiconductor". The energy at the touching points of valence and conduction bands

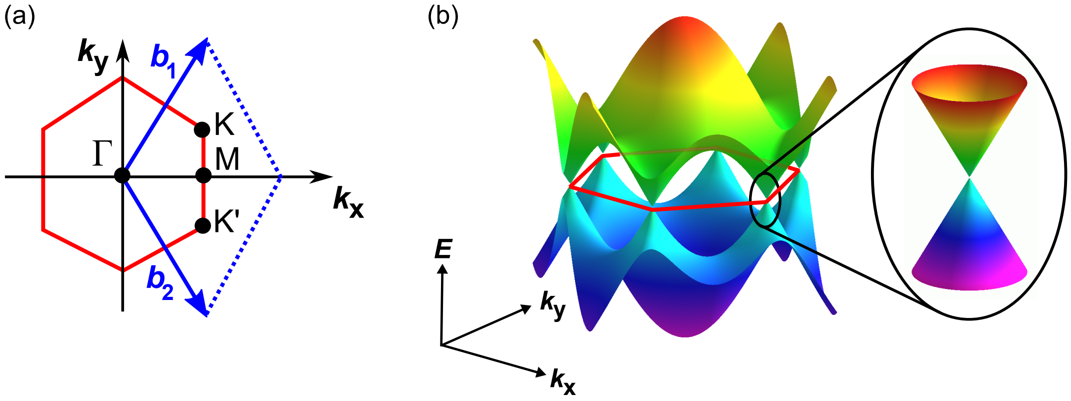

Figure 3.2: (a) Reciprocal lattice of graphene showing the Γ, K, K′ M point as well as the reciprocal lattice vectors $\vec{b}_1$ and $\vec{b}_2$. (b) Electronic dispersion in the graphene lattice obtained from the tight-binding model. The zoom shows the dispersion close to the Dirac points.

is equal to the Fermi energy in case of an undoped graphene sheet. In the vicinity of the K and K′ points the dispersion relation can be approximated by [76]

$$E(\vec{k}) = \pm\hbar v_f|\vec{k} - \vec{K}| \tag{3.5}$$

where the Fermi velocity $v_f \approx 10^6\,\frac{m}{s}$. Compared to a free electron gas where

$$v_f = k/m = \sqrt{2e/m} \quad (\hbar = 1) \tag{3.6}$$

the Fermi velocity of graphene does not depend on the energy or momentum and the dispersion relation is essentially linear in the vicinity of the K and K′ points. Due to this linearity these points are called Dirac points. The reason for this name lies in the fact that the electrons near the Dirac point obey the 2d Dirac equation

$$\hbar v_f \vec{k}\,\vec{\sigma}\,\vec{\Psi}(\vec{r}) = E\vec{\Psi}(\vec{r}) \tag{3.7}$$

where $\vec{\sigma} = (\sigma_x, \sigma_y)$ stands for the Pauli matrices. The wave functions around K and K′ are hence given by [76]

$$\Psi_K(\vec{k}) = \frac{1}{\sqrt{2}}\begin{pmatrix} e^{-i\Theta_{\vec{k}}/2} \\ \pm e^{i\Theta_{\vec{k}}/2} \end{pmatrix}, \; \Psi_{K'}(\vec{k}) = \frac{1}{\sqrt{2}}\begin{pmatrix} e^{i\Theta_{\vec{k}}/2} \\ \pm e^{-i\Theta_{\vec{k}}/2} \end{pmatrix}. \tag{3.8}$$

These wave functions are related by time-reversal symmetry. Furthermore, upon rotation the phase Θ changes by π, which is referred to as "Berry's phase" [76]. Therefore, the wave function is a spinor close to the Dirac points. This spinor characteristic has its origin in the sublattice structure of the graphene lattice. The wave functions $\Psi_{K,K'}(\vec{r})$ are also eigenstates of the helicity operator $\hat{h} = 1/2\vec{\sigma} \cdot \vec{(p)}/|\vec{p}|$. Helicity is de-

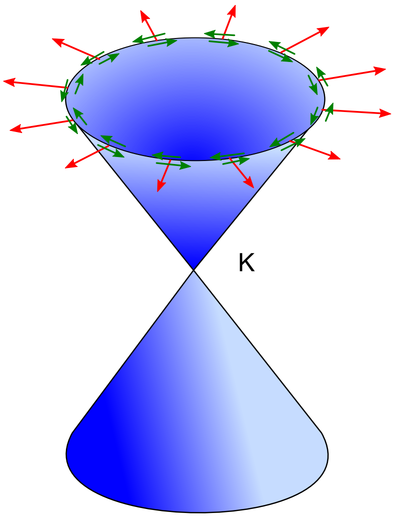

Figure 3.3: Spin (green arrows) and pseudo-spin (red arrows) directions at the Dirac points K and K′.

fined as the projection of the spin onto the direction of momentum $\vec{p}/|\vec{p}|$. It is trivial to obtain that

$$\hat{h}\Psi_K(\vec{r}) = \pm\frac{1}{2}\Psi_K(\vec{r}),\ \hat{h}\Psi_{K'}(\vec{r}) = \mp\frac{1}{2}\Psi_K(\vec{r}) \tag{3.9}$$

This directly implies that electrons (holes) have a positive (negative) helicity and that $\vec{\sigma}$ has its two eigenstates in or against the direction of momentum $\vec{p}$ [76]. Thus the helicity of states near the Dirac points is well defined. It is important to note that the helicity of the eigenstates is not due to the electronic spins but solely due to the spinor characteristic of the two component wave function. For a better discrimination between this variable and the real electronic spin, it is often referred to as pseudo-spin. The spin and pseudo-spin texture of graphene at K and K' is visualized in fig. 3.3.

One further conclusion can be drawn from eq. 3.7. It is not only equivalent to the Dirac equation but even to the Dirac-Weyl equation, a special case for massless relativistic fermions. Due to this formal equivalence the charge carriers in graphene can be described as massless ultra-relativistic particles, often referred to as Dirac fermions.

From eq. 3.3 the density of states (DOS) of graphene can be derived to [76]

$$D(E) = \frac{4}{\pi^2\sqrt{C_0}}\frac{|E|}{t_h^2}F\left(\frac{\pi}{2},\sqrt{\frac{C_1}{C_0}}\right) \tag{3.10}$$

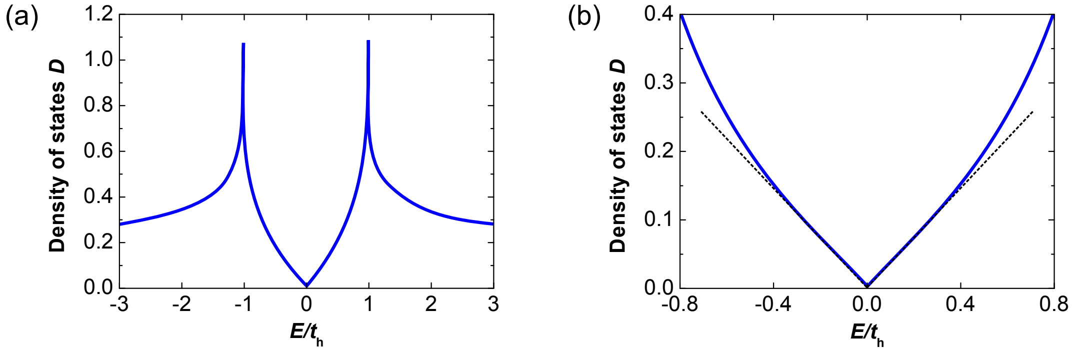

Figure 3.4: (a) DOS of graphene per unit cell from eq. 3.10. (b) Zoom into the DOS close to the charge neutrality point. Black dotted lines indicate the linear approximation $D(E) \propto |E|$.

with coefficients

$$C_0 = \begin{cases} \left(1+\left|\frac{E}{t_h}\right|\right)^2 - \frac{\left((E/t_h)^2-1\right)^2}{4} & , \quad -t \leqslant E \leqslant t_h \\[2em] 4\left|\frac{E}{t_h}\right| & , \quad -3t_h \leqslant E \leqslant -t_h \vee t \leqslant E \leqslant 3t_h \end{cases} \tag{3.11}$$

and

$$C_1 = \begin{cases} 4\left|\frac{E}{t_h}\right| & , \quad -t_h \leqslant E \leqslant t_h \\[2em] \left(1+\left|\frac{E}{t_h}\right|\right)^2 - \frac{\left((E/t_h)^2-1\right)^2}{4} & , \quad -3t \leqslant E \leqslant -t_h \vee t \leqslant E \leqslant 3t_h \end{cases} . \tag{3.12}$$

F is the complete elliptic integral of the first kind. Fig. 3.4(a) shows the DOS. In eq. 3.5 the Energy dispersion near the Dirac points was found to be linear with $\vec{k}$. Close to the Dirac point, the DOS can be expressed as

$$D(E) = \frac{2}{\pi}\frac{|E|}{(\hbar v_f)^2} . \tag{3.13}$$

In the vicinity of the Dirac points the DOS is linear with $D(E) \propto |E|$ as shown in fig. 3.4(b).

As concluding remark for this section, the charge carrier densities n for electrons and p for holes in a graphene sheet, dependent on the Fermi energy and temperature, shall be derived. Such an expression will become useful in order to extract mobilities from transport experiments. In general the carrier density is given by

$$n = \int_0^\infty D(E)f(E)dE \tag{3.14}$$

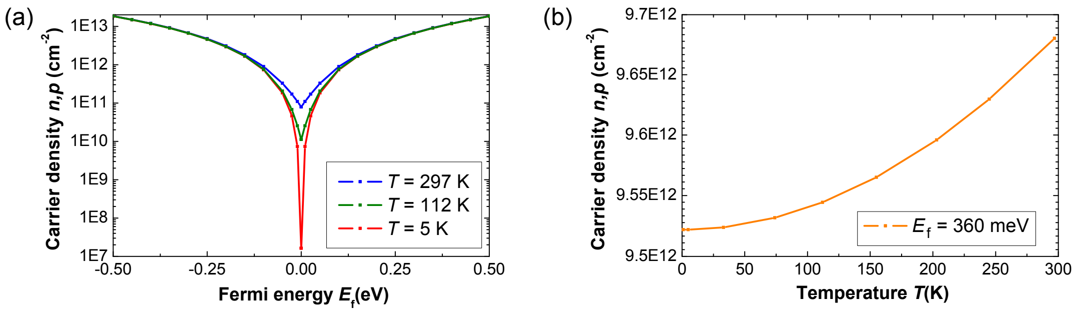

Figure 3.5: (a) Carrier density n, p in a graphene sheet plotted versus the Fermi energy relative to the Dirac point. (b) Carrier density n, p in a graphene sheet plotted versus temperature at a Fermi energy of $E_f = 360\,\text{meV}$.

with the Fermi-Dirac distribution $f(E)$. Introducing the two variables $u = E/k_BT$ and $\eta = E_f/k_BT$ the electron and hole density can be rewritten as [77]

$$n = \frac{2}{\pi}\left(\frac{k_BT}{\hbar v_f}\right)^2 \mathcal{J}_1(+\eta),\ p = \frac{2}{\pi}\left(\frac{k_BT}{\hbar v_f}\right)^2 \mathcal{J}_1(-\eta) \tag{3.15}$$

where $\mathcal{J}_1$ is the Fermi-Dirac integral

$$\mathcal{J}_j(\eta) = \frac{1}{\Gamma(j+1)}\int_0^\infty \frac{u^j}{1+e^{u-\eta}}\,du \tag{3.16}$$

for $j = 1$ and Γ is the gamma function. In fig. 3.5(a) the charge carrier densities are shown with respect to the Fermi level. Negative (positive) Fermi energies refer to p (n) doped graphene. With $|E_f| \to 0$ n and p decrease reaching a minimum value at charge neutrality. This minimum charge carrier concentration is drastically decreasing when going from room temperature to low temperatures. On the other hand, away from charge neutrality there is almost no temperature effect present. As an example the charge carrier density for $E_f = 360\,\text{meV}$ is shown in fig. 3.5(b). This is a typical charge carrier density found for epitaxial graphene on the Si-face of 6H-SiC (cf. chapter 5). It is almost temperature independent, only increasing about $1.6 \times 10^{11}\,\text{cm}^{-2}$ when increasing the temperature from $T < 5\,\text{K}$ to room temperature.

3.1.2 ELECTRONIC TRANSPORT IN GRAPHENE

The general expression for the diffusive conductivity $\sigma = qn\mu$ (cf. eq. 2.5) can also be applied to graphene. By means of the Boltzmann equation [76, 78]

$$\sigma = 4e^2 D(E)\Xi \tag{3.17}$$

with the DOS close to the Dirac point $D(E)$ given by eq. 3.13 and the diffusion coefficient $\Xi = v_f^2\tau/2$ the conductivity can be written as

$$\sigma = \frac{2e^2}{h} k_f \lambda_e \,. \tag{3.18}$$

Here, it was used that $|E| = \hbar v_f \sqrt{n}$ and $\lambda_e = v_f\tau$. Combining eq. 2.5 and eq. 3.18, the mean free is given by

$$\lambda_e = \frac{\hbar \mu}{e}\sqrt{n\pi} \,. \tag{3.19}$$

This expression is very useful since it depends only on μ and n which are relatively easy to obtain experimentally, and hence provides an easy access to the mean free path via transport experiments.

Eq. 3.18 holds true for large carrier densities, away from charge neutrality. For low carrier densities, it was already predicted in 1994 by Ludwig et al. that even at zero carrier density a finite conductivity of $\sigma_{min} = 4e^2/\pi h$ should remain [79]. Early transport experiments, however, observed a minimum conductivity close to $\sigma_{min} = 4e^2/h$ [80]. Due to the resemblance of this value with the resistance gained from ballistic transport theory (cf. eq. 2.28), this conductivity value was first believed to be universal. Later on, it was indicated that there is no universal character in this value but it is rather a consequence of the impurity concentration in the graphene sheet itself [78]. A conductivity of $\sigma_{min} = 4e^2/\pi h$ was indeed experimentally found for short and small graphene strips of length $L < 500\,\text{nm}$ and aspect ratios $W/L > 4$ [81]. Transport in this regime was characterized as ballistic. In devices with larger contact separation, transport was diffusive and conductivities close to $\sigma_{min} = 4e^2/h$ were found.

3.1.3 KLEIN TUNNELING

A conventional tunneling setup consists of an electron traveling through a potential barrier via quantum mechanical tunneling. It is characterized by a tunneling probability which is exponentially decaying with the height and the width of the barrier. In contrast to this conventional tunneling effect Klein predicted in 1929 that for a relativistic electron obeying the 3d Dirac equation the tunneling probability is independent of the height and width of the barrier [22]. This effect is referred to as “Klein paradox”. Furthermore, the tunneling probability can even reach 1 which means a perfect transmission of the electrons through the barrier. A similar effect can be observed for electrons in graphene, hence for electrons which obey the 2d Dirac equation. This effect is known as “Klein tunneling”.

The potential step required for the realization of Klein tunneling phenomena can be obtained by bringing a n-type doped graphene sheet in contact to a p-type doped sheet. The corresponding setup is depicted in fig. 3.6(a). The height of the potential step is given by the energy difference between the Dirac points of p- and n-type doped graphene. In case of the symmetric junction shown here, the Fermi energy is half of the potential height $E_f = V_0/2$. In the following, for simplicity, always such

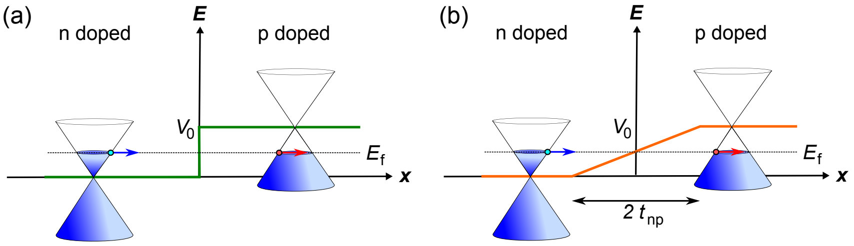

Figure 3.6: (a) Band diagram across a sharp n-p potential step. An electron in the n doped (p doped) region is indicated as light blue (light red) circle. The direction of motion of the electron is indicated by the red and blue arrows. (b) Band diagram across a smooth n-p potential step. The total length of the p-n junction is $2\,t_{np}$.

symmetric junctions shall be considered. The junction can be further classified with respect to the length $2\,t_{np}$. Length meaning the distance on which the doping changes from n-type to p-type or vice versa. The junction length can be set in relation to either the lattice or the Fermi wavelength scale. On the lattice scale every junction for which $t_{np} \gg a$ is smooth, implying that no inter-valley scattering is present in the junction [82] since the distance between K and K' is $\sim 1/a$. All junctions discussed in the following are of this type, smooth on the lattice scale.

A second classification relates to the Fermi wavelength scale. If $k_f t_{np} \ll 1$ the junction is classified as sharp, if $k_f t_{np} \gg 1$ the junction is smooth (cf. fig. 3.6(b)). The reason for this classification will become clear in an instant. First an electron shall be considered which moves within the conduction band of the n-type area and hits the potential barrier. The electron is transmitted into the step as an electron in the valence band. Since the electron has to maintain its moving direction (which is opposite to its momentum) the momentum of the electron inside the step has to be reversed [82]. Additionally, an electron hitting the potential step with normal incidence cannot backscatter. This is intuitively clear since backscattering would involve a reversal of the momentum $\vec{k} \to -\vec{k}$ and hence also a reversal of the pseudo-spin $\vec{\sigma} \to -\vec{\sigma}$. As discussed earlier, the potential step is not a source for inter-valley scattering (and therefore pseudo-spin reversal) since it is smooth on the lattice scale. By this means, the momentum cannot be reversed and, for normal incidence, no backscattering is allowed resulting in a transmission probability $T = 1$. This is true for smooth as well as sharp potential steps (with "smooth" and "sharp" referring to the wavelength scale). This absence of backscattering is what most often is called "Klein tunneling". It is important to note that, despite the name, this is not a tunneling effect in the quantum mechanical sense. It does not involve a classically forbidden region or evanescent waves. It is a simple consequence of the existence of energy states with negative kinetic energy (valence band) in the barrier which match the states with positive kinetic energy (conduction band) outside the barrier and the conservation of the pseudo-spin [82].

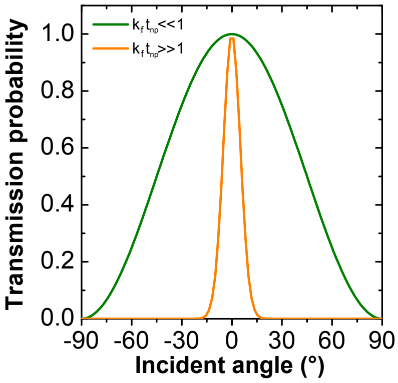

Figure 3.7: Transmission probability versus incidence angle for a smooth (orange) and sharp (green) p-n potential step according to eq. 3.20, 3.21. For the smooth junction $k_f t_{np} = 20$ was chosen for the graph.

Away from normal incidence the transmission probability can by obtained by solving the corresponding Dirac equations. For the special case of a symmetric junction with $E_f = V_0/2$ it is given by [24]

$$T_{sharp}(\Phi) = \cos^2(\Phi) \tag{3.20}$$

for a sharp ($k_f t_{np} \ll 1$) junction with incidence angle Φ. On the other hand a smooth junction ($k_f t_{np} \gg 1$) has a transmission function [82]

$$T_{smooth}(\Phi) = e^{-\pi k_f t_{np} \sin^2(\Phi)} \,. \tag{3.21}$$

A plot of both transmission functions is shown in fig. 3.7. Both transmission functions show $T = 1$ for normal incidence due to the suppression of backscattering. For a sharp junction, the transmission probability is generally high, even away from normal incidence. In contrast, a smooth junction shows a strong exponential decrease for increasing incidence angles. By this means, a smooth graphene p-n junction has a collimation effect, letting only electrons pass with incidence angles close to normal.

The conductance through a smooth and sharp potential step can be directly calculated from the transmission functions given in eq. 3.20, 3.21 via the Landauer formula

$$G_{np} = 4\frac{e^2}{h}\sum_n T_n \approx 4\frac{e^2}{h}\int_{-k_f}^{k_f} \frac{T(k_y)W}{2\pi} dk_y \,. \tag{3.22}$$

The prefactor of 4 accounts for spin and pseudo-spin degeneracy, W is the sample width (not to be confused with the junction length t_{np}) and $k_y = k_f \sin(\Phi)$. For a smooth potential step, with the transmission given by eq. 3.21, this results in [24]

$$G_{np}^{smooth} = \frac{2e^2}{\pi h} W \sqrt{\frac{F}{\hbar v_f}} \,. \tag{3.23}$$

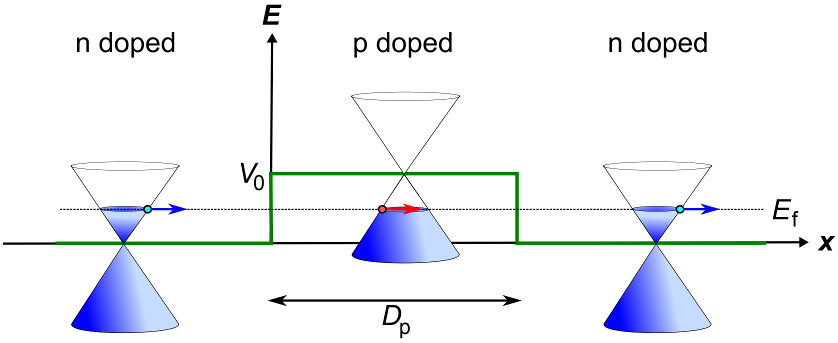

Figure 3.8: Band diagram across a sharp n-p-n potential step. An electron in the n doped (p doped) region is indicated as light blue (light red) circle. The direction of motion of the electron is indicated with a blue (red) arrow.

Here, F is the potential slope of the junction. On the other hand a sharp junction with a transmission function given by eq. 3.20 shows a conductance [82]

$$G_{np}^{sharp} = \frac{8e^2}{3h}\frac{k_f W}{\pi} . \tag{3.24}$$

For both eq. 3.23 and eq. 3.24 no scattering within the barrier is considered. Hence they are only valid as long as the mean free path λ_e is larger than the junction length t_{np}.

In the following a second potential step after the first one shall be considered. This results in a square potential barrier as shown in fig. 3.8 with a barrier length $D_{p,n}$. The transmission characteristic through such a barrier is immanently clear for normal incidence. Since upon normal incidence the first potential step transmits with $T = 1$ and no scattering within the barrier is present (as long as the barrier length $D_{p,n} < \lambda_e$) the electrons hit the second potential step again with normal incidence and the overall transmission $T = 1$. For oblique incidence the barrier is basically a double interface and can be seen as an analog of a Fabry-Pérot interferometer. Inside the barrier incoming waves might interfere with themselves which leads to a resonance condition [82]

$$2\frac{V_0 D_p}{2\pi\hbar v_f}\sqrt{1 - 2\frac{E}{V_0} + \left(\frac{E}{V_0}\right)^2 \cos^2(\Phi)} = \text{integer} . \tag{3.25}$$

At these resonances $T = 1$ at oblique angles. An example is shown in fig. 3.9. Measuring these interference patterns is a direct way to prove the presence of Klein tunneling in a graphene device.

For the interpretation of Klein tunneling related phenomena found in experiment it is important to know the relevant length scales. The theoretical considerations in this section assumed an electronic mean free path λ_e larger than the junction length t_{np} and the overall contact spacing L. This ensures that the sample is fully in the ballistic regime. Experimentally this is hard to achieve, typical mean free paths in

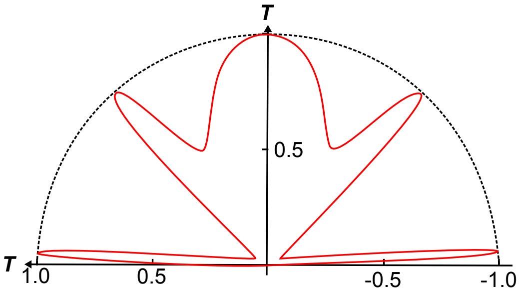

Figure 3.9: Polar plot of the transmission probability through a n-p-n potential step.

good graphene samples are in the order of $\lambda_e \sim 100\,\text{nm}$. If $t_{np} \ll \lambda_e \ll L$ the junctions themselves can be treated as ballistic and e.g. their resistances can be derived using eq. 3.23, 3.24. However, due to scattering within the diffusive n and p areas no angular dependence can be observed. Such an n-p-n structure can be treated like a simple serial connection of resistors and Klein tunneling manifests in the specific resistance of the barriers. If even more, the mean free path is in the order of the junction length, electronic scattering within the junction needs to be considered. A detailed description of the treatment of diffusive contributions within graphene p-n junctions can be found in [83].

3.1.4 EPITAXIAL GRAPHENE

The epitaxial growth of graphene on silicon carbide (SiC) is a promising technique for the integration of graphene into electronic circuits. The graphene layer does not need to be transfered onto an insulating substrate before carrying out transport experiments since the band gap of SiC is already sufficiently large ($E_g > 2.3\,\text{eV}$, exact value depends on the polytype). This is a big advantage because the dangerous transfer step which can lead to an enhancement of the defect concentration or unintentional doping can be avoided.

The growth of graphene on SiC substrates relies on the preferential sublimation of silicon. This is possible due to the higher vapor pressure of silicon in comparison to carbon. At a typical growth temperature of about 1300 °C the vapor pressure of carbon is approximately 10^{-10} mbar while that of silicon is about $2 \cdot 10^{-6}$ mbar [41, 84]. Upon silicon sublimation, a carbon layer resides on the surface which will arrange in the most stable configuration. Consequently one or multiple graphene layers are formed. Van Bommel et al. were the first to report that this method can be used for producing ultrathin graphite monolayer films [39]. The process of epitaxial graphene growth involves heating of the SiC substrate to very high temperatures above the melting point of silicon. It can be carried out in vacuum [85, 86] as well as an inert gas atmosphere [40]. The quality of the graphene sheets which can be obtained by epitaxial growth depends on the interplay between gas atmosphere and temperature as well as the defect concentration of the SiC substrate itself.

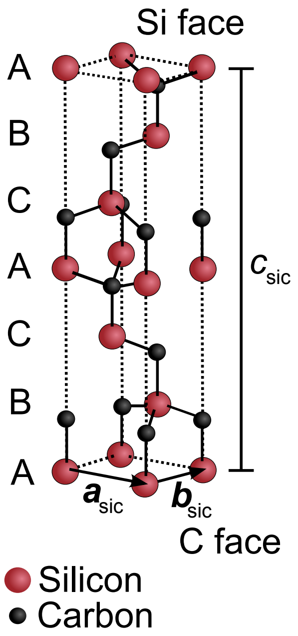

Figure 3.10: Unit cell of 6H-SiC.

A silicon carbide crystal is basically a stack of Si-C bilayers. Every new bilayer added to the crystal can be either stacked in the same orientation as the layer before or with a relative rotation of 60°. This degree of freedom allows for an enormous number of different SiC polytypes. The polytypes commonly used for graphene growth are the cubic 3C as well as the hexagonal 4H and 6H polytype. In this thesis only 6H-SiC is used and in the following the section will focus only on this polytype. The bilayers in 6H-SiC exhibit a stacking sequence of ABCACB as shown in fig. 3.10. It has a band gap $E_g = 3.02\,\mathrm{eV}$. Commonly used for graphene growth are the on-axis facets of hexagonal SiC. These are the SiC(0001) and SiC(000$\overline{1}$) facet. The SiC(0001) is silicon terminated and referred to as Si-face while the carbon terminated SiC(000$\overline{1}$) is called C-face.

Since every wafer, even a nominally on-axis one, has a small-miscut angle in the order of 0.1°, the SiC surface is not completely flat but is composed of SiC steps and terraces. Since the SiC surface is initially covered with silicon dioxide a pretreatment of the surface is necessary. For this purpose, two main preparation methods are used, silicon etching (Si etching) and hydrogen etching (H etching). Si etching is carried out by exposing the sample to an Si flux while keeping it at temperatures around 850 °C [87]. This leads to a reliable removal of silicon dioxide without changing the stochiometry of the substrate surface [88]. The second preparation method, the H etching procedure not only removes the oxide layer but also removes polishing scratches and leads to very smooth surfaces with large SiC terraces. The etching is carried out in a hydrogen atmosphere of about 1 bar and at temperatures of about 1500 °C. Hydrogen reacts with SiC forming elemental Si as well as hydrocarbons (CH_4, C_2H_2) and consequently several hundred nm of bulk material can be removed [89, 90]. By carefully controlling the etching parameters, smooth 6H-SiC surfaces can

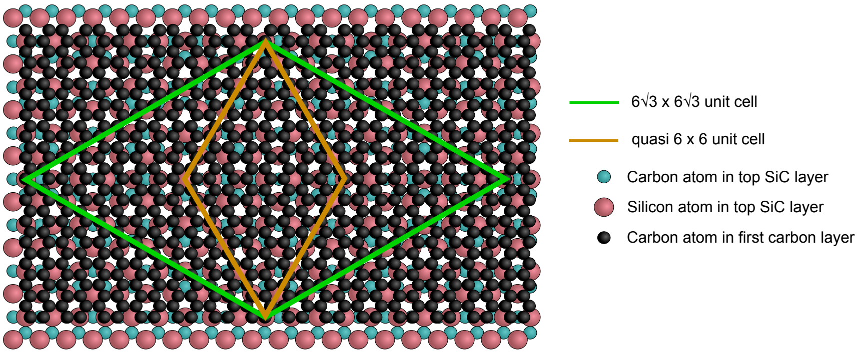

Figure 3.11: Schematic representation of the $(6\sqrt{3} \times 6\sqrt{3})R30°$ structure characteristic of the buffer layer. The unit cell of the $(6\sqrt{3} \times 6\sqrt{3})R30°$ as well as the quasi unit cell of the (6×6) reconstruction are indicated in green and orange.

be achieved with large atomically flat terraces of several µm terrace width and with a step height of 1.5 nm corresponding to a SiC unit cell [91].

The next step after surface cleaning and flattening is the graphene growth itself. Here, the C-face and Si-face show significant differences. The C-face growth is relatively fast [92] and typically leads to the formation of turbostratic, multilayer graphene. The individual layers are stacked with rotational faults and adjacent sheets are rotated relative to each other. Every graphene layer is rotated by about 30° or ±2° relative to the substrate [93]. This leads to a decoupling of the individual layers and the electronic properties of free-standing monolayer graphene are preserved [93, 94].

On the contrary, graphene growth on the Si-face is much slower and monolayer graphene is much easier to achieve. Prior to graphitization a number of surface reconstructions can be observed. After Si etching, a Si rich (3×3) reconstruction can be found [88]. Further annealing leads to the development of a $(\sqrt{3} \times \sqrt{3})R30°$ reconstruction which is followed by a complex $(6\sqrt{3} \times 6\sqrt{3})R30°$ reconstruction [95]. A fully developed $(6\sqrt{3} \times 6\sqrt{3})R30°$ reconstruction is indicative of the formation of the first fully developed hexagonal carbon layer. Its orientation on the substrate is shown in fig. 3.11. It is oriented 30° relative to the substrate and its unit cell consists of 13×13 unit cells of graphene. Four high-symmetry point within this large unit cell give rise to a smaller 6×6 quasi cell. It is important to note that this first carbon layer is not graphene because every third carbon atom within the layer is still bonded to the substrate. Due to the absence of the linear π bands, this layer is electronically inactive [96]. It is referred to as "buffer layer". In contrast, the next graphene layer grown on the buffer layer exhibits the typical linear dispersion of graphene. The graphene is highly n doped with $E_f = 400 - 500\,\text{meV}$ above the Dirac point [40, 97]. The origin of this doping can be explained by a charge transfer from the interface density of states to the graphene layer [98]. The carbon layer arrangement on the Si-face is schematically shown in fig. 3.12. The inactive buffer layer can be transfered into quasi free-standing monolayer graphene (QFSMLG) by intercalation with hydrogen [45].

The domain size of graphene on SiC is highly dependent on the growth kinetics, especially the gas atmosphere in which the SiC wafer is heated. In UHV, the sublima-

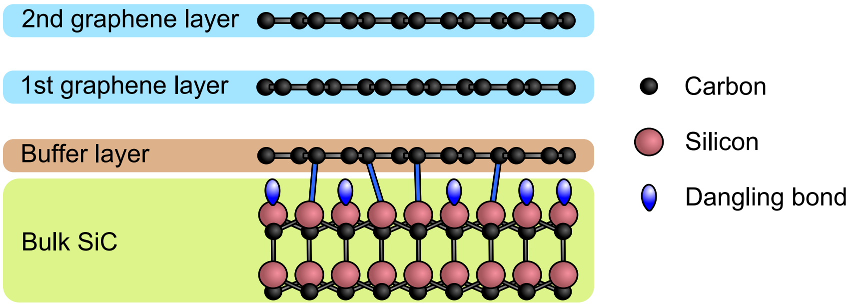

Figure 3.12: Schematic of the first and second graphene layer grown on Si face SiC. The first carbon layer is the buffer layer which is still partially bonded to the SiC substrate.

tion rate is very high, carbon atoms do not have enough time to rearrange properly. This results in the nucleation of small graphene islands and roughening of the substrate. The graphene domains are typically not larger than 100 nm [99]. The domain size can be increased by growing graphene in a gas atmosphere. For example, a high-pressure (900 mbar) Ar atmosphere can be used to produce large µm wide and long SiC terraces fully covered with monolayer graphene [40]. The argon hinders the Si atoms to leave the sample surface and hence decreases the sublimation rate. Increasing the growth temperature by about 100 °C increases the Si vapor pressure by a factor of seven [41]. Since the carbon vapor pressure is negligibly small in comparison, the growth rate is mainly determined by the Si vapor pressure. Thus, in general high temperatures are more favorable for low growth rates and high quality graphene formation. By providing excess Si in the form of Disilane, the graphene quality can be enhanced further [100]. Frequently used and known to produce graphene of very high quality is the confinement controlled sublimation (CCS) method [17, 41] which relies on the confinement of the SiC substrate in a graphite enclosure to maintain a high Si vapor pressure. Graphene growth is then carried out close to thermal equilibrium, resulting in high-quality mono- to multilayer films on the Si-face and C-face. The same effect of a locally enhanced Si vapor pressure is used in the so called face-to-face method [101]. Two SiC substrates facing each other, are heated simultaneously, creating a Si atmosphere in between. This method can not only be used to obtain high-quality graphene but also for an initial flattening of the SiC substrate. At temperatures below the graphitization temperature the two SiC substrates act as source and sink of SiC creating large, atomically flat terraces. The face-to-face method is, hence, a cheap alternative to obtain high-quality SiC surfaces and graphene layers.

The two crystal faces discussed so far, Si-face and C-face, are widely studied in literature. However, little is known about graphene growth on non-polar surfaces such as $(1\bar{1}00)$ or $(11\bar{2}0)$ [102]. A recent study shows that on these surfaces no buffer layer forms during graphene growth [103]. On the $(1\bar{1}00)$ plane, the graphene growth resembles the one on the C-face and the graphene exhibits large rotational disorder. On the other hand, the $(11\bar{2}0)$ graphene grows without rotational disorder and shows n-type doping (250 meV). It is important to keep in mind that the graphene growth on non-polar surfaces is different from the polar ones. Especially, with respect to

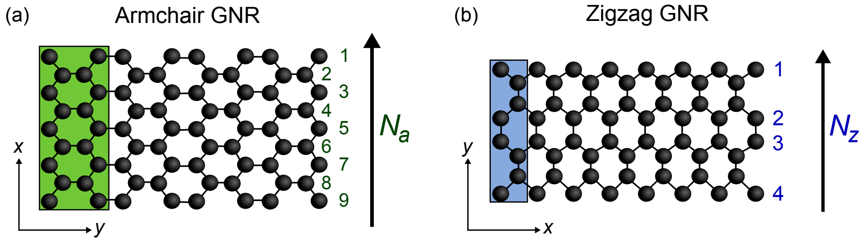

Figure 3.13: Schematic representation of an (a) 9-armchair GNR and (b) 4-zigzag GNR. The unit cells are indicated in green and blue. N_a (N_z) denotes the number of atoms along the width of an armchair (zigzag) GNR.

graphene growth on inclined ($1\bar{1}0n$) and ($11\bar{2}n$) facets which will be presented in chapter 7.

3.2 GRAPHENE NANORIBBONS

The reduction of the dimensionality of graphene from 2d to 1d can be obtained by cutting the graphene sheet into small stripes, the so called graphene nanoribbons (GNRs). The lateral confinement in these ribbons leads to a massive alteration of the band structure and hence opens up a pathway to completely new physical properties, e.g. band gap engineering or topologically protected electronic channels. In general, two main geometries of GNRs can be distinguished, the armchair and the zigzag type. An armchair GNR (AGNR) is cut from a graphene sheet parallel to the C-C bonds. In contrast, a zigzag GNR (ZZGNR) is rotated by 30° with respect to the armchair geometry. Cutting in any other direction results in a ribbon with a mixed armchair and zigzag edge, called chiral graphene nanoribbon. The armchair and zigzag geometries are depicted in fig. 3.13 and the names "armchair" and "zigzag" become obvious, looking at the shape of the edges of both ribbon types. A major difference between the two ribbon types is the origin of the edge atoms. While the armchair edge has alternating edge atoms from both sublattices, the edge atoms in a zigzag edge are all from the same sublattice. The electronic properties of these two ribbon types shall be reviewed in detail in the following two sections.

3.2.1 ARMCHAIR GRAPHENE NANORIBBONS

The band structure of an AGNR can be obtained by using the tight-binding model (cf. eq. 3.3). The cutting of a graphene sheet into a GNR causes boundary conditions which need to be considered. For an AGNR oriented along the y-direction, with the ribbon edges at $x = 0$ and $x = W$, these boundary conditions are

$$\Psi_A(0) = \Psi_B(0) = \Psi_A(W) = \Psi_B(W) = 0 \tag{3.26}$$

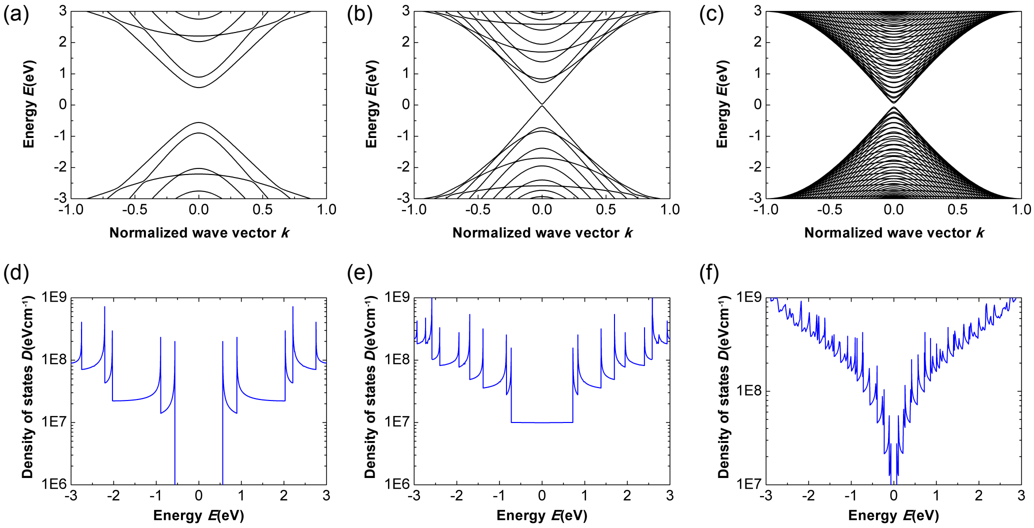

Figure 3.14: Band structure of armchair graphene nanoribbons for (a) a 10-AGNR, (b) a 20-AGNR and (c) a 100-AGNR. k is normalized to $\frac{\pi}{a}$. Corresponding density of states of armchair graphene nanoribbons for (d) a 10-AGNR, (e) a 20-AGNR and (f) a 100-AGNR.

where Ψ_A (Ψ_B) denotes the wave function in sublattice A (B). The resulting energy spectrum is given by [104]

$$E(k) = \pm t\sqrt{1 + 4\cos(p)\cos\left(\frac{k}{2}\right) + 4\cos^2(p)} \tag{3.27}$$

where p is the transverse wavenumber determined by the boundary condition of the edges to

$$p = \frac{n}{N_a + 1}\pi \ , n = 1, 2, 3, ...N_a \ . \tag{3.28}$$

The band structures and corresponding DOS of AGNRs with $N_a = 10, 20, 100$ are shown in fig. 3.14. The top of the valence band and the bottom of the conduction band are located at $k = 0$. While the 10-AGNR and 100-AGNR are semiconducting, the 20-AGNR is metallic. This is clear since the energy E in eq. 3.27 can only be zero at $k = 0$ if $N_a = 3n + 2$. This is the condition for having a metallic AGNR. The band gap for $3n$- and $3n+1$-AGNRs scales inversely with the ribbon width as shown in fig. 3.15(a). The band gap can be roughly estimated by $E_g(\mathrm{eV}) \sim 1\,\mathrm{eV}/W(\mathrm{nm})$. The absence of a band gap for $3n+2$-AGNRs is counter intuitive and shows the limitation of a conventional tight-binding approach. First-principle calculations within local density approximation (LDA) actually show that also the $3n+2$-AGNR has a small bandgap [105]. The discrepancy between the tight-binding and the LDA approach can be explained by the different treatment of the edge passivation of the GNRs. While in first-principle calculations the change of bonding characteristics at the edges (meaning change of hopping integrals or onsite energies) is well captured

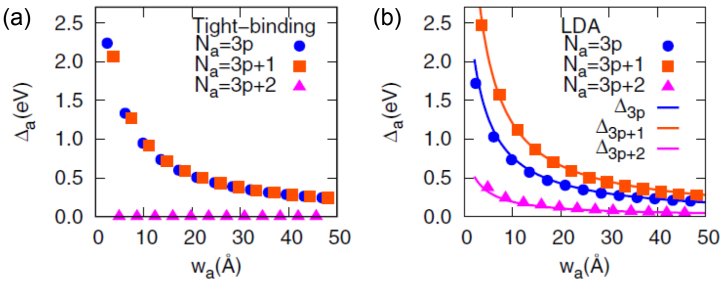

Figure 3.15: (a) Calculated band gap for armchair graphene nanoribbons with respect to the width within (a) tight-binding and (b) first-principle calculations (DFT) [105].

such considerations are lacking in tight-binding [106]. The width dependent band gaps for AGNRs obtained from LDA are shown in fig. 3.15(b). All three AGNR types exhibit a band gap, but the band gap of the $3n + 2$-AGNR is smaller by more than a factor of 3 compared to the other two configurations.

3.2.2 ZIGZAG GRAPHENE NANORIBBONS

In the same manner as for an AGNR, the band structure of a ZZGNR can be obtained from eq. 3.3 using appropriate boundary conditions. Considering a ZZGNR running

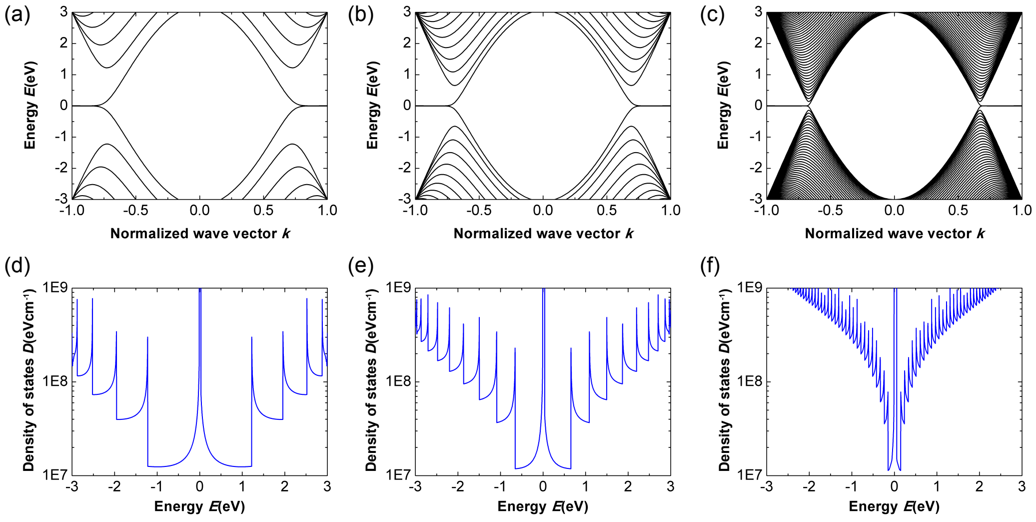

Figure 3.16: Band structure of zigzag graphene nanoribbons for (a) a 10-ZZGNR, (b) a 20-ZZGNR and (c) a 100-ZZGNR. Corresponding density of states of zigzag graphene nanoribbons for (d) a 10-ZZGNR, (e) a 20-ZZGNR and (f) a 100-ZZGNR.

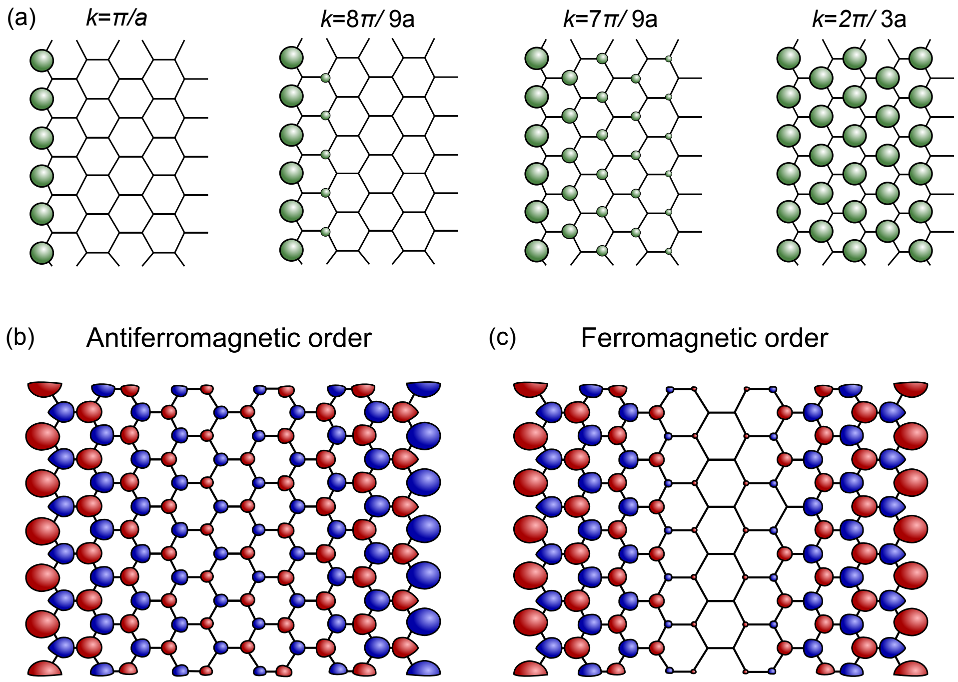

Figure 3.17: (a) Charge density for the edge states in a semi-infinite graphene sheet for $k = \pi/a$, $k = 8\pi/9a$, $k = 7\pi/9a$ and $k = 2\pi/3a$. Adapted from [30]. The radii of the circles is proportional to the charge density at each site. Spin density in a 10-zigzag GNR for (b) antiferromagnetic and (c) ferromagnetic coupling of the edges. Red (blue) color indicates spin up (down).

along the x-axis with ribbon edges at $y = 0$ and $y = W$, leads to the following boundary conditions

$$\Psi_A(L) = \Psi_B(0) = 0 \,. \tag{3.29}$$

This results in the energy spectrum [104]

$$E(k) = \pm\sqrt{1 + 4\cos^2\left(\frac{k}{2}\right) + 4\cos\left(\frac{k}{2}\right)\cos(p)} \,. \tag{3.30}$$

The transverse wave number p is the solution of

$$\sin(pN_z) + 2\cos\left(\frac{k}{2}\right)\sin(p(N_z+1)) = 0 \,. \tag{3.31}$$

This however, is not the complete energy spectrum. One state corresponding to the edge is missing. The edge state is localized and needs to be calculated separately. It is given by [104]

$$E(k) = \pm\sqrt{1 + 4\cos^2\left(\frac{k}{2}\right) - 4\left|\cos\left(\frac{k}{2}\right)\right|\cos(\eta)} \tag{3.32}$$

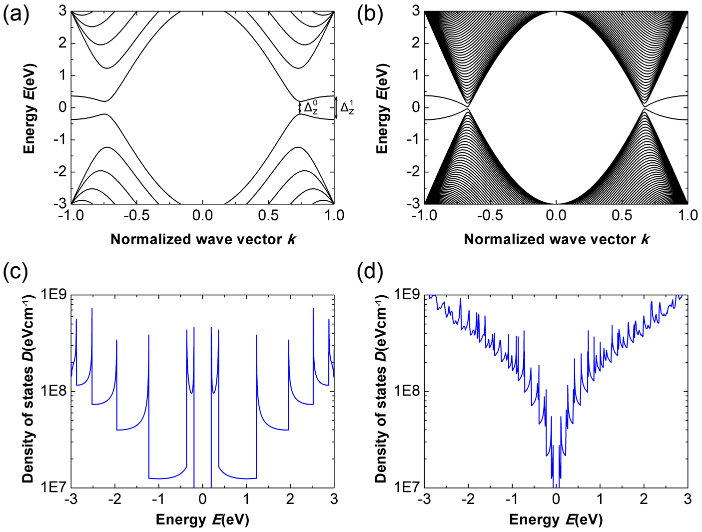

Figure 3.18: Band structure of anti-ferromagnetic zig-zag graphene nanoribbons for (a) a 10-ZZGNR and (b) a 100-ZZGNR. Corresponding density of states of anti-ferromagnetic zig-zag graphene nanoribbons for (c) a 10-ZZGNR and (d) a 100-ZZGNR.

with η being the solution of

$$\sinh(\eta N_z) - \left| 2\cos\left(\frac{k}{2}\right) \right| \sinh(\eta(N_z+1)) = 0 \,. \tag{3.33}$$

The band structures and corresponding DOS of ZZGNRs with $N_a = 10, 20, 100$ are shown in fig. 3.16. The most peculiar feature of the band structure is the degeneracy of the top valence and bottom conduction band at $k = \pi/a$. They stay flat roughly in between $2\pi/3a \leqslant k \leqslant \pi/a$ and this flattening even increases with increasing ribbon width. The flat bands originate from the localized states at the zigzag edges [27, 28]. The distribution of the charge density is shown in fig. 3.17(a). At $k = \pi/a$ the state is completely localized at the edge while it gradually moves to inner sites for $2\pi/3a \leqslant k \leqslant \pi/a$ reaching a completely extended state when $k = 2\pi/3a$ [104].

Due to the flat bands, the DOS of the ZZGNR exhibits a sharp peak at E_f in contrast to the zero DOS in a 2d graphene sheet. Such a high DOS at the Fermi level leads to an instability [105, 107, 108]. This instability can be resolved by considering spin degrees of freedom within LDA. As a result, the ground state of a ZZGNR has a parallel spin alignment along each edge but anti-parallel spin alignment between the edges, and is hence called antiferromagnetic ZZGNR (AM-ZZGNR). The corresponding spin density is shown in fig. 3.17(b). Besides the spin alignment at the edges, also nearest neighbors show anti-parallel spin-alignment. The spin-alignment decays towards the center of the ribbon. The energy difference between the nonmagnetic and the antiferromagnetic state increases with ribbon width and converges to about 0.38 eV for $N_z \sim 30$ [108].

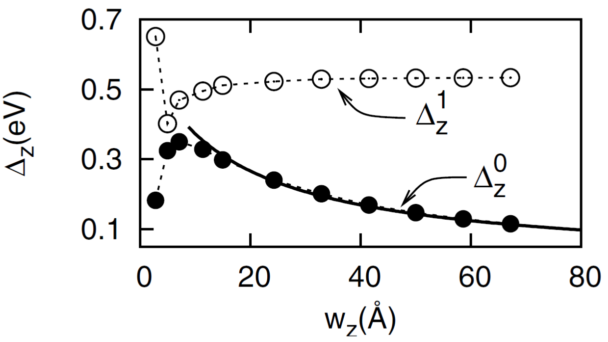

Figure 3.19: Band gap at $k = 2\pi/3a$ and energy splitting at $k = \pi/a$ of an AM-ZZGNR with respect to the ribbon width [105].

Fig. 3.18 shows the energy dispersion and DOS for a AM-ZZGNR with $N_z = 10$ and $N_z = 100$. The former flat bands at around $2\pi/3a \leqslant k \leqslant \pi/a$ have split up, exhibiting a band gap at $k = 2\pi/3a$ and an additional energy splitting at $k = \pi/a$. The AM-ZZGNR is hence semiconducting and no longer metallic. The opening of a band gap due to the antiferromagnetic ordering makes the AM-ZZGNR a so called Slater insulator [109]. Consequently, the peak in the DOS at E_f has been resolved. Interestingly, the band gap at $k = 2\pi/3a$ disappears with increasing ribbon width while the energy splitting at $k = \pi/a$ remains almost unaltered. This can be seen in detail in fig. 3.19. The energy splitting saturates at about 0.5 eV and does not change for a larger ribbon width. The band gap, however, is inversely proportional to the ribbon width but stays above the room temperature thermal limit up to $N_z \approx 400$, hence, a ribbon width of about 80 nm.

Consequently, also a ferromagnetic ZZGNR (FM-ZZGNR) should be considered. The corresponding spin density is shown in fig. 3.17(c). The spins at the two edges of the ribbon are aligned in parallel while the nearest neighbors still exhibit an antiparallel spin alignment. The spin-density decays away from the edges like in the case of an AM-ZZGNR. The penetration of the spin-polarization into the ribbon is not as deep as in the case of antiferromagnetic coupling. The band structure of a FM-ZZGNR can be found in fig. 3.20 together with the local DOS (LDOS). No band gap is present in the case of ferromagnetic ordering, hence the ribbon is metallic (a so called Stoner metal). The ribbon is always metallic, independent of its width. At E_f and $k = 2\pi/3a$ the spin up and spin down bands cross.

For both, the FM-ZZGNR as well as the AM-ZZGNR, magnetic effects on the bulk bands are negligibly small [108]. With increasing ribbon width, the bulk bands approach each other and finally recover the graphene band structure. The edge magnetization however, is not affected. The edges remain spin-polarized even for very wide ribbons but naturally the magnetic ordering between the two edges vanishes.

As previously stated the ferromagnetic ordering is energetically less favorable than the antiferromagnetic one, making the AM-ZZGNR the ground state. The energetic difference between the two states obeys a power-law behavior $E_{FM} - E_{AM} \sim 1/N^n$ with $n = 1.4 - 1.9$ [108]. Room temperature magnetic ordering ($E_{FM} - E_{AM} > 25$ meV)

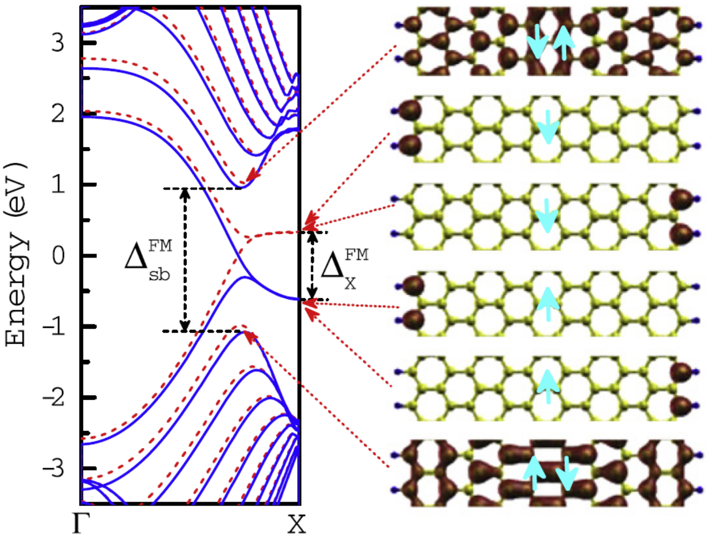

Figure 3.20: Band structure of a FM-ZZGNR with spin up (down) states indicated in blue (red). The LDOS is shown alongside [110].

can only be obtained for very narrow ribbons with $N_z < 8$. This makes the exploitation of magnetic order of GNRs in nanoelectronic applications very challenging. In contrast, the bandgap of an AM-ZZGNR might be more interesting in this sense, since a bandgap larger than the thermal limit is present for ribbons as wide as 80 nm [108]. Switching between the antiferromagnetic and ferromagnetic states and hence between semiconducting and metallic states was theoretically suggested to be possible by application of a magnetic field [111]. However for room temperature operation of such a device magnetic fields as high as 200 T are needed. At $T = 4\,\text{K}$ the required magnetic field reduces to about 30 mT which can be reached easily in a laboratory.

A final remark shall be made on behalf of the possible half-metallicity of AM-ZZGNRs upon application of an electric field across the ribbon [107]. Since the spins at opposite edges are oriented in opposite directions, the electric field will shift the occupied and unoccupied states of one spin type closer together and those of the other spin type further apart (cf. fig. 3.21). In the extreme case of fully closing the energy gap between occupied and unoccupied states of one spin type, the ribbon becomes half-metallic and transport along the ribbon is spin polarized. The critical field for which half-metallicity is present, decreases with increasing ribbon width due to the lowered electrostatic potential difference between the edges in wider ribbons.

3.2.3 TRANSPORT IN GRAPHENE NANORIBBONS

In the clean limit at zero temperature, the electrical conductance in a graphene nanoribbon follows the Landauer formula

$$G(E) = \frac{2e^2}{h} g(E) \tag{3.34}$$

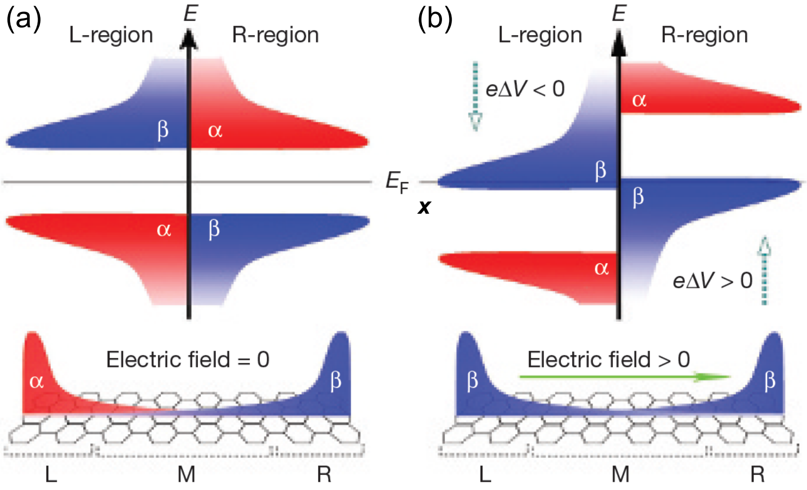

Figure 3.21: Schematic density of states diagram for an AM-ZZGNR (a) without and (b) with application of a transverse electric field [107]. States corresponding to spin directions α and β are shown in red and blue. The transverse electric field closes the bandgap for electrons with spin β.

where $g(E)$ is simply the number of subbands crossed by the Fermi energy. Thus,

$$g(E) = \begin{cases} n & , \text{ semiconducting AGNR} \\ n+1 & , \text{ metallic AGNR} \\ 2n+1 & , \text{ ZZGNR} \end{cases} \tag{3.35}$$

neglecting electron-electron interaction and spin polarization of the edge states. Disorder will lead to localization of transport in the subbands making it very challenging to observe ballistic transport in GNRs. One exception from that is the so called perfectly conducting channel (PCC) which exists in ZZGNR due to the flat bands originating from the localized edge states [30, 112]. In all the other parabolic subbands intravalley as well as intervalley scattering is allowed. In the zeroth subband (the flat band) no intravalley scattering is possible due to the absence of backward moving states in the same valley as obvious from fig. 3.22. Thus, in the left valley there is always one excess right going channel. The same is true for the right valley, here one excess left going mode is present. In the presence of long range impurities this gives rise to a PCC. The conductance $G \sim 1 + \exp(-L/\lambda_0)$, hence a channel with $G = 2e^2/h$ is always present independent of the ribbon length. Upon the introduction of short range impurities this PCC vanishes because now intervalley scattering is present and localization occurs. The conductance decreases exponentially $G \sim \exp(-L/\lambda_0)$. Intervalley scattering needs a large momentum transfer which is only given for short range scatterers such as lattice defects. Hence, the presence of a PCC can only be expected in well-ordered GNRs. In lithographically patterned graphene nanoribbons the realization of such ideal transport conditions is very challenging because the etch-

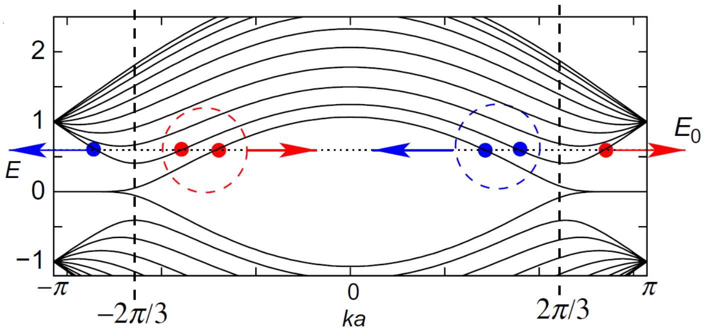

Figure 3.22: Band structure of a 10-ZZGNR. The red (blue) circles denote the right (left) moving channel at E_0. In the left (right) valley the degeneracy between left and right moving channels is missing due to one excess right (left) going channel [30].

ing process itself introduces a large amount of defects, especially in the edges, which are crucial for the transport characteristics [31, 32, 34].

4

EXPERIMENTAL SETUP

All transport experiments in this thesis were carried out by means of a 4-tip STM commercially purchased from Omicron NanoTechnology GmbH. In the following the key components of this system shall be explained.

4.1 SETUP OF THE UHV CHAMBER

In order to ensure an ultra-clean environment, the transport investigations were carried out under UHV conditions. The base pressure of the system is typically below 3×10^{-10} mbar. Therefore, the influence of defect adsorption, usually present in ambient conditions, can be minimized. A general overview over the UHV chamber is given in fig. 4.1. It consists of two main parts, a preparation and an analysis chamber separated by a gate valve. Both chamber parts feature a load lock chamber separated from the main chambers by gate valves. Hence samples and replacement tips can be passed through the locks without breaking the UHV conditions in the main chambers. The preparation chamber features a heating station on which samples can be heated either via direct current or via a backside filament. Additionally the sample can be cooled down to liquid nitrogen temperature on a separate cooling stage. Up to three evaporators can be used for thin film deposition directly within the preparation chamber. A spot profile analysis low energy electron diffraction (SPA-LEED) system provides access to the crystallographic properties of the samples. Up to ten samples can be stored in a sample garage. Unless stated otherwise, all samples which were brought into the the UHV chamber were first degassed for at least 3 hours at a minimum of 700 °C. For transport investigations, the samples were transfered into the analysis chamber which hosts a multi-tip scanning tunneling microscope (STM) in combination with a high resolution scanning electron microscope (SEM). The sample stage can be cooled with liquid nitrogen or helium and a minimum sample temperature of 25 K can be reached. Up to ten samples or replacement tips can be stored in a sample garage within the analysis chamber. Since the two chambers can be separated via a gate valve, sample preparation at elevated pressures in the preparation chamber does not compromise the pressure in the analysis chamber.

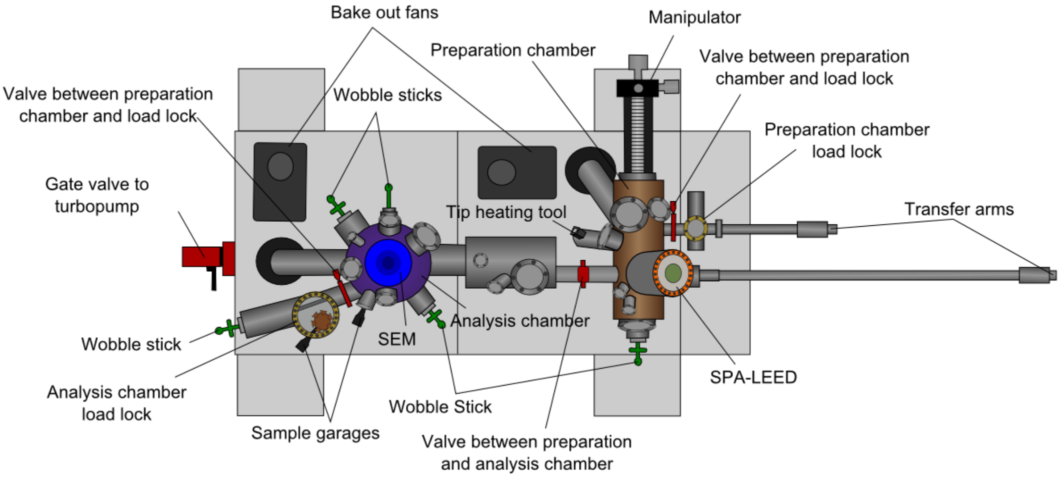

Figure 4.1: Schematic overview of the UHV chamber hosting the 4-tip STM.

4.2 SETUP OF THE MULTI-TIP STM/SEM COMBINATION

Schematics of both the multi-tip STM and the SEM can be found in fig. 4.2(a, b). The multi-tip STM consists of four tip-hosting scanners of two different types. Three so called standard scanners and one high resolution scanner. The high resolution scanner is better protected against vibration and is usually used for recording STM images. It can reach atomic resolution of graphene on SiC (section A.1 in the appendix provides a detailed description of STM). The other three are mainly used just for transport experiments. Nevertheless, all scanners are full-fledged feedback controlled STMs. The STM capabilities of the three standard scanners are necessary in order to navigate the tips on the sample surface on a nanometer scale without damaging the tips or the sample. All transport as well as all STM and STS measurements were made with electrochemically etched tungsten tips. All tips were cleaned by the application of several voltage pulses between tip and sample prior to all experiments. Voltage pulses with up to $\pm 10\,\mathrm{V}$, applied for up to $500\,\mathrm{ms}$ were used for cleaning.

In order to position the tips on the sample surface, a SEM is positioned right atop the multi-tip STM. The SEM is a GEMINI type SEM commercially available from Carl Zeiss AG. A detailed description of SEM in general can be found in the appendix section A.3. The GEMINI type SEM features a hot field emission cathode. Electrons are extracted from a sharp tip by a strong electrostatic field. In hot field emission the tip is additionally heated. This results in a much higher emission current and beam stability compared to cold field emission. The most striking feature of the GEMINI column is the so called Booster voltage. After extraction from the field emitter the electrons are accelerated by an additional Booster voltage which maintains a high beam energy throughout the whole column. At close distance to the sample surface, the electrons are decelerated to the chosen primary beam energy. This ensures a minimal suffering from aberration and a very small beam diameter. The aberration correction is especially important because in the combination with a multi-tip STM the SEM

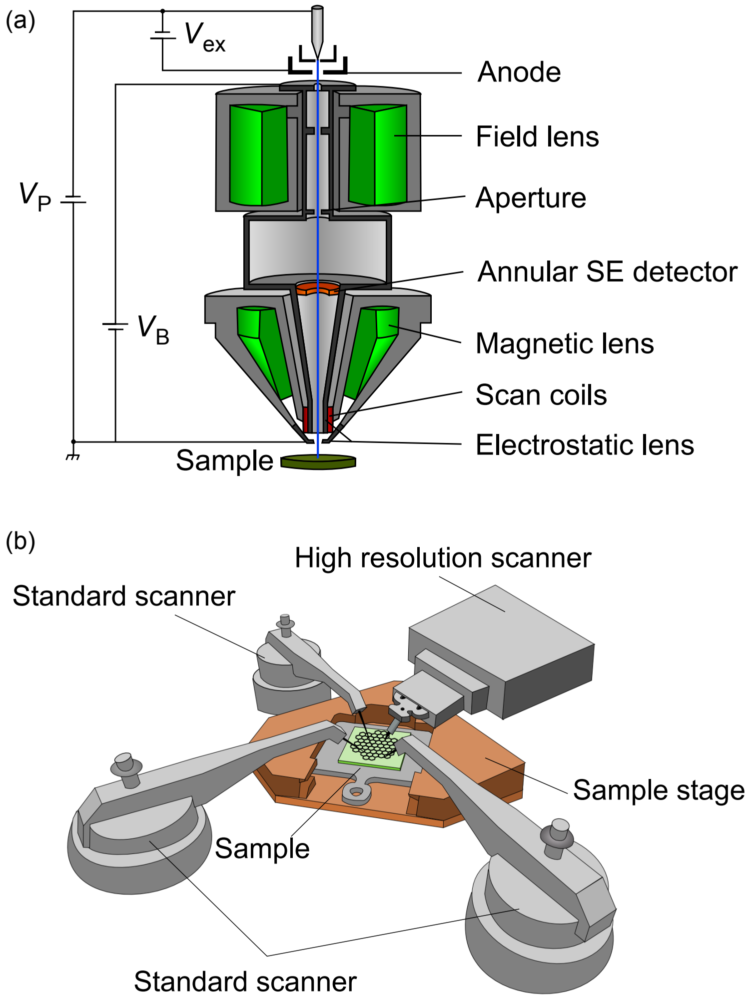

Figure 4.2: (a) Cross-sectional view of the GEMINI type SEM column. Adapted from [113]. (b) Schematic of the 4-tip STM used for transport experiments.

has to be operated at a relatively large working distance of 1.5 cm. As discussed in section A.3.3 a large working distance leads to a larger beam spot on the surface due to spherical aberration. Due to the extensive aberration correction the GEMINI type SEM used in the experiments in this thesis has a maximum resolution of 4 nm. On the other hand, the large working distance is advantageous for the experiments on structured samples due to the larger depth of focus (see also section A.3.3).

4.3 TRANSPORT EXPERIMENTS WITH THE MULTI-TIP STM

While navigating the tips over the sample surface to their desired position, the tips are held in feedback controlled tunneling mode. For the transport measurements itself, feedback loops are turned of and the tips are brought closer to the surface in 1 nm steps. During this approach, the resistances between sample and tips are checked to

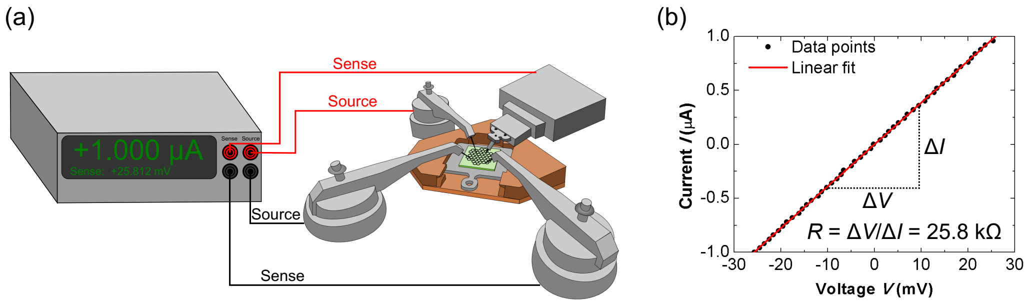

Figure 4.3: (a) Schematic of the 4-tip transport setup featuring a Keithley sourcemeter. (b) Example for an IV curve with corresponding linear fit.

avoid crashing and to find stable contact conditions. Tips are always brought into direct contact with the sample, hence typically an ohmic contact is present between tip and sample. Subsequently, the resistances between each of the probes are checked to make sure that all are in good contact. Currents and voltages are sourced and probed by means of a Keithley sourcemeter connected to the tips as schematically shown in fig. 4.3(a). In case of a 2pp measurement each tip serves as current source and voltage probe. If not stated otherwise each resistance value given in the following chapters was obtained from IV curves with at least 50 points by a linear fit. An example for a fitted IV curve is presented in fig. 4.3(b). The maximum source current was typically between ±1 µA and ±10 µA.

The big advantage of a multi-tip STM is its flexibility. The only limitation for the probe arrangement is the size of the tips itself. Besides that, any kind of geometry or probe spacing can be obtained easily.

Details about the physical concepts as well as the setups of all other experimental methods which were used in this thesis can be found in appendix A.

Part II

EPITAXIAL GRAPHENE SHEETS

5

LOCAL TRANSPORT PROPERTIES OF EPITAXIAL GRAPHENE MONOLAYERS

In this chapter the local electronic properties of a graphene monolayer (ML) epitaxially grown on the Si-face of SiC shall be discussed. It serves as a reference system for further local transport investigations on defective graphene sheets in chapter 6, graphene p-n junctions in chapter 11 and graphene nanoribbons in chapter 8.

This chapter features a short description of the growth technique followed by a characterization of epitaxial graphene sheets by means of SEM, LEED, Raman spectroscopy and STS. The local transport properties are evaluated with respect to measurement configurations and temperature. The results are published in [114].

5.1 EPITAXIAL GROWTH OF GRAPHENE

The synthesis of high-quality graphene is usually done in an rf furnace [40] or by the confinement controlled sublimation (CCS) method [17, 41] as already described in detail in section 3.1.4. During this thesis, graphene growth was carried out using two different home built setups which in contrast rely on direct current resistive heating. Both setups are shown in fig. 5.1.

The first one is an all carbon heater which contacts the SiC sample with two pairs of guillotine clamps at each side. The clamps are also made from carbon. The whole setup is shown in fig. 5.1(a). The clamps fix the sample rather loosely ensuring a minimum amount of tension. With all parts of the heater made from carbon the evaporation of impurity atoms during the heating process is prevented. The heating is carried out in a HV chamber with a base pressure of 1×10^{-6} mbar. The sample temperature is measured with an infrared pyrometer. The initial flattening of the substrate and removal of the oxide layer was achieved by heating the sample in 1 bar hydrogen atmosphere at a temperature of 1400 °C for 30 minutes. The graphene growth itself was subsequently carried out in a 1 bar argon atmosphere at temperatures around 1500 °C for several minutes.

The second home built heater relies on the face-to-face method [101] where two SiC substrates facing each other are heated simultaneously to create a locally enhanced Si pressure as described in section 3.1.4. The clamps holding the samples are made from a 100 µm thick tantalum foil ensuring a constant spacing of 100 µm between the two samples. The heating steps were carried out in a UHV chamber with a base pressure of 5×10^{-8} mbar and all temperatures were measured with a two-color infrared

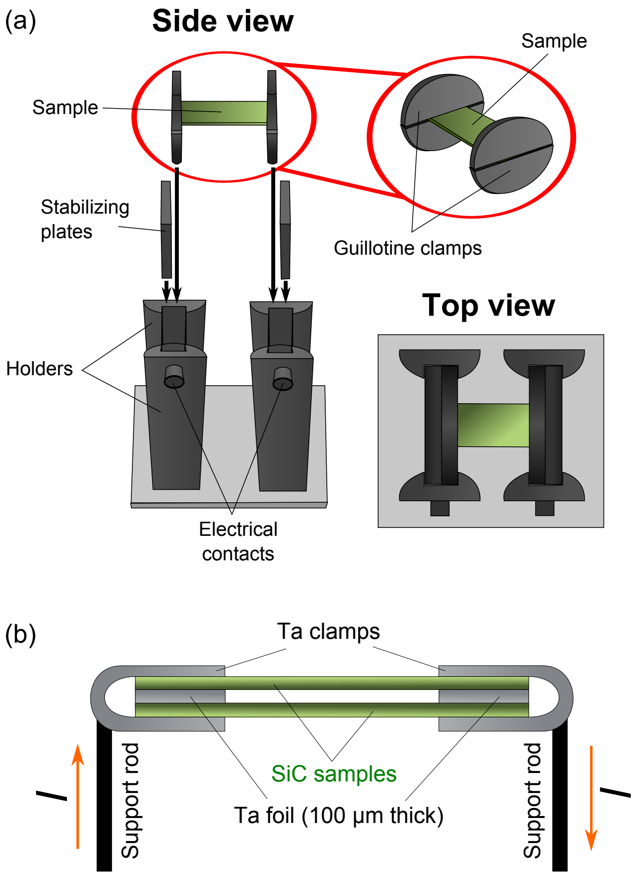

Figure 5.1: Schematic of the (a) all carbon heater in top and side view and (b) the face-to-face heater used for graphene synthesis.

pyrometer. For the initial flattening of the substrate the sample was heated up to 1200 – 1400 °C and kept there for 5 hours. To initialize the graphene growth, the temperature was elevated to about 1550 °C – 1600 °C and maintained for a few minutes. The Si vapor pressure at this growth temperature is about 10^{-3} mbar. The growth temperature is consequently about 300 °C higher compared to graphene growth in UHV.

Besides graphene samples synthesized in these home built heaters also epitaxial graphene produced in collaboration with the Starke group at MPI Stuttgart as well as the Schumacher group at the PTB Braunschweig by means of annealing in an argon atmosphere in a rf furnace were investigated. Either n-type doped or semi-insulating 6H-SiC(0001) was used as substrate material. Since no significant differences of the graphene growth were observed between the differently processed samples, they shall not be distinguished in the following. A detailed characterization of the growth processes itself is not in the scope of this thesis. Instead, the influence of morphological and electronic features on the transport characteristics of the graphene sheets shall be discussed in detail.

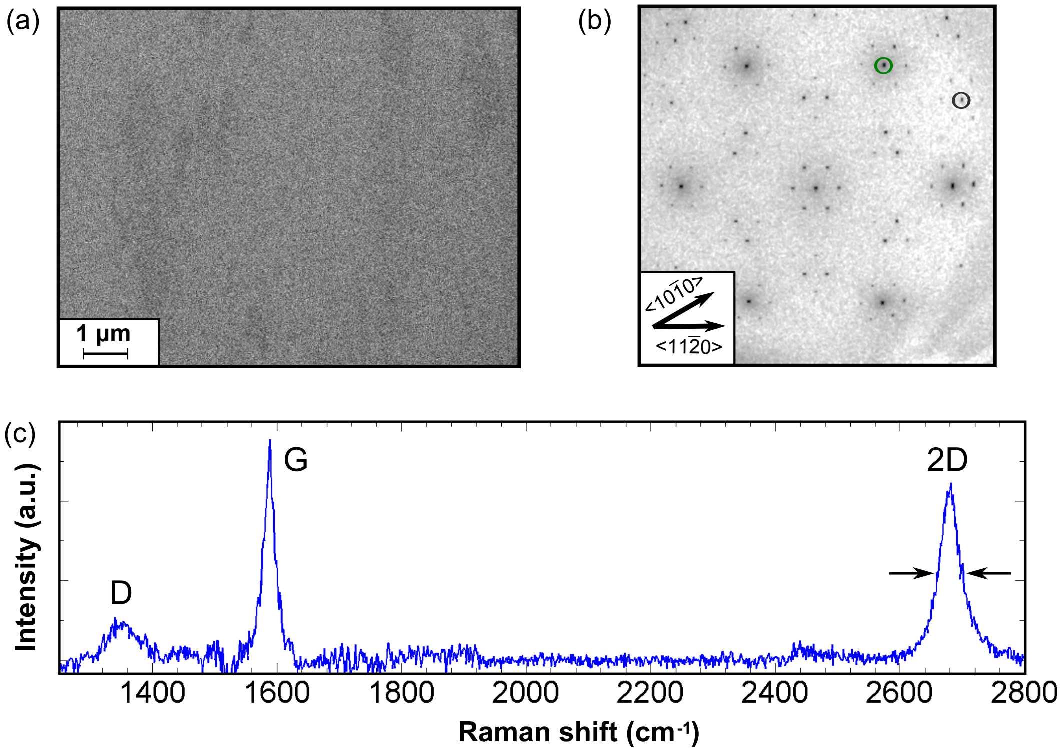

Figure 5.2: (a) SEM image of an epitaxial graphene ML on SiC ($E = 15\,\text{keV}$). Only one contrast level can be identified. (b) LEED pattern of an epitaxial graphene ML ($E = 137\,\text{eV}$) revealing a $(6\sqrt{3} \times 6\sqrt{3})R30°$ structure. The SiC(10) reflex is indicated in green and the graphene(10) in grey. (c) Raman spectrum of an epitaxial graphene ML showing the characteristic D, G and 2D peak of graphene.

5.2 TRANSPORT CHARACTERISTICS

In the following the transport characteristics of an epitaxial graphene ML shall be discussed. An epitaxial graphene sheet can be identified as a ML by means of several methods. SEM, LEED, Raman spectroscopy and STS were used to confirm the presence of a ML sheet.

5.2.1 CHARACTERIZATION OF A GRAPHENE MONOLAYER

The SEM image in fig. 5.2(a) shows only one contrast level which indicates that the surface is homogeneously covered with only one phase. It will be shown later in section 6.1 that a sample surface exhibiting multiple phases such as bilayer or buffer layer contributions would give rise to different contrast levels for each phase. Nevertheless, the SEM alone does not allow to identify which specific phase is present on the sample surface.

The LEED pattern in fig. 5.2(b) gives further insight into the crystal structure of the surface. It shows the characteristic $(6\sqrt{3} \times 6\sqrt{3})R30°$ reflecting the arrangement of the buffer layer on the SiC surface (cf. fig. 3.11 in section 3.1.4). All observed

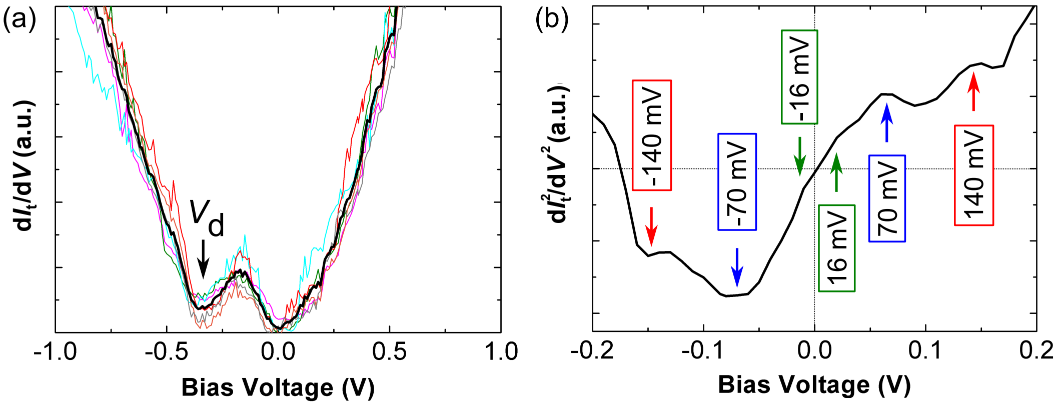

Figure 5.3: (a) Scanning tunneling spectra taken on an epitaxial graphene ML. The black curve is the mean spectrum. The dip associated with the Dirac point (V_d) is indicated by the black arrow. (b) $\frac{d^2 I_t}{dV^2}$ spectrum of an epitaxial graphene ML. The arrows indicate features assigned to phonon contributions.

spots belong to the $(6\sqrt{3} \times 6\sqrt{3})R30°$ reconstruction. Especially, no spots belonging to the $(\sqrt{3} \times \sqrt{3})R30°$ which develops previous to the $(6\sqrt{3} \times 6\sqrt{3})R30°$ are found. This implies that at least a pure buffer layer is present on the sample [95]. The LEED pattern does not allow to clearly distinguish between a buffer layer and ML graphene. An increase in the layer number would manifest in an increased intensity of the first order graphene spots relative to the first order SiC spots under the assumption of identical form-factors. Thus, this requires a careful analysis of the intensity profiles.

A fast method to determine the number of graphene layers is Raman spectroscopy. A corresponding Raman spectrum of an epitaxial ML is shown in fig. 5.2(c). The characteristic D, G and 2D peak which are described in detail in section A.5.2 are clearly visible. The G line position ($1588\,\text{cm}^{-1}$) and 2D line position ($2680\,\text{cm}^{-1}$) are characteristic for ML epitaxial graphene [115]. Furthermore, the 2D peak can be fitted with a single Lorentzian with a full width at half maximum (FWHM) of $40\,\text{cm}^{-1}$, a clear signature of ML graphene [116, 117]. The presence of a D peak at a Raman shift of $1352\,\text{cm}^{-1}$ indicates the presence of Raman active defects [118]. The ratio $I(D)/I(G) \approx 0.2$ is comparable to Raman spectra for epitaxial graphene reported in literature [115, 119]. The mean distance of Raman active defects can be determined from eq. A.27 to about $(37 \pm 5)\,\text{nm}$.

Further insight into the electronic properties of the graphene layer can be gained by STS. Fig. 5.3(a) shows a tunneling spectrum of an epitaxial ML. The spectrum is recorded using a lock-in technique with a modulation amplitude of $20\,\text{mV}$ and frequency of $1.5\,\text{kHz}$. The characteristic linear band edges are clearly visible in the spectrum. Furthermore, two minima at zero bias and at about $V = V_d = -360\,\text{mV}$ can be identified. The latter is assigned to the Dirac point throughout literature [120–124]. The energetic location of the Dirac point is given by $E_d = e\,V_d$ which yields $E_d = -(360 \pm 30)\,\text{meV}$ for the spectra shown in fig. 5.3(a). This implies a strong n-doping ($n \approx 1 \cdot 10^{13}\,\text{cm}^{-2}$), the Fermi level is located 360 meV above the Dirac point. The spectra were taken at different positions on the sample within a $3 \times 3\,\mu\text{m}^2$ range.

The variation in the doping level is hence very small. The observed doping agrees well with the doping levels typically extracted from ARPES data of ML epitaxial graphene [40, 97, 114, 125].

The origin of the second minimum at zero bias is not that clear although it is extensively reported in tunneling spectroscopy studies on epitaxial graphene on SiC. It has been observed as a dip with the tunneling conductance remaining finite [121, 123, 126, 127] or even dropping to zero [128]. Similar suppressions of the tunneling conductance in dI_t/dV spectra on exfoliated graphene have been interpreted to arise from a phonon-assisted inelastic tunneling process [120, 129]. A fingerprint of inelastic tunneling processes is the presence of antisymmetric peaks on opposite edges of the Fermi energy in the corresponding $\frac{d^2I_t}{dV^2}$ spectrum [130]. Such peaks are clearly visible in fig. 5.3(b) with one minimum and related maximum at ± 140 mV, at ± 70 mV and at ± 16 mV. They correspond to two out-of-plane acoustic phonon modes in graphene at 16 meV at the Γ point and at 70 meV at the K point [131–133]. The features at ± 140 mV are caused by the sideband of the 70 meV phonon mode [132]. In a similar manner, in exfoliated graphene this phonon mode was found at 63 meV [122] and its large inelastic signal was identified to mimic the opening of a central 126 meV gap in the dI_t/dV spectra [120, 129]. However, for epitaxial graphene on SiC the inelastic contributions to the tunneling spectrum have been shown to be spatially dependent which makes phonon-assisted tunneling unlikely [133]. Other explanations for the minimum in the tunneling conductance have been suggested. The influence of electronic states of the graphene/SiC interface and local charging of the graphene layer underneath the STM tip due to the large electric fields present there [128] have been considered. The local gating below an STM tip during STS measurements has been observed indeed on other systems [134, 135]. However, a conclusive theory for the zero bias minimum is not yet validated.

In conclusion, the measurement methods presented in this section allow to clearly identify ML graphene. The SEM can be used to collect informations about the overall homogeneity of the sample. In case of a sample homogeneously covered with one phase, Raman spectroscopy alone is enough to clearly identify ML graphene. LEED can distinguish between the buffer layer and prior reconstructions. The STS gives access to the LDOS of the graphene layer.

5.2.2 LOCAL MULTI-PROBE TRANSPORT ON MONOLAYER GRAPHENE

Having characterized the epitaxial graphene ML in detail in the previous section its local transport properties are now investigated by means of a multi-tip STM. In fig. 5.4 an SEM image of the collinear tip arrangement is shown. The underlying graphene sheet appears highly uniform as already discussed in the previous section. The tungsten tips used here, allow contact spacings down to $L = 250$ nm. The indicated contact geometry with the outer probes as current source and the inner two as voltage probes can be easily interchanged providing the possibility to measure different configurations in a minimum amount of time.

It is reasonable to assume that the epitaxial graphene ML can be treated as an infinite 2d sheet. However, this assumption can be easily justified by performing dual

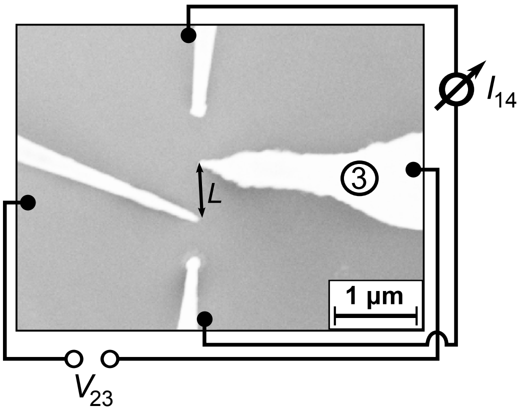

Figure 5.4: SEM image of a collinear tip arrangement. Tip 3 is also used for high-resolution imaging and spectroscopy.

configuration measurements (cf. section 2.1.2) which allow to probe directly the dimensionality of transport. For the two configurations A and B schematically shown in fig. 5.5(a) the resistance values are independent of the probe spacing. This is the first indication for 2d transport (cf. 2.1.2). Secondly, dividing the mean value of the resistances ($R_A = (198 \pm 6)\,\Omega$ and $R_B = (157 \pm 6)\,\Omega$) yields $R_A/R_B = 1.26 \approx \ln(4)/\ln(3)$ which is characteristic for a continuous 2d sheet [60]. Hence the assumption that the probe spacing L is much larger than the sheet thickness but much smaller than the lateral sample dimensions is valid. This implies that the extraction of the corresponding sheet resistances R_s is possible via to ways. The resistance R_A can be simply multiplied with the correction factor accounting for a thin infinite 2d sheet resulting in $R_s = R_A\,\pi/\ln(2)$ or R_s can be calculated directly from R_A and R_B by means of eq. 2.20. The results of both methods are given in fig. 5.5(b), showing the sheet resistances obtained by geometric correction and from the dual configuration versus the probe spacing. The dual configuration yields a mean value $R_s = (911 \pm 17)\,\Omega/\square$ while the geometric correction results in $R_s = (899 \pm 27)\,\Omega/\square$. Hence the two values agree within 1%. The standard deviation is slightly higher for the geometric correction. The agreement of both values is a strong proof that no lateral finite size effects have to be taken into account.

The major error source in a 4pp resistance measurement is a non-equidistant arrangement of the tips. Due to the finite tip radius as well as SEM resolution, the tip position can be usually determined with an accuracy of about 100 nm. Consequently, 4pp measurements with small probe spacings are more error prone. This also explains why the scattering of the data points in fig. 5.5(a) is the same for configuration A and B. A non-equidistant placement of tips will lead to a similar error in both configurations.

So far, all the transport characteristics were investigated at room temperature. In order to reveal the dominant electron scattering mechanism in an epitaxial graphene ML also temperature dependent measurements were performed. The sample temperature was lowered down to 30 K via cooling with liquid helium. The sheet resistances were calculated by means of geometric correction. The corresponding mobilities were

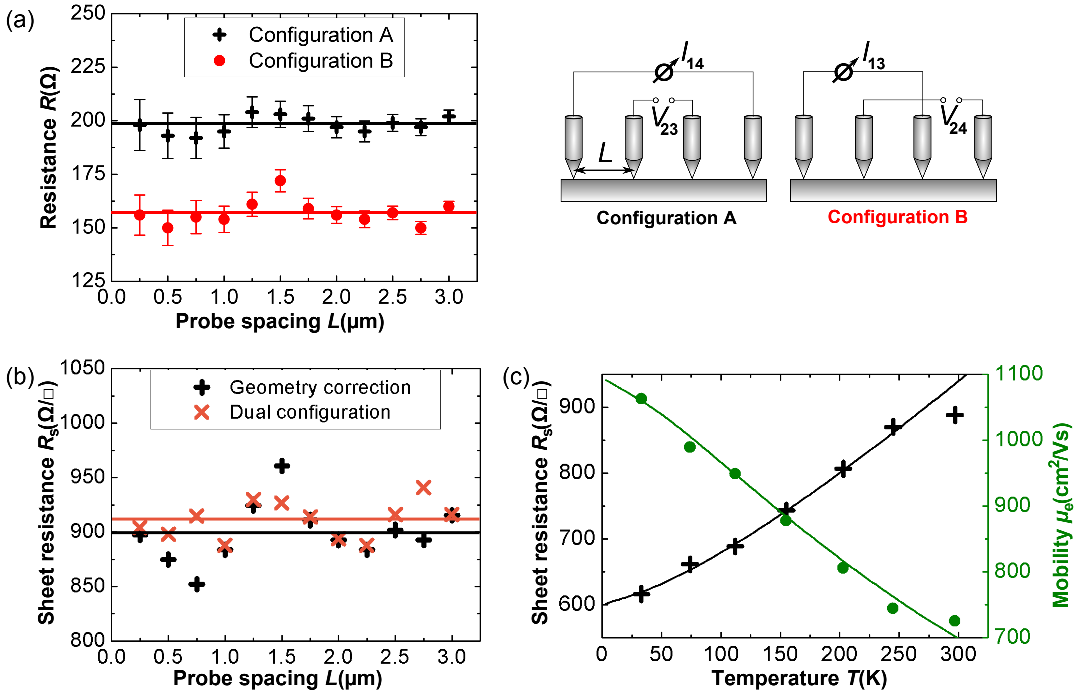

Figure 5.5: (a) Local 4pp transport measurements on an epitaxial graphene ML in dual configuration. The resistance in configuration A and B is plotted with respect to the probe spacing. The mean values are indicated. The two configurations are shown schematically. Sheet resistances from local transport measurements as function of (b) probe spacing ($T = 300\,K$) and (c) temperature ($L = 1\,\mu m$). The sheet resistances in (b) are deduced from dual configuration and by applying the geometrical correction factor for a thin sheet. Details about the calculation of mobilities and fit functions in (c) are given in the main text.

extracted from the sheet resistances following section 3.1.2. The charge carrier density was calculated by means of eq. 3.15 using the doping level deduced from STS in the previous section (−360 meV). The resulting sheet resistances and mobilities as a function of temperature are shown in fig. 5.5(c). The mobility is found to increase from $720\,cm^2/Vs$ at room temperature to $912\,cm^2/Vs$ at 30K. These values are in good agreement with previous studies [136, 137].

With decreasing temperature, the sheet resistances decreases, reaching a minimum value of $R_s = 616\,\Omega/\square$ at $T = 30\,K$. This behavior is well understood in terms of phonon assisted scattering. The sheet resistance can be modeled by assuming three contributions [33, 138–141], a residual resistivity ρ_0 at low temperatures, a resistivity due to acoustic phonon scattering ρ_{LA} and an activated contribution ρ_p from low-energy phonon modes. Altogether $R_s = \rho_0 + \rho_{LA} + \rho_p$. The individual components are given by

$$\rho_{LA} = \frac{\pi D_a^2 k_B T}{e^2 \hbar \rho_s v_s^2 v_f^2} \tag{5.1}$$

with the acoustic deformation potential D_a, the 2d mass density ρ_s and the sound velocity $\nu_s = 1.73 \times 10^4$ m/s and

$$\rho_p = \sum_{i=1}^{2} \frac{C_i}{e^{\frac{E_i}{k_B T}} - 1} \tag{5.2}$$

where C_i is the electron phonon coupling constant and E_i is the phonon energy. The phonon modes used for the fit in fig. 5.5(c) are chosen to match the low energy phonon modes in epitaxial graphene $E_1 = 70\,\text{meV}$ and $E_2 = 16\,\text{meV}$ which can be extracted from the $\frac{d^2 I_t}{dV^2}$ spectrum in fig. 5.3(b) and are also reported in literature [132, 133]. These modes are related to out-of-plane acoustic modes found in graphite [142]. The out-of-plane character of the modes implies that the graphene layer is still coupled to the underlying buffer layer forming a quasi 3d structure [138]. Hence this mechanism can be treated as a remote interfacial phonon scattering [33]. The other parameters obtained from the fit are the coupling constants $C_1 = 112\,\Omega$ and $C_2 = 282\,\Omega$. Compared to previous work [138] these values are significantly lower resulting in a much weaker temperature dependence. The contribution from the acoustic phonon scattering ρ_{LA} has only one free fit parameter, the acoustic deformation potential D_a. Here, a value of $D_a = 18\,\text{eV}$ gives the best result, in good agreement with theory [143–145]. This is remarkable because previous studies of the temperature dependence of the sheet resistance in ML epitaxial graphene failed to reproduce this value [138]. The reason for this and subsequently the higher coupling strengths was assumed to be additional temperature dependent Coulomb interaction or strain. The absence of such effects in the temperature dependent measurements presented in this section leads to the conclusion that contacting a graphene sheet with a multi-tip STM does not introduce extrinsic strain. Thus it is suitable to extract the real intrinsic transport properties of a graphene sheet.

5.3 CONCLUSIONS

It was shown in this chapter that the transport characteristics such as sheet resistance or mobility of an epitaxial graphene monolayer can be analyzed by means of a multi-tip STM with high precision. ML graphene can be identified by both ex-situ and in-situ characterization methods. Ex-situ, Raman spectroscopy is the method of choice due to the characteristic D, G and 2D features which allow to clearly identify ML graphene. In-situ, by means of SEM, LEED and STS the homogeneity as well as electronic characteristics such as the doping of the graphene sheets can be further evaluated. Very homogeneous ML graphene films were identified exhibiting the typical high n-type doping. This creates the prerequisites for the understanding of the subsequent local transport experiments. The ML graphene was characterized as a 2d system by means of the dual configuration method. The sheet resistance was found to be as low as $616\,\Omega/\square$ at 30K with a corresponding mobility of $912\,\text{cm}^2/\text{Vs}$. A previously reported remote phonon scattering mechanism was identified as main source for the temperature dependence of the conductivity. Characteristic parameters of the involved phonons such as the deformation potential were shown to be in full agreement with theory. Hence, by means of the multi-tip STM it was possible to probe the transport characteristics of a graphene ML without perturbing the system.

6

INFLUENCE OF DEFECTS ON LOCAL TRANSPORT PROPERTIES

In the previous chapter 5 the local transport characteristics of a uniform graphene ML were investigated. In the following the influence of defects in the ML will be studied. A defect in the sense of this chapter is every alteration from a perfect ML. Especially, this chapter will focus on the influence of substrate step edges introducing excess coverage in the form of additional bilayer fractions as well as incomplete graphenization in the form of nano-inhomogeneities. Most of the results presented in this chapter are published in [114, 146].

6.1 LAYER-NUMBER DETERMINATION IN THE SEM

Since the transport characteristics of imperfect graphene sheets are investigated with the multi-tip STM, it is necessary to find a way to quantify the local graphene coverage with the SEM which will be used later on for the placement of the tips. In this section, it will be shown that the contrast levels seen in the SEM directly correspond to different coverages. Fig. 6.1 presents a comparison of an AFM topographic and phase image with the SEM image of an inhomogeneously graphitized SiC substrate. The presence of ML and bilayer graphene is known for this sample from ARPES and Raman (not shown here). Focusing first on the AFM topographic image in fig. 6.1(a) only very few details of the sample surface are apparent. Substrate steps of $3-7\,\mathrm{nm}$ in height are clearly visible. They originate from step bunching during the initial substrate flattening. On the terraces, additional contrast levels can be seen with a height of about $2\,\text{Å}$ which might be related to differences in the coverage. Nevertheless, just the AFM topography is not enough to clearly identify the different areas.

For this purpose, the AFM phase is of relevance. Phase contrast arises from different rates of energy dissipation between tip and sample [147]. This gives rise to a phase contrast between different areas with different number of graphene layers [148]. An area consisting of ML graphene will exhibit a brighter phase contrast level than a bilayer [148] while the buffer layer is reported to show a darker contrast level than the ML [149–151]. With this knowledge the AFM phase image presented in fig. 6.1(b), which shows the same area as the topographic image in fig. 6.1(a), can be directly interpreted. The terraces are mainly covered with ML graphene (light gray) and smaller bilayer stripes (medium gray) are located along the step edges. Furthermore, the ML graphene on the terraces incorporates darker areas where buffer layer (dark gray) is

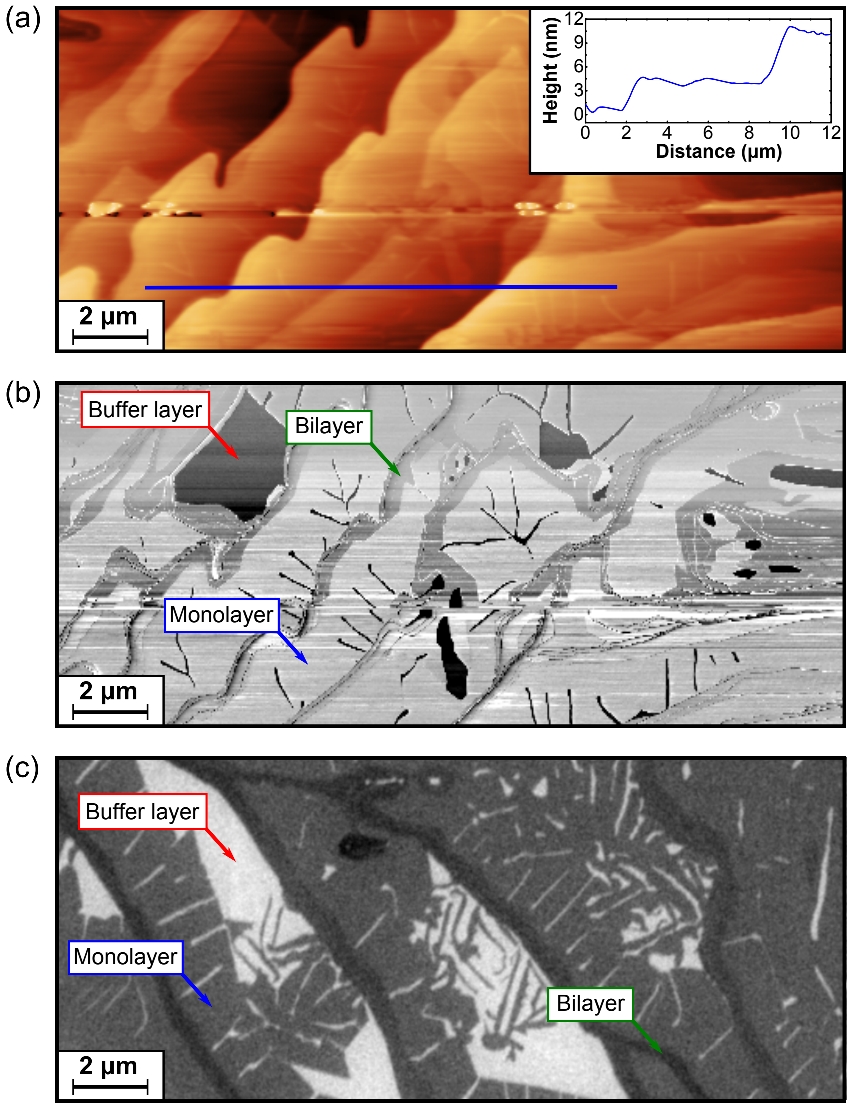

Figure 6.1: (a-c) Epitaxial graphene imaged with (a) AFM topography, (b) AFM phase and (c) SEM. The contrast levels corresponding to the buffer layer, monolayer graphene and bilayer graphene are indicated in (b) and (c). The SEM image was taken at a different sample position. The origin of the AFM topography linescan in (a) is marked in blue.

still present. The change of phase contrast coincides with a change in the height level of about a few Å as observed in the topographic image.

A SEM image taken on the same sample also exhibits three contrast levels (light gray, medium gray, dark gray). With the informations from the phase image the three contrast levels can be directly related to the presence of ML graphene (medium gray), bilayer graphene (dark gray) and the buffer layer (light gray). The identification of the three types of areas is straightforward although the SEM image is taken at a different sample position. These contrast levels in SEM are frequently used and reported for the estimation of graphene layer thicknesses [152–154]. The contrast between

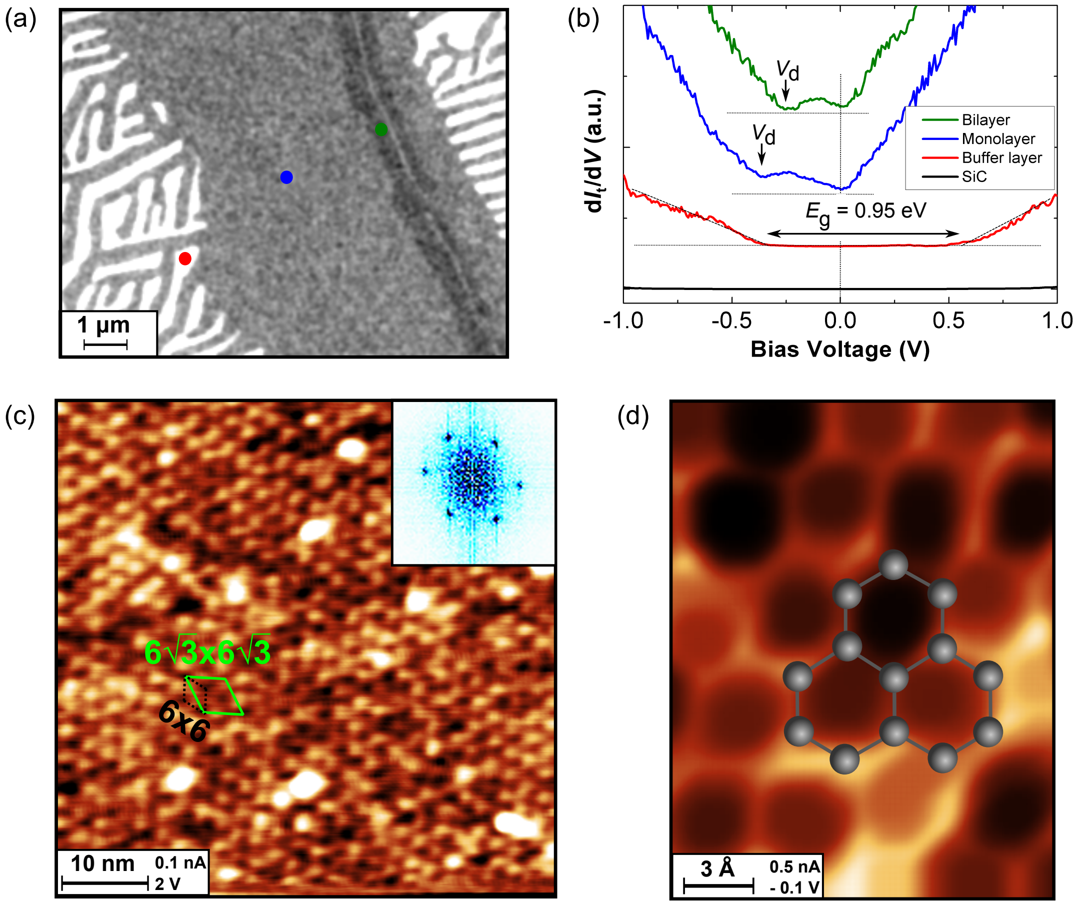

Figure 6.2: (a) SEM image of an epitaxial graphene sheet on SiC showing three contrast levels (light, medium, dark gray). (b) STS identifying the three contrast levels seen in SEM as buffer layer (light gray), monolayer graphene (medium gray) and bilayer graphene (dark gray). The dip corresponding to the Dirac point at bias voltages $V_d = -380\,\mathrm{mV}$ and $V_d = -260\,\mathrm{mV}$ is indicated for mono- and bilayer graphene as well as the energy gap (E_g) for the buffer layer. A spectrum taken on bare SiC is shown for comparison. The spectra are shifted for better visibility. The dotted lines indicate zero for every spectrum. (c) STM image of the buffer layer showing the characteristic $(6\sqrt{3} \times 6\sqrt{3})R30^\circ$ and 6×6 overstructure. The inset displays the 2d Fast Fourier Transform. (d) STM image of the epitaxial graphene monolayer revealing the typical honeycomb lattice.

graphene and the buffer layer or SiC substrate is typically attributed to the higher conductivity of the graphene. Less electrons are reflected back to the secondary electron detector from the more conductive graphene making it darker in appearance [154]. Furthermore, the secondary electron intensity measured with SEM was found to linearly decrease with the number of layers [155]. This linear relationship is explained by the increased attenuation of the secondary electrons. Additionally the work function of graphene increases with an increasing number of layers [156]. This can also account for the observed contrast since a higher work function leads in general to a lower secondary electron yield [157]. Although a determination of the absolute layer number in SEM is not straightforward, relative thicknesses are easily accessible.

Moreover, STS can be used to validate that the three contrast levels seen in SEM indeed belong to the buffer layer, ML graphene and bilayer graphene. In fig. 6.2(a) a SEM image with three contrast levels (light gray, medium gray and dark gray) is shown. The dots mark the positions on which the tunneling spectra in fig. 6.2(b) are recorded. For comparison also a spectrum from a pure SiC substrate is shown. The tunneling spectra clearly identify the buffer layer with a band gap around 1 eV. The spectrum of the buffer layer agrees qualitatively with previous experimental studies [126, 149]. It can be clearly distinguished from the tunneling spectrum on bare SiC, which exhibits a large band gap $E_g > 2\,\text{eV}$. The STM image in fig. 6.2(c) shows the buffer layer region. The visible structure is the $(6\sqrt{3} \times 6\sqrt{3})R30°$ reconstruction which is characteristic for the buffer layer. The unit cell of the $(6\sqrt{3} \times 6\sqrt{3})R30°$ and the quasi 6×6 are indicated. This shows that the region exhibiting the brightest contrast level in SEM corresponds to the buffer layer.

The tunneling spectrum on the medium gray area in the SEM shows the double dip feature which is characteristic for doped graphene (cf. section 5.2.1). The dip corresponding to the Dirac point is clearly visible and yields $E_d = -380\,\text{meV}$. Fig. 6.2(d) shows an atomically resolved STM image of the region were the STS spectrum was taken. The honeycomb lattice of graphene is clearly visible.

Moving further to the areas with dark gray contrast in the SEM image the tunneling spectrum in fig. 6.2(b) shows a slight change compared to the spectrum on the ML. The Dirac point dip is shifted to $E_d = -260\,\text{meV}$. The shift of the doping level from ML to bilayer graphene is consistent with ARPES data [125, 158]. The additional opening of a band gap of about 100 meV as observed in ARPES and suggested by tight-binding calculations [159, 160] is not visible. Most likely, the resolution of the spectrum is not sufficient to see such a small gap. Nevertheless, the STS and STM investigations further support the correlation of SEM contrast with the layer thickness.

6.2 INFLUENCE OF NANO-INHOMOGENEITIES

In this section the influence of an incomplete graphene growth on the local transport properties will be discussed. For this purpose the graphene growth is intentionally stopped before a full graphene layer has developed. The morphological and electronic consequences will be presented in the following.

6.2.1 CHARACTERIZATION OF AN IMPERFECT GRAPHENE MONOLAYER

On a sample with incomplete graphene growth typically two types of graphene are found which will be referred to as imperfect graphene and quasi-perfect graphene. The overview SEM image in fig. 6.3(a) shows two shaded areas corresponding to quasi-perfect graphene (blue shaded) and imperfect graphene (green shaded). The

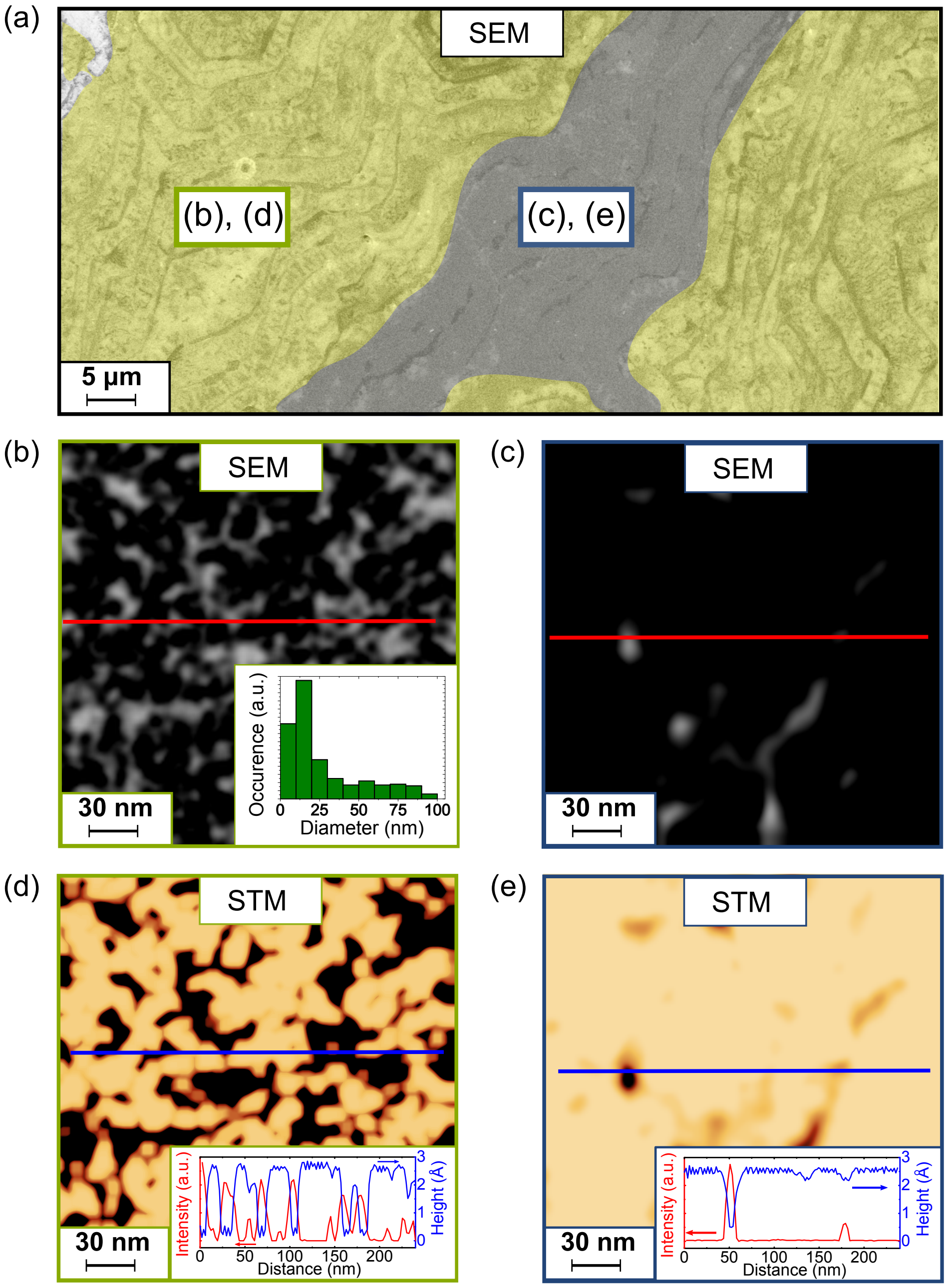

Figure 6.3: (a) Overview SEM image of epitaxial graphene showing areas with homogeneous quasi-perfect monolayer (blue shaded) and imperfect inhomogeneous (green shaded) graphene. Zoomed SEM image of the (b) inhomogeneous and (c) homogeneous areas. (d, e) STM images of the same areas shown in (b) and (c). The origin of the SEM (red) and STM (blue) linescans shown in the inset of (d) and (e) are indicated in the corresponding figures (b-e). The inset in (b) shows a histogram of the island size of low contrast seen in SEM on a total area of $3 \times 3\,\mu\mathrm{m}^2$. Set point for the STM images (d, e) was 1.1 V, 0.5 nA.

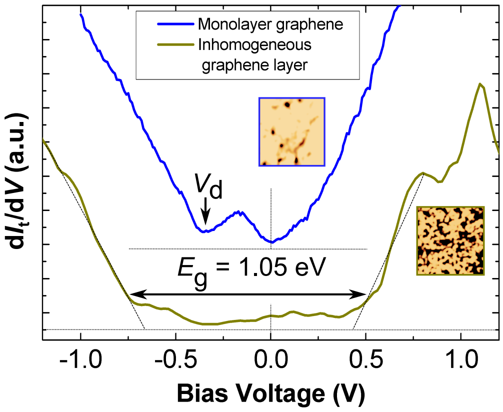

Figure 6.4: Scanning tunneling spectra taken on the homogeneous quasi-perfect graphene monolayer and inhomogeneous imperfect graphene which were identified in fig. 6.3. The Dirac point (V_d) is indicated for the graphene monolayer as well as the energy gap (E_g) for the spectrum of the inhomogeneous layer. The spectra are shifted for better visibility. The dotted lines indicate the zero level for every spectrum. The insets show the corresponding STM images from fig. 6.3.

large scale SEM image does not reveal any significant difference between the two areas.

However, a remarkable difference becomes obvious from the SEM images with higher resolution shown in fig. 6.3(b, c). Fig. 6.3(b) shows the imperfect area which exhibits two intensity levels (bright and dark) and appears very inhomogeneous. On the other hand the quasi-perfect area also shows these two contrast levels but with a much smaller amount of bright contrast. Based on the discussion in the previous section 6.1 the bright areas are identified as buffer-layer and the dark ones as ML graphene. Thus, in the imperfect area a large amount of residual buffer layer is present. Performing STM on the same sample positions (presented in fig. 6.3(d, e)) a height variation is found coinciding nicely with the contrast seen in the SEM. The height difference is deduced to 2.3 Å which correlates well with the previously reported step height between graphene and the buffer layer [126]. The average graphene island diameter in the imperfect regions is about 12 nm as shown in the histogram in the inset of fig. 6.3(b).

To evaluate the electronic properties of the imperfect and quasi-perfect area STS was performed on both sites. The resulting tunneling spectra are plotted in fig. 6.4. The quasi-perfect graphene exhibits the typical dI_t/dV signature of epitaxial ML graphene seen before in sections 6.1 and 5.2.1. The dip corresponding to the Dirac point is located at around -350 mV. In contrast, the tunneling spectrum from the imperfect area reveals a gap like feature of about 1 eV close to the value reported for the buffer layer [126, 149]. No significant difference is found in tunneling spectra taken at different positions within the imperfect area. Hence, the local presence of graphene or buffer layer cannot be confirmed with STS. It is important to note that the dI_t/dV signal does not go down to zero completely even around zero bias. Such a constant DOS within a gap like feature is known to give rise to 2d variable range hop-

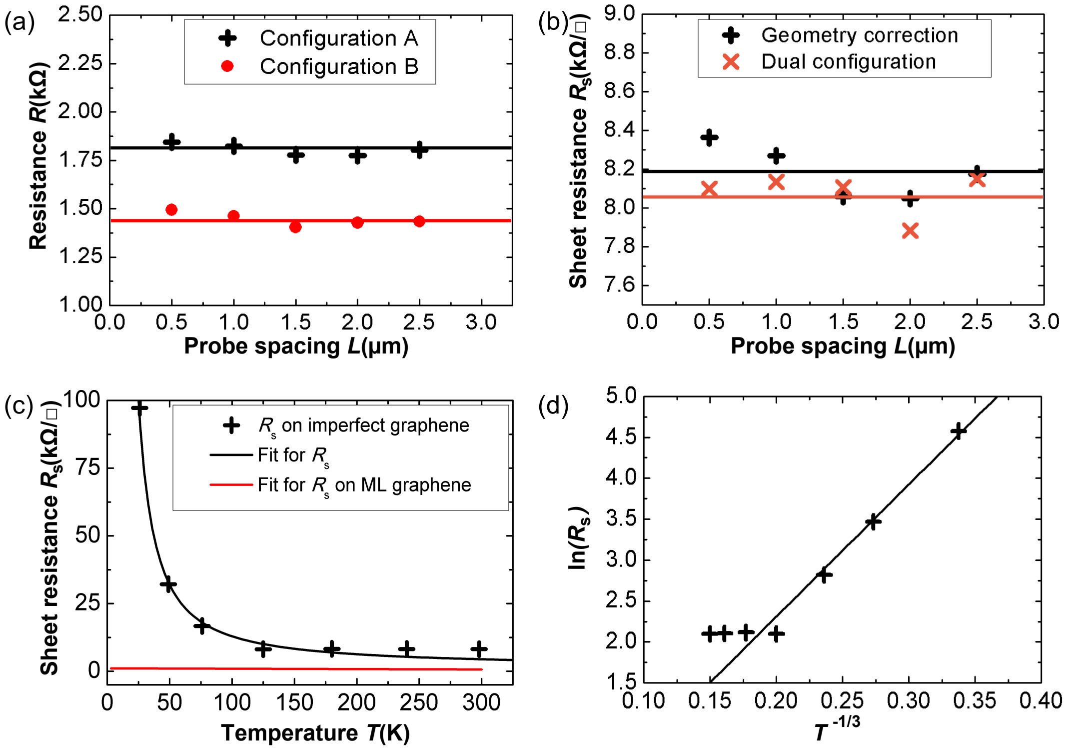

Figure 6.5: (a) Local 4pp transport measurements on an inhomogeneous epitaxial graphene sheet in dual configuration. The resistance in configuration A and B is plotted against the probe spacing. The mean values are indicated. (b) Sheet resistances from local transport measurements as function of probe spacing ($T = 300\,\mathrm{K}$). The sheet resistances were deduced from dual configuration measurements and by applying the geometrical correction factor for a thin sheet. (c, d) Temperature dependence of the sheet resistance ($L = 1\,\mu\mathrm{m}$) and corresponding fit to VRH. Details about the fit are given in the main text. The fit for a quasi-perfect ML from section 5.2.2 is displayed as red line for comparison.

ping (cf. section 2.2.2) [161]. Thus, the investigation of the corresponding transport characteristics is of great interest.

6.2.2 LOCAL MULTI-PROBE TRANSPORT ON IMPERFECT GRAPHENE

The transport characteristics of the quasi-perfect graphene are found to be fully consistent with those reported in section 5.2.2 for ML graphene. Hence they shall not be discussed here again. On the other hand the transport properties of areas incorporating imperfect graphene clearly differ. In fig. 6.5(a) the 4pp resistances measured with the multi-tip STM in configuration A and B (cf. fig. 5.5(a)) are plotted against the probe spacing. The probe spacing independence as well as the ratio $R_A/R_A = 1.25 \approx \ln(4)/\ln(3)$ indicates a 2d conductivity [60] similar to the perfect ML graphene. Compared to the perfect ML, the resistance is enhanced by a factor of roughly 10 resulting in mean values of $R_A = 1.81\,\mathrm{k}\Omega$ and $R_B = 1.44\,\mathrm{k}\Omega$.

The corresponding sheet resistances obtained by applying the geometric correction factor $R_s = R_A \pi / \ln(2)$ and by using the dual configuration by means of eq. 2.20 are shown in fig. 6.6(b). The sheet resistance from dual configuration is given by $R_s = (8.07 \pm 0.11)\,\mathrm{k\Omega/\Box}$ and geometry correction yields $R_s = (8.18 \pm 0.14)\,\mathrm{k\Omega/\Box}$. Both values agree within 1%, hence, the assumption of a semi-infinite 2d sheet remains valid for the imperfect graphene sheet.

From these data, the only difference between the transport characteristics of an imperfect and a homogeneous graphene layer turns out to be an increased sheet resistance of the imperfect layer. Especially the 2d characteristic of transport is fully preserved. This similarity does not apply to the temperature dependence of the sheet resistance. The imperfect graphene shows an exponentially increasing sheet resistance with decreasing temperature in strong contrast to the sheet resistance of a quasi-perfect ML which is weakly decreasing with temperature (cf. fig. 5.5(c)). Hence, the remote phonon scattering mechanism dominating the temperature dependence of the conductivity in a homogeneous ML is not relevant for imperfect graphene.

In fact, the temperature dependence can be described by Anderson localization (cf. section 2.2.2). The change of sheet resistance with temperature is well reproduced by fitting with eq. 2.47 with dimension $d = 2$ and a characteristic Mott temperature $T_m = 4200\,\mathrm{K}$. Assuming the localization length to be in the order of the size of the graphene islands (which was deduced to 12 nm), the density of defect states at the Fermi energy $D(E_f) = 2 \times 10^{13}\,\mathrm{cm^{-2}/eV}$ following eq. 2.48. The quality of the fit can be evaluated in more detail by plotting $\ln(R_s)$ versus $T^{-1/3}$ as shown in fig. 6.5(d). It agrees well with the experimental data up to around 200 K. The origin of the deviation for higher temperatures is not clear. Since there is only a weak temperature dependence present, phonon assisted contributions might play a role. The description in terms of Anderson localization and variable range hopping (VRH) however is similar to transport studies on graphene antidot lattices [161, 162]. This similarity is not surprising since the imperfect graphene areas show a structure comparable to an antidot lattice.

The overall influence of imperfections in the graphene sheet on the transport properties shows that a perfect graphene sheet is an essential prerequisite in order to obtain low sheet resistances and high mobilities. The Anderson localization present in imperfect graphene leads to drastically enhanced resistance values especially at low temperatures.

6.3 INFLUENCE OF STEP EDGES

As shown in section 6.1 ML graphene samples on SiC often feature bilayer stripes along the step-bunched substrate steps. The influence of such step edges on the transport characteristics of a graphene ML will be discussed in this section. The SEM image in fig. 6.6(a) illustrates the situation. A homogeneous graphene ML is intersected by bilayer stripes at the step edges which show almost parallel alignment. The identification of bilayer, ML and buffer layer is done based on the findings from section 6.1.

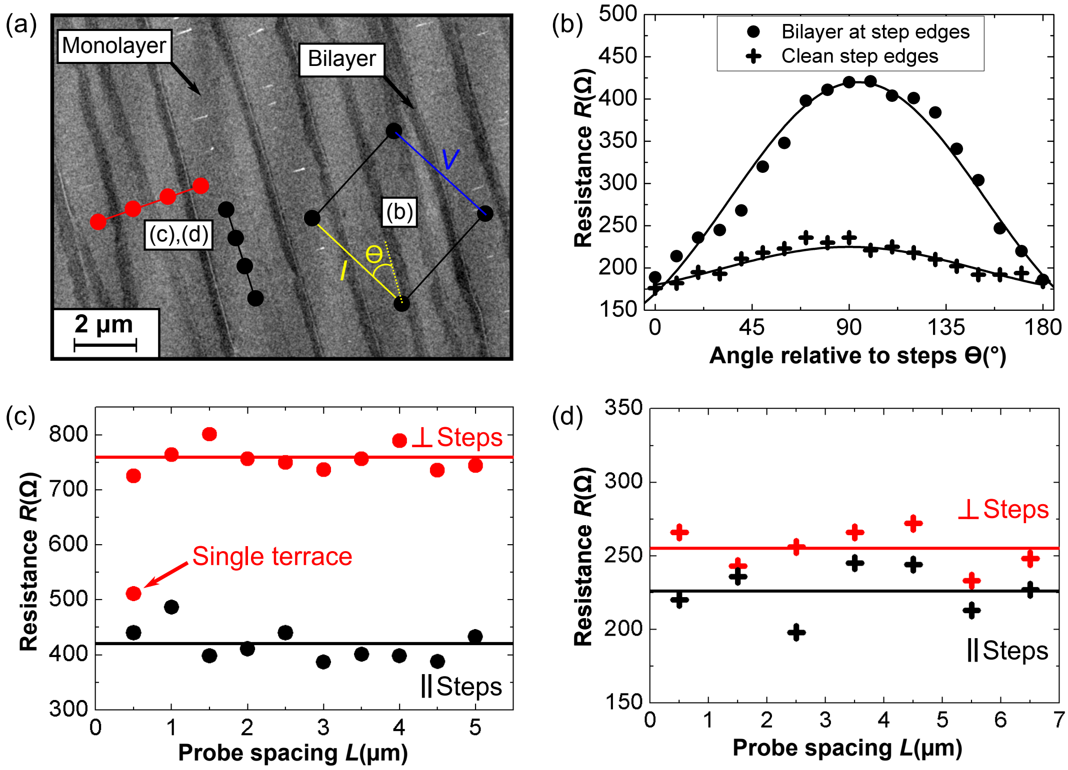

Figure 6.6: (a) SEM image of an epitaxial graphene ML with bilayer stripes at the step edges. (b-d) Local 4pp transport measurements on an epitaxial graphene monolayer (c) with and (d) without bilayer stripes at the step edges. The resistances in (b) are obtained with square tip arrangement with the current driving tips at an angle of Θ relative to the step edges. The fit is explained in the main text. The resistances in (c) and (d) are obtained in a linear tip arrangement parallel and perpendicular to the step edges (c) with and (d) without bilayer stripes. In (c) at $L = 500\,\text{nm}$, in perpendicular tip arrangement an additional measurement was made with all tips placed on a single terrace.

The conductivity is expected to be anisotropic and dependent on the arrangement of the probes parallel or perpendicular to the step edges. Thus a square arrangement is chosen because it is more sensitive to intrinsic anisotropies in a 2d sheet [62]. The arrangement is schematically shown in fig. 6.6(a). For the measurements shown in fig. 6.6(b) the probe spacing is kept fixed at about 10 µm and the whole square arrangement is rotated by an angle Θ relative to the step edges. The measured resistance is increasing from 189 Ω at parallel alignment ($\Theta = 0°$) to 420 Ω at perpendicular alignment ($\Theta = 90°$). This clearly indicates an anisotropic conductivity. The angular dependence can be rationalized by a simple phenomenological model assuming straight and evenly distributed steps [163]. The resistance can be expressed as

$$R \sim R_0 + \frac{R_{\text{step}} \sin(180° - 2\Theta)}{(1 - \frac{\Theta}{90°})\pi} \qquad (6.1)$$

where R_0 is the angle independent resistance of the sheet at $\Theta = 0°$ and R_{step} is the additional resistance caused by the steps. The resistance of the steps can be deduced from the fit to $R_{step} = 240\,\Omega$. Performing the same experiment on a graphene sheet with no bilayer stripes at the step edges (cf. section 5.2.2) results in a much smaller resistance anisotropy which is also shown in fig. 6.6(b). The resistance at $\Theta = 0°$ ($R_0 = 176\,\Omega$) is almost the same as for the case with bilayer stripes. Increasing the angle leads to a resistance increase up to $236\,\Omega$ for perpendicular alignment which is almost a factor of 2 lower than in the presence of bilayer stripes. The fit according to eq. 6.1 yields an additional resistance induced by the steps $R_{step} = 45\,\Omega$ roughly a factor of 5 lower than the step resistance when the edges are covered with bilayer stripes.

It is important to note that the evolution of bilayer stripes is directly related to the presence of step bunched substrate steps of $5-7\,\text{nm}$ height. In contrast, the sample with no bilayer stripes exhibited substrate steps with half-unit cell height ($0.75\,\text{nm}$) even after graphene growth. Hence it is not possible to conclude whether the bilayer stripes or the larger step height is responsible for the enhanced step resistance. To make sure that the observed anisotropy is really stemming from the step edges also 4pp measurements in linear probe arrangement were performed. In a homogeneous material the measured resistivity in a linear configuration is not dependent on the probe alignment relative to the sample [62]. However, in an inhomogeneous material where the anisotropy arises from extrinsic influences such as step edges, a linear probe arrangement is sensitive to the arrangement of probes relative to the direction of anisotropy [63]. Thus, probing an anisotropic surface with a linear 4pp probe arrangement reveals the nature of anisotropy.

The probe spacing dependent resistances in a linear probe arrangement parallel and perpendicular to the step edges are plotted in fig. 6.6(c) and fig. 6.6(d) for a sample with and without bilayer stripes along the step edges. The graphene ML intersected by the bilayer stripes shows an increase of the resistance when switching from parallel to perpendicular alignment. In parallel direction the mean resistance $R_{||} = 420\,\Omega$ while perpendicular $R_{\perp} = 759\,\Omega$. The higher resistances compared to the square arrangement do not imply an increased sheet resistance but are rather caused by the different measurement geometry. The resistance from the step edges is simply given by the difference between the parallel and perpendicular alignment which amounts to $339\,\Omega$. This is in reasonable agreement with the value obtained by the rotational square method. The resistances show no probe spacing dependence as expected for a 2d system. In perpendicular direction, an additional measurement was made with $L = 500\,\text{nm}$ and all tips placed on the same terrace. The resistance drops sharply down to the parallel value. This is easy to understand since no influence of the step edge can be seen if not a single step edge is located between the probes. It is however remarkable that no further step like increase of the resistance is observed when crossing additional steps at larger L. The resistance seems to depend only on the relative amount of bilayer region within the graphene ML not on the total number of steps.

In comparison, the sample with a homogeneous ML graphene without bilayer stripes at the step edges shown in fig. 6.6(b) exhibits a resistance increase of only

29 Ω when switching from parallel ($R_{||} = 226\,\Omega$) to perpendicular ($R_{||} = 255\,\Omega$) alignment. Again, the values are fully consistent with those obtained in the rotational square arrangement. No resistance drop is observed in perpendicular alignment for small probe spacings. The reason for the absence of such a drop is the smaller terrace width $\Gamma < 2\,\mu m$ present on this sample. Thus it was not possible to place all tips on the same terrace in a linear arrangement.

In both cases, with and without bilayer stripes at the step edges, the dependence of the resistance in linear 4pp arrangement on the direction relative to the step edges shows that the conductance anisotropy is caused by the step edges and is not an intrinsic property of the sheet. The origin of the enhanced resistance of substrate step edges has been discussed intensively. In [163] similar 4pp measurements in linear and square configuration are presented. The only difference is the much larger probe spacing of about 100 µm. The resistance increase in perpendicular alignment was found to be around 180 Ω, in good agreement with the results found here. The enhanced resistance was attributed to trapped silicon atoms aggregating around step edges which serve as the dominant scattering source. Furthermore, an enhanced resistance due to curvature of the graphene film was excluded because the 1% change in lattice constant from compressive strain across step edges [164] is not enough to induce a significant transport gap which would account for the observed anisotropy [165]. These conclusions are supported further by the theoretical work in [166] where structural deformations are found to give only a small contribution to electron scattering and the increased resistance over step edges is explained in terms of the abrupt potential and doping variation due to detachment of the graphene from the underlying substrate across a step. The resistivity of a step in the graphene sheet is shown to linearly increase with the step height for small steps up to 1.5 nm in height by scanning tunneling potentiometry [51] and for even higher steps up to 11 nm by macroscopic transport measurements [167]. A linear increase of the resistance of a substrate step with increasing step height was also found by means of local current measurments with a conductive AFM [168]. The resistance ratio between the step resistance and planar graphene for a step height of 1.5 nm was found to be 1.5 and almost the same value was obtained for a step caused by a transition from monolayer to bilayer graphene.

The enhanced resistance of graphene crossing over an underlying substrate step is well reported both experimentally and theoretically. In the case of the step edges covered with bilayer fraction, which were investigated in this section, it is not possible to determine if the bilayer contribution or the substrate step itself causes the resistance enhancement. There is definitely a contribution from the step height itself because even for step edges without bilayer coverage an additional resistance perpendicular to the steps was measured. However, whether the increase of this additional resistance with increased step height is mainly caused by the step itself following the linear dependency reported before [51, 166–168] or by the bilayer monolayer junction [51, 168] cannot be decided from the measurements presented here. A recent experimental study identified bilayer domains as the main source for scattering and highlighted that substrate steps as high as 2 nm do not have a significant effect on the resistivity of the graphene layer [169]. In order to disentangle the influence of bilayer stripes and substrate steps it is necessary to grow a graphene ML over bunched substrate steps without bilayer contributions. This is a challenging task that could not be accomplished during this thesis.

6.4 CONCLUSIONS

The influence of defects on the transport properties of epitaxial ML graphene have been considered in this chapter. Two different types of defects were discriminated, inhomogeneities on the nm scale within the graphene ML caused by an incomplete graphene growth and step bunching induced step edges covered with bilayer fractions. The presence of nano-inhomogeneities directly manifests in a sheet resistance increase by about a factor of 10 at room temperature compared to a perfect ML sheet. This resistance increase is even more pronounced at low temperatures because the inhomogeneous graphene ML shows a localization behavior which was well described in terms of VRH. The sheet resistance at low temperatures was increased by more than a factor of 100 compared to the quasi-perfect graphene ML where no Anderson localization was observed.

In comparison, the effect of bilayer covered step edges is not that dramatic. Roughly a factor of 2 was found for the resistance increase measured in transport geometries perpendicular to the step edges. The resistance increase over bilayer covered step edges could be caused by the step edge itself or the bilayer monolayer junctions. Nevertheless, the presented linear and square 4pp measurements proved that the source for the anisotropy is located at the step edges.

In order to gain insight into the intrinsic transport characteristics of graphene the formation of these defects needs to be avoided. This implies that the growth of high-quality graphene and graphene nanostructures on SiC demands careful control of the graphene formation as well as the substrate morphology. A closed graphene layer without incorporation of nano-inhomogeneities is essential but also the substrate step formation on the substrate needs to be taken into account for the interpretation of transport data.

Part III

SELF-ASSEMBLED EPITAXIAL SIDEWALL GRAPHENE NANORIBBONS

7

GROWTH AND CHARACTERIZATION OF SIDEWALL NANORIBBONS

Graphene nanoribbons are an essential building block in future graphene based electronic devices. Two main properties are of special interest for this purpose, the width dependent bandgap in armchair type ribbons [170, 171] (cf. section 3.2.1) and the possibility of topologically protected edges states in zig-zag GNR [112] (cf. section 3.2.3). However, in order to observe these peculiar transport phenomena, the edges of the GNRs need to be well-ordered on the atomic scale. Defects in the edges will immanently prohibit the observation of the special transport properties of GNRs. Lithographically patterned GNRs are known to suffer severely from the patterning process, showing rough and disordered edges [31–34]. In order to protect the edges during the patterning process sophisticated techniques such as the encapsulation of graphene into boron nitride have been used successfully [172]. However, they are not suitable for the implementation in an industrial manufacturing process. A very promising technique for this purpose, makes use of the self-assembling growth of graphene nanostructures on pre-patterned SiC substrates [44]. In this chapter this growth process shall be adapted and used for the growth of well-ordered graphene nanoribbons. The results of this chapter are published in [173–175].

7.1 GROWTH OF SIDEWALL GRAPHENE NANORIBBONS

In order to grow graphene nanostructures by self-assembly a mechanism needs to be found which catalyzes the graphene growth at predefined sample positions. For epitaxial graphene it is well-known that the growth processes faster on inclined nanofacets such as $(11\bar{2}n)$ [176] or $(1\bar{1}0n)$ facets [177]. This is intuitively clear since silicon atoms on such nanofacets have a weaker bonding compared to the plane surface. Thus, the controlled synthesis of SiC nanofacets is the key for the subsequent self-assembled growth of GNRs. The formation of such nanofacets is reported on step bunched SiC surfaces [178–180] and can be related to the minimization of surface free energy. For the growth of perfect 2d graphene sheets this preferential growth on nanofacets at bunched substrates steps is unwanted because, as shown in section 6.3, additional graphene layers at step edges give rise to enhanced electron scattering. However, if carefully controlled, this mechanism opens up a pathway to grow graphene nanoribbons directly without destructive post-processing.

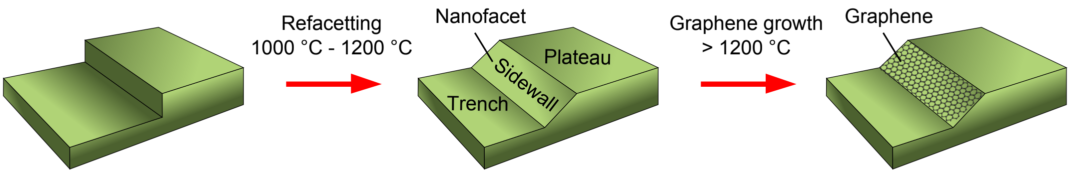

Figure 7.1: Illustration of the synthesis process of epitaxial sidewall graphene nanoribbons. First, a nanometer scale step is etched into the SiC by RIE. Heating of the SiC induces step flow, resulting in an inclined nanofacet. In the last step graphene is grown preferentially on the facet.

It has been shown that the formation of SiC nanofacets can be induced by lithographic patterning of the SiC substrate and subsequent annealing [44]. The growth principle is schematically shown in fig. 7.1. First, an edge with several nm in height is patterned into the substrate by RIE using a mixture of 20/7 SF_6/O_2 resulting in a slow etching rate of 3 Å/s. This provides careful control over the etching depth which will later on determine the width of the GNR. Subsequent annealing transforms this sidewall into an inclined nanofacet via step-flow. Elevating the annealing temperature will induce graphene growth on the sidewall facets (cf. fig. 7.2(a)). With this technique a variety of graphene nanostructures with different geometries can be realized [181]. This thesis concentrates solely on GNRs. For this purpose mesa structures are used in the initial substrate patterning step in order to achieve an array of GNRs after the graphene growth is completed.

The annealing of the sample for refacetting and graphene growth was carried out resistively either in a face-to-face heater which was presented in section 5.1 or by simple UHV annealing with the heater shown in fig. 7.2(b). Typical annealing temperatures and times in the face-to-face heater were 1300 °C for 30 min during the refacetting and 1500 °C for 10 min for graphene growth. The temperatures were measured with a two-color infrared pyrometer. The UHV annealing uses lower temperatures and shorter annealing times. Typical parameters were 1000 °C for 10 min for the refacetting and 1115 °C for 1 min to induce graphene growth. Temperatures in UHV annealing were measured with a single-color pyrometer with an emissivity value of

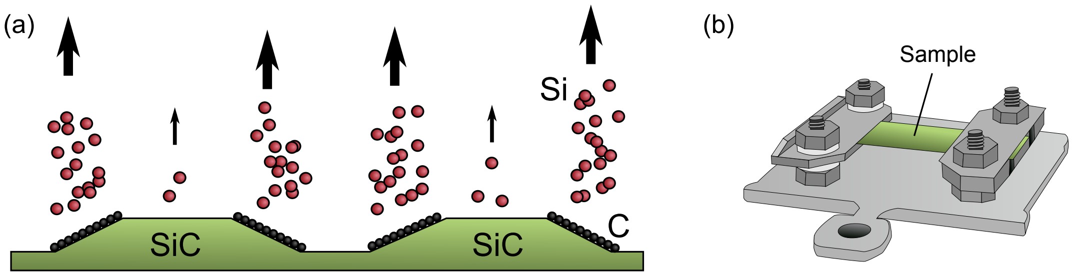

Figure 7.2: (a) Illustration of the preferential desorption of silicon atoms from SiC facets. The formation of the first graphene layer is indicated. (b) Schematic of the resistive heater used for graphene growth in UHV.

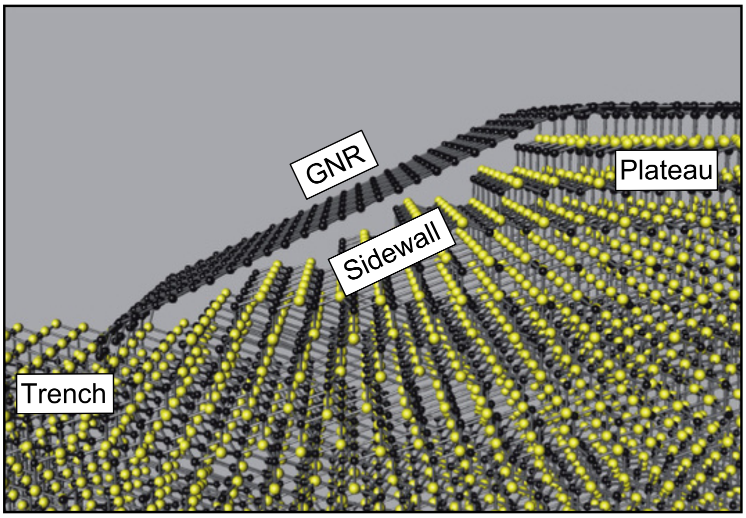

Figure 7.3: Schematic of a sidewall graphene nanoribbon [174]. Carbon atoms are shown in black, silicon atoms in yellow. The lower ribbon edge at the trench is covalently bonded to the SiC. The upper edge at the plateau merges into the buffer layer on the plateau. The graphene covering the sidewall is not bonded to the SiC.

$\epsilon = 0.96$. The current was always driven through the sample parallel to the orientation of the mesa structures. On-axis SiC(0001) substrates were used for all experiments.

7.2 MORPHOLOGICAL AND ELECTRONIC PROPERTIES

After completion of the GNR growth all samples were extensively characterized. Typical findings concerning the electronic and morphological properties of sidewall GNRs will be presented in the following. All GNRs characterized in this section are grown on 20 nm deep mesa structures yielding approximately 40 nm wide ribbons. The width of the mesa structures was varied between 1 µm and 8 µm. The lateral size of the mesa structure has no influence on any of the sidewall ribbon properties presented below.

A general model for the morphology of a sidewall GNR is shown in fig. 7.3. The lower edge of the ribbon bonds to the substrate in the mesa trench while the upper edge connects seamlessly to the buffer layer on the mesa plateau. This causes heavy bending of the graphene layer close to the trench edge. The model follows directly from TEM investigations of the epitaxial growth process [182, 183]. Most importantly the carbon layer covering the sidewall facet is not bonded to the substrate as normally expected for the first carbon layer on SiC(0001). This picture is strongly motivated by TEM and electron energy loss spectroscopy studies which show that the buffer layer delaminates on SiC facets forming quasi-freestanding graphene [184, 185].

The experimental results presented in the following will show that this model is highly justified. The most important questions concerning the ribbon growth are the number of layers on the sidewalls, the edge orientation and the doping level. All these questions will be addressed.

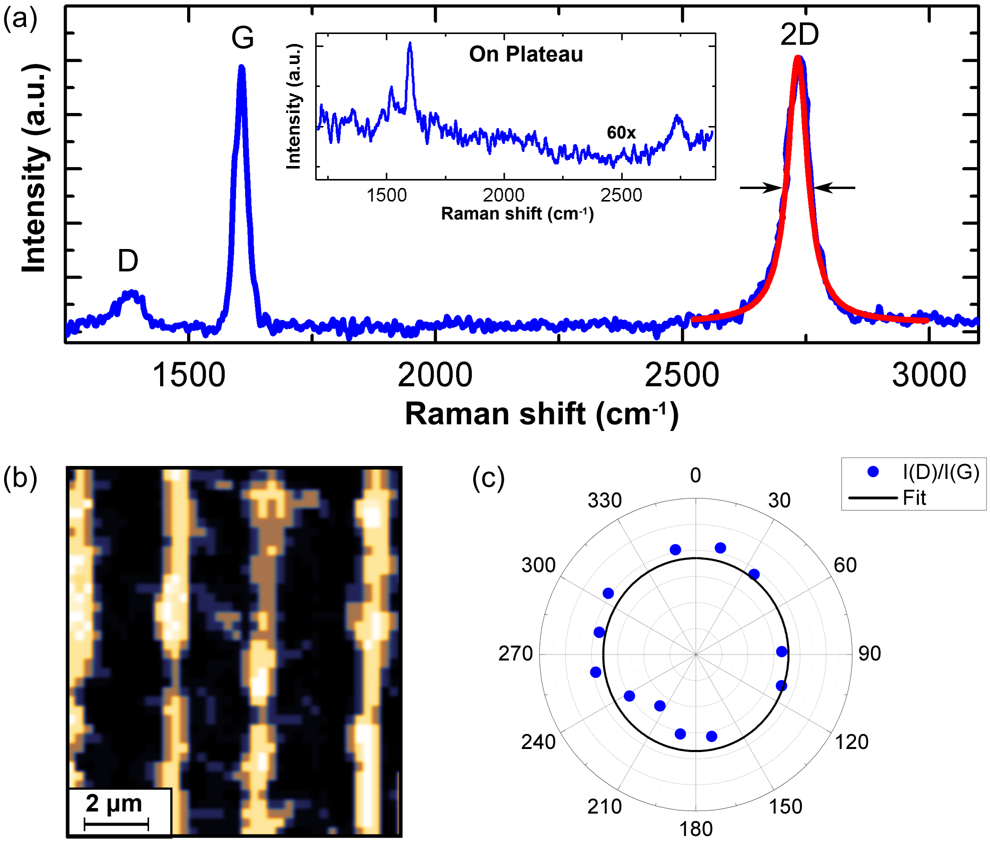

Figure 7.4: (a) Raman spectrum of a sidewall GNR. The fit of the 2D peak with a single Lorentzian (FWHM 40 cm^{-1}) is indicated in red. The inset shows a Raman spectrum from the plateau. The Raman intensity was multiplied by 60 compared to the sidewall spectrum to make the peaks visible. The low intensity of the peaks indicates contributions from small graphene patches. (b) Mapping of the 2D peak intensity. High intensity is observed at the location of the sidewalls indicating preferential graphene growth. (c) Polarization angle dependence of I(D)/I(G) fitted according to eq. 7.1.

7.2.1 RAMAN SPECTROSCOPY ON SIDEWALL GRAPHENE NANORIBBONS

Raman spectroscopy is the method of choice for the determination of the number of graphene layers as explained in section A.5.2. A typical Raman spectrum of a sidewall GNR can be found in fig. 7.4(a). It exhibits the characteristic D (1382 cm^{-1}), G (1606 cm^{-1}) and 2D (2735 cm^{-1}) peaks. The positions of the peaks are in line with previous Raman studies of epitaxial ML graphene reported in literature [115] and in this thesis (cf. section 5.2.1). The intensity of the D peak is rather low indicating a low defect density. The mean distance between defects can be estimated from the ratio I(D)/I(G) = 0.14 to more than 40 nm [186]. In order to determine the number of graphene layers the most convenient way is to fit the 2D peak with Lorentzian peaks. The 2D peak in the spectrum in fig. 7.4(a) can be fitted with a single Lorentzian with a FWHM of $40\,\mathrm{cm}^{-1}$ which clearly indicates ML graphene [40]. With a Raman spectrometer it is furthermore possible to record spatial mappings of the peak intensities on the sample surface. Such a mapping of the 2D peak intensity is shown in fig. 7.4(b). It clearly reveals that graphene has been grown almost exclusively on the mesa sidewalls. The 3 µm wide plateaus and trenches exhibit only small graphene patches which do not interconnect the sidewall ribbons. An example Raman spectrum from the plateau is shown in the inset of fig. 7.4(a). It reveals very small G and 2D peaks. In order to make these peaks visible, the intensity had to be multiplied by a factor of 60 compared to the spectrum from the sidewall. This indicates that only very small graphene patches contribute to the spectrum which is consistent with the 2D mapping.

Further insight into the influence of the ribbon edge to the Raman spectrum can be gained by performing polarization dependent Raman measurements. Since only the phonon wave vectors perpendicular to the incident light polarization contribute to the Raman signal in graphene [187–189] phonon wave vectors along the nanoribbon axis should not be influenced by the ribbon edge. A polar plot of I(D)/I(G) versus the polarization angle Θ is shown in fig. 7.4(c). For polarization angles of 90° and 270° the phonon wave vector is aligned parallel to the ribbon axis. The data shows almost no polarization dependence of the I(D)/I(G) ratio. For quantification the angular dependence can be fitted with the following expression [187, 190]

$$\frac{I(D)}{I(G)}(\Theta) \sim (c + (1-c)\cos^2(\Theta)) \tag{7.1}$$

with $c = I(D)_{\mathrm{min}}/I(D)_{\mathrm{max}}$. The fit yields $c = 0.96$ which is close to $c = 1$ indicating complete independence from the polarization angle. Hence it can be concluded that the sidewall GNR edges do not significantly contribute to the Raman D peak. This implies that the edges are of zigzag type because in contrast to armchair edges a zigzag edge is not Raman active [190, 191] as discussed also in the appendix A.5.2. The D peak intensity hence reflects the defect density of the ribbon itself and is not influenced by additional scattering events at the edges. The edge orientation will be investigated in detail by STM in section 7.2.3.

7.2.2 LEED ON SIDEWALL GRAPHENE NANORIBBONS

LEED is an extremely powerful method in order to analyze the crystallographic structure of the sample surface. As presented in section 5.2.1 it can reveal the complex $(6\sqrt{3} \times 6\sqrt{3})$R30° reconstruction of the interfacial buffer layer. A typical LEED image of a sample after completed sidewall graphene growth is shown in fig. 7.5. It exhibits the $(6\sqrt{3} \times 6\sqrt{3})$R30° reconstruction characteristic for the buffer layer in coexistence with a $(\sqrt{3} \times \sqrt{3})$R30°. The $(1/3, 1/3)$ spots belonging to the $(\sqrt{3} \times \sqrt{3})$R30° reconstruction are indicated in orange. At the $(\sqrt{3} \times \sqrt{3})$R30°, which develops before the $(6\sqrt{3}\mathrm{x}6\sqrt{3})$R30°, the surface is still covered with Si adatoms [192]. The coexistence of $(6\sqrt{3} \times 6\sqrt{3})$R30° and $(\sqrt{3} \times \sqrt{3})$R30° indicates that the majority of the sample is covered by a not fully developed buffer layer [95]. It is directly clear that the LEED

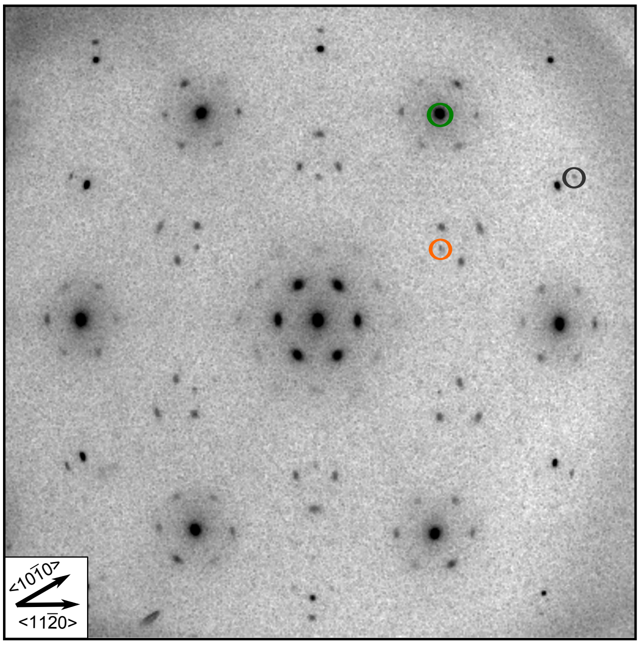

Figure 7.5: LEED pattern ($E = 137\,\mathrm{eV}$) of a sample with sidewall GNRs showing the coexistence of the $(6\sqrt{3} \times 6\sqrt{3})$R30° and the $(\sqrt{3} \times \sqrt{3})$R30° structures. Indicated are the SiC(10) (green), the graphene(10) (grey) and the $(1/3, 1/3)$ spot (orange). The $(1/3, 1/3)$ belongs to the $(\sqrt{3} \times \sqrt{3})$R30° reconstruction and indicates that the buffer layer is not completely developed.

image is entirely determined by the crystallographic structure of the plateaus and trenches of the mesa. The lateral width of the mesa of at least $1\,\mu\mathrm{m}$, which was used throughout this thesis, makes the sidewall ribbon density too small to detect a signal from them in the LEED. Hence no conclusions can be drawn from a LEED analysis concerning the GNRs but it is useful to ensure that plateau and trench are still in a very early stage of the graphitization process and not overgrown with graphene.

7.2.3 STM AND STS ON SIDEWALL GRAPHENE NANORIBBONS

Regarding the microscopic orientation and the LDOS of the sidewall ribbons STM and STS are the methods of choice. In a naive guess the orientation of the ribbon should be determined by the orientation of the substrate such as for epitaxial graphene on the SiC(0001) plane. Consequently mesa structures oriented parallel to $\langle\bar{1}100\rangle$ should result in the growth of zigzag GNRs and mesas along $\langle 11\bar{2}0\rangle$ should give armchair GNRs [193]. Surprisingly, this is not the case. Fig. 7.6(a) shows a STM image obtained on the center of the sidewall of a mesa oriented parallel to $\langle 11\bar{2}0\rangle$. Atomic resolution is clearly achieved, showing nicely the typical honeycomb pattern of graphene. In contrast to the previous guess the ribbon does not show an armchair-like orientation but a zigzag one. A zigzag orientation was also found for sidewall ribbons on mesa sidewalls aligned parallel to the $\langle\bar{1}100\rangle$ direction of the substrate as obvious from the atomically resolved STM image in fig. 7.6(b). However, in this case the zigzag orien-

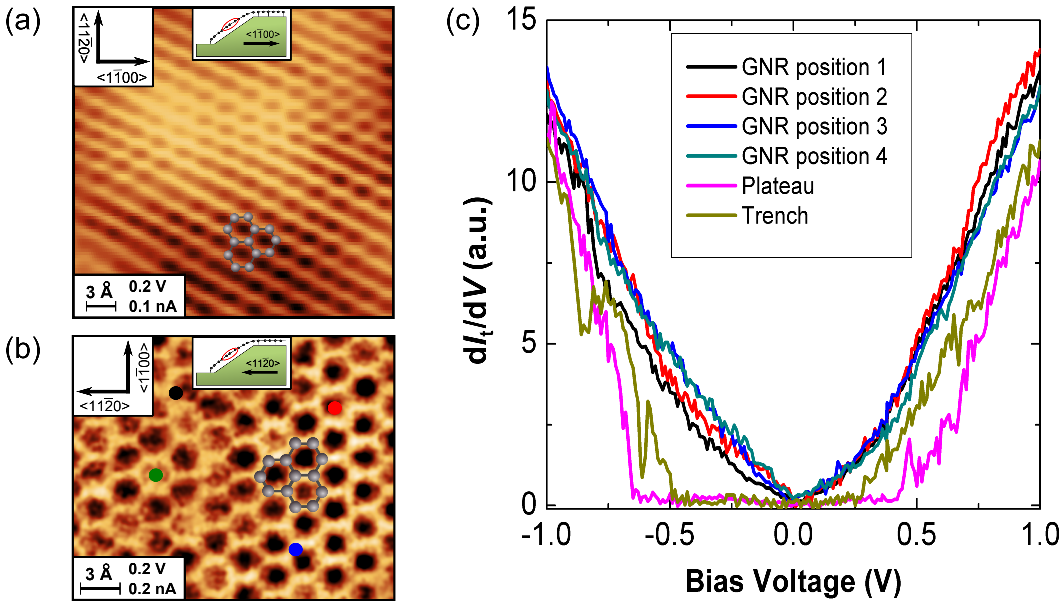

Figure 7.6: (a, b) Atomically resolved STM images taken in the center of sidewall graphene nanoribbons. The ribbon in (a) is grown on a mesa sidewall oriented parallel to the $\langle 11\bar{2}0\rangle$ direction whereas the sidewall in (b) is oriented along $\langle \bar{1}100\rangle$. Both GNRs exhibit a zigzag like orientation. The insets depict the orientation of the ribbon. STM images were taken in the central area marked in red. (c) STS of a sidewall GNR and of the surrounding buffer layer. The positions on which the spectra on the GNR were acquired are marked in (b).

tation was expected. Unfortunately, atomic resolution of the edges was not possible due to the transition from graphene to buffer layer or substrate at the edge, which results in indefinite tunneling conditions. Furthermore, according to the model presented in fig. 7.3 the lower edge to the trench is heavily bended which makes it almost impossible to image this edge directly.

Nevertheless, the observed preference of the sidewall graphene to grow in zigzag orientation is striking. It might be caused by the high growth rates during UHV annealing. In contrast, sidewall ribbons produced via the CCS method in a rf-furnace have been shown to exhibit both armchair and zigzag edges, dependent on substrate orientation as revealed by a detailed LEED study [193]. The zigzag configuration was even identified as less stable compared to the armchair one, which is in complete contrast to the observations made here. Furthermore, a TEM and STM study of sidewall GNRs grown in a CCS furnace showed the existence of so called mini-ribbons of $1-2\,$nm in width, bordering the main facet in armchair direction [185]. The existence of mini-ribbons explains the observation of the $0.5\,$eV bandgap in sidewall GNRs in a recent ARPES study [194]. During the measurements in this thesis no hint for the presence of mini-ribbons was found. This discrepancies between the sidewall GNRs grown via different annealing procedures is remarkable. In general, the preferential zigzag growth found in UHV can be rationalized by looking at the atomic arrangement of the edges on the SiC surface. Since the carbon atoms in the lower edge of the

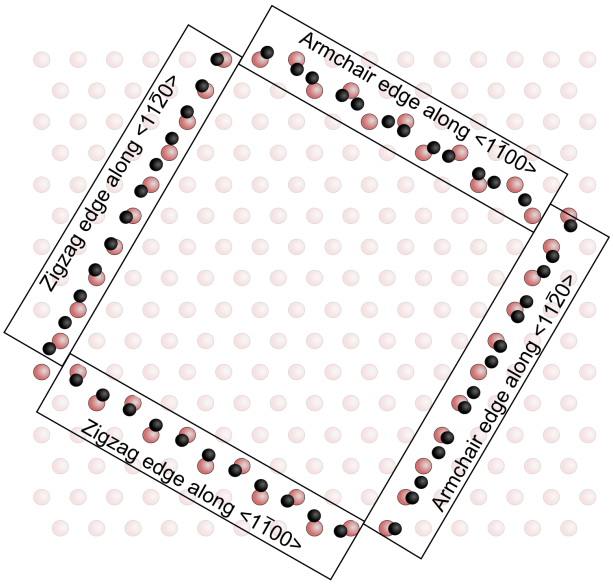

Figure 7.7: Schematic of the possible arrangements of graphene armchair and zigzag edges on the SiC(0001) surface along $\langle\bar{1}100\rangle$ and $\langle 11\bar{2}0\rangle$. The carbon atoms in the graphene edges are shown in black, the Si atoms in the top SiC layer in light red.

ribbon bond to Si atoms in the top SiC layer (cf. model in fig. 7.3), those edges should be favored which allow for such bonding without atomic displacements. In fig. 7.7 a schematic of zigzag and armchair edges are shown in $\langle\bar{1}100\rangle$ and $\langle 11\bar{2}0\rangle$ orientation on the top SiC layer. The zigzag edge parallel to $\langle\bar{1}100\rangle$ (which is the natural zigzag direction for graphene on hexagonal SiC) fits best to the arrangement of Si atoms. Furthermore, even along $\langle 11\bar{2}0\rangle$ (which is the nominal armchair direction), a zigzag edge fits better to the Si atom arrangement than an armchair edge. If the ribbon growth starts at the lower edge it is hence highly reasonable that the development of zigzag edges is more favored. The high growth rates during UHV annealing might be also supportive of the preferential development of zigzag edges. Furthermore, since a current is driven directly through the sample during the annealing, a temperature gradient of about $50 - 100\,^\circ\mathrm{C}$ over the length of the sample is unavoidable. Such large gradients are not present in the case of the CCS method. The influence of both, temperature gradients as well as fast growth rates needs to be investigated more closely to gain a better understanding of the growth process of sidewall GNRs. However, such an analysis is beyond the scope of this thesis.

In order to get insight into the electronic properties, STS was carried out on the sidewall GNRs. All tunneling spectroscopy experiments on the sidewall GNRs were recorded using standard lock-in techniques. The resulting dI_t/dV spectra are shown in fig. 7.6(c). They exhibit the typical V-shape with a minimum at zero bias as expected for undoped graphene. In contrast, spectra acquired on the mesa plateau (trench) show a clear gap feature of about 1.3 eV (0.8 eV). This indicates the presence of a buffer layer. The graphene growth was successfully restricted to the mesa sidewalls. Consequently the ribbons are well isolated from each other. The peaks in the buffer layer spectra at around ±500 mV might be caused by localized states in the buffer layer [195].

The most important finding from the tunneling spectroscopy on the sidewall ribbon is the doping level. The minimum of the dI_t/dV and hence the minimum of the LDOS is precisely located at zero bias. No further minimum indicating a Dirac point shifted from the Fermi level [120–123] is present in the spectra. This clearly indicates that the sidewall GNRs are charge neutral. The resemblance of all tunneling spectra acquired on the ribbon clearly shows that the varying background visible in the STM image in fig. 7.6(b) does not affect the LDOS. The charge neutrality is in contrast to the strong n-type doping found in epitaxial ML graphene on SiC(0001) (cf. section 5.2.1). The reason for this charge neutrality is most likely the absence of a buffer layer underneath the sidewall graphene. As stated previously, graphene growing over SiC nanofacets delaminates from the surface forming quasi-freestanding graphene [184, 185]. Consequently, the local resistance of the epitaxial graphene on the facets is enhanced due to the reduced carrier concentration [196]. On the other hand, it is not even clear, if a buffer-layer can form at all on the facet because the sidewall surface is a $(1\bar{1}0n)$ or $(11\bar{2}n)$ facet rather than a plane polar SiC(0001). For example, epitaxial graphene grown on the non-polar $(11\bar{2}0)$ and $(1\bar{1}00)$ surfaces [102] of a SiC crystal does not develop a buffer layer because the formation of tetrahedral bonds between the graphene layer and the non-polar surfaces is hindered [103]. In [184] the bonding behavior of epitaxial graphene on $(11\bar{2}n)$ facets on 4H-SiC surfaces was evaluated. Facet angles larger than 27° were found to prohibit the formation of a buffer layer. Furthermore, local strain in the graphene layer was suggested to decrease this critical angle [184]. Since the sidewalls of refacetted SiC mesas show comparable inclination angles, the charge neutrality found for graphene grown on these sidewalls is not surprising but fully supports the model of a quasi-freestanding ribbon depicted in fig. 7.3.

Despite the proof of charge neutrality, the tunneling spectra of the sidewall GNR presented in fig. 7.6(c) do not show any ribbon specific features. Furthermore, recording of tunneling spectra at the edges was not possible due to the more complex tunneling conditions. It should be noted that the recording of tunnel spectra happened with the same tip with which atomic resolution was achieved. Hence the tip was relatively sharp. It is known that blunt tips might be more suitable for tunneling spectroscopy because sharp features in the DOS of the tip are diminished [197–200]. Following this argumentation the sidewall GNRs were probed again with a blunt tip which was not able to achieve atomic resolution. Despite the failure to obtain atomic resolution a tip was chosen that produced reproducible tunneling spectra. The bias voltage in this case was applied by a second tungsten tip contacting the sidewall ribbon ohmically in the vicinity of the STM tip. This biasing procedure was not possible for the measurements shown in fig. 7.6 because the biasing tip induces to much vibration to obtain atomic resolution. The result of measurements with a blunt tip and close-by biasing are presented in fig. 7.8. The STM image shows the whole facet which is covered with graphene. The STM tip is moved over the facet and tunneling spectra are recorded at the positions marked in the STM image. The most prominent characteristic of the spectrum taken in the center of the ribbon is a gap-like feature

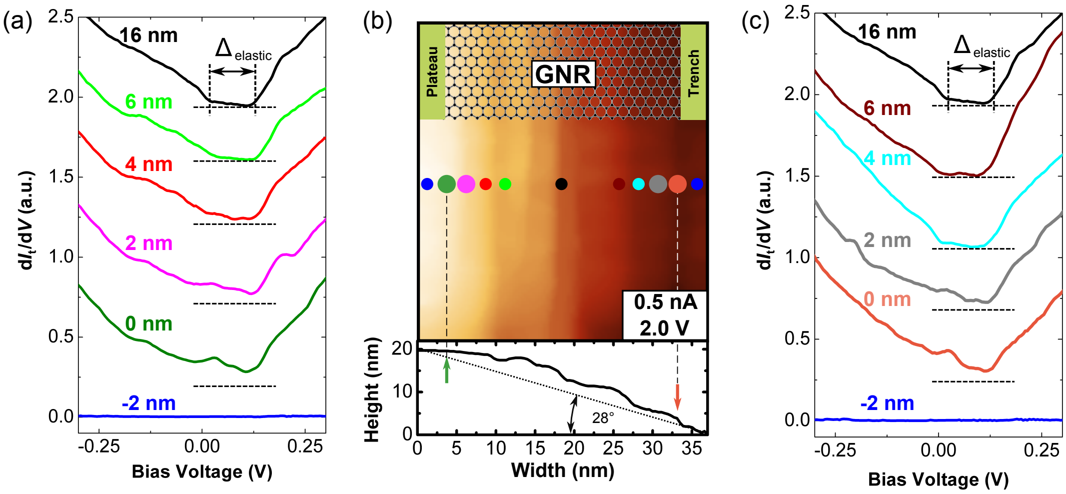

Figure 7.8: STS across a sidewall GNR. The dI_t/dV spectra are shown in (a) and (b), the corresponding positions on which the spectra were acquired are marked in the STM image shown in (c). The spectra are shifted for better visibility, the dashed line indicates zero for the individual spectra.

.

of about 120 – 130 mV. Additional features appear when moving the STM tip away from the center towards the plateau and trench edge. At the energetic location of the gap two peaks show up which are most clearly visible directly at the edges. Moving the tip over the edge onto the plateau or trench changes the spectrum drastically. Only the insulating nature of the buffer layer or residual substrate on the trench and plateau can be detected. Hence even if atomic resolution is not possible with this tip the edge of the sidewall GNR can be localized within 1 nm due to the distinct change in the tunneling spectrum.

In the following a closer look shall be taken at the spectra recorded in the center and at the edges of the ribbon. A close-up of these spectra is shown in fig. 7.9(a). The gap-like feature in the central spectrum is clearly visible. With a width of about 120 – 130 meV it is much larger than the energy gap expected for a zigzag GNR of this width which is in the order of 25 meV [105]. Hence a different mechanism has to account for this gap feature. The d^2I_t/dV^2 spectrum in fig. 7.9(b) reveals two antisymmetric peaks at zero bias and 140 mV hence at the edges of the gap in the dI_t/V spectrum. Interestingly the features in the d^2I_t/dV^2 and the corresponding gap in the dI_t/dV are not symmetric around zero bias but offset by about 70 mV. The same offset is found for the peak structure observed at the ribbon edges which is also symmetric around $V = 70$ mV. This offset seems to be intrinsic of all spectra. The origin of this shift is not clear. It is most likely not due to p-type doping because the sidewall GNR were previously identified as charge neutral. Secondly the antisymmetry of the peaks in the d^2I_t/dV^2 spectrum indicates phonon mediated inelastic tunneling [122]. However, such inelastic features should not depend on the carrier density. Hence, the origin of the 70 mV offset cannot be resolved here. However, the resemblance of the gap structure in the dI_t/dV and the corresponding peaks in the d^2I_t/dV^2 spectrum

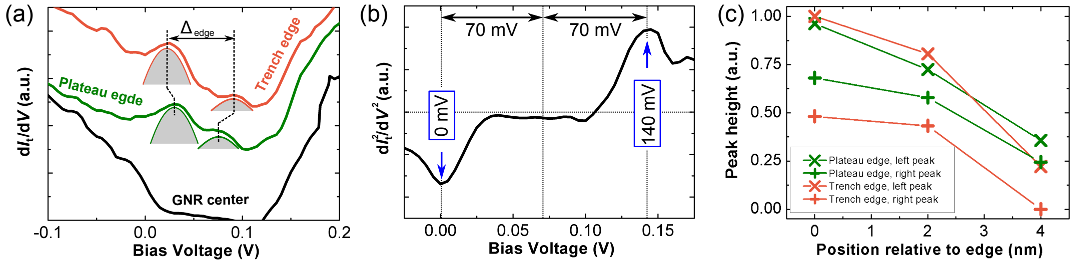

Figure 7.9: (a) Close up of the peaks in the dI_t/dV spectra at the ribbon edges. The splitting Δ_{edge} of the peaks is about 20 mV larger for the edge at the trench compared to the edge at the plateau. The spectra taken in the GNR center is shown for comparison. (b) $\frac{d^2I_t}{dV^2}$ spectrum taken in the ribbon center. Antisymmetric features in the spectrum are indicated by arrows. (c) Decay of the intensity of the edge state peaks with increasing distance away from the edges to the ribbon center.

to an elastic tunneling gap which is overcome by inelastic phonon-mediated tunneling [120, 122] is striking. The phonon energy is deduced from the d^2I_t/dV^2 spectrum in fig. 7.9(b) to about 70 meV (taking into account the shift of 70 mV) which corresponds well to a graphene K-point phonon [131]. It should be noted that in section 5.2.1 the explanation of the gap-like feature in the dI_t/dV of epitaxial ML graphene on SiC(0001) by inelastic tunneling was ruled out due to the spatial inhomogeneity of the inelastic contributions [133]. However this is no discrepancy because the observations on ML graphene on SiC(0001) are largely influenced by the underlying buffer layer. Since no buffer layer is present in the case of a sidewall GNR the interpretation that the gap feature is caused by inelastic phonon-mediated tunneling is reasonable.

Focusing now on the double peak structure within the gap, it can be clearly seen from fig. 7.9(c) that the two peaks are localized around the edges. The intensity drops as soon as the distance from the edge is increased. This is in qualitative agreement with the decay of the edge states of GNRs physisorbed on Au(111) [201]. However, the data density is not high enough to proof an exponential behavior of the decay. Nevertheless, the experimental finding strongly suggests the presence of localized states in the edges of sidewall GNRs. As shown in fig. 7.9(a) the splitting of the edge state peaks is slightly higher for the trench edge (60 mV) compared to the plateau edge (50 mV).

The key question is that of the mechanism which gives rise to the edge states. A natural guess for a zigzag GNR would be the well described edge states arising from the flat bands in the energy spectrum [27, 28]. Such edge states have indeed been observed by STS at the zigzag edges of graphite [202–204], GNRs etched out of highly oriented pyrolytic graphite [205] and graphene quantum dots [206]. This however does not explain the double peak structure in the tunneling spectra. Such a double peak structure has been observed already in GNRs physisorbed on Au(111) [201], CVD graphene nanoribbons [207] and epitaxial GNRs on SiC obtained by Fe nanoparticle-assisted hydrogen etching [38]. The energy splitting of the peaks was attributed to the presence of magnetic ordering. The splitting observed here for the sidewall GNRs is larger by almost a factor of three compared to chiral GNRs on

Au(111) of the same width [201]. Yet the exact value of the splitting depends on the on-site Coulomb repulsion which is typically assumed to be in the range of $1.1 - 1.3\,t$ for zigzag GNRs but can also be effectively screened by the substrate resulting for example in $U = 0.5\,t$ for GNRs on Au(111). Hence, a different splitting for GNRs on different substrates is expected. For example, in 14 nm wide ribbons on SiC substrates edge state peaks splitted by about 130 meV have been observed [38]. In CVD grown GNRs the energy splitting of the edge states was found to be much larger than the theoretically calculated values [207] illustrating that a match between theory and experiment concerning the edge-state splitting is no trivial task.

A further point which needs to be considered in the case of sidewall GNRs is strain. As obvious from the model presented in fig. 7.3 a significant amount of strain is expected around the edges of the sidewall GNR because of the local bending of the ribbon. Such strain can lead to a further modification of the band structure. Tensile strain was predicted to increase the band gap of a zigzag GNR while compressive and sheer strain has the opposite effect [208]. There are also experimental evidences for the influence of strain. The bandgap of a GNR deposited on SiO_2 was successfully tuned by uniaxial strain applied via an AFM tip [209]. Band gap variations of more than a factor of 2 were observed. Concerning the sidewall ribbons it is highly reasonable to assume that different amounts of strain are present in the trench and plateau edge considering their different morphological structure. This might be the reason for the different energy splittings of the edge states in the upper and lower edge.

Edge magnetism is not the only possible explanation for the presence of edge state peaks. Similar features can be caused by the interaction of the ribbon edges with the substrate. For zigzag GNRs on various metal surfaces such as Au(111), DFT calculations have shown that nonmagnetic edge states can be caused by the bonding of the ribbon edge to the substrate [210]. On the other hand GNRs with hydrogen terminated edges on Au(111) surfaces were identified not to suffer from interactions with the substrate and their magnetic properties remain unaffected. Similarly the σ-bond between the sidewall ribbon edge and the SiC substrate may protect the sp^2-hybridization of the edge atoms making the edge state robust against external influences. In lack of a DFT study of the sidewall GNRs, the origin of the edge states cannot be fully clarified. The presence of edge states, nonetheless, reflects the well-ordered character of the edges of a sidewall GNR.

7.3 TRANSPORT PROPERTIES OF SIDEWALL RIBBONS

The most important characteristics of GNRs, in foresight to use them in electronic applications, are their transport properties. In order to extract the intrinsic properties of the GNRs no contacts defined by conventional lithography shall be used, because any kind of resist can lead to unintentional doping [48–50]. As already demonstrated in chapter 5 and 6, a multi-tip STM equipped with tungsten tips can be reliably used to perform transport measurements on graphene. All transport experiments were performed in a UHV environment after degassing the samples for a minimum of

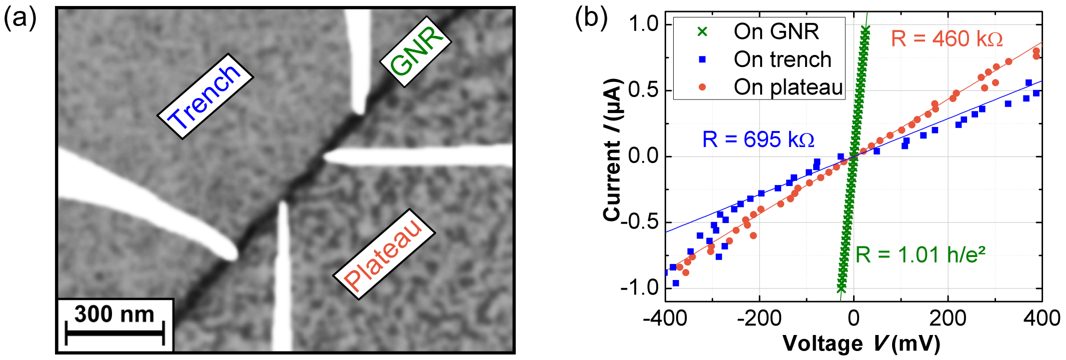

Figure 7.10: (a) SEM image showing four tungsten tips contacting a sidewall GNR. (b) IV curves taken on the GNR as well as on the trench and the plateau of the mesa. The indicated resistances are obtained by a linear fit. The GNR shows a resistance close to $1\,h/e^2$. The resistance on the trench and the plateau are significantly higher.

5 h at 800 °C. Thus, all transport results were obtained in a very clean environment leaving almost no room for the detrimental influence of adsorbates.

7.3.1 LOCAL RESISTANCE MEASUREMENTS

The local resistance of the sidewall GNRs was measured in a linear 4pp arrangement. An SEM image of the geometry is presented in fig. 7.10(a). The GNR on the sidewall can be clearly identified by its dark contrast compared to the trench and plateau of the mesa where only buffer layer or very small graphene patches are present. The low SEM intensity of the graphene ML on the sidewall is consistent with the SEM investigations of epitaxial graphene layers on SiC(0001) in section 6.1. The tungsten tips are placed directly on the ribbon following the contacting procedure described in section 4.3. An ohmic contact is formed between tip and ribbon with contact resistances below 500 Ω.

A typical IV curve of a sidewall GNR with a probe spacing $L = 1\,\mu m$ is displayed in fig. 7.10(b). It exhibits a purely metallic behavior with a resistance $R = 1.01\,h/e^2$. The IV curves obtained on the sidewall GNRs were always metallic regardless of probe spacing or temperature. No sign of any semiconducting behavior was found. In contrast, 4pp measurements on the trench and the plateau of the mesa reveal significantly increased resistances compared to the sidewall GNR. The example IV curve on the plateau yields a resistance of 460 kΩ. The resistance on the trench $R = 695\,k\Omega$ is even higher. The local resistances on the trench and plateau are largely varying when probed at different sample positions. But they were typically at least 15 times higher than the resistance of the sidewall GNRs. The influence of parasitic current paths through the plateau and trench is hence small enough to extract the transport properties of individual sidewall GNRs. In general, the resistance of the trench was found to be higher than that of the plateau which is most likely due to an enhanced disorder induced by the RIE process.

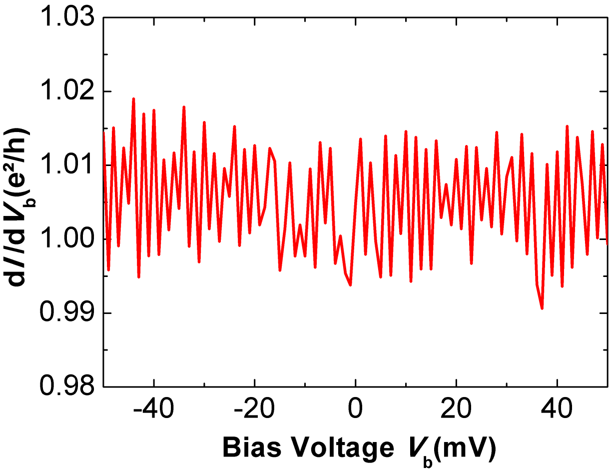

Figure 7.11: 4pp resistance of a sidewall GNR measured at room temperature and plotted against the bias voltage V_b. Resistances were measured using low-frequency lock-in techniques (50 Hz, 10 nA) and a probe spacing of $L = 5\,\mu m$.

The linearity of the IV curves of sidewall GNRs suggests that the resistance is bias independent. In contrast, a large bias dependence was reported for sidewall GNRs measured in a fixed geometry at low temperatures [174]. The increase of conductance with increasing bias voltage was attributed to electronic heating [32]. In order to test whether a similar behavior can be found here, the bias voltage of the sidewall GNRs was measured in a 4pp configuration with low-frequency lock-in technique. The resulting resistance with respect to the bias voltage is exemplarily shown in fig. 7.11. No bias voltage dependence was found in any of the sidewall GNRs. This is most likely due to the relatively high minimum temperatures which can be reached in the multi-tip STM. For observing a significant bias voltage dependence temperatures below 30 K are needed [174] which cannot be realized here.

The main advantage of a multi-tip STM is the possibility of a fast change of the tip arrangement. This allows to perform resistance measurements with variable probe spacings. The probe spacing dependent resistance of five different sidewall GNRs is shown in fig. 7.12(a). All ribbons show a resistance which is linearly increasing with the probe spacing. The offset resistance at $L = 0$ is always given by $R = 1\,h/e^2$. This is in line with the resistance relation expected for a ballistic conductor (cf. eq. 2.38) $R(L) = h/e^2(1 + L/\lambda_0)$. The offset resistance of $R = 1\,h/e^2$ indicates ballistic transport through a single non-degenerate channel. The mean free paths λ_0 extracted from the linear fit show a large variation for the individual ribbons. It ranges from $1.6\,\mu m$ to practically infinity in case of ribbons which do not show any resistance increase with increasing probe spacing at all. These mean free paths are of course only extrapolations from the limited transport length scale shown here. Nonetheless, mean free paths largely exceeding the probe spacing show that it is possible to conduct electrons through the ribbons without back scattering over length scales of more than $5\,\mu m$. This is reflected in the resistance per unit length R_l which can be directly deduced from the fit taking into account the width of the GNRs of 40 nm. For the five

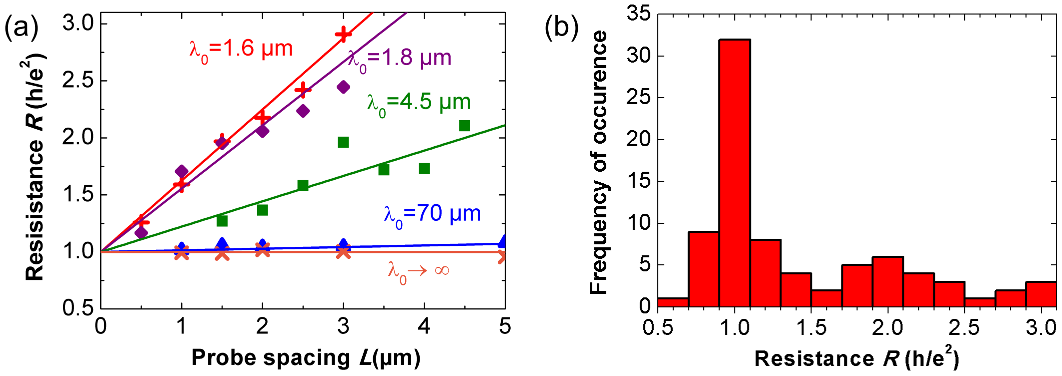

Figure 7.12: 4pp transport measurement on various sidewall GNRs. In (a) the resistance is plotted versus the probe spacing for five ribbons. The linear fits extrapolate to $R_0 = 1 h/e^2$. The mean free paths λ_0 deduced from the fit according to eq. 2.38 are indicated in the graph. (b) Histogram of the resistance values of 80 sidewall GNRs measured with probe spacings between 1 μm and 5 μm.

sidewall GNRs shown here R_l ranges from $16\,\mathrm{k\Omega/\mu m}$ down to below $300\,\Omega/\mathrm{\mu m}$ and reaches practically zero for the best ribbons.

To clarify whether this single-channel ballistic transport is only an occasional property of a few sidewall ribbons, the resistance of a large number of ribbons was recorded. Fig. 7.12(b) shows a histogram of the resistances of 80 different ribbons in the probe spacing regime between 1μm and 5μm. The resistance values clearly exhibit a peak at $1\,h/e^2$ indicating that the majority of sidewall GNRs does show single-channel ballistic transport with resistances only moderately increasing with probe spacing. Hence it can be concluded that the single-channel ballistic transport is a general property of sidewall GNRs.

The finding of single-channel ballistic transport in the sidewall GNRs is remarkable for three reasons. First, it implies that both the spin and the valley degeneracy are lifted. Furthermore, the transport experiments shown here were carried out at room temperature. Room temperature ballistic transport is theoretically predicted for zigzag GNRs [211] and was experimentally observed for example in carbon nanotubes [12, 212] or graphene encapsulated in boron nitride [213]. The third remarkable fact is that the ballistic conduction was probed in a 4pp geometry which is in principle not sensitive to the quantized contact resistances which characterize a ballistic conductor. The reason why a 4pp measurement is essentially the same as a 2pp here, is related to the invasiveness of the probes and will be discussed in detail in section 8.1.

The next chapter 8 will be solely devoted to the investigation of the exceptional single-channel ballistic transport in sidewall GNRs. The rest of this chapter however, will investigate the origin of the different mean free paths of the ribbons in fig. 7.12(a). This is utterly important in order to optimize the growth process. It should be noted that the different mean free paths are not related to any morphological or spectroscopic feature seen in STM, STS and Raman. The results presented in section 7.2 are

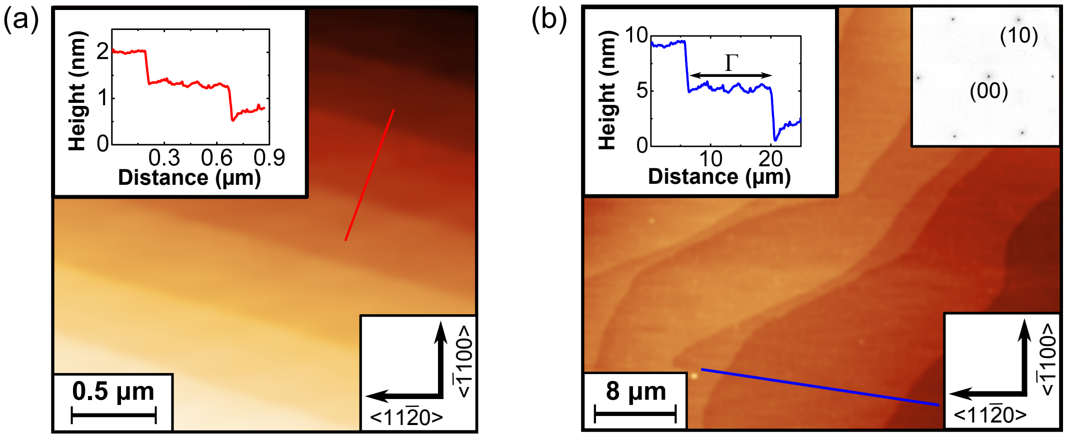

Figure 7.13: AFM images of flattened SiC surfaces exhibiting (a) half-unit cell steps and (b) large steps with several nm height created by step bunching. The insets show corresponding linescans. The terrace width Γ is much larger on the step bunched surface. No graphene or buffer layer is present on the surface and the LEED image in the inset shows consequently only a SiC(1×1).

valid for all ballistic sidewall ribbons regardless of their mean free path. Hence, the limitation of the mean free path needs to be caused by an extrinsic influence.

7.3.2 INFLUENCE OF SUBSTRATE ROUGHNESS

So far the surface structure of the underlying SiC substrate has been completely neglected during the characterization of sidewall GNRs. In order to understand the large spread in the mean free path, observed in the previous section, it is now necessary to take a closer look at the substrate morphology. All SiC substrates were flattened prior to mesa structuring in order to remove polishing scratches. For this purpose the face-to-face heater was used following the recipe presented in section 5.1. By altering the annealing temperature in this first step, the width of the resulting SiC terraces can be controlled, as shown in the AFM images in fig. 7.13. Samples processed at 1200 °C exhibit small terraces up to 500 nm in width with step heights of half a SiC unit cell (0.75 nm). Annealing at higher temperatures of about $1300 - 1400\,^\circ$C leads to step bunching which increases the terrace width Γ up to several µm. The height of the steps simultaneously increases up to several nm. The roughness of the surfaces is low with typical rms values of about 0.4 nm. These are significantly smaller than those of the pristine surface which usually shows rms values of about 3 nm due to residual polishing scratches. LEED reveals that the surface contains pure, unreconstructed SiC after the flattening. The LEED pattern shows only a SiC(1×1). This ensures that no graphene or even buffer layer growth has started at this early stage.

How the different terrace widths influence the growth of sidewall GNRs can be seen from the AFM and EFM analysis in fig. 7.14, showing samples after completed mesa structuring, refacetting and graphene growth. The sample in fig. 7.14(a) exhib-

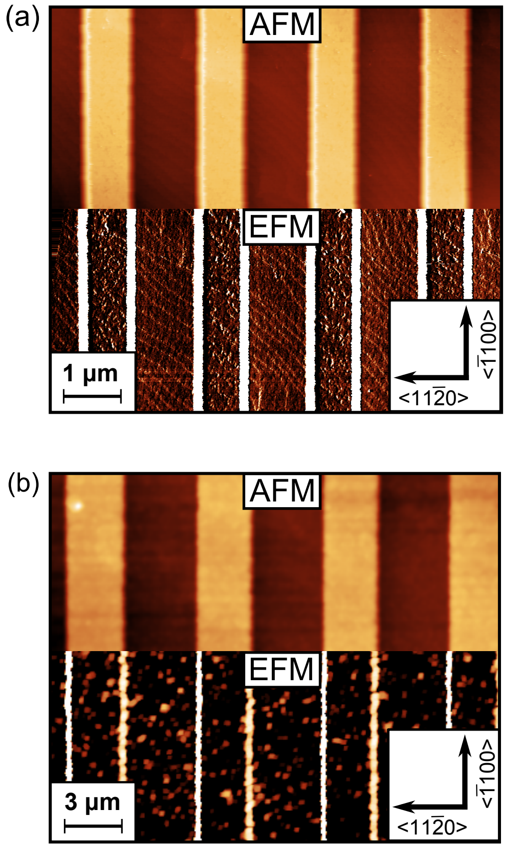

Figure 7.14: AFM and corresponding EFM image of samples with (a) small and (b) large substrate terraces after mesa structuring and graphene growth. Both samples show preferential graphene growth on the sidewalls. A large number of interconnecting narrow ribbons is present at the step edges of the sample shown in (a).

ited small terraces and half-unit cell steps prior to GNR growth while fig. 7.14(b) shows a step bunched sample with terraces up to 20µm in width. The rms values of the trench and plateau deduced from AFM are typically slightly enhanced to about 0.7 nm after the mesa structuring. Yet after the refacetting process the roughness is again reduced to about 0.4 nm. Hence the patterning of the SiC substrate is very gentle and does not enhance the roughness of the surface.

The onset of graphene growth can be directly imaged with the EFM. It can be seen from fig. 7.14 that the EFM amplitude reveals a characteristic contrast which can be attributed to the local work function on the sample surface. The work function of graphene is about 0.14 eV higher compared to the buffer layer [214]. Thus, the parts of the sample which cause a large EFM amplitude are covered with graphene. This clearly demonstrates the preferential growth of GNRs on the mesa sidewalls for both, samples with large and small terrace width. Unfortunately, graphene did not only grow on the mesa sidewalls but also on the substrate step edges. This has dramatic consequences for the sample with narrow terraces because every substrate step edge is essentially the host of an interconnecting graphene ribbon. In contrast, for the

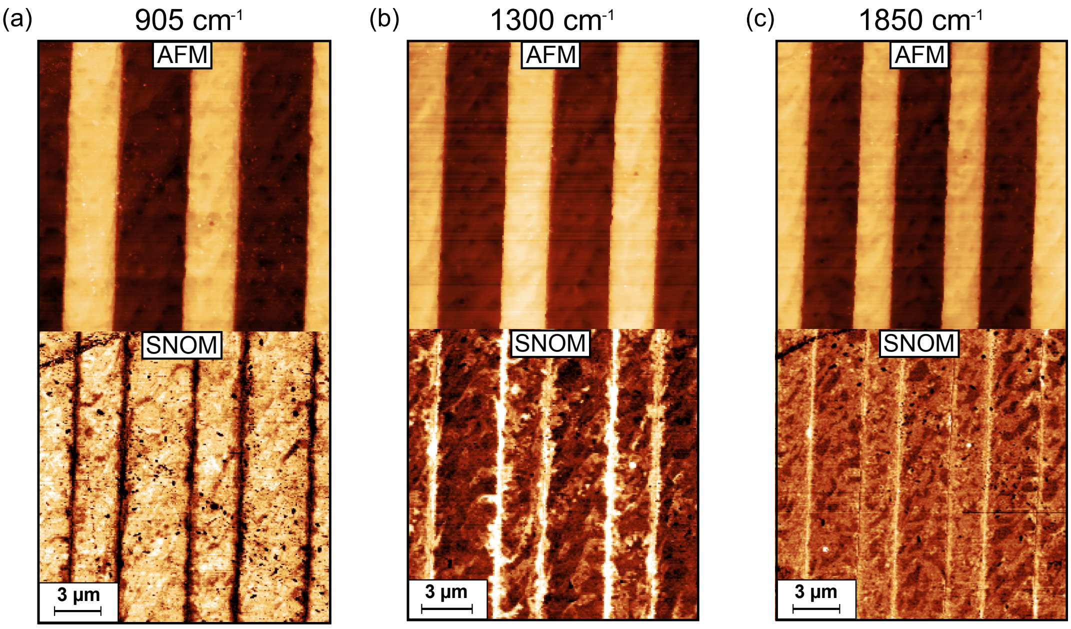

Figure 7.15: AFM and corresponding SNOM images of sidewall GNRs with excitation laser frequencies of (a) 905 cm^{-1}, (b) 1300 cm^{-1} and (c) 1850 cm^{-1}. The facets appear dark in (a) due to a resonance in the near-field spectrum of SiC at 905 cm^{-1}.

sample with wide terraces no indication of interconnecting ribbons can be found in the EFM image.

To make sure that the presence of interconnecting ribbons is really related to substrate steps further s-SNOM and SEM analysis were performed. In fig. 7.15 AFM and corresponding near field amplitude images of sidewall GNRs grown on a SiC substrate with terrace width $\Gamma > 20\,\mu\text{m}$ are shown. Three different excitation laser frequencies (905 cm^{-1}, 1300 cm^{-1}, 1850 cm^{-1}) were used for the recording of the near field amplitude in order to access different points in the near field spectrum. For the excitation frequency of 905 cm^{-1} which is shown in fig. 7.15(a) the mesa sidewalls appear darker than the trenches and plateaus. This contrast is inverted for the other two frequencies as obvious from fig. 7.15(b, c). The contrast inversion can be easily understood and is caused by a phonon resonance in the near field spectrum of SiC close to 905 cm^{-1} [215, 216]. As a consequence, the graphene covered areas appear dark at this excitation frequency. At the higher frequencies, the near-field spectrum of graphene is related to its universal conductivity, and the near field amplitude is expected to be larger than that of the SiC or buffer layer. This is clearly the case in fig. 7.15(b, c). In neither of the s-SNOM images any sign of interconnecting ribbons could be detected. Some small patches of graphene might be located between the sidewall ribbons but they should not be detrimental to the transport within the ribbons itself.

The sidewall GNRs are further analyzed by means of SEM. Fig. 7.16 presents mesa structured samples after refacetting but before graphene growth in (a) and after graphene growth in (b-d). Before graphene growth, the refacetted sidewall shows a high secondary electron contrast due to its inclination. After completed sidewall

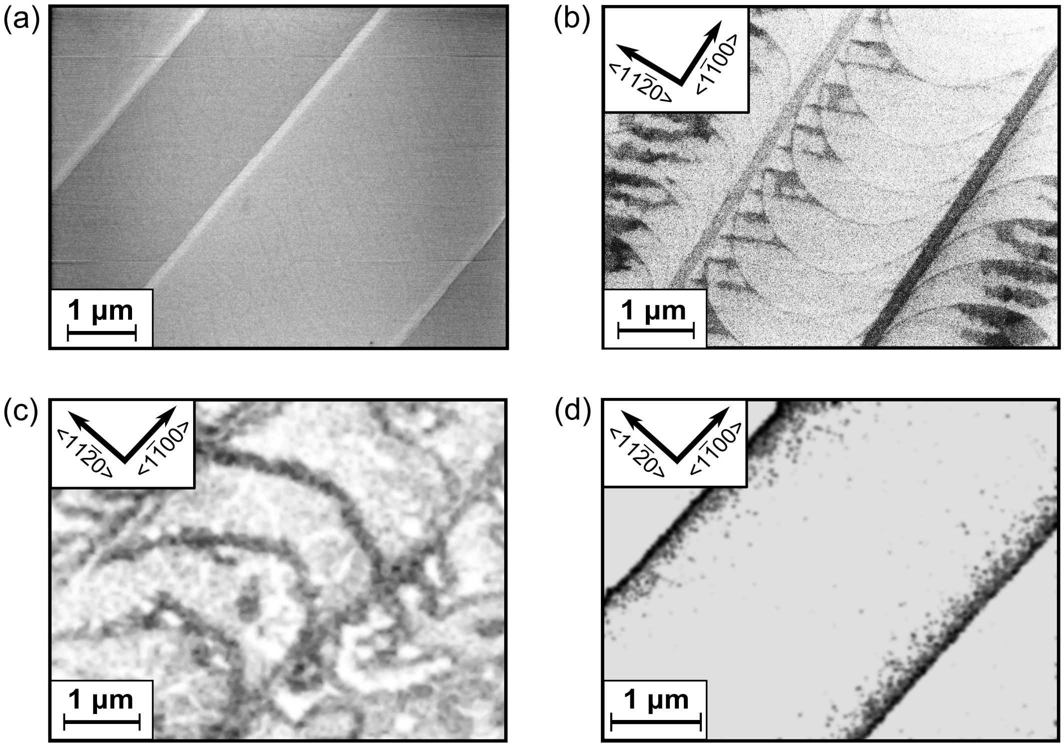

Figure 7.16: SEM images of samples after mesa structuring and refacetting (a) before and (b-d) after graphene growth on the mesa sidewalls. The facets in (a) appear bright due to their inclination relative to the flat plateaus and trenches. Samples with (b) small ($\Gamma = 500\,\text{nm}$), (c) medium ($\Gamma < 4\,\mu\text{m}$) and (d) large ($\Gamma > 20\,\mu\text{m}$) substrate terraces are shown for comparison after graphene was grown on the sidewalls. The density of step edges and hence interconnecting ribbons is decreasing with increasing terrace width.

graphene growth the facets appear darker than the surrounding surface indicating the selective growth of graphene. Three different substrates with small (Γ around $500\,\text{nm}$), medium ($\Gamma < 4\,\mu\text{m}$) and large terrace width ($\Gamma > 20\,\mu\text{m}$) were used. The SEM images clearly reveal a decreasing number of interconnecting ribbons with increasing Γ.

From these observations it can be concluded that the substrate terrace width has direct influence on the growth of sidewall GNRs by providing sources for preferential graphene growth on step edges. The effect of the resulting interconnecting ribbons on the ballistic transport properties of the sidewall GNR will be discussed in the following. For this purpose, probe spacing dependent 4pp resistance measurements have been carried out on sidewall ribbons on substrates with different terrace widths. It was not possible to grow a ballistic sidewall GNR on a substrate with half-unit cell steps and small terrace widths in the order of $100\,\text{nm}$. Hence the analysis is restricted to medium and large terrace width.

Fig. 7.17 shows exemplarily the resistance of two sidewall GNRs with respect to the probe spacing. The sidewall GNRs were grown on a substrate with either medium

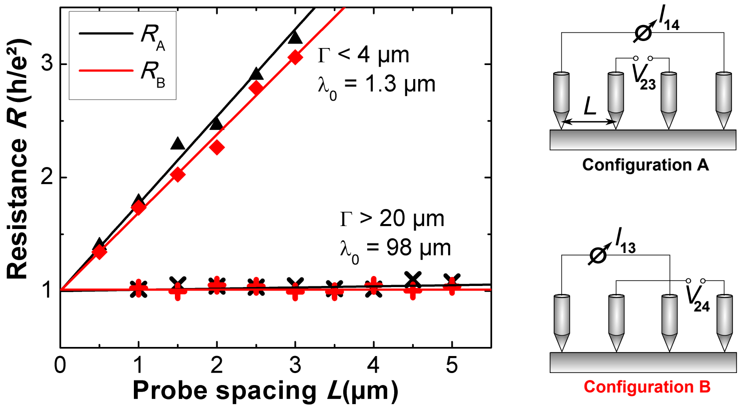

Figure 7.17: 4pp resistance of sidewall GNRs on a substrate with medium ($\Gamma < 4\,\mu$m) and large ($\Gamma > 20\,\mu$m) terrace width (cf. fig. 7.16(b, c)). The resistances are plotted with respect to the probe spacing and fitted to eq. 2.38. The measurement configurations A and B are shown schematically.

($\Gamma < 4\,\mu$m) or large terrace widths ($\Gamma > 20\,\mu$m). On the sample with large Γ the ribbon shows an almost probe spacing independent resistance of $1\,e^2/h$. Its mean free path is hence much larger than the investigated maximum probe spacing of $5\,\mu$m. The two measurement configurations A and B schematically depicted in fig. 7.17 yield almost identical resistances R_A and R_B. The resistance ratio of $R_A/R_B = 1.02$ which is a fingerprint of 1d conductivity [60]. Increasing the density of substrate steps by reducing the terrace width changes the probe spacing dependence drastically. The resistance is no longer probe spacing independent but linearly increasing. The electronic mean free path can be extracted from the fit to $\lambda_0 = 1.3\,\mu$m. The transport is still ballistic which is indicated by the offset resistance of $1\,e^2/h$ at $L = 0$ and it is still 1d with an only slightly enhanced ratio $R_A/R_B = 1.06$. However, the mean free path is strongly reduced by the presence of additional substrate steps and hence the presence of interconnecting ribbons. The density of substrate steps is found to limit the achievable mean free path of sidewall GNRs. In order to grow exceptionally long range ballistic ribbons, the roughness of the SiC template needs to be closely monitored.

7.3.3 INFLUENCE OF FACET ROUGHNESS

Despite the roughness of the SiC substrate, also the morphological properties of the mesa sidewall itself are of importance. All experiments presented so far were made on 20 nm deep mesa structures which develop smooth sidewall facets and subsequently host well-defined GNRs on these facets. If the etching depth is increased the mesa sidewalls turn out to be less stable upon facet formation. This is nicely illustrated in the TEM image of a 40 nm deep mesa sidewall recorded after the refacetting process but prior to graphene growth shown in fig. 7.18. The bottom half of the sidewall appears atomically smooth and well-ordered. A typical inclination angle of about 22° is found in this region. In the middle of the facet a small sub-terrace is visible

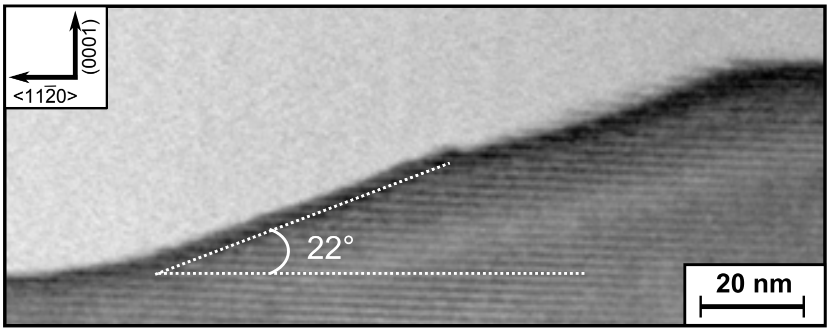

Figure 7.18: TEM image of the sidewall of a 40 nm deep mesa after the refacetting step.

which is most likely caused by a defect induced enhanced step bunching during the refacetting process. The sub-terrace simultaneously marks the transition point from the atomically smooth bottom half to the less ordered top half of the facet. The top half appears much rougher and less ordered.

The enhanced roughness of the sidewalls of mesas with etching depth larger than 20 nm also has severe consequences for the subsequent growth of graphene. Fig. 7.19(a) shows the AFM and corresponding EFM image of the sidewall of a 30 nm deep mesa sidewall upon completed refacetting and graphene growth. Three sub-facets have formed within the sidewall hosting three narrow GNRs. This becomes clear from the linescans in fig. 7.19(c). The peaks of the EFM amplitude indicate preferential graphene growth on the sub-facets. The AFM and EFM on the sidewall of a

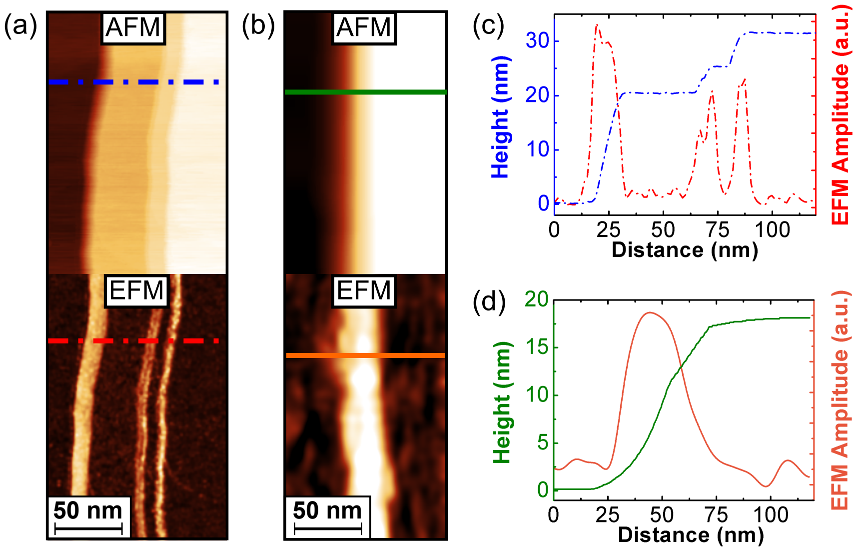

Figure 7.19: AFM and corresponding EFM image of the sidewall of a (a) 30 nm and (b) 20 nm deep mesa after graphene growth. The corresponding linescans are shown in (c) and (d). In case of the 30 nm deep sidewall the formation of 3 sub-facets each hosting a GNR is clearly visible.

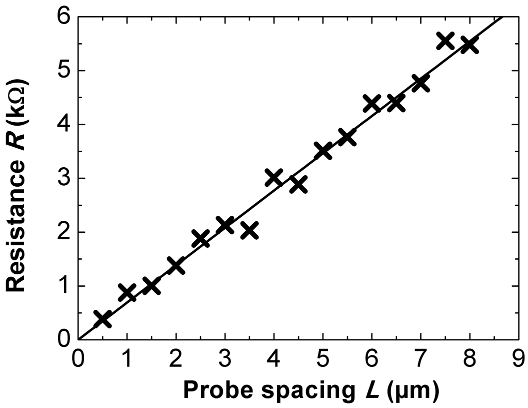

Figure 7.20: 4pp resistance of the sidewall GNRs shown in fig. 7.19(a, c). The linear fit extrapolates to zero indicating 1d diffusive transport.

20 nm deep mesa is shown for comparison in fig. 7.19(b) with corresponding linescans in fig. 7.19(d). Clearly, the whole facet is homogeneously covered with graphene and no sub-facet formation is visible. The facet inclination on 20 nm deep mesas is typically found to be in the range of $20° - 30°$. In contrast, the sub-facets on the sidewall of the 30 nm deep mesa exhibit an inclination angle of about 50°.

It should be expected that the only partial covering with graphene and the formation of sub-facet GNRs also has an impact on the transport properties. Indeed, transport in the the sub-facet GNRs follows a completely different mechanism. The 4pp resistance versus the probe spacing is plotted in fig. 7.20. It is linearly increasing up to about 5.5kΩ at $L = 8$µm. Most importantly, the linear fit reveals that there is no offset at $L = 0$ and hence no indication for ballistic conduction. This probe spacing dependence is expected for a diffusive 1d conductor measured in 4pp configuration [58]. From the fit, the resistivity of the diffusive sub-facet GNR can be deduced to about 690 Ω/µm. The resistivity is large compared to other diffusive 1d systems such as $CoSi_2$ nanowires which exhibit a more than ten times lower resistivity at a comparable width.

The observation of diffuse rather than ballistic transport in these sub-facet GNRs directly implies that their electronic mean free path is dramatically lower compared to the sidewall GNRs characterized before. It is unclear what causes the transition to the diffusive transport regime. However, it is likely that the interface between the ribbon and the facet is altered due to the large angle of inclination found for the sub-facet GNRs. For example a local bonding of the ribbon to the substrate facet would destroy the free-standing nature of the GNR. Unfortunately it was not possible to contact a single sub-facet GNR. The tip apex of the tungsten tips is typically larger than 100 nm and therefore it is reasonable to assume that always all sub-facet GNR are contacted during a transport experiment. Hence it is not clear if all sub-facet ribbons are diffusive.

Regardless of the origin of the 1d diffusive transport in sub-facet ribbons it can be concluded that a smooth facet is essential in order to observe ballistic transport in sidewall GNRs. This implies that the mesa etching depth and the facet formation

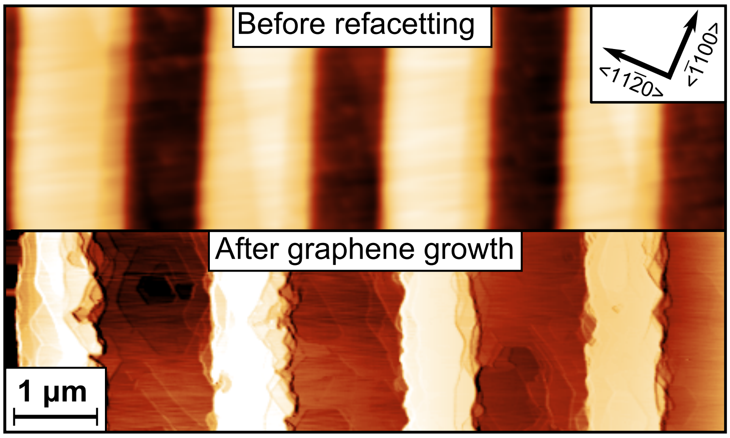

Figure 7.21: AFM images of a mesa structured sample before and after refacetting and graphene growth. The mesa structures are not aligned parallel to $\langle\bar{1}100\rangle$ or $\langle 11\bar{2}0\rangle$.

on the sidewalls needs to be closely monitored. Furthermore, the etching depth and hence the ribbon width is restricted due to the enhanced facet roughness for mesa structures deeper than 20 nm

7.4 LIMITATIONS OF THE GROWTH PROCESS

Two final remarks shall be made on the sidewall GNR growth process regarding the mesa orientation and the heating current direction. First, a mesa orientation in arbitrary direction shall be evaluated and secondly, the direction of the heating current will be changed from parallel to perpendicular with respect to the mesa alignment.

7.4.1 MESA ALIGNMENT IN INTERMEDIATE CRYSTALLOGRAPHIC DIRECTIONS

From the STM investigations in section 7.2.3 the orientation of sidewall GNRs was identified as zigzag regardless of the mesa orientation in $\langle 11\bar{2}0\rangle$ or $\langle\bar{1}100\rangle$ direction. This leaves the question of what happens in intermediate crystallographic directions. An educated guess suggests two possibilities. Either the sidewall GNRs still prefer the zigzag orientation or they arrange accordingly to the substrate orientation in a chiral manner. The possibility to align the mesa structures in an intermediate angle would have the advantage that their alignment can be chosen to be parallel to substrate steps. This would drastically reduce the formation of interconnecting ribbons in between the sidewall GNRs which were identified to have a limiting effect on the electronic mean free path in section 7.3.2. The AFM image of a mesa structure with intermediate alignment before and after graphene growth is presented in fig. 7.21. Unfortunately, it reveals that the mesa structures are not stable in such crystallographic direction. Upon graphene growth their sidewalls are severely eroded. Since a minimum roughness of the substrate and the sidewalls is needed to observe ballistic

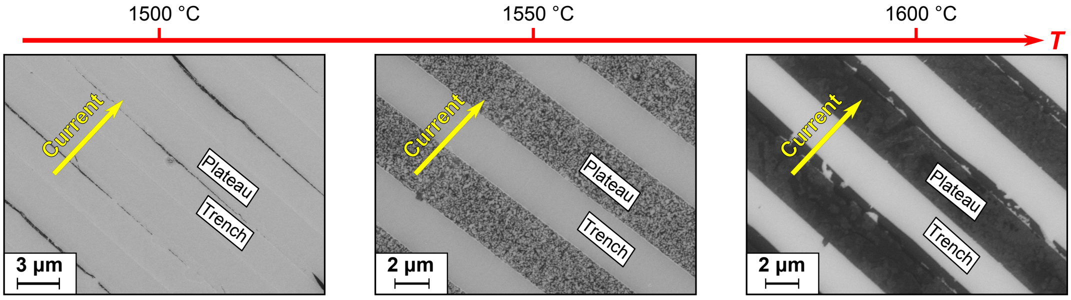

Figure 7.22: SEM images taken during graphene growth on a mesa structured SiC surface. The heating current is driven through the sample in perpendicular direction to the mesa orientation.

transport properties, this mesa orientation is not suitable for the growth of sidewall GNRs. It can be concluded that the mesa alignment needs to be carefully controlled and it is limited to crystallographic directions parallel to $\langle 11\bar{2}0\rangle$ or $\langle \bar{1}100\rangle$.

7.4.2 ALTERATION OF THE HEATING CURRENT DIRECTION

One last remark concerns the direction of the heating current direction used for annealing of the samples. As mentioned in the beginning of this chapter for all annealing steps done so far the current was always driven through the sample parallel to the mesa orientation and hence, parallel to the sidewalls. If the heating current is driven through the sample in perpendicular direction the graphene growth mechanism is completely different. The SEM images in fig. 7.22 show three samples after graphene growth at different temperatures. The heating current was driven through the sample perpendicular to the mesa sidewalls. Dark areas in the SEM images indicate the formation of graphene. At the lowest temperature of 1500 °C only every second sidewall is covered with graphene. It is always the facet which faces the incoming current. Even on these facets the graphene growth is inhomogeneous. By increasing the annealing temperature up to 1550 °C graphene growth on the plateaus can be triggered. The development of small graphene patches can be observed. After increasing the annealing temperature further to 1600 °C the plateaus are fully covered with few-layer graphene. The graphene growth proceeds on the trenches as well, again following the direction of current.

The growth mechanism seen here can be rationalized in terms of electromigration. The electrons of the heating current transfer their momentum to the Si atoms of the SiC which will be preferentially desorbed. This process is most effective at the facets facing the current. This growth profile might be useful for the purpose of selectively growing graphene only on the mesa plateaus and should be also a possible pathway for the self-organizational growth of graphene nanostructures. On the other hand, for the growth of sidewall graphene nanoribbons this growth method is not suited because of the rather inhomogeneous graphene formation on the sidewalls. Hence, in order to synthesize well-ordered sidewall GNRs by resistive heating the heating current should always be driven through the sample in the direction parallel to the mesa sidewalls. This implies further that graphene nanostructures in other geometries such as circles or kinked structures might be difficult to prepare by resistive heating. Switching to heating with an AC current instead of DC, could be a possible route to overcome this obstacle.

7.5 CONCLUSIONS

In this chapter it was shown that GNRs can be grown by self-assembly, making use of the preferential graphene growth on the sidewalls of SiC mesa structures. This process eliminates the parasitic influences of conventional lithography such as unintentional doping via the resist. The presence of monolayer graphene on the sidewalls was demonstrated by means of Raman spectroscopy. STM revealed that the graphene layers on the sidewalls are atomically well-ordered. Surprisingly, the sidewall GNRs are always oriented in zigzag direction regardless of the mesa orientation relative to the substrate. Charge neutrality as well as the presence of edge-states was indicated by local tunneling spectroscopy. These findings support the model of a freestanding GNR and disprove the presence of an underlying bufferlayer.

The sidewall GNRs were characterized by local 4pp transport as room temperature ballistic conductors. The presence of only a single transport channel indicates the lifting of both spin and valley degeneracy. Furthermore, mean free paths larger than 5 μm can be reached. Minimization of the roughness of the SiC substrate and the mesa sidewall was identified to be crucial in order to grow long range ballistic GNRs. The mean free path of the sidewall GNRs was shown to be directly limited by the initial terrace width of the SiC substrate.

8

BALLISTIC TRANSPORT IN SIDEWALL GRAPHENE NANORIBBONS

In the previous chapter 7, sidewall graphene nanoribbons were identified as room temperature, single-channel ballistic conductors. In this chapter a detailed transport characterization of the ballistic channel shall be presented. First, the role of the voltage probes in a local 4pp measurement on a ballistic conductor will be evaluated to give further evidence for the ballistic nature of transport. Furthermore, in order to get a thorough understanding of the peculiar transport properties of sidewall GNRs it is necessary to investigate the localization behavior of the ballistic channel as well as its low temperature characteristics. These investigations will allow to suggest possible mechanisms for the origin of single-channel transport in sidewall GNRs.

8.1 INFLUENCE OF INVASIVE PROBES

The transport data presented in chapter 7 were collected in 4pp configuration. Following the discussion in section 2.2.5 the invasiveness of voltage probes in a 4pp measurement configuration can be evaluated by comparing the resistances gained from a 4pp measurement R_{4pp} with those from the 2pp configuration R_{2pp}. A corresponding plot showing R_{4pp} and R_{2pp} at different probe spacings is given in fig. 8.1. Naturally, a sidewall GNR with a long mean free path was chosen for this investigation (cf. section 7.3.1). Hence only a very small linear increase of the resistance with increasing probe spacing can be detected. The fits according to $R(L) = R_0(1 + L/\lambda_0)$ yield a mean free path $\lambda_0 = 265\mu m$ for both arrangements. The offset $R_0 = 1\,h/e^2$ for the 4pp measurement and is slightly enhanced to $R_0 = 1.04\,h/e^2$ in the 2pp case. Moreover, the resistance ratio can be extracted to $R_{4pp}/R_{2pp} = (0.95 \pm 0.02)$. According to eq. 2.64 this resistance ratio yields an invasiveness of the voltage probes $P = 0.97$. Hence the voltage probes are almost completely invasive. Consequently the resistance obtained in a 4pp and in a 2pp configuration are almost equal because the invasive voltage probes separate the ballistic conductor into three equal sections [74].

The resistance in the 4pp measurement is in general only slightly lower than that extracted from a 2pp one. This reflects nicely that besides the quantized contact resistance from ballistic conduction other contact resistances arising at the probe ribbon interface are small. The 2pp resistance is enhanced by about $0.04\,h/e^2$ which suggests an additional mean contact resistance between probe and ribbon of about $500\,\Omega$.

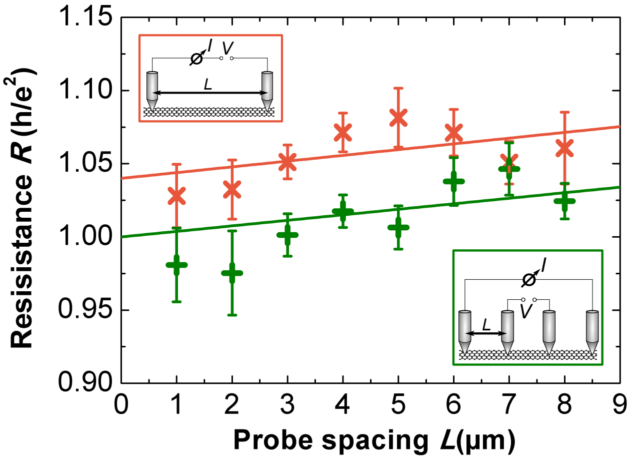

Figure 8.1: Comparison of 4pp and 2pp resistance of a sidewall GNR plotted against the probe spacing. The measurement setups are shown schematically.

Hence measurements in a 2pp configuration are sufficient in order to detect ballistic signatures with fairly high accuracy.

The invasiveness of the probes can be exploited in an elegant way to provide further evidence for the ballistic nature of transport. As discussed in section 2.2.5 a fully invasive voltage probe acts on a ballistic conductor like a scattering center with transmission probability $T = 1/2$. Hence, introducing one or two passive probes in a 2pp setup should strongly modify R_{2pp}. A general expression for multiple scattering centers with different transmission probabilities has already been derived in section 2.2.1 in eq. 2.33. Consequently, introducing one passive probe with $T = 1/2$ should result in a doubling of R_{2pp} while two passive probes cause a tripling.

The corresponding measurement is presented in fig. 8.2(a). It clearly shows that placing one or two probes onto the ballistic conductor in between the contacting probes has a distinct effect on R_{2pp}. It increases step like with every additional passive probe. This is a clear signature of ballistic transport. Placing probes on a diffusive wire would have no effect on the measured resistance. Neither the distance between the contact probes nor the position of the invasive probes relative to the contact probes has an effect on the observed resistance values as apparent from fig. 8.2(b). This illustrates that the probe spacings are smaller than the mean free path of the system.

The invasive probe experiment was repeated several times resulting in the large spread of the resistance values shown in fig. 8.2(a). The mean invasiveness extracted from the resistances with one and two passive probes in between adds up to about $0.48 - 0.86$. It does not completely reach the value obtained previously in this section from the comparison of R_{2pp} and R_{4pp} ($P = 0.97$). However the measurement setup with a passive probe (meaning a probe with a large resistance to ground) is not exactly the same as a 4pp setup with the voltage probes connected to a multimeter. The passive probe setup is much more demanding in experimental terms which also explains the large spread of values for the mean invasiveness. Placing the passive probes several times on the ballistic conductor can always result in modifications of the probe ribbon interface and hence alterations of the invasiveness. In the case of

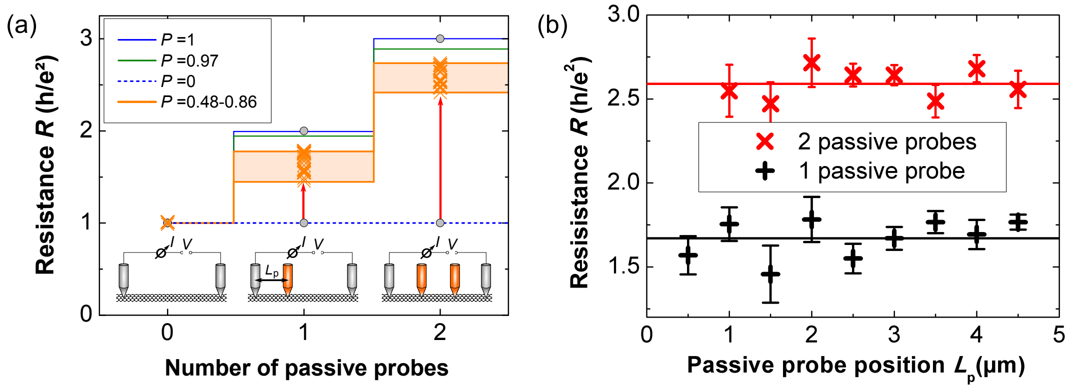

Figure 8.2: (a) Effect of passive probes (orange in the schematic illustration) contacting a sidewall GNR in between the current/voltage probes. The measured resistances are expected to double for one passive probe and triple for two passive probes in the case of perfect invasiveness. The measurements are indicated in orange. The values expected for fully invasive probes ($P = 1$), non-invasive probes ($P = 0$) and probes with the invasiveness deduced from the comparison of 4pp and 2pp measurements ($P = 0.97$) are shown for comparison. The invasiveness of the passive probes was assumed to be equal. (b) Plot of the resistance measured with 1 and 2 passive probes with respect to their position. L_p is the distance of the passive probe to the left current/voltage probe as shown in the sketch in (a). In the case of 2 passive probes, the position of the second passive probe is kept fixed in $0.5\,\mu m$ distance to the right current/voltage probe.

two passive probes only a mean invasiveness was extracted from the measurements in fig. 8.2(a). This means that the invasiveness of both probes was assumed to be equal. This assumption is not really justified due to the large spread in resistance. However, the main purpose of the passive probe experiment was to provide evidence for the ballistic nature of transport and not to extract the individual invasiveness of the probes. Nonetheless the large number of measurements provides a good estimate of the range in which the probe invasiveness can be found.

A final remark on the passive probe experiments concerns the question of possible damage to the ribbon by placing the passive probes repeatedly on the ribbon. It is important to exclude the possibility of a damaged ribbon because in principle damage could also account for a resistance increase. Therefore only passive probes experiments were considered which were fully reversible, meaning that the original resistance value of $1\,e^2/h$ was recovered after removing the passive probes. This ensures that the sidewall GNR and its single ballistic channel were still intact after the passive probe experiment.

8.2 LOCALIZATION AND THE SECOND BALLISTIC CHANNEL

The transport investigations of the ballistic channel in sidewall GNRs concentrated so far on the probe spacing regime between $1\,\mu m$ and $5\,\mu m$. Some remarkable observations can be made, expanding this regime down to $L = 100\,nm$ and up to $L = 25\,\mu m$.

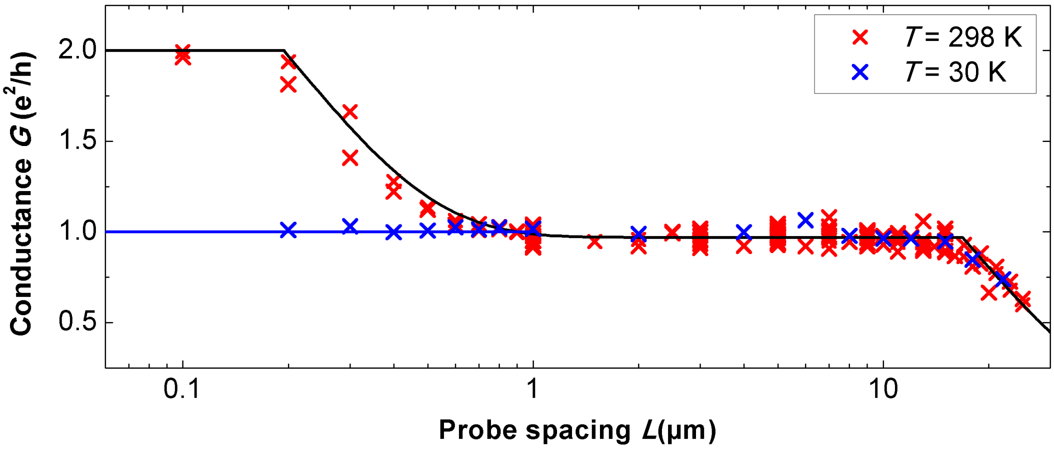

Figure 8.3: Conductance of sidewall GNRs versus probe spacing at room temperature ($T = 298\,K$) and low temperature ($T = 30\,K$). At room temperature, the conductance decreases nonlinearly at $L = 200\,nm$ and $L = 17\,\mu m$. If $L < 200\,nm$, the quantized conductance of two ballistic channels $G = 2e^2/h$ is obtained. If $200\,nm < L < 17\,\mu m$, only a single ballistic channel ($G = 1\,e^2/h$) is present. The fit functions are given in eq. 8.1 and eq. 8.2. At low temperatures the second ballistic channel is not present even for small L.

The resulting conductances are plotted in fig. 8.3 for room temperature as well as $T = 30\,K$. The low temperature curve shows a probe spacing independent conductance of $G = 1\,e^2/h$ up to about $L = 17\,\mu m$. For larger L the conductance decreases indicating localization of the ballistic channel. The same behavior is found at $T = 298\,K$ for $L > 1\,\mu m$. However for $L < 1\,\mu m$ the conductance at room temperature is increasing nonlinearly up to $G = 2\,e^2/h$. Hence, for small probe spacings at room temperature a second channel is contributing to the conductance. The conductance at room temperature is well described by the following expression

$$G_{RT}(L) = \begin{cases} 2\,\frac{e^2}{h} & , \quad L < 200\,nm \\ \frac{e^2}{h} + \frac{e^2}{h}\exp\left(1 - L/L_0^-\right) & , \quad 200\,nm \leqslant L < 1\,\mu m \\ 1\,\frac{e^2}{h} & , \quad 1\,\mu m \leqslant L < 17\,\mu m \\ \frac{e^2}{h}\exp\left(1 - L/L_0^+\right) & , \quad L \geqslant 17\,\mu m \end{cases} . \tag{8.1}$$

The conductance increase for both channels can be fitted with the same exponential relation. They differ only in the localization parameter $L_0^{\pm}$ which is given by $L_0^- = 200\,nm$ for the short and $L_0^+ = 17\,\mu m$ for the long channel. Hence two ballistic channels with very different localization lengths are present in the sidewall GNRs.

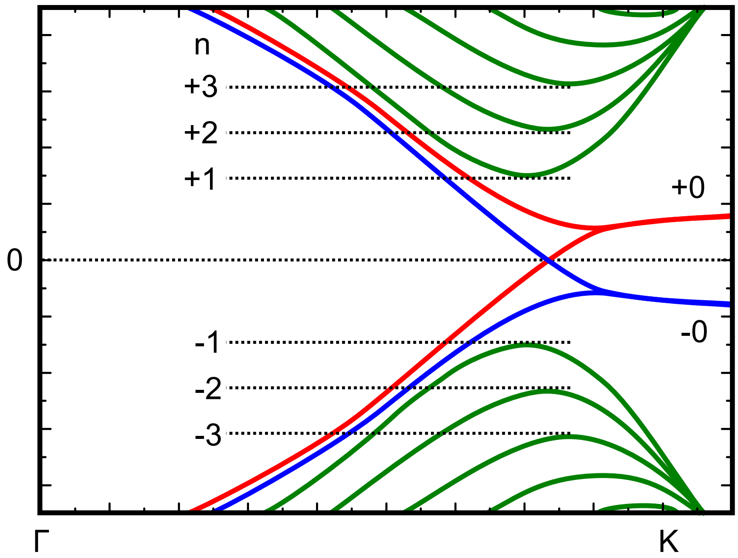

Figure 8.4: Schematic bandstructure of a zigzag GNR with ferromagnetically coupled edges. The spin split zeroth subbands are indicated in red and blue.

Furthermore, the short channel appears to be thermally activated and is consequently missing in low temperature measurements. The conductance at low temperatures ($T = 30\,\mathrm{K}$) is hence given by

$$G_{LT}(L) = \begin{cases} 1\,\frac{e^2}{h} & , \quad 1\,\mu\mathrm{m} \leqslant L < 17\,\mu\mathrm{m} \\ \frac{e^2}{h}\exp\left(1 - L/L_0^+\right) & , \quad L \geqslant 17\,\mu\mathrm{m} \end{cases} . \tag{8.2}$$

A detailed discussion of the temperature dependence of the two ballistic channels will be given in the next section.

In the following, the short range ballistic channel will be referred to as $0-$ and the long range as $0+$ channel. The reason behind this assignment is the origin of the ballistic channels which can be understood from the band structure of a zigzag GNR with ferromagnetically coupled edges. It is schematically shown in fig. 8.4. In general, the energy spectrum of a graphene nanoribbon with length L and width W is approximately given by

$$E_{n,m} = \pm\hbar v_f \sqrt{\left(\frac{n\pi}{W}\right)^2 + \left(\frac{m\pi}{L}\right)^2} . \tag{8.3}$$

For $W = 40\,\mathrm{nm}$ the first subband $E_{1,0} \approx 52\,\mathrm{meV}$. Turning now to subbands with $n \geqslant 1$, for $|E_f| \geqslant |E_{n,0}|$ the conductance is simply given by the Landauer equation 2.28. Hence

$$G = 4\frac{e^2}{h}\sum_n T_n \tag{8.4}$$

with T_n being the transmission through subband n; the factor of 4 is caused by the spin and valley degeneracy.

Consequently, for $|E_f| < |E_{n,0}|$, $T_n = 0$ and the subbands with $n \geqslant 1$ do not contribute to transport. This leaves the subbands for $n = 0$, the so called zeroth subbands. They are related to the edge states of a GNR. The spin degeneracy of the zeroth subbands is lifted due to magnetic ordering (cf. section 3.2.2). The assumption of ferromagnetic coupling between the edges is motivated by the absence of a band gap. As discussed in section 3.2.2, antiferromagnetic coupling would introduce a significant band gap. Since no evidence for semiconducting behavior was found in the sidewall GNRs the presence of a band gap can be excluded. This leaves the question of the cause for the ferromagnetic coupling. In a recent experimental and theoretical study ferromagnetic coupling was suggested to be present in zigzag GNRs at room temperatures [37]. The magnetic coupling was proposed to depend on the ribbon width and a transition from antiferromagnetic to ferromagnetic coupling was found for ribbons wider than 8 nm. The extraordinary claim of room temperature ferromagnetism however needs to be further backed up by a local probe of the magnetic order in the edges [217].

The spin correlation length is in the order of 1 nm in a zigzag graphene edge at room temperature [218]. This suggests that spintronic devices based on edge magnetism cannot exceed this length scale if they shall be operated at room temperature. Hence, spin polarization in the sidewall GNRs demands for a mechanism which enhances the spin correlation length. As already mentioned in section 7.2.3 a significant amount of curvature and strain is expected to be present in the sidewall GNRs. Pseudo-magnetic fields caused by curvature were shown to be able to severely alter the spin texture and the edge state properties of a GNR [219, 220]. Furthermore, transverse electric fields were reported to cause half-metallicity in GNRs [107]. The different bondings at the upper and lower edge of the sidewall GNR (cf. fig. 7.3) might cause such transverse fields. Moreover even a single line defect was shown to induce an intense spin polarization [221]. It is up to date not possible to say how the spin polarization in the sidewall GNRs really looks like and which of the mechanisms mentioned before actually makes a contribution. A lot more experimental and especially theoretical work is needed to gain a realistic picture of the band and spin structure.

8.3 TEMPERATURE DEPENDENCE

To gain a better understanding of the nature of the two ballistic channels found in the previous section, temperature dependent measurements were performed. Fig. 8.5 shows the conductances versus the temperature for probe spacings $L = 300$ nm and $L = 1$ μm. For $L = 300$ nm the contribution of both ballistic channels is expected while for $L = 1$ μm only the long ballistic channel (0+) is still present. This is well reflected in the experiment where the conductances found at $L = 300$ nm are always above

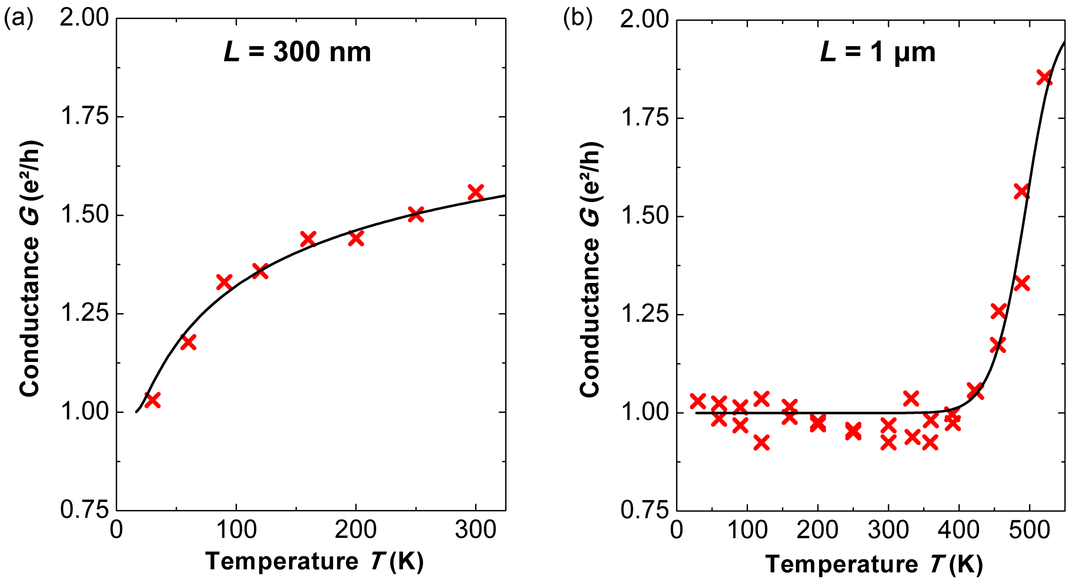

Figure 8.5: Conductance of sidewall GNRs plotted against the sample temperature for a fixed probe spacing of (a) $L = 300\,\mathrm{nm}$ and (b) $L = 1\,\mu\mathrm{m}$. In the case of $L = 300\,\mathrm{nm}$ two channels contribute to the conductance and one of them is temperature dependent. The fit according to eq. 8.5 is explained in the main text. For $L = 1\,\mu\mathrm{m}$ only the exceptional single-channel is probed. Below 400 K the conductance shows no temperature dependences and less than 10% variation. The conductance for $T > 400\mathrm{K}$ increases exponentially. This increase can be attributed to thermally activated transport through the substrate as shown by the fit function according to eq. 8.7.

$1\,e^2/h$. The temperature dependence is described by a thermal activation relation [174]

$$G(T) = \frac{e^2}{h}\left(1 + 0.5\exp\left[-\left(\frac{T^*}{T - T_0}\right)^{\frac{1}{2}}\right]\right) \tag{8.5}$$

with $T^* = 111\,\mathrm{K}$ and $T_0 = 14\,\mathrm{K}$. It consists of a temperature independent contribution of $1\,e^2/h$ for the $0+$ channel and the thermally activated contribution of the $0-$ channel. The activation temperature T^* was determined via the following expression [174]

$$T^* = 1.4\,\frac{\pi\hbar v_f}{k_B L}\,. \tag{8.6}$$

which relates T^* to the probe spacing L. Due to the resemblance of eq. 8.6 to 1d variable range hopping (cf. section 2.2.2) a similar transport mechanism was proposed for the sidewall GNRs [174]. It was suggested that transport in the $0-$ channel involves thermally activated longitudinal modes of the GNR.

A completely different behavior is found for the $0+$ channel. The conductance measured at a probe spacing of $1\,\mu\mathrm{m}$ shows no temperature dependence up to about

400 K. $G = 1\,e^2/h$ with less than 10% variation. The sudden increase for $T > 400\,\mathrm{K}$ coincides with an increased conductance measured in between the ribbons. Hence it is reasonable to assume that the SiC substrate becomes conductive. Consequently, the exponential increase can be described by the temperature dependence of the conductance of doped SiC caused by the ionization of donor atoms. The carrier concentration in the SiC can be related to the temperature by the following expression [138]

$$n_{\mathrm{SiC}} = \frac{-1 + \sqrt{1 + 8\frac{N_d}{N_c} e^{\frac{\Delta E_d}{k_B T}}}}{4\frac{N_d}{N_c} e^{\frac{\Delta E_d}{k_B T}}} N_d \tag{8.7}$$

where $N_c = 2(2\pi m_e k_B T/h^2)^{3/2}$ is the effective density of states in the conduction band, $N_d \approx 10^{18}\,\mathrm{cm}^{-3}$ is the donor concentration and $\Delta E_d = 140\,\mathrm{meV}$ is the donor level for nitrogen doping in SiC. The corresponding fit of the conductance reproduces nicely the temperature dependence found in fig. 8.5(b). Hence at temperatures exceeding 400 K transport is no longer dominated by the sidewall ribbons but by the SiC substrate.

8.4 TRANSPORT IN HIGHER SUBBANDS

All transport experiments on the sidewall GNRs so far were done with charge neutral ribbons. Hence only the zeroth subbands contributed to transport. In the following a local gate will be used to tune the charge density away from charge neutrality to access higher subbands. The concept of local gating by using an STM tip is depicted in the SEM image in fig. 8.6(a). Three of the tips were used, one as gate electrode, the other two serve as source and drain. The tip used for gating was intentionally broadened by crashing it repeatedly into the sample surface. After this procedure the tip exhibits a wide contact area which roughly corresponds to its tip apex seen in the SEM image. This is necessary in order to gate a large fraction of the ribbon. A similar procedure was successfully used before to locally gate graphene sheets on Mica [222]. In this case the tip was coated with Al_2O_3 which served as gate oxide. For the measurement presented in the following no gate oxide was used. The gating tip was simply held in a distance of a few nm over the sample surface between the source and drain tip. The source drain distance was $L = 1.3\,\mu\mathrm{m}$ and the sample temperature was kept at about 30 K.

In fig. 8.6(b) the conductance measured between the source and drain tips is plotted against the gate voltage V_g. A single conductance minimum is located at $V_g = 0\,\mathrm{V}$. This clearly reveals that Fermi energy and Dirac point are coinciding and the pristine ribbon is charge neutral. The conductance of $1\,e^2/h$ is nicely reproduced for $|V_g| < 150\,\mathrm{mV}$. The conductance increases with increasing V_g due to the population of higher subbands. The subband population should set in as soon as the Fermi energy reaches $E_{1,0} \approx 52\,\mathrm{meV}$. Therefore the Fermi energy can be related to the gate voltage via $|E_f| = 0.13\,V_g^{1/2}\,\mathrm{eVV}^{-1/2}$. From the slope of $G(V_g)$ the transmission of the subbands $T_{n\geqslant 1}$ is deduced to about 0.045. This yields a mean free path $\lambda_n = 61\,\mathrm{nm}$ according to eq. 2.38. This value correlates nicely with the transport experiments on

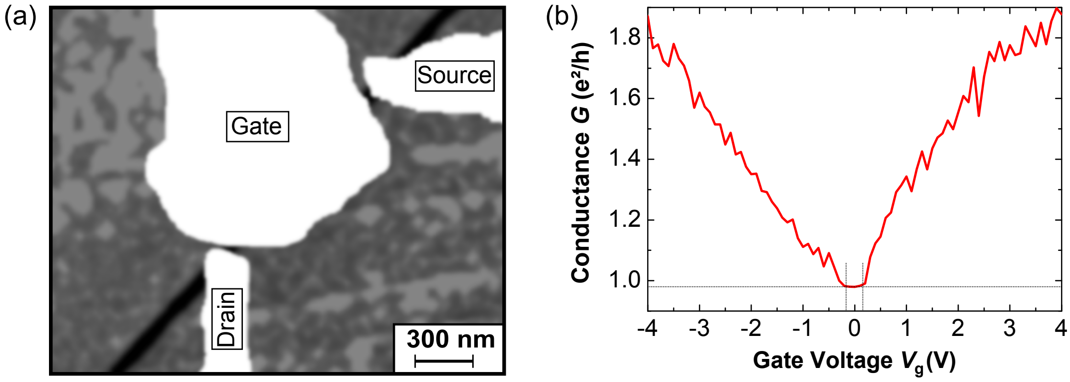

Figure 8.6: Gated transport across a sidewall GNR. The measurement setup is shown in the SEM image in (a). Two tips were used as source and drain current, a larger tip serves as gate electrode. The source and drain tip are in direct contact with the ribbon while the gate tip floats above. The contact resistance between gate tip and GNR was larger than 50 MΩ. (b) Conductance of a sidewall GNR plotted as a function of gate voltage V_g. The minimum conductance $G_{min} = 0.98\,e^2/h$ is found at $V_g = 0\,V$ which corresponds to charge neutrality ($E_f = 0$). For $|V_g| > 150\,mV$ further subbands are opened and the conductance increases.

sidewall ribbons in a fixed geometry [174]. The mean free path of the $n \geqslant 1$ subbands is significantly smaller than those of the zeroth subbands.

8.5 ORIGIN OF SINGLE-CHANNEL BALLISTIC TRANSPORT

The transport experiments reported up to now make clear that there are three contributions to the conductance of a sidewall GNR, the 0−, 0+ channels and the $n \geqslant 1$ subbands. The $n \geqslant 1$ subbands have the smallest mean free path of the three. Nevertheless the observed 60 nm are much larger than the mean free paths typically observed in lithographically patterned exfoliated GNRs [32, 223]. This demonstrates again that the self-assembling growth technique leads to well-ordered edges.

The 0− channel is thermally activated and shows a rather small localization length of about 200 nm. Finally, the most prominent contribution is made by the 0+ channel which yields a conductance of $1\,e^2/h$ regardless of temperature or probe spacing as long as $L \leqslant 17\,\mu m$. The 0+ channel can be attributed to the 0+ subband while the 0− channel is derived from the 0− subband [174]. Their completely different properties indicate a fundamental difference between the two modes such as a broken symmetry. It has to be kept in mind that the upper and lower edges of a sidewall GNR are significantly different in terms of the local bonding and mechanical deformation such as curvature (cf. fig. 7.3). It is hence a reasonable assumption that the properties of the edge states differ.

Nevertheless, the most puzzling question which remains is that of the origin of the single-channel ballistic transport. The mean free path which is extremely long even at room temperature suggests that transport needs to be topologically protected. A Quantum Spin Hall (QSH) phase actually was predicted in graphene [224]. Con-

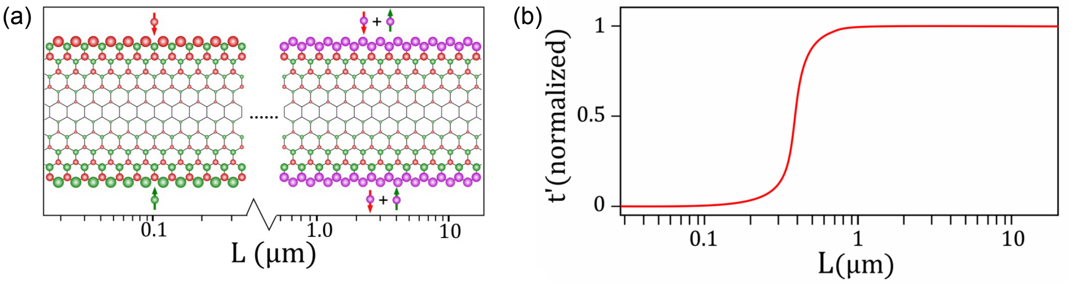

Figure 8.7: (a) Schematic spatial distribution of the edge state wave functions in a zigzag GNR with a finite amount of sp^3 hybridized edge atoms [231]. The charge density of spin-up and spin-down electrons is shown in green and red, the superposition state is shown in purple. (b) Interedge coupling t' versus probe spacing in a zigzag GNR where 80% of the edge atoms exhibit sp^3 orbitals [231].

sequently, graphene can be a topological insulator with spin filtered, gapless edge states in which electronic transport is protected against backscattering by time reversal symmetry [225]. A Quantum Anomalous Hall (QAH) phase was predicted which is also driven by spin-orbit coupling but the edge states lack spin chirality in contrast to the QSH phase [217]. Unfortunately the spin-orbit gap in graphene was predicted to be in the range of 10^{-3} meV to 0.1 meV [226–228] which makes both phases experimentally inaccessible. However, curvature of the graphene layer, which is also present in the lower edge of the sidewall GNR, was reported to enhance the spin-orbit gap [229, 230]. Despite these special Quantum Hall phases, the presence of a perfectly conducting channel (cf. 3.2.3) could also be responsible for the observed long mean free path. Since such a channel requires a zigzag nanoribbon with well ordered edges its presence would underline the quality of the nanostructures produced by the self-assembling growth technique.

However, neither the special Quantum Hall phases nor the perfectly conducting channel would explain the lifting of both spin and valley degeneracy. Interestingly, a very similar behavior was found for carbon nanotubes. They were reported to be ballistic conductors at room temperature [11, 12] with a conductance of $2\,e^2/h$ in contrast to the theoretically predicted $4\,e^2/h$ [11]. Despite the missing explanation for this discrepancy, the similarity to the observed properties of sidewall GNRs is striking. It suggests that the mechanism which lifts both degeneracies is not a unique property of GNRs.

A recent preprint [231] addressed the question of the origin of the transition from double-channel to single-channel transport in the sidewall GNR. It was proposed that the transition is caused by an intrinsic spin orbit coupling in the edges. Impurities were predicted to induce a sp^2 to sp^3 hybridization which consequently results in a large enhancement of spin-orbit coupling [232]. Spin-flip scattering is greatly enhanced which removes the spin degree of freedom for sufficiently long probe spacings as depicted in fig. 8.7(a). Furthermore, the metallic probes contacting the ribbon were proposed to act as a medium for the coupling of the two edges. Therefore the coupling becomes weak for small probe spacing and is enhanced for larger spacings as shown in fig. 8.7(b). Altogether, these two effects should result in a edge state wave function which is a superposition of both spin components.

This model can be used to describe the transition from $2\,e^2/h$ to $1\,e^2/h$ if the coupling parameters are chosen accordingly [231]. Unfortunately, the influence of disorder was not considered in this study which is remarkable since the sp^3 hybridization at the edges was proposed to be caused by impurity adsorption. Naturally, even a small amount of misplaced atoms at the edge would lead to intervalley scattering and consequently localization. The absence of localization on such huge length scales which were reported in this thesis, demands for a transport mechanism which is intrinsically protected against backscattering. Furthermore, the model presented in [231] does not account for the fact the $0-$ channel is thermally activated. Hence it is highly questionable if it is sufficient to describe the observed ballistic transport phenomena.

8.6 CONCLUSIONS

This chapter provided clear evidence that sidewall GNRs are room temperature single-channel ballistic conductors. The ballistic nature of transport was underlined by the equivalence of 2pp and 4pp measurements. This equivalence can be well understood considering fully invasive voltage probes. The invasiveness was further exploited by using invasive probes as individual scattering centers to demonstrate that the description of sidewall GNRs as ballistic conductors is consistent.

The transport behavior was found to be dominated by a channel arising from the zeroth subband of a ferromagnetically coupled zigzag GNR. Extremely large mean free paths were demonstrated by probe spacing dependent measurements. The ballistic channel was found to localize only for ribbon lengths larger than 17 µm. Transport in a second ballistic channel with a much shorter localization length was identified to be thermally activated. Transport within the channels derived from the zeroth subbands was shown to be clearly different from the behavior of higher subbands. The mean free path for transport in higher subbands was demonstrated to be only about 60 nm.

The single-channel ballistic transport is the most striking property of sidewall GNRs. The robustness of the observed transport properties make their potential for nanoelectronic applications indisputable, despite the lack of a conclusive explanation for their origin. It needs to be explored in the future, to what extend the exceptional ballistic properties are an intrinsic property of the graphene layer or if they are also protected by the interaction with the SiC substrate, e.g. by the covalent bonding of the edges.

9

SIDEWALL GRAPHENE NANOCONSTRICTIONS

The previous chapters 7 and 8 have shown that GNRs grown on the sidewalls of SiC mesa structures exhibit exceptional ballistic transport properties such as extremely large mean free paths at room temperature within a single channel. The transport properties of the ribbons were found to be extremely robust. Hence the ribbons are an ideal playground to apply structural alterations in order to modify their electronic properties.

In this chapter, narrow constrictions shall be patterned into the sidewall GNRs. Graphene nanoconstrictions (GNCs) are known to host a variety of highly interesting physical properties and are important building blocks for carbon based electronics [233, 234]. For example, a valley filter was proposed on the basis of a zigzag GNC [235]. By connecting two valley filters in series, an electrostatically controlled valley valve could be obtained. On the experimental side, lithographically patterned nanoconstrictions in graphene on SiO_2 were found to be essentially serial connections of graphene quantum dots [34, 236] due to their rough edges and the formation of charged graphene islands. In transport experiments, this manifests in the observation of Coulomb blockade effects. On the other hand, in analogy with subwavelength optics, GNCs with smooth edges were proposed to serve as electronic diffraction barriers, giving rise to interference phenomena [237]. Due to the diffraction barrier at the graphene constriction interface, transmission resonances occur which originate from localized currents through the GNC [238, 239].

For the interpretation of the transport data of GNCs it is important to be well aware of the transport properties of the graphene system in which the GNCs are subsequently defined. In case of the sidewall GNRs the transport was extensively characterized and the transport characteristics of the constriction can be clearly discriminated from the GNR itself.

9.1 SETUP OF STM LITHOGRAPHY

A key factor for the extraordinary transport characteristics of sidewall GNRs is the self-assembling growth process. By renouncing the use of conventional lithography, the exceptional properties of the edges can be maintained. A careful patterning process is now also needed in order to define GNCs as non-destructive as possible. For this purpose STM lithography is the method of choice. By applying high bias voltages between the STM tip and the graphene sample and simultaneously moving the tip

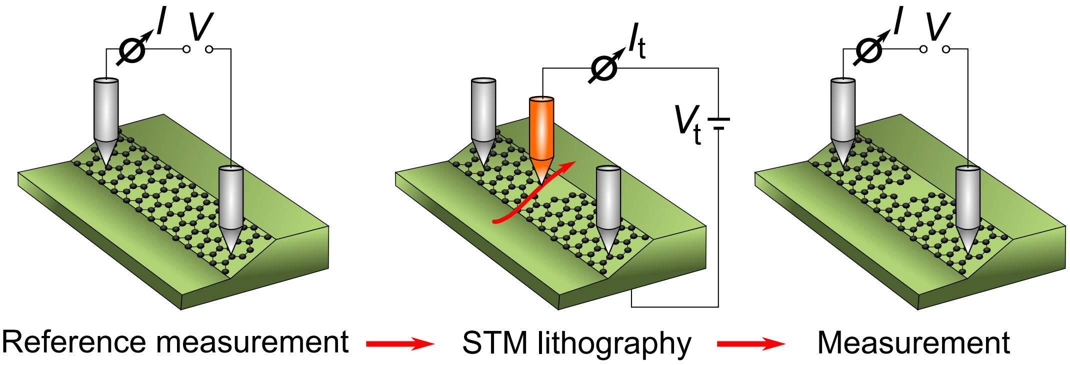

Figure 9.1: Schematic illustration of STM lithography on a sidewall GNR. In the first step, a reference 2pp measurement is carried out to ensure the ballistic nature of the ribbon. For lithography, a third tip which is in tunneling mode is driven transversely over the sidewall, removing atoms from the GNR. The transport properties of the lithographically defined structure are probed again in a 2pp transport configuration.

over the sample surface the graphene can be locally etched away [36]. The underlying etching mechanism is most likely chemical etching assisted by electronic field emission from the STM tip [240] which locally breaks the C-C bonds. STM lithography was demonstrated to be able to define GNRs with atomically precise edges. Consequently, width dependent band gaps consistent with theoretical predictions [36] have been observed. Furthermore, in zigzag GNRs produced by STM lithography, the presence of magnetic order in the edges at room temperature was suggested [37]. This demonstrates that the etching process is very gentle and non-destructive to the edges.

The setup for the STM lithography on the sidewall GNRs is shown in fig. 9.1. In the first step, a reference measurement is made which ensures that the ribbon is ballistic. The contact spacing $L > 2\,\mu m$ was chosen to ensure that only one ballistic channel contributes to electronic transport (cf. section 8.2). In the lithography step, a STM tip is driven transversely over the sidewall to locally etch away the graphene on the sidewall. The tip is moved with a slow speed of about 1 nm/s. The tip was driven only once along the desired etching line, starting always from the trench and moving to the plateau. A subsequent 2pp measurement is performed to deduce the effect of the etching step on the transport characteristics.

9.1.1 IV CHARACTERISTICS OF STRUCTURED SIDEWALL RIBBONS

The IV characteristics obtained after the STM lithography step serve as a first indication for a successful etching process. In fig. 9.2 three IV characteristics are shown. First, the reference measurement on the pristine sidewall GNR exhibits the already well-known linear character with a resistance of h/e^2 indicating single-channel ballistic transport. The shape of the IV curve drastically changes after STM lithography steps with a bias voltage of $V_b = 5\,V$ and tunneling current setpoints of $I_t = 200\,nA$ and $I_t = 50\,nA$. After the lithography step with $I_t = 200\,nA$ the IV becomes flat indi-

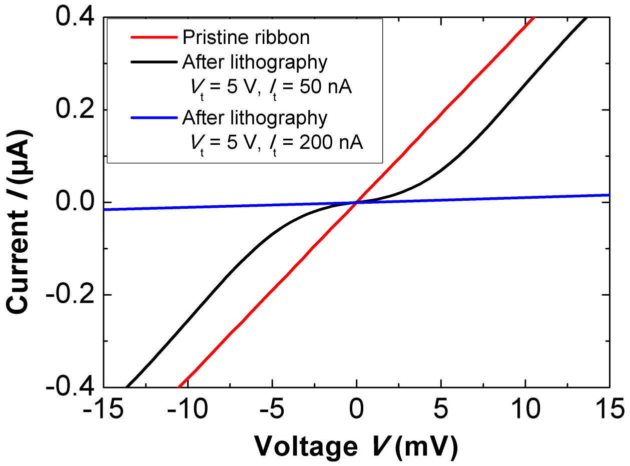

Figure 9.2: IV characteristics of a sidewall GNR before (red) and after STM lithography (black, blue) at $T = 300\,\mathrm{K}$. Depending on the tunneling conditions used during the lithography step, the IV shows either a distinct nonlinearity (black) or an insulating character.

cating a large resistance. From a linear fit near zero bias the resistance was deduced to about $500\,\mathrm{k\Omega}$. This resistance is in the range of the resistance found on the plateau and trench of the mesa in section 7.3. It is hence reasonable to assume that the ribbon was fully cut during the lithography step. In contrast, lowering the tunneling current (which implies increasing the distance between STM tip and sample) to $I_t = 50\,\mathrm{nA}$ results in a nonlinear IV characteristic. The conductance is low but finite around zero bias and increases linearly for higher bias voltages. Hence, by tuning the tunneling current I_t structures with distinct transport properties can be produced. In the following, evidence will be provided that the nonlinear IV curve is indeed characteristic for a GNC.

9.1.2 MORPHOLOGY OF THE CONSTRICTIONS

In order to gain insight into the morphology of the structure with a nonlinear IV characteristic, STM measurements were performed along the etching line. Three STM images of the etching line are shown in fig. 9.3. They were recorded at the lower ribbon edge to the trench shown in (a), in the center of the sidewall shown in (b) and at the upper edge to the plateau displayed in (c). It can be clearly seen that the cut extends completely through the ribbon center and the plateau edge. In contrast, the lower edge to the trench is not fully cut. The cut ends approximately 2 nm before the graphene terminates into the trench. Recording of a complete STM image showing also the transition region from GNR to trench was not possible due to the geometry of the sidewall ribbon (cf. fig. 7.3). Also atomic resolution of the edges of the cut was not possible because relatively large bias voltages had to be used in order to achieve stable tunneling conditions. Nevertheless it becomes clear that the STM lithography resulted in the formation of a GNC with a width of more than 2 nm and a length of

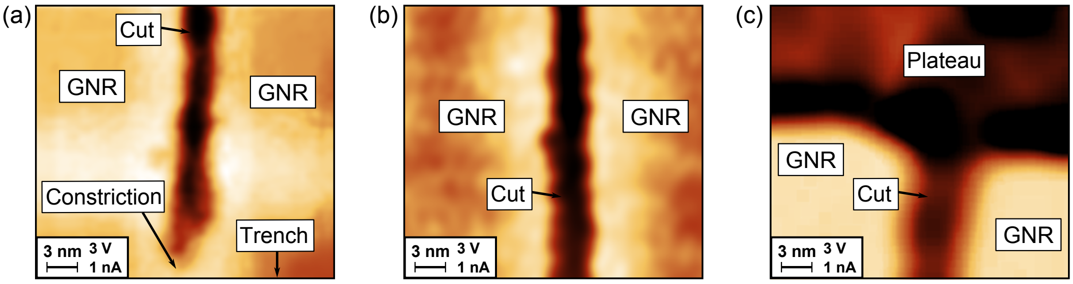

Figure 9.3: STM images of the sidewall ribbon after the STM lithography. (a) At the lower ribbon edge to the trench a small graphene constriction is formed due to an incomplete cutting of the ribbon. (b) The middle part is fully cut as well as (c) the upper edge to the plateau.

$5-6\,\text{nm}$. The width cannot be determined more precisely because STM imaging of the lower sidewall ribbon edge is hard to accomplish due to the large bending of the ribbon. The nonlinear IV characteristic observed in the previous section for precisely this structure can hence be attributed to electronic transport through a GNC.

The IV characteristic of the GNC were recorded for different probe spacings L between $2\,\mu\text{m}$ and $10\,\mu\text{m}$. The shape of the IV curve was found to be independent of the probe spacing as expected. For the following measurements the probe spacing is kept fixed at $L = 3\,\mu\text{m}$.

9.2 TEMPERATURE DEPENDENT TRANSPORT

The IV characteristics obtained during the patterning process at room temperature, already highlight a large modification of the transport characteristics upon formation of a GNC. Now, the temperature dependence shall be evaluated.

9.2.1 KAISER EXPRESSION

The Kaiser expression [241] can be used to describe the nonlinear IV characteristics of the GNCs phenomenologically. It is a generic expression frequently used to describe nonlinear voltage characteristics of carbon nanotubes or nanofibres. It can be expressed as [241]

$$\frac{I}{V} = \frac{G_0 \exp(\frac{V}{V_0})}{1 + \frac{G_0}{G_h}(\exp(\frac{V}{V_0}) - 1)} \tag{9.1}$$

where G_0 denotes the conductance for $V \to 0\,\text{V}$, G_h is the saturation voltage at large bias and V_0 is a voltage scale factor. The good agreement of this expression with the IV data from GNCs is obvious from fig. 9.4(a). The description with this generic function allows to easily determine the differential conductance by simple derivation of the fit function. Fig. 9.4(b) shows the resulting differential conductance. Additionally the differential conductance values extracted from the raw data IV curves by numeri-

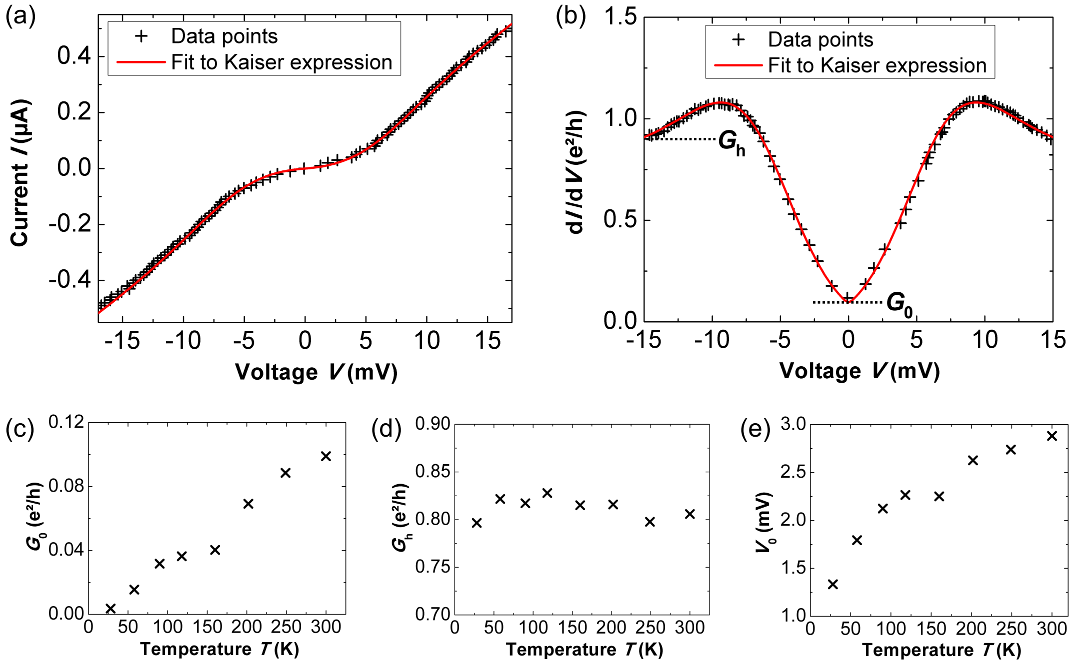

Figure 9.4: (a) IV curve of a sidewall constriction fitted with the Kaiser expression from eq. 9.1. Details can be found in the main text. (b) Corresponding differential conductance versus bias voltage gained from derivation of the fit function shown in (a) (red line) and by numerical derivation of the raw data IV curves (black data points). A good agreement with the fit function is reached. For the numerical derivation 60 IV curves were derived and averaged. (c-e) Temperature dependence of the fit parameters G_0, G_h and V_0 used in the Kaiser expression.

cal derivation are shown as data points. To reduce the noise level after the numerical derivation the derivatives of 60 IV curves were averaged. This results in a very good agreement of the differential conductances obtained by both methods and highlights the accuracy of the fit.

The parameters, used for fitting the individual IV curves to the Kaiser expression, are plotted against temperature in fig. 9.4(c-e). The zero bias conductance G_0 increases with increasing temperature as well as the voltage scale factor V_0. The high bias conductance G_h of about $0.8\,e^2/h$ is almost constant throughout the whole temperature range.

9.2.2 IV CHARACTERISTICS AND DIFFERENTIAL CONDUCTANCE

After the generic description of the measured IV curves in the previous section a detailed look at the temperature dependent IV and differential conductance curves is in the focus of this section. The fits according to eq. 9.1 of the IV characteristics for eight different temperatures between 28 K and 300 K are plotted in fig. 9.5(a). Two key observations can be made form the IV curves. First, for low temperatures a small transport gap opens around zero bias. Consequently the zero bias conductance

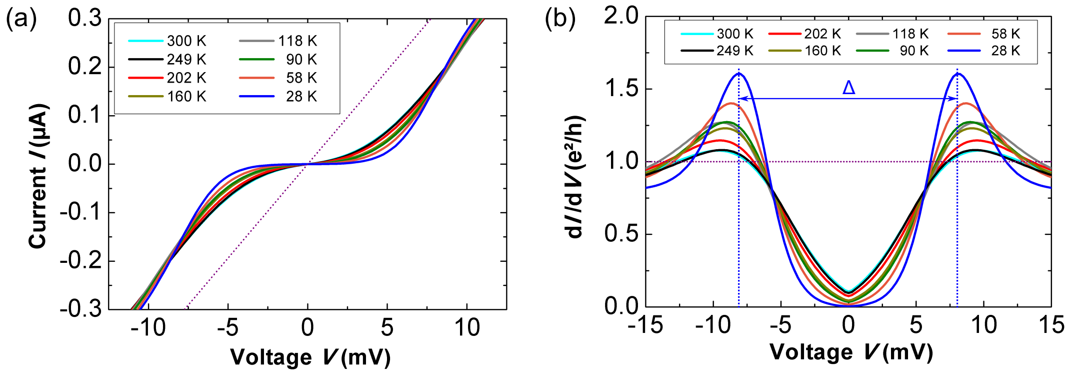

Figure 9.5: (a) IV curves of a sidewall constriction for different temperatures. The IV of the pristine sidewall GNR is shown for comparison as dotted purple line. (b) Corresponding differential conductance versus bias voltage from the IV curves in (a). With increasing temperature the zero bias conductance increases and the resonances features around $V = \pm 8.5\,\mathrm{mV}$ decrease. The conductance of the pristine ribbon $1\,e^2/h$ is marked by the dotted purple line. The separation of the resonance features Δ is indicated for the curve at $T = 28\,\mathrm{K}$.

approaches zero at low T which can also be seen from the plot of the zero bias conductance in fig. 9.4(c). Furthermore, at larger bias voltages the slope of all IV curves seems to approach a value close to the original slope of the pristine ribbon. This is an indication that the former ballistic channel is still present. The conductance value at high bias can be determined from fig. 9.4(d) to about $0.8\,e^2/h$. Hence it is lowered compared to the pristine ribbon by $0.2\,e^2/h$ indicating a lowered transmission of the ballistic channel. Interestingly the ballistic channel is suppressed close to zero bias.

The features of the IV curves can be identified even more clearly in the differential conductance plot shown in fig. 9.5(b). Both the occurrence of a gap-like feature Δ as well as the recovery of a conductance close to $0.8\,e^2/h$ at high bias voltages is clearly visible. Furthermore, the dI/dV shows pronounced conductance peaks at the edges of the energy gap around $8-9\,\mathrm{mV}$. The conductance overshoot is most prominent at low temperatures and slowly washed out with increasing T.

9.3 COHERENT TRANSPORT IN SIDEWALL CONSTRICTIONS

In order to find the origin of the gap feature Δ as well as the transmission overshoot their properties shall be further quantified. In fig. 9.6(a) the temperature dependence of the FWHM of the overshoot peaks and the gap size Δ are shown. With increasing temperature the resonances broaden and the FWHM increases almost linearly. The FWHM of the resonance features are extremely small. For $T > 160\,\mathrm{K}$ they are even below $k_B T$ which is clearly irrational. However, extracting the FWHM from the dI/dV might be error prone since a complete theoretical description of the differential conductance curve is missing. Furthermore, the temperature dependent measurements were performed during a warm up of the sample from liquid He cooling. Hence, the error in the temperature measurement is rather large. Concerning the size of the gap

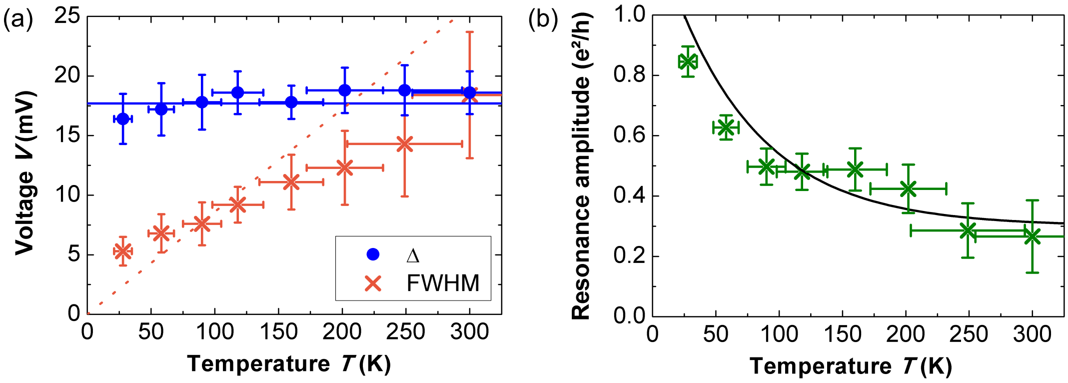

Figure 9.6: (a) Gap size Δ and FWHM of the transmission resonances with respect to the sample temperature. The mean value $\Delta = 17.7\,\mathrm{meV}$ (blue line) as well as k_BT (orange dotted line) are indicated. (b) Height of the resonance peak plotted against the temperature. The fit shows the exponential character of the decrease.

feature (and hence the position of the conductance peaks), it is found to be almost independent of temperature, showing only a slight increase with increasing temperature. The amplitude of the overshoot peak is decreasing with increasing temperature in an exponential manner as shown in fig. 9.6(b).

9.3.1 CONDUCTANCE OVERSHOOTS

The most intriguing features of the the differential conductance of the sidewall constrictions are the conductance peaks coinciding with the opening of a transport gap. The origin for both the peak and the gap is not immanently clear. Electronic confinement could open a band gap within the constriction. However, the band gap expected for an only $2-3\,\mathrm{nm}$ wide constriction is in the order of several $100\,\mathrm{meV}$ and hence much larger than the observed one. Transport gaps are well reported in disordered graphene nanoconstrictions and nanoribbons [34, 242, 243] and have been proposed to arise from Coulomb blockade [244] or Anderson localization caused by edge disorder [245, 246]. However, neither the steep logarithmic increase of current [32, 247] nor the temperature dependence [32] expected for these transport gaps fits the data of the sidewall constrictions. Furthermore, also the origin of the conductance overshoot cannot be explained by these models.

Gap features and especially conductance overshoots similar to the ones observed here, have been reported for bilayer graphene samples at low temperatures in a comparable energy range [248–251]. A large number of possible phases have been discussed in this regard, e.g. quantum spin hall insulators of layer ferromagnets [252]. However, extensive magneto transport investigations were necessary in order to identify the possible phases [249]. Since such measurements are beyond the available measurement capabilities during this thesis it cannot be claimed that such a phase is also responsible for the gap opening in graphene nanoconstrictions.

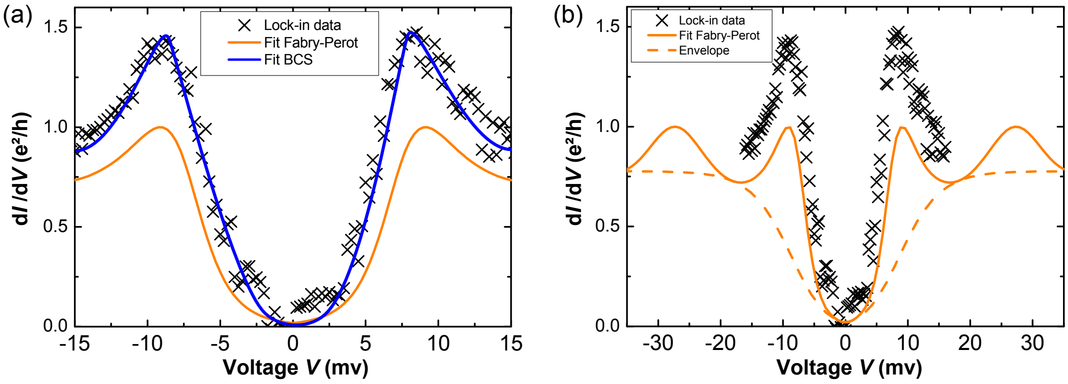

Figure 9.7: (a) Differential conductance versus bias voltage of a sidewall constriction measured with low-frequency lock-in technique at $T = 40\,K$. The orange line shows the Fabry-Perot oscillations expected according to eq. 9.3. A fit considering a BCS-like conductance (cf. eq. 9.2) is given by the blue line. (b) Fit of Fabry-Perot oscillations shown in (a) for a larger bias window. The orange dotted line presents the envelope function of the conductance minima (cf. eq. 9.4).

In [251] the conductance peaks observed in bilayer graphene were referred to as BCS-like. A similar observation can be made in the case of the sidewall GNCs. The differential conductance can be fitted with a BCS-like density of states [253, 254]

$$\frac{dI}{dV}(V) \sim \int -\frac{\partial f(E-eV)}{\partial E}\,\mathrm{Re}\left(\frac{E-i\Gamma_d}{\sqrt{(E-i\Gamma_d)^2-(\frac{\Delta_{BCS}}{2})^2}}\right)dE \tag{9.2}$$

where Δ_{BCS} denotes the BCS gap, Γ_d is the Dyne's smoothing parameter and $f(E)$ is the Fermi distribution. The first term is the standard thermal broadening function. With $\Delta_{BCS} = 17\,meV$ and $\Gamma_d = 1\,meV$ this expression describes the differential conductance quite accurately as obvious from fig. 9.7(a). Of course, this does not imply that the sidewall constrictions are superconducting. Neither the temperature dependence of the transport gap (cf. fig. 9.6(a)) nor any other performed measurement indicate a superconducting state. Nevertheless, the observed similarity of the differential conductance to a BCS-like one is indeed striking. It suggests that the underlying transport mechanism through both, sidewall ribbons and constrictions is not yet fully understood.

9.3.2 ELECTRONIC DIFFRACTION

A further option for the origin of the conductance peaks at the gap edges shall be considered in the following. Transmission resonances, which arise from localized currents through the constriction [239] are known to occur at abrupt graphene interfaces due to electronic diffraction [237, 238]. In analogy to subwavelength optics, the system can be viewed as a Fabry-Perot cavity where the transmission is described by the Airy function [237]

$$T_{FP}(E) = \frac{1}{1 + F(E)\sin^2\left(\frac{\Theta(E)}{2}\right)} \tag{9.3}$$

where the finesse $F(E) = 4R(E)/(1 - R(E))^2$ with the reflection coefficient $R(E) = 1 - T(E)$ and the phase difference $\Theta(E) = 2k(E)L + 2\widetilde{\Theta}(E)$ with $\widetilde{\Theta}$ being the phase factor acquired at each reflection. The Airy function shows a maximum when $\Theta/2$ is an integer multiple of π. The envelope function of the minima is given by [237]

$$T_{FP}^{min}(E) = \frac{1}{1 + F(E)} \; . \tag{9.4}$$

A fit according to eq. 9.3 of the differential conductance of a sidewall constriction measured at $T = 40\,K$ by using lock-in technique is shown in fig. 9.7(a). The overall shape of the curve, the gap feature and the conductance peaks are well reproduced. Only the first Fabry-Perot resonance is visible due to the limited bias window (cf. fig. 9.7(b)). However, this model cannot explain the observation of conductance overshoots with $G > 1\,e^2/h$.

9.3.3 GREEN'S FUNCTION APPROACH

So far, the differential conductance of the sidewall constriction was described using phenomenological models. For a more detailed analysis, the bias dependence of the transmission function of the constriction was modeled by using a standard tight-binding recursive Green's function approach. The calculations were done in collaboration with the DTU Nanotech, Center of Nanostructured Graphene. The simulated system is shown in fig. 9.8(a). The width of the ribbon was chosen to be 10 nm, a factor of 4 smaller than the experimentally realized system. Furthermore, also the length L and the width W were reduced. This smaller geometry enhanced the calculation time significantly, and it can be used to qualitatively verify the presence of transmission resonances. In fig. 9.8(b, c) the transmission coefficients are plotted for two combinations of L and W. Multiple resonance peaks are clearly visible. With increasing width more resonances occur. This can be rationalized by the standard particle-in-a-box picture. The corresponding differential conductance for the two geometries at different temperatures is shown in fig. 9.8(d, e). The resonance peaks get washed out at high temperatures which is in line with the experimental findings. The ballistic $1\,e^2/h$ channel is not included in the calculations because its origin is unknown at the moment (cf. section 8.5).

It is reasonable to assume that the STM lithography step introduces defects along the cutting edges. Hence it shall be investigated in the following if the transmission resonances found in the simulation of a clean constriction also survive in the presence of disorder. Two different types of disorder shall be considered, the buckling and reordering of atoms around the cutting edge and the presence of Anderson disorder. The first one is introduced by changing every hopping energy around the cutting

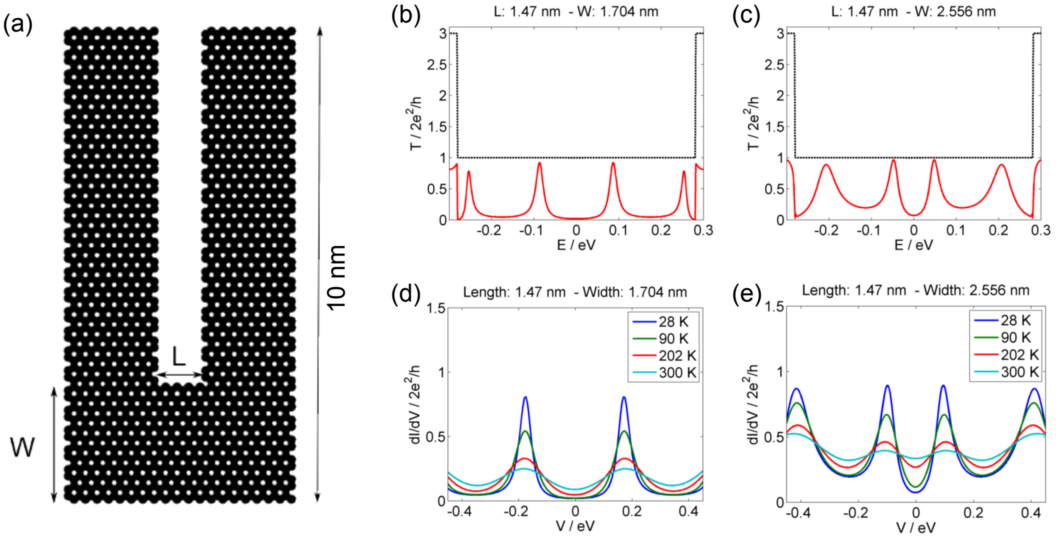

Figure 9.8: (a) Model of the simulated graphene nanoconstriction. The length L and the width W of the constriction are indicated. The right and left side are connected to ideal infinite leads. Transmission coefficient through geometries with (b) $L = 1.47\,\text{nm}$, $W = 1.70\,\text{nm}$ and (c) $L = 1.47\,\text{nm}$, $W = 2.56\,\text{nm}$. The transmission through the pristine ribbon is indicated by the black dotted line. (d, e) Differential conductance versus bias voltage obtained from the transmission coefficients of the geometries shown in (b) and (c) for different temperatures.

edge from t_h to $t_h \pm \delta t_h$ where δt_h is chosen randomly between $[-0.1\,t_h, 0.1\,t_h]$. The result is shown for 25 different configurations together with their average in fig. 9.9(a). Obviously the effect of this kind of disorder is small and only slight changes in the peak position can be detected. For the Anderson type disorder the onsite energy is chosen randomly between $[-0.1\,t_h, 0.1\,t_h]$. Hence randomness of the cutting edge of the constriction is modeled. The result is plotted in fig. 9.9(b) and shows that the transmission peaks are still visible but their spread in energetic position becomes larger compared to the hopping disorder. Nevertheless, the transmission resonance is still clearly visible in the average curve.

Altogether localized currents within the constriction might be able to explain the resonance features. For quantification, the simulation of the larger, experimentally realized geometry is needed. Hence, the width of the hosting GNR was increased to 38 nm and the width and length of the constriction to $L = 5-7\,\text{nm}$ and $W = 2-3\,\text{nm}$. Furthermore, a third-nearest neighbor model was applied to account more realistically for propagating edge states in the zigzag nanoribbon. The hopping integrals were chosen to be $t_h = -2.97\,\text{eV}$, $t'_h = -0.073\,\text{eV}$ and $t''_h = -0.33\,\text{eV}$.

The results of the calculation are displayed in fig. 9.10(a). Only the energetically lowest transmission resonance on the positive bias side is considered. By changing the width and length of the constriction slightly within the range of $W = 2.5-3.0\,\text{nm}$ and $L = 6.1-7.3\,\text{nm}$ the energetic position of the resonance can be shifted. Both, increasing the length and width, shifts the resonance to lower energies. The energy of the resonance position varies between 4 meV and 24 meV. Hence, it is in good agree-

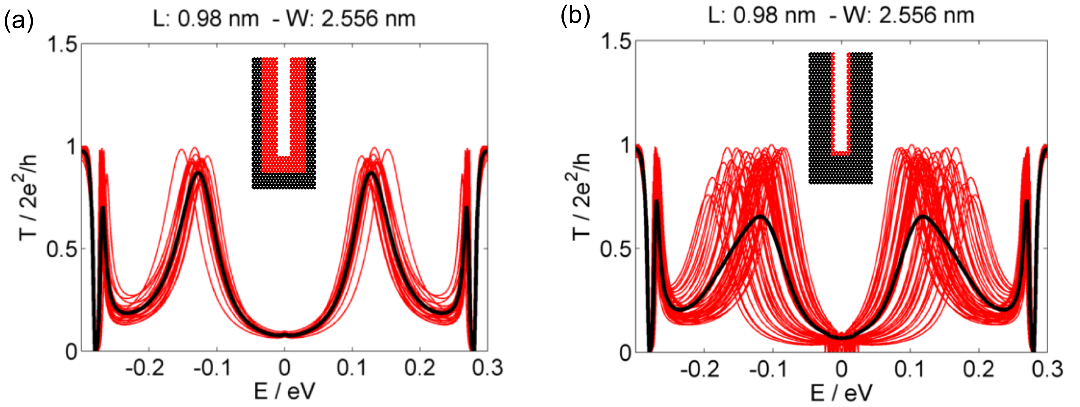

Figure 9.9: Effect of disorder on the transmission function through a graphene nanoconstriction. (a) Buckling and reordering of edge atoms and (b) Anderson type disorder are considered. The transmission curves are shown for (a) 25 different and (b) 50 different configurations and their average is indicated in black. The insets depict the area for which disorder is included.

ment with the resonance energies observed in experiment. Furthermore, the influence of the width of the ribbon which hosts the constriction was considered. In fig. 9.10(b) the first transmission resonance is shown for GNRs of 21 nm, 30 nm and 38 nm in width. The resonance peak sharpens when the ribbon is widened. The position of the resonance remains almost unchanged. Only a slight shift to lower energies with increasing width can be detected. Hence, the width of the hosting ribbon has only little influence on the transmission properties through the constriction.

These calculations support the picture of transmission resonances caused by electronic diffraction at the constriction interface. The transmission resonances are robust against disorder. The temperature dependence as well as the energetic location of the resonance features are in reasonable agreement with the experiment. Altering the size of the constriction would be an effective way in order to verify this further due to

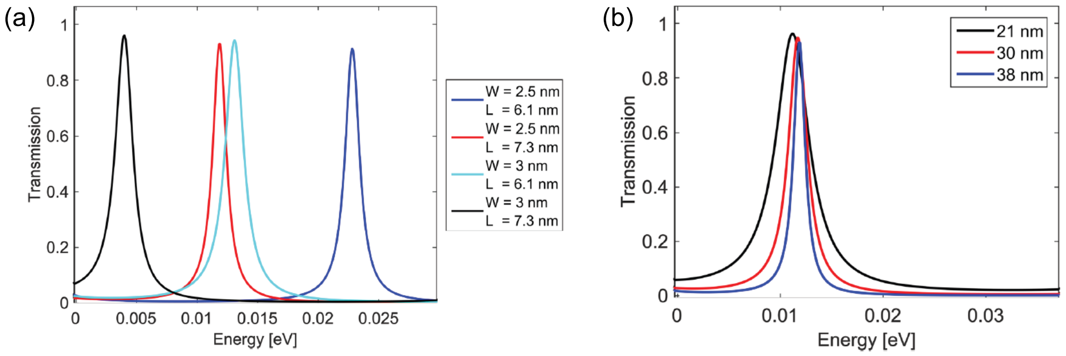

Figure 9.10: First transmission resonance in a third-nearest neighbor model for different (a) constriction geometries and (b) widths of the hosting ribbon.

the strong dependence of the resonance energy on the geometry of the constriction. These experiments, however, could not be completed during the work on this thesis.

9.4 CONCLUSIONS

It can be concluded from this chapter that the transport properties of sidewall graphene nanoribbons can be effectively altered by structural modifications. It was demonstrated that STM lithography can be used to create graphene nanoconstrictions in-situ with dimensions of only a few nm. The multi-tip STM provides access to their transport properties directly after the lithography process. The constrictions were shown to exhibit distinct transport features separating them from the pristine ribbons. Transport gaps of a few meV were accompanied by conductance overshoot peaks. The differential conductance can be reproduced by treating the constriction boundaries as electronic diffraction barriers. Corresponding tight-binding simulations yield a qualitative agreement with the experimental findings.

Part IV

EPITAXIAL GRAPHENE P-N JUNCTIONS

10

CHEMICAL GATING OF EPITAXIAL GRAPHENE

For the realization of graphene based electronic devices control over the chemical potential is of great interest. Especially p-n junctions are an essential building block in this sense. Tuning of the chemical potential in graphene can be obtained via various pathways. Most commonly used is the method of gating by an electric field [18, 75]. The implementation of two electrostatic gates allows to control the charge type locally and to create p-n junctions with tunable polarity [25, 26, 255–257]. Furthermore, tuning of the charge carrier density is possible by doping via adsorbates [258–260]. An elegant technique is the intercalation of foreign elements, meaning their interdiffusion between the carbon layer and the substrate. Intercalation works on epitaxial graphene on metals [261, 262] and SiC [47] with various elements such as Au [46] or Li [263]. One of the most famous examples is the hydrogen intercalation of the buffer layer on Si-face SiC to transform it into quasi-freestanding graphene [45].

For the realization of local p-n junctions the intercalation of the buffer layer with Ge [264] is highly interesting due to the ambipolar doping profile of the resulting freestanding graphene layers. The coexistence of n-type and p-type doped phases was shown in an extensive low energy electron microscopy (LEEM) and ARPES study [265]. In this chapter the intercalation of Ge and the formation of n-type and p-type doping shall be monitored by SEM, STM, local spectroscopy and transport in order to gain insight into the local electronic properties. The results of this chapter are published in [266].

10.1 GERMANIUM INTERCALATION OF THE BUFFER LAYER

A general scheme of Ge intercalation is shown in fig. 10.1. The buffer layer was grown in a rf furnace in an Ar environment at 1670 K. For the intercalation itself, first several ML Ge are deposited on the sample at room temperature in UHV. The Ge forms non-wetting islands on the surface [264]. Subsequent annealing results in the formation of Ge layers which can diffuse under the carbon layer. The amount of intercalated Ge depends on the annealing temperature and time. By diffusing under the buffer layer, the Ge breaks its covalent bonds to the substrate and therefore decouples the buffer layer from the SiC. The intercalation of Ge was suggested to proceed by local rupture of the buffer layer domains [265] opening up possible diffusion paths. The mobility of carbon atoms is high enough that the layer heals completely afterwards. Intercalation underneath the buffer layer was found to be favored compared to ML

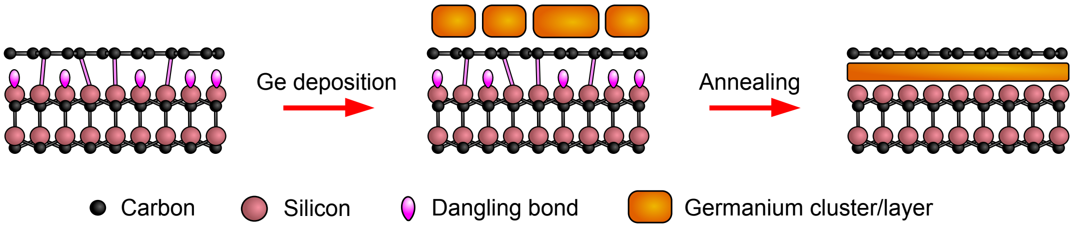

Figure 10.1: Schematic illustration of the intercalation of the buffer layer with Ge. First, several monolayers of Ge are deposited on the surface. Upon annealing the Ge intercalates and decouples the buffer layer from the substrate.

graphene [265]. This was attributed to the large amount of sp^3 coordinated atoms in the buffer layer which are more responsive to chemical reactions.

By using XPS it was quantified that the n-type phase is created by the intercalation of 1 ML Ge and the p-type phase by intercalation of 2 ML Ge [265]. Therefore, it is possible to create fully p-type or n-type doped graphene layers as well as an intermediate phase with coexisting n-type and p-type patches. It should be noted that DFT calculations were able to reproduce the detachment of the buffer layer as well as the n-type doping but so far failed to reproduce the p-type phase [267]. The experimentally observed hole doping was suggested to be defect induced [268].

All experiments presented in the following were performed on a sample with coexisting n-type and p-type phases achieved by annealing the sample to 1090 K after Ge deposition. A corresponding ARPES is shown in fig. 10.2(a). Two Dirac cones are clearly visible with the Dirac points located at $E_{d,n} = -310\,\text{meV}$ and $E_{d,p} = 290\,\text{meV}$ with respect to the Fermi level. Hence the coexistence of an n-type and a p-type doped graphene phase can be clearly seen. The LEED pattern in fig. 10.2(b) exhibits only the first order SiC as well as first order graphene spots. No spots belonging to superstructures are present. This implies that the initial $(6\sqrt{3} \times 6\sqrt{3})R30°$ reconstruction of the buffer layer has completely vanished and no other long-range reconstruction is induced. This is in contrast to other intercalates such as Au [46, 269].

10.2 STRUCTURAL AND ELECTRONIC CHARACTERIZATION

In the previous chapters 5-9 the characterization of the electronic properties of graphene sheets and nanostructures by STM, SEM, STS and 4pp measurements has been demonstrated. The Ge intercalated samples shall be investigated in the same manner in this section. The morphology will be characterized by STM and SEM while the local doping level will be deduced from STS. Finally, 4pp measurements will provide information about the transport characteristics of n-type and p-type areas.

10.2.1 SAMPLE MORPHOLOGY

In order to perform STS as well as transport experiments at specific p-type or n-type areas it is essential to be able to identify both phases in the SEM. Fig. 10.3 presents an

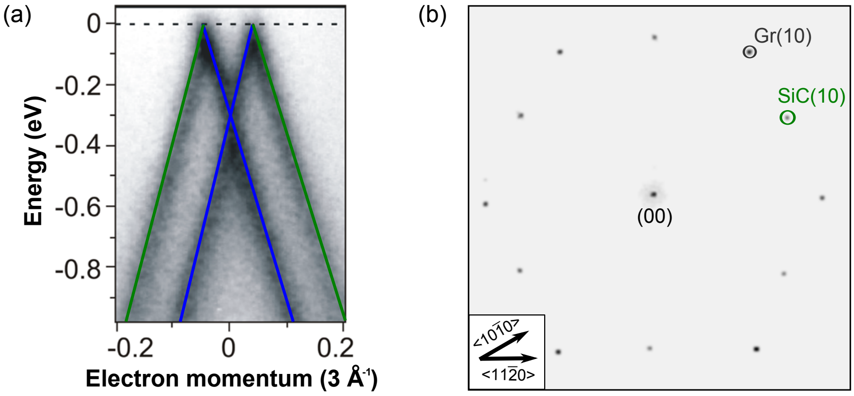

Figure 10.2: (a) ARPES on a Ge intercalated graphene ML. Dirac cones of p-type (marked in green) and n-type (marked in blue) doped graphene can be clearly identified. The energetic position of the Dirac point is deduced to 290 meV for p-type doping and −310 meV for the n-type. (b) LEED pattern of a Ge intercalated graphene ML at 137 eV beam energy showing a SiC(1 × 1) and Gr(1 × 1). The SiC(10) spot is marked by the green and the Gr(10) by the gray circle.

overview SEM image of a Ge intercalated sample which showed an n-type as well as a p-type Dirac cone in ARPES. The sample surface exhibits three contrast levels (light, medium and dark gray). The light gray areas can be immediately identified as residual non-intercalated buffer layer by STS (not shown here). Hence only the other two contrast levels are of further interest. The close-up SEM image and a corresponding STM image shown in fig. 10.3(b, c) were recorded at the very same sample position and reveal two contrast levels. The spatial contrast distributions are remarkably well correlated. This is further supported by the linescans in fig. 10.3(d). Medium gray areas in the SEM image are shown to be elevated by about 2 Å compared to the dark gray areas. The height difference is close to the nearest neighbor distance in a Ge lattice of 2.45 Å. Hence, the height difference supports the picture of a difference of one intercalated Ge layer between the p-type and n-type phase. Consequently, this indicates that the regions with high SEM intensity correspond to p-type graphene and with low intensity to n-type. The enhanced SEM intensity of the p-type regions can be understood by the higher atomic number of Ge compared to carbon since the secondary electron yield is generally higher for a high atomic number Z and also depends on the quantity of the high Z material [270].

It should be noted that even in regions which show only one contrast level on large scale SEM images, small nm sized islands of other contrast can be found in higher resolved images. This indicates that no large areas consisting of purely n-type or p-type graphene can be synthesized. A minority fraction of patches with the other doping type is always present. Similar observations were made by means of LEEM [265].

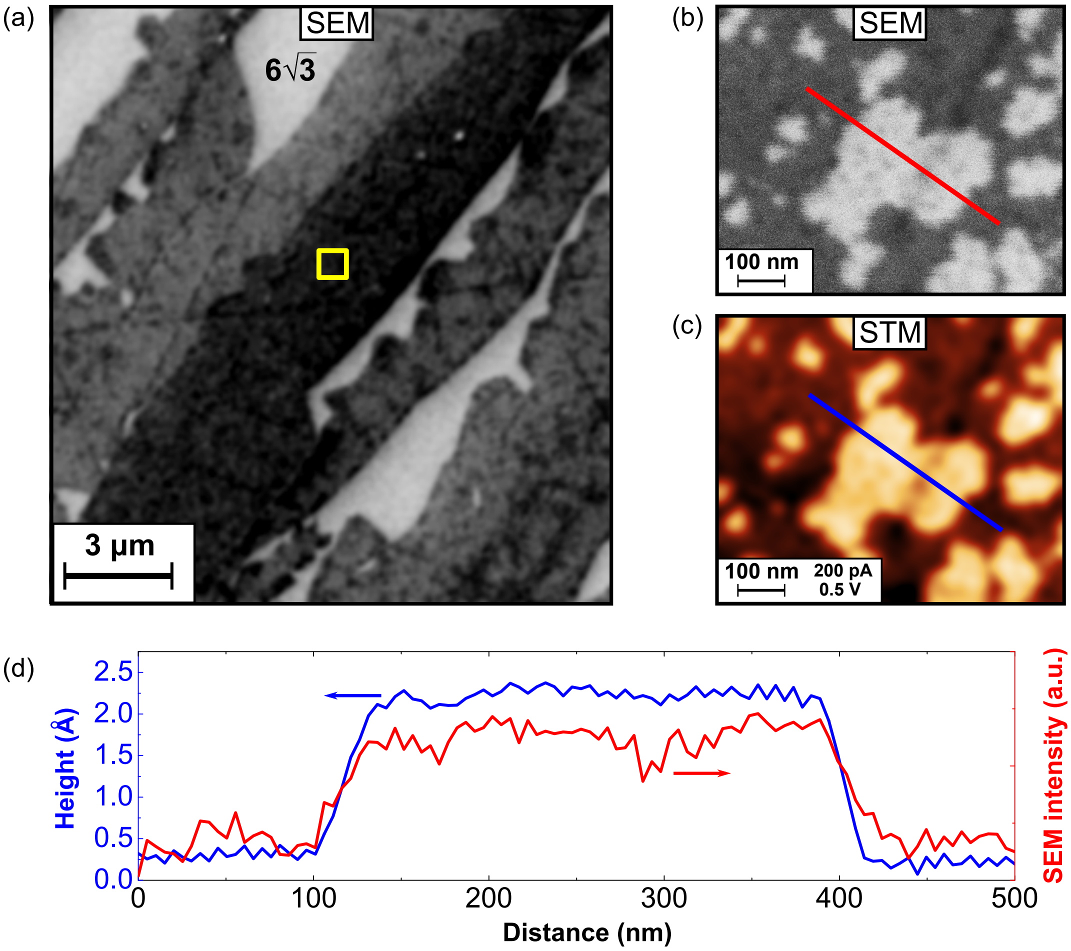

Figure 10.3: (a) SEM image of a Ge intercalated sample showing three contrast levels (light, medium and dark gray). The light gray areas can be identified as residual buffer layer. (b) Close-up SEM image of the position marked in (a). The two contrast levels correspond to medium and dark gray in (a). (c) STM image of the area in (b). (d) Linescans along the directions indicated in (b) and (c) showing nicely the correlation between STM and SEM contrast.

10.2.2 CORRELATION OF TOPOGRAPHY AND TUNNELING SPECTROSCOPY

To further support the assignment of n-type and p-type graphene to regions showing lower or higher SEM intensity, STS measurements were performed. In fig. 10.4(a, b) the SEM images from fig. 10.3(a, b) are shown in color-code. Corresponding tunneling dI_t/dV spectra are presented in fig. 10.4(c,d). They are characteristic for doped epitaxial graphene (cf. section 6.1). The dip associated with the energetic location of the Dirac point can be clearly identified in both spectra. Hence, the areas of medium SEM intensity are p-type graphene with $E_{d,p} = 296\,\text{meV}$ and the areas with low SEM intensity are n-type graphene with $E_{d,p} = -333\,\text{meV}$. Three conclusions can be drawn from this observation. First, the Ge intercalation process transforms the buffer layer into graphene. No indication for a band gap was found in the spectra ruling out

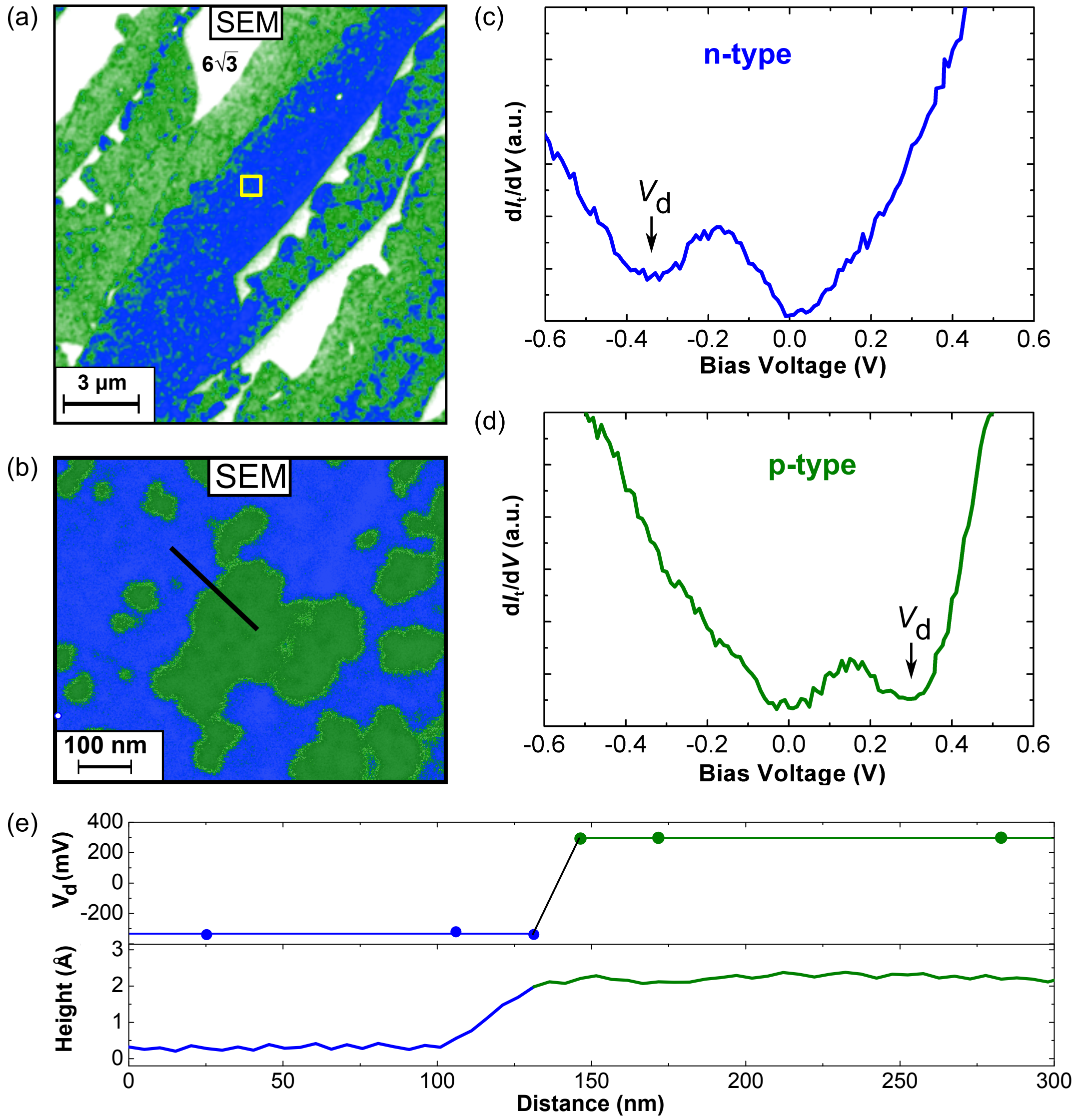

Figure 10.4: (a, b) Color-coded SEM image from fig. 10.3(a, b). The corresponding tunneling spectra taken on the green and blue area are shown in (c, d). The blue (dark gray) areas are n-type doped with the Dirac point at a bias voltage $V_d = -333$ mV and the green (medium gray) areas are p-type doped with $V_d = 296$ mV. (e) Profile of topographic height and bias voltage of the Dirac point along the line marked in (b). The transition from n-type to p-type doping coincides with an increase in height of about 2 Å.

the presence of buffer layer. Secondly, the n-type and p-type doping correlates nicely with the values deduced from the ARPES spectrum in fig. 10.2(a). Therefore, the global chemical potentials can also be found locally. Furthermore, the assignment of p-type and n-type doped graphene to areas with high and low SEM intensity made in the previous section is indeed correct. Hence it is possible to identify the two doping levels directly in the SEM. The height difference of about 2 Å between the n-type and

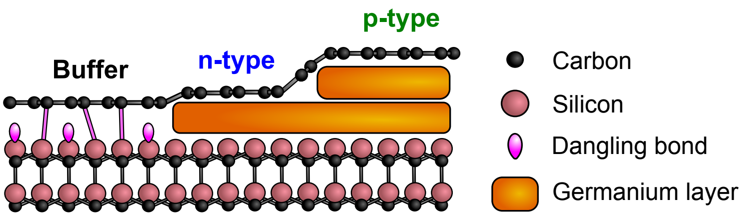

Figure 10.5: Schematic illustration of the epitaxial graphene sample after Ge intercalation. Three different phases (buffer layer, n-type graphene, p-type graphene) are present depending on the amount of Ge underneath the carbon layer.

p-type phase indicates the presence of an additional Ge layer underneath the p-type phase as schematically shown in fig. 10.5.

The carrier concentrations $p = 6.1 \times 10^{12}\,\mathrm{cm}^{-2}$ and $n = 8.4 \times 10^{12}\,\mathrm{cm}^{-2}$ of the p-type and n-type areas are quite similar, resulting in very symmetric p-n junctions at the interface. The evolution of the chemical potential across such a p-n junction is shown in fig. 10.4(e) in comparison to a STM linescan. The chemical potentials were deduced from dI_t/dV spectra taken at different lateral positions across the junction. The structural transition seen by the STM occurs on a length scale of about 30 nm which is by a factor of three larger compared to the electronic transition. The transition to p-type coincides with the edge of the upper terrace. Thus, it can be concluded that 2 complete Ge layers are needed in order to shift the doping level to p-type. It was not possible to resolve the electronic transition with a better resolution. Especially, no intermediate doping levels were found.

From the experiments made so far it is not clear to what extend the intercalated Ge layers modify the interface between SiC substrate and the graphene layer. Concerning possible inelastic contributions to the tunneling spectrum, which were found for example in ML epitaxial graphene (cf. section 5.2.1), the analysis of the d^2I_t/dV^2

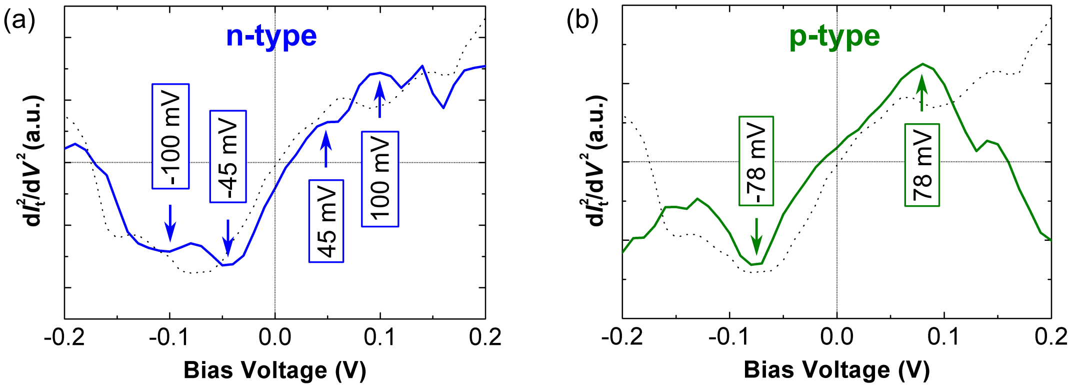

Figure 10.6: $\frac{d^2I_t}{dV^2}$ spectra of the (a) n-type and (b) p-type doped areas of a Ge intercalated graphene ML. The arrows indicate features assigned to phonon contributions. The $\frac{d^2I_t}{dV^2}$ spectrum of non-intercalated ML graphene is shown as black dotted line.

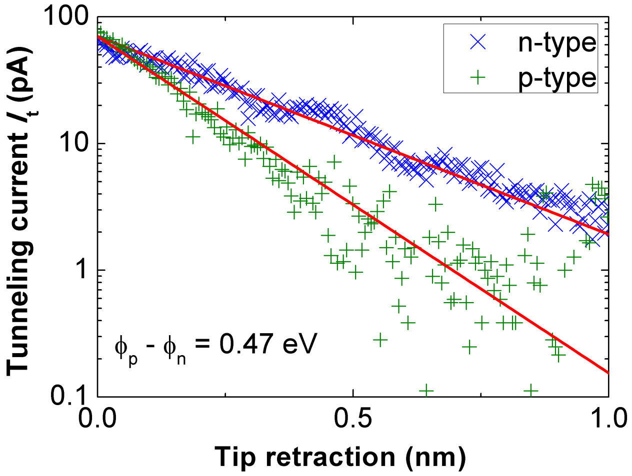

Figure 10.7: Tunneling current with respect to tip retraction on n-type and p-type doped graphene areas. A difference in local work function of 0.47 eV can be deduced from the fits.

spectra is necessary. They are shown for both n-type and p-type areas in fig. 10.6. Interestingly, both spectra do not exhibit any of the phonon related features at 70 meV and 140 meV found for the non-intercalated epitaxial graphene ML. For the n-type phase, two features at 45 meV and 100 meV can be identified while for the p-type phase only one feature at 78 meV is present. None of these features can be assigned to any known phononic excitation in epitaxial graphene. Hence their physical origin remains unclear. Nonetheless, this finding demonstrates that the Ge layers intercalated in between the SiC substrate and the buffer layer severely alter the interface properties.

Information about the local work function of the n-type and p-type graphene can be gained by a local measurement of the tunneling current with respect to the tip sample distance as described in section A.1.2. The STM tip is slowly retracted while recording the decay of the tunneling current. Corresponding measurements on the n-type and p-type phase are shown in fig. 10.7. They exhibit the expected exponential behavior. Since no reference sample was used in order to determine the work function of the tip, only the local work function difference between the n-type and p-type phase can be obtained but not their absolute values. A work function difference of $\Phi_p - \Phi_n = 470$ meV was deduced from the fits. This value is in reasonable agreement with the difference in doping found with ARPES and STS as well as the work function difference found in photoemission experiments [266].

10.2.3 TRANSPORT PROPERTIES OF GE INTERCALATED GRAPHENE

After the morphological and electronic characterization of the p-type and n-type phase created by Ge intercalation, this section focuses on their transport properties. The measurements are done in a similar manner as those on the non-intercalated epitaxial graphene ML presented in section 5.2.2. As mentioned before in section

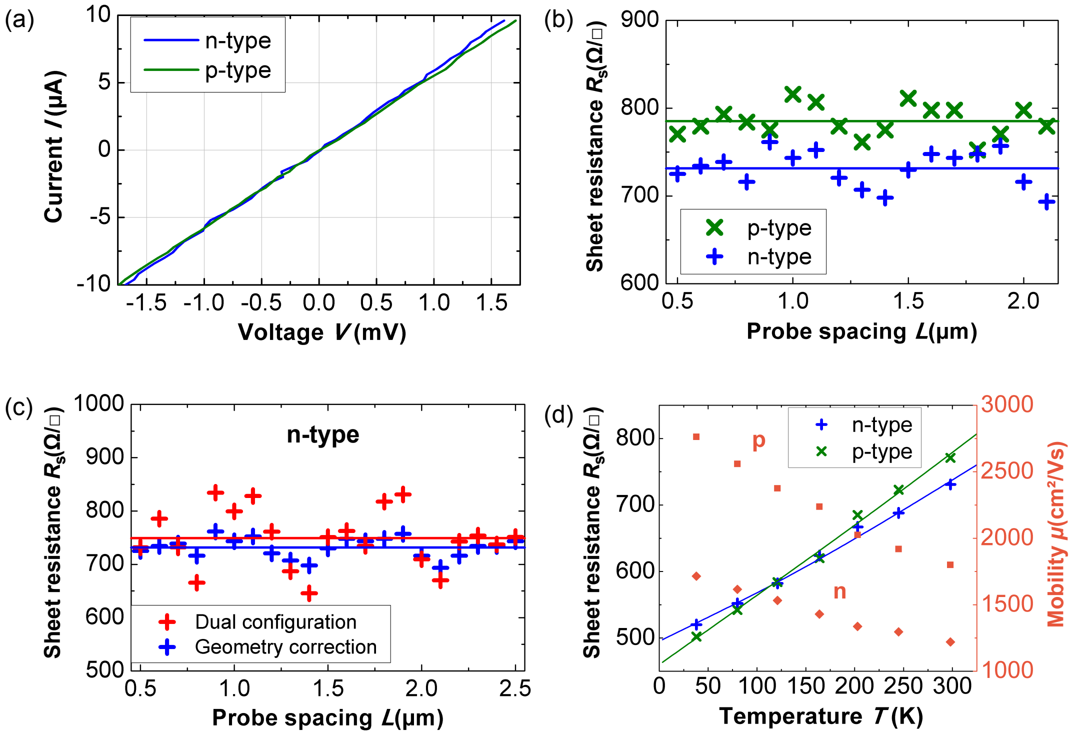

Figure 10.8: Local 4pp transport measurements on Ge intercalated n-type and p-type doped graphene. (a) IV curves show a linear characteristic. (b) Sheet resistance as a function of probe spacing at $T = 300\,\mathrm{K}$. The mean values are indicated. The sheet resistances are calculated from the resistance values by applying the geometrical correction factor for an infinite 2d sheet. (c) Comparison of sheet resistance of the n-type doped area deduced from dual configuration and by applying the geometrical correction factor for an infinite 2d sheet. The mean values agree within 3%. (d) Temperature dependence of the sheet resistance and mobility of n-type and p-type graphene for a fixed probe spacing $L = 1\,\mu\mathrm{m}$. Details about the fit are given in the main text.

10.2.1 large areas with either pure n-type or p-type doping could not be found. A small contribution of the other doping type is always present. Therefore, areas with a minimum amount of this minority contribution were used for the transport experiments. The regions will be referred to as n-type or p-type for simplicity reasons but it should be kept in mind that they always host small islands of minority doping type. The lateral size of the majority regions is in the order of several μm (cf. fig. 10.3(a)).

A multi-tip STM is used to perform local 4pp measurements. All measurements are performed with linear arrangement of the probes. The shape of the IV curve on both n-type and p-type areas is always linear indicating the expected metallic behavior (cf. 10.8(a)). Probe spacing dependent resistance measurements were performed in order to probe the dimensionality of the electronic transport. As evident from fig. 10.8(b) the resistance is not dependent on the probe spacing for both n-type and p-type graphene. This indicates 2d transport in both phases. The sheet resistance of the p-type domain $R_{s,p} = (785 \pm 17)\,\Omega/\square$ is slightly higher compared to the n-type $R_{s,n} = (730 \pm 55)\,\Omega/\square$.

The sheet resistances were deduced by multiplying the measured resistance with the geometrical correction factor for a semi-infinite 2d sheet $\pi/\ln(2)$. Given the finite dimensions of the n-type and p-type domains it is necessary to justify this procedure especially for large probe spacings. For this purpose, fig. 10.8(c) shows the comparison of the sheet resistance obtained by geometrical correction with the sheet resistance obtained by the dual configuration method (cf. 2.1.2). Both values agree within 3% justifying the assumption of an infinite 2d sheet. The resistances ratio of the two resistances measured in dual configuration $R_A/R_B = 1.28$, which is very close to the value expected for an ideal continuous 2d sheet, $R_A/R_B = \ln(4)/\ln(3) \approx 1.26$.

The lower sheet resistance of the n-type region cannot be explained by the difference in charge carrier concentration because the mobility of the p-type region ($\mu_p = 1800\,\mathrm{cm}^2/\mathrm{Vs}$) is higher by about 30% than the mobility of the n-type graphene ($\mu_n = 1220\,\mathrm{cm}^2/\mathrm{Vs}$) at room temperature. Mobilities were calculated directly from the measured sheet resistances using the carrier concentrations found by ARPES and STS. The difference in mobility between n-type and p-type graphene is even enhanced at low temperatures and reaches almost 40% at $T = 38\,\mathrm{K}$ as shown in fig. 10.8(d). The maximum mobility is achieved by the p-type area at $T = 38\,\mathrm{K}$ with $\mu_p = 2760\,\mathrm{cm}^2/\mathrm{Vs}$ ($\mu_n = 1710\,\mathrm{cm}^2/\mathrm{Vs}$). The mobilities indicate that the p-type region is less defective. Hence, it can be ruled out that the p-type doping is induced by defects formed during the annealing process as recently suggested by theory [268]. Furthermore, the contribution of parasitic current paths through the intercalated Ge layer seems also rather unlikely since the mobility of the p-type area, where a larger amount of Ge is intercalated, is higher compared to the n-type domain. The mobilities of both phases are higher than those found for an almost defect free epitaxial graphene ML in section 5.2.2. This finding provides evidence that the defect density of the graphene sheet is not enhanced by the intercalation process in contrast to other doping techniques such as substitutional doping [271]. Furthermore, the enhanced mobilities reflect the free-standing character of the Ge intercalated graphene layer.

The temperature dependence of the sheet resistance is also plotted in fig. 10.8(d). The sheet resistances of both n-type and p-type domains are decreasing with decreasing temperature. A minimum value of $R_{s,p} = 500\,\Omega/\square$ is reached by the p-type phase ($R_{s,n} = 520\,\Omega/\square$). The temperature dependence can be described in a similar manner as in the case of an epitaxial graphene ML (cf. section 5.2.2) where the sheet resistance was modeled by assuming three contributions, a residual resistivity at low temperatures, a resistivity due to acoustic phonon scattering and an activated contribution from low-energy phonon modes. The low-energy phonon modes are chosen to match the features seen in the d^2I_t/V^2 spectra (cf. fig. 10.6) at 45 meV and 100 meV for the n-type and at 78 meV for the p-type region. These values yield a remarkably good fit of the experimental data. The electron-phonon coupling is reduced compared to epitaxial ML graphene with an underlying buffer layer. This is reasonable since the low energy phonon modes have been shown to couple to electrons via defects in the buffer layer or the SiC substrate [138, 141]. A reduced electron-phonon coupling strength has also been observed in QFSMLG obtained by hydrogen intercalation [137]. Thus, the reduced coupling strength reflects the decoupling of the graphene layer from the underlying substrate.

It should be noted that due to the rather small coupling constants also other phonon energies such as the ones found in epitaxial ML graphene (at 18 meV and 70 meV) still yield reasonable fits. Hence it cannot be ruled out that these phonons might be still present although they do not show up in the d^2I_t/V^2 spectra. Nevertheless, it is clear that phonon scattering is the major process that causes the temperature dependence of the resistance also in the case of Ge intercalated graphene.

Interestingly, the presence of n-type islands within the p-type regions and vice versa does not seem to influence the transport properties significantly in strong contrast to inhomogeneities of comparable size found in ML epitaxial graphene (cf. section 6.2.2). As long as a percolated path of the majority doping is present, the islands of minority doping do not have a significant effect. This finding makes a transport experiment across a single isolated p-n junction highly desirable. Unfortunately, such a measurement is not possible on the sample structure presented in this chapter due to two reasons. First, the n-p transitions coinciding with a structural transition of about 2 Å in height as seen in fig. 10.4 are only present at the interface of the n-type or p-type islands embedded in larger areas of the respective counterpart doping. Since the islands have a maximum lateral size of a few 100 nm it is very challenging to perform a local 4pp measurement. This leaves only the interface between the larger areas of majority p-type or n-type doping whose transport properties were investigated in this section. Unfortunately, the large p-type and n-type areas are typically located on individual terraces of the SiC substrate as obvious from the SEM image in fig. 10.3(a). This finding is also supported by LEEM results [265]. Hence, the electronic p- to n-type transition coincides with a structural transition over the substrate. Since substrate steps are known to be a source for electronic scattering and to cause resistance enhancements (cf. section 6.3) these structures are no ideal templates to study the transport characteristic of a single p-n junction. The p-n junctions which exhibit only the structural transition caused by the additional Ge layer seem much more suitable for this purpose. In order to make them accessible for 4pp transport, structural modifications of the sample are needed. This approach will be discussed in detail in chapter 11.

10.3 CONCLUSIONS

In this chapter, it was demonstrated that the n-type and p-type doping in Ge intercalated graphene can be unambiguously proven by scanning tunneling spectroscopy. An almost symmetric n-type and p-type doping was found in remarkable agreement with ARPES results. The discrimination of p-type and n-type graphene was shown to be possible directly by means of SEM. This allows for a very fast identification of different doping sites. The electronic transition from p-type to n-type doping was shown to coincide with a structural height difference of about 2 Å indicating the presence of an additional Ge layer underneath the p-type phase. The transport properties of both phases were found to be comparable to epitaxial ML graphene. Hence, the intercalation process does not significantly influence the defect concentration of the graphene layer. Unintentionally created p-n junctions were found to be embedded in larger p-type or n-type graphene patches. However, their influence on the transport properties was not significant. Overall, the decoupling of the buffer layer by the intercalation of Ge was shown to be suitable in order to create p-n junctions without electronic gating. However, in order to extract the transport properties of individual junctions, nanostructuring is unavoidable to contact a single isolated junction.

11

KLEIN TUNNELING IN CHEMICALLY GATED GRAPHENE RIBBONS

After having established the possibility to create narrow graphene p-n junctions by Ge intercalation in chapter 10, now the transport properties of such junctions shall be studied. The inhomogeneous development of these junctions was identified as a major obstacle. Spatially restricted p-n junctions will be demonstrated to overcome this problem providing access to the transport properties of single isolated p-n junctions as well as n-p-n or p-n-p structures. Transport signatures of Klein tunneling will be identified. Most of the results presented in this chapter are published in [272].

11.1 SYNTHESIS OF ISOLATED P-N JUNCTIONS

In order to make a single p-n junction accessible for transport experiments it is necessary to restrict the current paths in a way that the current is directed fully through the junction and parasitic current paths through the surrounding are suppressed. The schematic illustration in fig. 11.1 shows a suitable process. Compared to the intercalation scheme used in the previous chapter it differs by an additional patterning step. The buffer layer is structured into $0.5 - 1\ \mu\text{m}$ wide ribbons by UV lithography and

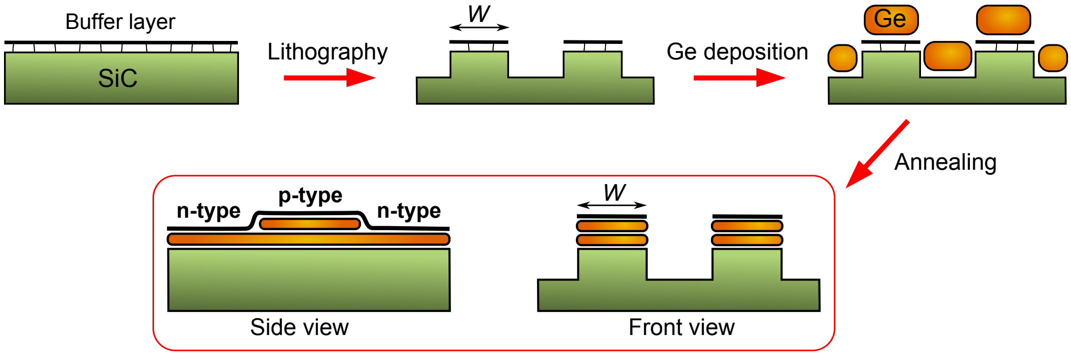

Figure 11.1: Schematic illustration of the synthesis of ambipolar doped graphene ribbons. First, an array of buffer layer ribbons is defined by UV lithography and RIE. After deposition of several ML Ge and subsequent annealing, the Ge intercalation transforms the buffer layer ribbons into intercalated ML graphene ribbons. Different amounts of Ge underneath the graphene give rise to local n-type and p-type doping.

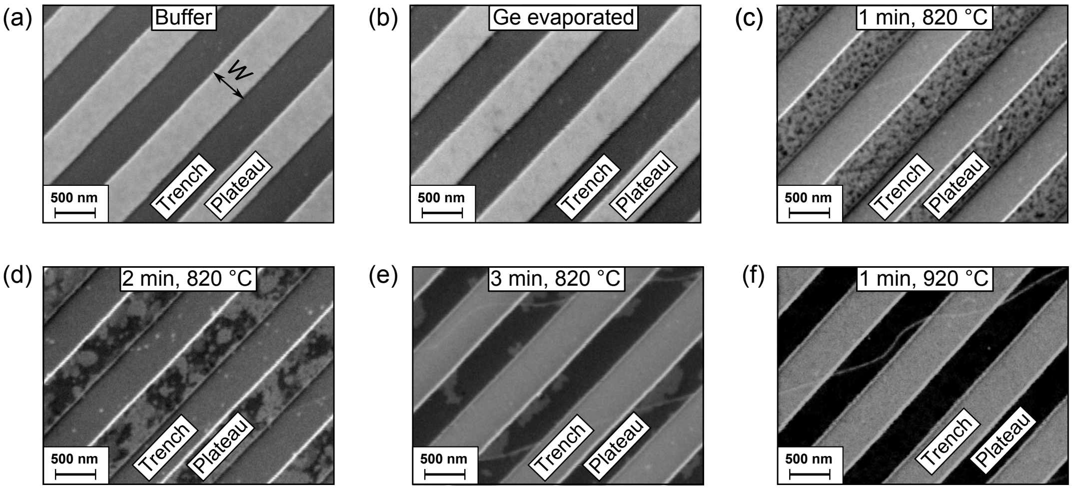

Figure 11.2: SEM investigation of the Ge intercalation of buffer layer ribbons. The pristine buffer layer ribbons with a width of $W = 500\,\mathrm{nm}$ are shown in (a). (b) Buffer layer ribbons after the deposition of several ML Ge. The contrast levels remain unchanged. The intercalation is induced by UHV annealing of the sample at $T = 820\,°\mathrm{C}$. Corresponding SEM images for annealing times of (c) 1 min, (d) 2 min and (e) 3 min reveal nicely the coexistence of n-type (dark gray) and p-type (medium gray) graphene. With increasing annealing time more p-type doped graphene is transfered into n-type graphene. (f) An annealing step at $T = 920\,°\mathrm{C}$ removes the p-type phase leaving the ribbons completely n-type doped.

RIE (cf. sections A.6). Subsequently, several ML Ge were deposited and the sample was annealed. The intercalation of 1 or 2 layers of Ge will lead to the formation of n-type or p-type graphene islands.

11.1.1 STRUCTURAL CHARACTERIZATION

In section 10.2.2 it was shown that p-type and n-type doping leads to characteristic contrast levels in the SEM. Hence, it is a suitable method to monitor the intercalation process. In fig. 11.2 a series of SEM images shows all steps during intercalation. The mesa structure pattern written into the buffer layer is visible in fig. 11.2(a). The buffer layer ribbons are located on top of the plateaus of the mesa structure and appear bright in the SEM image. The SEM image does not change substantially after the evaporation of several ML Ge as obvious from fig. 11.2(b). The plateaus of the mesa appear still bright compared to the trenches. No substructure is visible which indicates a homogeneous Ge film. Upon annealing to 820 °C the appearance of the mesa plateaus changes drastically (cf. fig. 11.2(c-e)). The temperature is the same which was previously used in chapter 10 to synthesize coexisting p-type and n-type phases. Similarly, two phases develop on the mesa plateaus indicating the successful intercalation of the buffer layer and the creation of p-type and n-type doped graphene islands. The low SEM intensity was previously identified to be characteristic for the n-type phase. Consequently, with increasing annealing time the amount of p-type

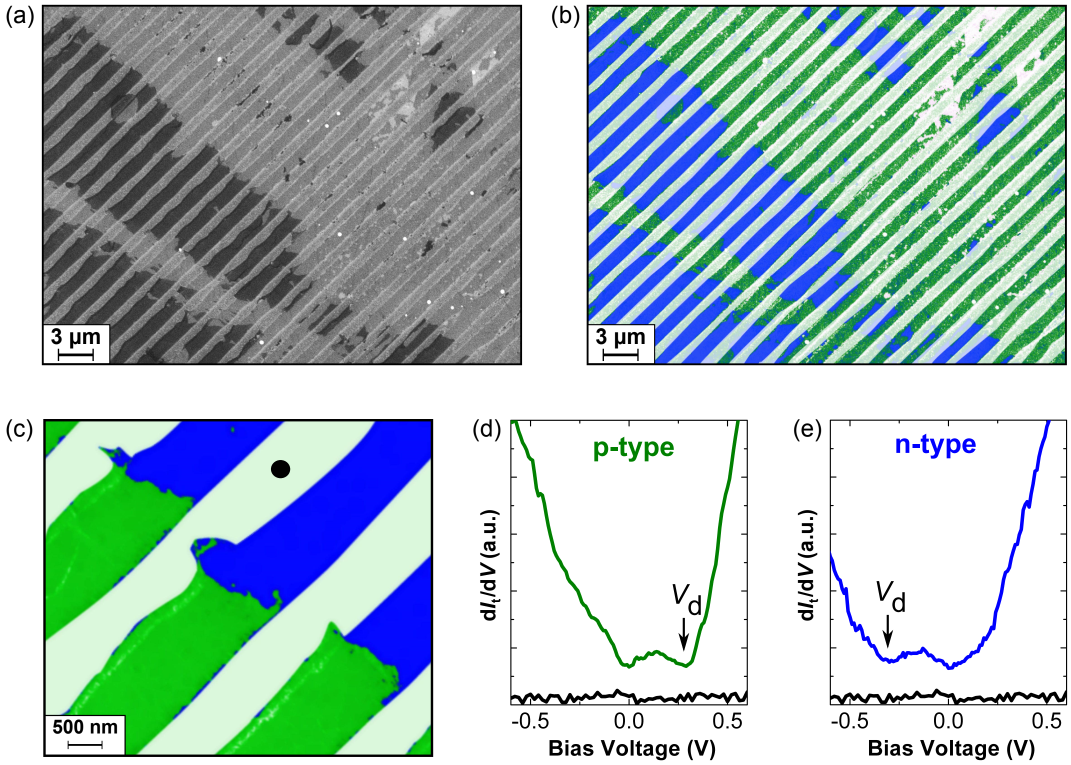

Figure 11.3: Large scale SEM images of Ge intercalated graphene ribbons in (a) gray scale and (b) as color-coded image. Dark gray/blue areas correspond to n-type graphene, medium gray/green areas to p-type. (c) Close-up color-coded SEM image showing the substrate in between the graphene ribbons (white), n-type (blue) and p-type (green) graphene. In the tunneling spectra in (d) and (e) the Dirac point is found at a bias voltage $V_d = -312\,\text{mV}$ for n-type and $V_d = 274\,\text{mV}$ for p-type graphene. A tunneling spectrum from the mesa trenches is shown for comparison (black).

graphene is decreasing and the size of the n-type islands is increasing. This is a reasonable observation since Ge is evaporated from underneath the carbon layer with increasing annealing time and a larger amount of Ge is needed to create a p-type phase. An annealing step at 920 °C completely removes the p-type phase and homogeneous n-type graphene ribbons are created. Consequently the SEM image in fig. 11.2(f) exhibits only dark contrast on the plateaus. By heating to even higher temperatures all Ge can be desorbed converting the sample back into the initial buffer layer state.

11.1.2 SPECTROSCOPIC CHARACTERIZATION

Control over the annealing time and temperature offers the possibility to manipulate the lateral size of p-type an n-type islands. This will be exploited in the following to create p-n junctions which fully extend over the whole width of a 1 µm wide ribbon structures. An example SEM image for such a structure is presented in fig. 11.3(a).

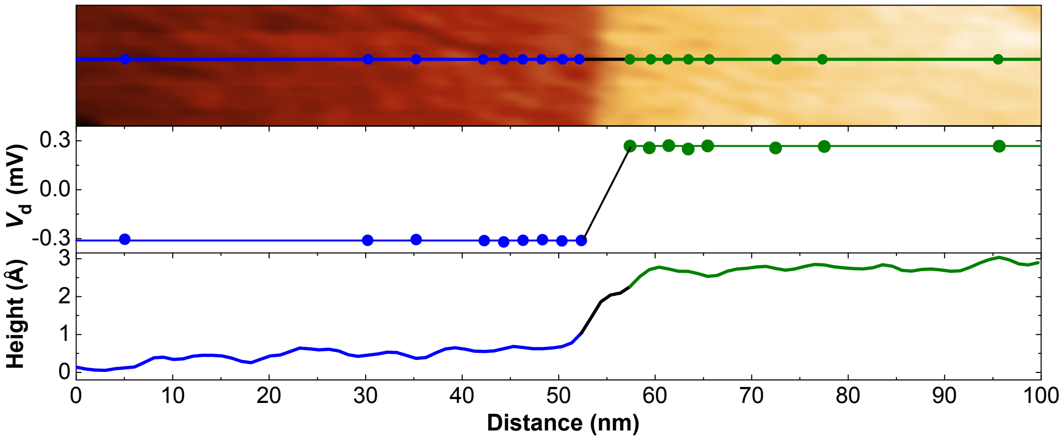

Figure 11.4: STM image of a graphene p-n junction with corresponding profile of the topographic height and of the bias voltage at which the Dirac point was found in tunneling spectroscopy. The profiles are taken along the line and at the positions marked in the STM image. The transition from n-type to p-type doping coincides with an increase in height of about 2.4 Å. The doping level varies less than 10%.

Based on the knowledge gained in chapter 10 the image can be color coded as shown in fig. 11.3(b). Here, the SiC substrate is marked in white, n-type graphene in blue and p-type graphene in green. It becomes clear immediately that isolated p-n junctions have evolved and p-n-p as well as n-p-n structures are present on the sample. To make sure that the assignment of the individual areas is correct, local spectroscopy was performed. In fig. 11.3(c) a close-up SEM image shows a sample area where all three phases are present. The corresponding tunneling spectra are plotted in fig. 11.3(d) for the nominally p-type area and in fig. 11.3(e) for the nominally n-type area. Obviously, the assignment is indeed correct. The characteristic double dip structure of doped epitaxial graphene is clearly visible and the spectra are consistent with the ones measured on the unpatterned Ge intercalated samples (cf. section 10.2.2).

The shift of the Dirac point is almost symmetric. For the p-type phase the Dirac point is located at $E_{d,p} = 274\,\text{meV}$ and for the n-type phase $E_{d,p} = -312\,\text{meV}$. Both phases exhibit almost the same doping levels which were previously found for the unstructured samples in section 10.2.2. Hence, it can be concluded that the restriction to µm wide ribbons has no influence on the intercalation process. A spectrum from in between the ribbons in the mesa trenches is shown for comparison in fig. 11.3(d, e). A band gap larger than 1 eV can be identified. Hence, the ambipolar ribbons are fully isolated from adjacent ribbons.

For the analysis of the transport data of graphene p-n junctions it is important to find two main parameters, the junction length t_{np} and the potential height V_0 (cf. section 3.1.3). Both parameters can be easily extracted using a combination of STM and STS in the same manner as for the unstructured samples (cf. fig. 10.4). In fig. 11.4 an STM image across a p-n junction is shown in correspondence with a linescan of the topographic height and the chemical potential at certain points along the linescan. The STM linescan reveals that the p-type phase is elevated by about 2.4 Å compared to the n-type phase. This is consistent with the picture of an additional Ge layer present underneath the p-type phase as already discussed in section 10.2.2. However, the height difference between n-type and p-type phases is larger by about 0.4 Å compared to the height difference found for p-n junctions on unpatterned samples (2 Å) in section 10.2.2. The reason for this discrepancy is not clear at the moment and needs to be investigated in more detail. The chemical potential is extremely constant in both phases. It is even completely unaffected by the corrugations seen in the STM image. The potential height can be accurately determined to $V_0 = V_{d,p} + |V_{d,n}| = (580 \pm 6)\,\text{meV}$. The junction length $2t_{np}$ is below 5 nm. The structural transition observed in the STM linescan occurs on a larger scale of about 10 nm. Hence the electronic transition is even sharper than the structural one. In total, the narrow length results in very high potential slopes $F \approx 1.2 \times 10^6\,\text{V/cm}$.

To elucidate the exceptionality of the p-n junctions created by Ge intercalation they shall be shortly compared to similar structures reported in literature. Usually, p-n interfaces are created by electrostatic gating [25, 26, 255–257]. The use of a combination of a top gate and a back gate allows to control E_f and V_0 independently [82]. Typically, junction lengths are reported to be in the order of $2t_{np} = 80\,\text{nm}$ [257]. Sophisticated gate structures such as "Air-Bridge" top gates [25] can be used to reduce the junction length further down to $2t_{np} = 40\,\text{nm}$. Since the junction length is in these cases comparable to the electronic mean free path $\lambda_e \approx 100\,\text{nm}$ diffusive scattering within the junction needs to be taken into account. Consequently, rather low carrier densities are mandatory in order to achieve charge carrier wavelengths which exceed the lateral size of the junctions. Typically, the junctions created by gating can be classified as smooth junctions with $k_f t_{np} \gg 1$. Further progress can be made by using suspended graphene. Corresponding devices were shown to be fully ballistic with mean free paths larger than the device geometry [273]. Consequently, quantum interference phenomena such as Fabry-Perot oscillations have been observed [273, 274]. Furthermore, magneto-conductance measurements on suspended p-n devices have shown the presence of snake states (curved trajectories of charge carriers along the interface) [275]. However, these advances come at the high price of rather complex device fabrication. In comparison, the p-n interfaces created by Ge intercalation of the buffer layer create p-n interfaces narrower than even the smallest junctions obtained by electrostatic gating. The narrow interface as well as the remarkable regularity of the chemical potential in the ambipolar regions makes the potential profiles in this system close to the ones considered in theory (cf. section 3.1.3).

11.2 TRANSPORT ACROSS GRAPHENE KLEIN BARRIERS

In the following the charge carrier transport through isolated p-n interfaces as well as p-n-p and n-p-n shall be studied. For this purpose a multi-tip STM will be used which was shown to be suitable for transport measurements on graphene sheets (cf. chapters 5, 6 and 10) as well as graphene nanostructures (cf. chapter 8 and 9). In order to extract the contribution of the p-n interfaces also the transport properties of the pure n-type and p-type phase shall be evaluated. The corresponding measurement

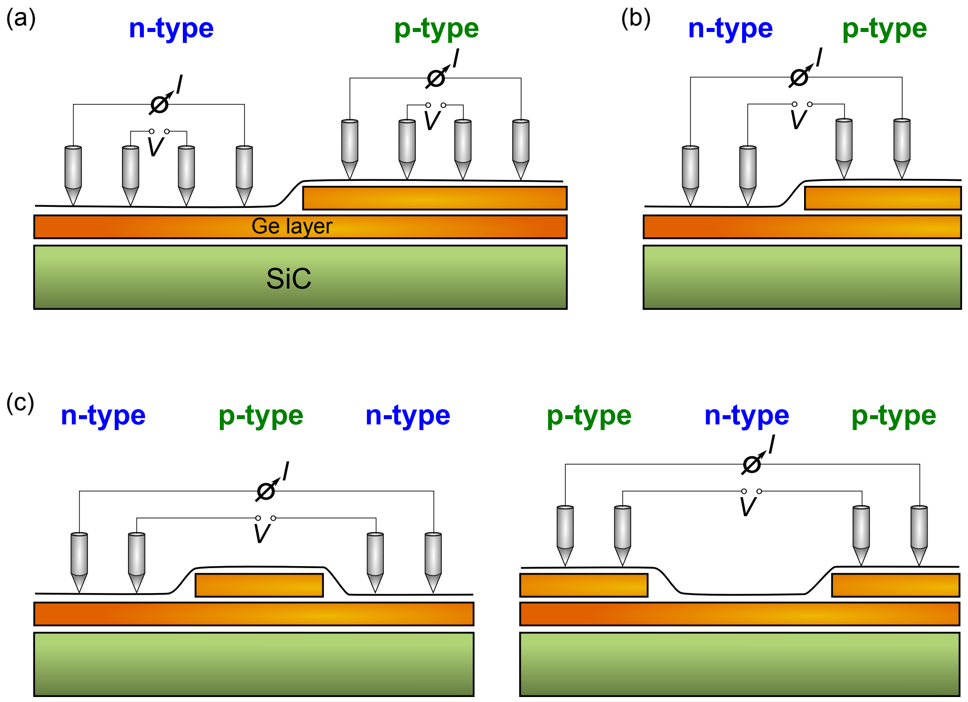

Figure 11.5: 4pp measurement configurations used for the transport characterization of ambipolar doped graphene ribbons. (a) To evaluate the transport characteristics of the pure n-type or p-type region all tips are placed on the same area. (b) Transport across a n-p junction is measured by placing one pair of current/voltage probes on the n-type and the other on the p-type area. (c) For n-p-n or p-n-p structures the probes are placed on the outside regions. No probe is placed in the inner region. All measurements were performed in linear configuration with the probes placed in the center of the ribbons and aligned in parallel to the ribbon edges.

setups are schematically shown in fig. 11.5. All measurements were performed in a linear configuration. The tips were placed in the center of the ribbons in parallel alignment to their edges. For the measurements on the pure n-type or p-type areas all four tips are placed on these areas. For n-p interfaces, one pair of current sourcing and voltage probing tips was placed on each of the two phases. On n-p-n and p-n-p structures, the two tip pairs were placed on the outside phase. The injected current has to pass the p-n interfaces since the surrounding area of the ribbons (the trenches) are insulating.

11.2.1 TRANSPORT ON PURE N-TYPE AND P-TYPE RIBBONS

The pure n-type and p-type phases were already characterized in section 10.2.3. Their transport properties shall be reviewed here again especially with respect to the influence of the restricted geometry. Since the width of the ribbon is rather large (1 µm) confinement effects can be ruled out. Nevertheless, the ribbon edges might cause

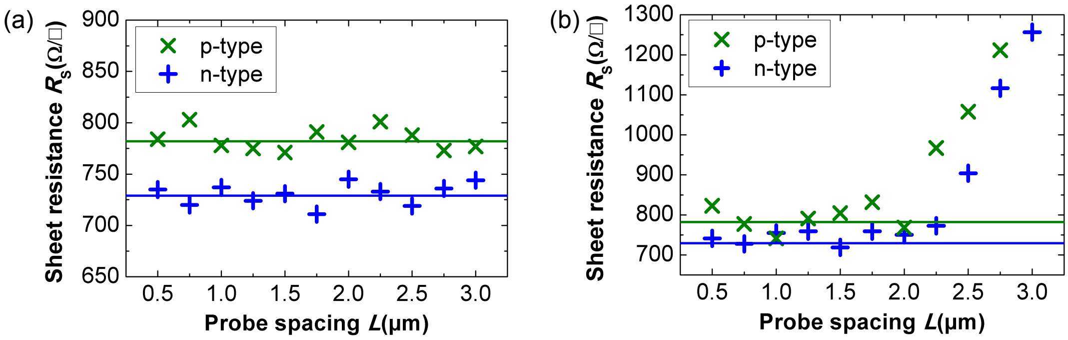

Figure 11.6: Sheet resistance as a function of probe spacing for pure n-type and p-type graphene ribbons with width $W = 1\,\mu\text{m}$ measured at $T = 300\,\text{K}$. The sheet resistances are deduced from (a) dual configuration measurements and (b) by applying the geometrical correction factor for a thin sheet. The lines indicate the mean values of the sheet resistance for $L \leqslant 2.25\,\mu\text{m}$. For probe spacings $L > 2.25\,\mu\text{m}$ the sheet resistances obtained by geometrical correction increase due to the finite width of the ribbon.

a geometry dependence of the transport characteristics, especially for larger probe spacings (cf. section 2.1.2).

In fig. 11.6(a, b) the sheet resistances of the pure n-type and p-type phase are shown with respect to the probe spacing. The measurements were done at room temperature. The values in (a) were obtained by applying the dual configuration method as described in section 2.1.2. For the p-type area $R_{s,p} = (729 \pm 17)\,\Omega/\square$ and for the n-type phase $R_{s,n} = (782 \pm 11)\,\Omega/\square$. These are almost precisely the values obtained before on the unstructured sample in section 10.2.3. This is not surprising since the dual configuration method cancels out possible contributions from the restricted geometry. Nevertheless it is convenient that the intercalation of the structured buffer layer leads to free-standing graphene with sheet resistances equal to the unpatterned case.

For the measurements across p-n interfaces however a dual configuration measurement is not suitable. Here, the standard configuration of current injection through the outer probes and voltage probing with the inner probes shall be used. Hence it is important to know the influence of the restricted geometry. This can be evaluated from the measurements shown in fig. 11.6(b). The sheet resistance is obtained by multiplying the measured resistance with the geometric correction factor for a semi-infinite 2d sheet $\pi/\ln(2)$. It is obvious that this procedure only works for probe spacings $L \leqslant 2\,\mu\text{m}$. The sheet resistances agree well with those obtained by the dual configuration method. The resistance increase seen for larger values of L can be attributed to the influence of the restricted geometry. Hence, simply applying the correction factor of a semi-infinite sheet is not sufficient and other correction factors are needed (cf. section 2.1.2). The correction factors shall not be determined here in detail. Rather, a simple consequence will be drawn by restricting the following experiments to probe spacings below 2 µm. Hence the influence of the restricted geometry can be neglected.

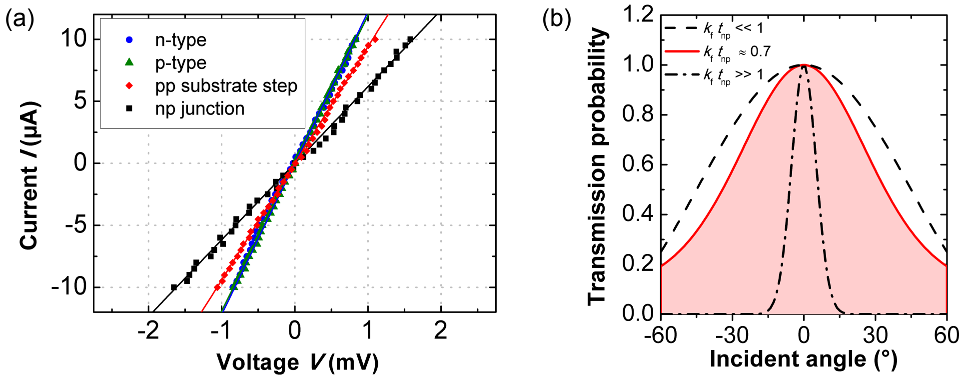

Figure 11.7: (a) IV measurements at $T = 30\,\text{K}$ on a pure n-type and p-type area, across a single n-p junction and on a pure p-type area across an underlying substrate step. The resistance of the n-p junction is about $80\,\Omega$ larger than the resistance of a pure n-type or p-type region. The resistance increase caused by an underlying substrate step (about $20\,\Omega$) is much smaller. (b) Plot of the transmission probability through a graphene p-n junction as a function of the angle of incidence. The angular dependence is strongly varied for different values of $k_f t_{np}$. The red curve shows the transmission probability expected for the p-n junctions investigated here.

11.2.2 TRANSPORT ACROSS SINGLE P-N JUNCTIONS

Before focusing on more complex structures, the transport properties of a single p-n junction shall be discussed. In order to see effects related to Klein tunneling, coherent propagation of the charge carriers is mandatory. Therefore, all following experiments were done at $T = 30\,\text{K}$. The probe spacing between adjacent probes was kept at a fixed distance of $1.5\,\mu\text{m}$. According to the previous section this ensures that the ribbon edges have no influence on the measured resistance. In the following, only the resistances not the sheet resistances will be compared. The definition of a sheet resistance is rather pointless for a measurement across a p-n interface. All resistances are mean values of at least 10 measurements on different junctions.

The IV curve across a single p-n junction is shown in fig. 11.7(a). The IV curves obtained on a pure n-type and p-type phase are plotted for comparison. They are almost identical with $R_n = (82 \pm 4)\,\Omega$ and $R_p = (84 \pm 3)\,\Omega$ reflecting the almost equal resistivity of the p-type and n-type graphene. The IV curve across the p-n interface is also strictly linear as expected and experimentally observed before for Klein tunneling barriers [256]. The resistance of the p-n junction can be deduced from a linear fit to $R_{pn} = (162 \pm 5)\,\Omega$. The mean free path in the n-type and p-type is in the order of $\lambda_e \approx 100\,\text{nm}$. Hence, due to the large probe spacing of $1.5\,\mu\text{m}$, transport is globally diffusive. Consequently, the resistance stemming from the p-n interface can be simply calculated by $R_{pn-junc} = R_{pn} - R_{n,p} = (79 \pm 4)\,\Omega$.

Since the p-n interface coincides with a structural height transition of about 2.4 Å it might be argued that the increased resistance is caused by the step rather than the p-n interface. This seems reasonable since steps are a potential source for electron scattering and consequently a resistance enhancement is expected according to section 6.3. To determine the influence of the step, the resistance measured across a p-n interface is compared with the resistance measured across a substrate step of roughly 6 Å in height which is located in a pure p-type graphene area. The corresponding IV curve is shown in fig. 11.7(a). The observed resistance increase caused by the substrate step $R_{step} = (22 \pm 3)\,\Omega$ is much smaller than the effect of the p-n interface. Since the structural height difference of the p-n interface is furthermore by almost a factor of 3 lower than the height of the substrate step, its influence on the resistance should be negligible small.

In the following the measured resistance of the p-n interface shall be compared with theory. Since the mean free path in the p-type and n-type area is much larger than the junction length $2t_{np}$, the junction can be treated as a ballistic barrier. In general graphene p-n junctions can be classified as either smooth ($k_f t_{np} \gg 1$) or sharp ($k_f t_{np} \ll 1$) with important consequences for the transmission probability as already discussed in section 3.1.3. In fig. 11.7(b) the transmission probabilities for a sharp and a smooth junction are plotted versus the angle of incidence of the electron according to eq. 3.20 and 3.21. For the junctions presented in this chapter $k_f t_{np} \approx 0.7$. Consequently the resistance is in reasonable agreement with the theoretical expectation for a sharp junction $R_{pn}^{sharp} = 82\,\Omega$ (cf. eq. 3.24). This excellent agreement indicates again that the height increase at the p-n interface has no significant influence on the resistance. The resulting transmission function is also shown in fig. 11.7(b). The assumption of a smooth junction leads to an enhanced resistance of $R_{pn}^{smooth} = 101\,\Omega$ (cf. eq. 3.23) which does not match the experimental data.

So far, scattering within the barrier was fully neglected in all considerations due to the very small junction length. This can be further justified by applying a quantitative model which takes into account diffusive contributions [83]. Within this model the resistance of the p-n junction is given by the sum of a diffusive and a ballistic contribution $R_{pn} = R_{bal} + R_{diff}$. With $R_{bal} = \frac{h}{e^2}\frac{1}{\alpha^{1/6} n'^{1/3} W}$ and $R_{diff} = 2\frac{h}{e^2}\frac{n_i}{n' W}\ln\left(\frac{4\pi\gamma}{\beta^{4/3}}\right)$ where α is the strength of the Coulomb interaction, n' the gradient of carrier concentration, $n_i = e/h\mu_e$, $\beta = n'/{n_i}^{3/2}$ and $\gamma = n'^{1/3} t_{np}$. The application of this model to the p-n junctions created by Ge intercalation leads to a ballistic component $R_{bal} = 96\,\Omega$ and a vanishing diffusive contribution. Although the overall resistance predicted by this model is slightly higher than the experimental one, the vanishing diffusive contribution underlines that scattering within the barrier does not need to be taken into account.

As a final remark for this section it should be noted that different (especially smaller) probe spacings than the reported 1.5 µm were also tested. Probe spacings as small as 200 nm were found to have no influence on the observed resistance values. Hence, crosstalk between the voltage probes and the barriers can be ruled out.

11.2.3 TRANSPORT ACROSS N-P-N AND P-N-P JUNCTIONS

Having characterized a single p-n junction, now transport across a double junction will be investigated. Such n-p-n and p-n-p structures are readily provided on the intercalated ribbons as apparent from fig. 11.3(a, b) and the insets in fig. 11.8(a, b).

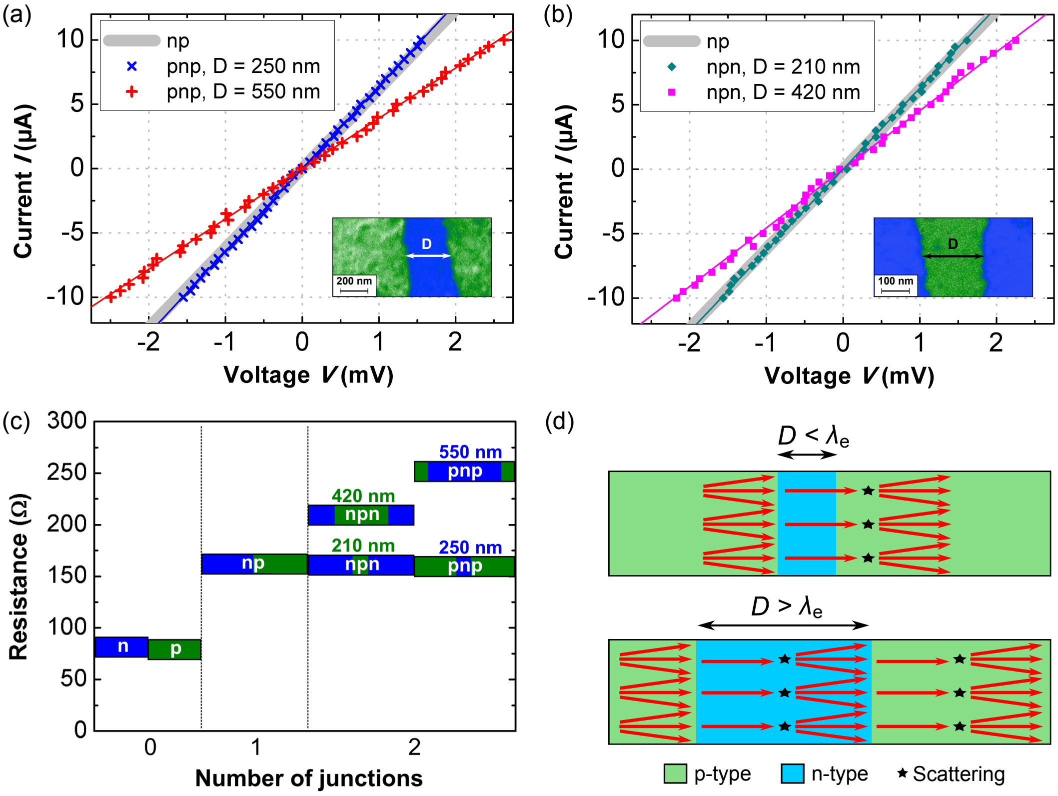

Figure 11.8: Transport across n-p-n and p-n-p structures at $T = 30\,\mathrm{K}$. IV curves across (a) p-n-p and (b) n-p-n structures for different barrier lengths D. The gray shaded area indicates the IV curve of a single n-p junction. The insets show color-coded SEM images of the corresponding structures. For small barrier lengths the resistance of n-p-n, p-n-p is the same as for a single n-p junction. (c) Summarizing plot of the resistances found for pure n-type and p-type areas (0 junctions), a single n-p junction and for a serial connection of two junctions as n-p-n or p-n-p. For the n-p-n and p-n-p structures different barrier lengths are shown. (d) Schematic illustration of scattering events in a p-n-p structure. If the barrier length D is smaller than the electronic mean free path no scattering events occur inside the barrier and the electrons hit the second n-p junction with normal incidence.

Structures with different inner barrier lengths $D_{n,p}$ can be found. Corresponding IV curves across p-n-p and n-p-n structures with various D are shown in fig. 11.8(a, b) in comparison with the IV of a single p-n interface. The probe spacing was kept fixed again at $1.5\,\mu\mathrm{m}$. The measured resistances are obviously dependent on the length of the inner barrier. For D in the order of $200\,\mathrm{nm}$ ($\approx 2\,\lambda_e$) the total resistance across the n-p-n and p-n-p structures is the same as across a single p-n interface. The second junction seems to be fully transparent for the electrons. On the other hand, increasing D leads to a resistance increase. All resistances are summarized in fig. 11.8(c).

The observed behavior can be understood in terms of a polarizer analyzer optics analogy [24, 25, 276]. This is schematically depicted in fig. 11.8(d). Electrons which hit the first junction at normal incidence are fully transmitted. Electrons at oblique incidence angles are filtered out more or less according to the transmission function (cf. fig. 11.7(b)). Thus, after the first junction the electrons are collimated. The electrons which were fully transmitted through the first junction can also pass the second junction without reflection because they still have an angle of incidence of zero. Hence the second junction is transparent for these electrons. This is of course only true as long as no scattering events occur inside the barrier. Scattering events will randomize the angles of incidence and the second junction will not be transparent anymore. The key parameter is therefore the inner barrier length D. If it is in the order of the mean free path only few scattering events will occur and the polarized electron beam can pass the second junction without reflection. Thus, the resistance of the p-n-p or n-p-n structure should be the same as for a single p-n junction. If the barrier length is larger than the mean free path both junctions are basically independent from each other and the measured resistance $R_{npn,pnp} \geqslant 2\,R_{pn}$ [25].

This behavior is a clear signature of the angle dependent transmission caused by Klein tunneling. However, it should be mentioned that these measurements provide only an indirect access to the angular dependence. A direct proof is challenging on these samples since the electronic mean free path is in the order of the lowest possible probe spacings. Hence it demands for measurements with very sharp tips which have not yet been accomplished. There are only a few experimental studies which directly address the angular dependence [277, 278]. Both, extensive sample preparation (e.g. lithography) and data analysis are needed in order to extract the angular dependent components of the transmission function [279].

The Klein tunneling signatures seen in the p-n junctions created by Ge intercalation are remarkably stable. The effect of both n-p-n and p-n-p structures is very similar hence the slightly higher n-type doping does not have a significant influence. Furthermore even the imperfect parallelism (cf. inset of fig. 11.8(a, b)) of the two junctions seems to have no effect on the perfect transmission through the second junction. Overall, the simple polarizer analyzer model fits the experimental data surprisingly well. Naturally, the polarizer analyzer model is expected to work best for a smooth junction because it has the largest collimation effect. The barriers treated here were characterized as sharp hence it is remarkable that the second junction becomes fully transparent. It remains unclear to what extend the roughness of the p-n interface influences the transmission. To get further insight and to develop a more realistic model a microscopic characterization of the p-n interface is definitely needed.

11.3 CONCLUSIONS

In summary, graphene p-n junctions created by Ge intercalation of the SiC buffer layer were shown to be Klein tunneling barriers. Isolated p-n junctions were created through a prepatterning of the initial buffer layer. The transport properties of the graphene layers were shown to be unperturbed by this prepatterning step. The doping profile of the p-n junctions was described in detail by means of local spectroscopy. Due to their ultra small length the p-n junctions can be treated as fully ballistic barriers in a diffusive background. Together with the extreme stability of the chemical potential in both the p-type and the n-type phase, these narrow p-n junctions can be used to create n-p-n and p-n-p structures with potential profiles close to the theoretical ideal. Signatures of the angular dependence of transmission through the Klein tunneling junctions can be established by varying the inner barrier length. For barrier lengths in the order of the electronic mean free path the collimation of the electron beam manifested in the full transparency of the second junction. Hence the intercalation of Ge was shown to be a viable route to create Klein tunneling barriers by chemical rather than electrostatic gating.

Part V

SUMMARY AND OUTLOOK

12

SUMMARY

In this thesis, ballistic transport phenomena were realized in graphene nanostructures. Various epitaxial graphene based systems, such as 2d graphene sheets, graphene nanoribbons and p-n interfaces were studied with respect to their individual transport characteristics. Exceptional features such as room temperature ballistic conduction with a mean free path exceeding 15 µm or ultra-narrow ambipolar junctions with junction lengths below 10 nm were demonstrated. These findings open up novel routes for graphene based electronic devices.

The key to access the local properties of individual nanostructures is the high flexibility of the multi-probe STM which was used for the transport investigations. On epitaxial ML sheets, it was demonstrated that transport properties can be probed reliably and non-invasively. Hence, the local conductivity can be consistently merged with the local morphology or electronic structure of the sample, deduced by means of SEM, tunneling spectroscopy or Raman scattering. The enhanced electronic scattering caused by substrate steps overgrown with bilayer graphene as well as by incomplete graphene growth could be quantified. While small bilayer fractions at step bunched SiC substrate steps cause mediocre resistance increases, incomplete growth of the graphene layer is detrimental to its inherent transport characteristics. Consequently, while phonon scattering is the dominant scattering mechanism in perfect ML graphene, transport in an imperfect graphene layer turned out to be dominated by Anderson localization. This highlights that graphene layers of high homogeneity on both the lattice as well as the nm scale are mandatory in order to achieve highly conductive samples.

Following the results on 2d sheets, graphene nanoribbbons were grown by a self-assembling growth process. Making use of the development of nanofacets at the sidewall of SiC mesa structures by thermal annealing, graphene nanoribbons could be synthesized without applying any conventional lithography or post-processing to the graphene. The free-standing nature of the ribbons was shown to leave them in a charge neutral state. Their zigzag orientation and consequently the presence of edge states make them a prime candidate for 1d transport characteristics. Surprisingly, electrons were found to travel not only ballistically through the sidewall ribbons but also within a single non-degenerate channel. The localization behavior and mean free path of this exceptional channel was shown to be independent of temperature. Substrate steps were identified as major limiting factor for the mean free path, underlining the importance of a careful surface preparation. A second, strongly localized ballistic channel was found for small probe spacings as well as high temperatures. The

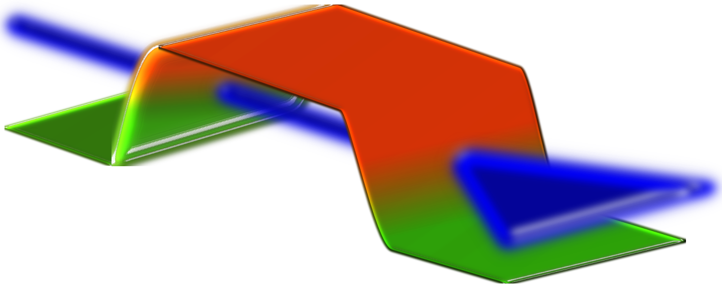

Figure 12.1: Artistic view of a graphene n-p-n potential barrier. The electron beam is collimated while passing the p-n junctions due to Klein tunneling.

occurrence of these two fundamentally different ballistic modes was not suggested by theory so far and their origin remains unclear at the moment. Nevertheless, the stability of the ballistic properties is remarkable. Even further nanostructuring of the sidewall GNRs by means of STM lithography did not destroy the long-range ballistic channel. Furthermore, transport through the created sidewall nanoconstriction was shown to be dominated by conductance peaks arising from resonances in the electronic transmission function. The survival of the ballistic channel and the remarkable agreement between theory and experiment concerning the transmission resonances, demonstrates the robustness of the electronic system as well as the structural quality of the sidewall ribbons and constrictions.

As a second approach to reach the ballistic transport regime in graphene nanostructures, the intercalation of Ge was presented. The ambipolar doping behavior due to the intercalation of different amounts of Ge forms ultra-narrow p-n interfaces. The potential barriers created by these p-n interfaces were found to be extremely homogeneous concerning the two doping levels. The intercalation process proceeds very gentle and hence no sign of additional defect formation could be detected. Due to the intrinsically symmetric doping level of about ±300 meV Klein tunneling could be proven easily by local transport. The characteristic angular dependence of the transmission function through individual p-n junction was demonstrated by using two junctions in serial connection as polarizer and analyzer. The expected reflectionless Klein tunneling was found for potential barriers with lateral dimensions smaller than the mean free path. Hence, chemical doping of epitaxial graphene sheets was proven to create fully ballistic potential barriers.

These results show that ballistic graphene nanostructures can be readily achieved by modifying the interface between graphene and SiC as well as by exploiting the specific growth characteristics. The combination of the high versatility and stability of epitaxial graphene on SiC with the high flexibility of a multi-tip STM system allowed to access novel and previously unreported transport phenomena. Most importantly, the demonstration of electron transport with extremely large mean free paths at room temperature opens up a complete new pathway towards graphene based ballistic electronics.

13

OUTLOOK

In the following, possible subsequent work on the topics presented in this thesis shall be mentioned. The most pressing question is probably the origin of the room temperature single-channel ballistic transport. To explore its origin, both theoretical and experimental progress is needed. Theoretical calculations should include the interactions with the SiC substrates (e.g. bonding at the edges, polarization) from the beginning as well as the characteristic curvature. Probable explanations include a largely enhanced spin-orbit interaction in the graphene ribbon. The importance of spin-orbit coupling can be further explored experimentally by adsorption of transition metals such as Co which can alter the magnetic order of the nanoribbons [280] or by hydrogenation of the edges which enhances the spin-orbit coupling [232, 281]. The spin polarized nature of the ballistic channel naturally suggests the fabrication of spin-valve devices with tunable magnetic fields to perform non-local transport. This would provide access to characteristic parameters such as spin lifetimes [282, 283]. First non-local measurements might be realizable even within the multi-tip STM by using ferromagnetic tips. To support this work on the spin signatures, the electronic structure of the sidewall GNRs needs to be further explored by spectroscopy techniques such as STS or ARPES. First STS results were already presented in this thesis, however higher resolved data are highly desirable in order to explore the specific nature of the edge states. Spin-resolved STS as well as ARPES might become useful for a deeper insight into the spin texture. For ARPES investigations, a high ribbon density as well as homogeneity is needed for reliable results. Hence the growth process of the ribbons needs to be further optimized to produce ballistic ribbons on large scale samples. Scanning photoemission with high lateral resolution (Nano-ARPES) [284] might be an option to circumvent the problem of large scale homogeneity. Nevertheless, wafer-scale production is essential for future device integration. A detailed LEEM study would hence be highly desirable for a detailed look at the growth kinetics.

Regarding the graphene nanoconstriction obtained by STM lithography, the influence of the lateral dimensions of the constrictions on the transport characteristics should be considered. The theoretical description of the observed conductance resonances predicts a strong dependence of the energetic position of the resonance peaks on the constriction size. Hence an alteration of the constriction size is an easy way to validate this model. Furthermore, also other constriction geometries, e.g. different shapes or positions relative to the sidewall ribbon, should result in distinct alterations of the transmission function.

Concerning the synthesis of 2d graphene sheets, it needs to be explored if other substrates besides SiC might be suitable for electronic applications. In this sense, ongoing work about MBE growth of graphene for example on Mica [222, 285] or Germanium [286–288] needs to be intensified. These growth techniques are of special interest due to their compatibility with standard CMOS technology. Regarding the high cost of SiC bulk material, epitaxial growth of graphene on thin SiC films deposited on Si substrates became an active research field [289, 290]. Local transport experiments can be used to investigate the quality of these systems as already demonstrated for epitaxial graphene on bulk SiC.

Intercalation of foreign atoms was shown to enable ambipolar doping and consequently provide access to Klein tunneling. Unfortunately, the development of p- and n-type doping was rather uncontrolled, resulting in a random distribution of p-n junctions. In order to make the p-n interfaces accessible for other transport techniques, e.g. additional electrostatic gating, a way to control the doping sites would be highly desirable. Since the Ge intercalation seems to be triggered by substrate steps, additional patterning of the substrate might result in areas which are predefined for n-type or p-type doping. Control over the doping sites would also be beneficial to produce potential barriers in the desired shapes and dimensions. Especially, the synthesis of more than two p-n interfaces in serial connection would allow to investigate the effectiveness of the angular selectivity of the transmission function in detail. In this sense, extremely local heating techniques such as Thermochemical Nanolithography (TCNL) [291] are very promising. Furthermore, other intercalates than Ge or even a mixture of intercalates might be used to achieve variations in the doping level.

Part VI

APPENDIX

A

EXPERIMENTAL METHODS

A.1 SCANNING TUNNELING MICROSCOPY

The scanning tunneling microscope (STM) can be used for imaging sample surfaces with up to atomic precision. It relies on the quantum mechanical tunnel effect. Therefore, a bias voltage in the mV or V range is applied between the sample and an atomically sharp metal tip as illustrated in fig. A.1(a). If the distance d between the tip and the sample is small enough a small current between tip and sample can be detected. It is caused by electronic tunneling from tip to sample or vice versa. The tunnel effect is schematically depicted in fig. A.1(b). A potential barrier is present between sample and tip through which, classically, the electrons cannot pass. In the quantum mechanical picture, however, the electronic wave function exponentially decays in the barrier, resulting in a wave function with a finite amplitude at the other side of the barrier. Hence, there is a finite probability that the electrons pass through the barrier. In a simplified picture (without accounting for unequal Fermi energies in tip and sample) the tunneling probability is given by [292]

$$|W(E)|^2 \cong e^{-2\sqrt{2m_e(V_0-E)}\frac{d}{\hbar}} \, . \tag{A.1}$$

Due to the exponential dependence of the tunneling probability on the tip sample distance, the tunneling current is very sensitive to alterations of this distance. The tunneling current itself has the form of Fermi's golden rule and can be expressed as [293, 294]

$$I_t = \frac{4\pi e}{\hbar} \int\limits_{-\infty}^{\infty} dE \; D_s(E_{fs}+E) D_t(E_{fs}-eV+E)[f_s(E_{fs}+E)-f_t(E_{ft}-eV+E)]|M_{\mu\nu}|^2 \tag{A.2}$$

where D_s (D_t) denotes the density of states of the sample (tip) and f_s (f_t) the corresponding Fermi distribution. The matrix element $M_{\mu\nu}$ is given by [295]

$$M_{\mu\nu} = \frac{\hbar^2}{2m_e} \int d\vec{s}(\Psi_\mu^* \vec{\nabla} \Psi_\nu - \Psi_\nu \vec{\nabla} \Psi_\mu^*) \, . \tag{A.3}$$

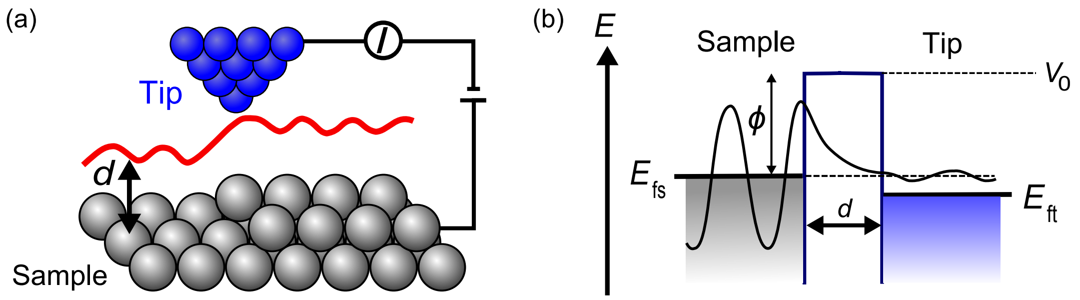

Figure A.1: (a) Illustration of tip and sample in a STM operating in constant current mode. (b) Tunneling process at a 1d potential barrier of height V_0. The Fermi energy of the tip (sample) is denoted as E_{ft} (E_{fs}) and ϕ is the work function of the sample.

The tunneling current in eq. A.2 can be rewritten in the following form [295]

$$I_t = \frac{32\pi^3 e^2 V \phi^2 r^2 e^{2\kappa r}}{\hbar \kappa^4} D_t(E_{ft}) \underbrace{\sum_{\nu} |\Psi_\nu(\vec{r}_0)|^2 \delta(E_\nu - E_{fs})}_{\equiv D_s(\vec{r}_0, E_{fs})} \tag{A.4}$$

with $\kappa = \hbar^{-1}(2m\phi)^{\frac{1}{2}}$, the work function ϕ and the radius of the tip r. This leads to a tunneling conductance of [295]

$$G_t \approx 0,1 r^2 e^{2\kappa r} D_s(\vec{r}_0, E_{fs}) \tag{A.5}$$

where $D_s(\vec{r}_0, E_{fs})$ is the LDOS of the sample at the Fermi energy at position $\vec{r}_0$. This means that if the tunneling current is kept fixed, the tip follows a contour of the constant LDOS of the sample. Hence, the resolution as well as the sensitivity of the STM are determined by the LDOS of the surface as well as the tip radius.

By switching the sign of the bias voltage, the tunneling direction can be reversed as shown in fig. A.2. If the sample is at a higher potential compared to the tip, the electrons can tunnel from occupied states of the sample into unoccupied states of the tip (cf. fig. A.2(a)). In the same manner, if the sample is at a lower potential, tunneling occurs from occupied states of the tip into unoccupied states in the sample.

A.1.1 IMAGING MODES

For imaging, two modes are typically used in STM, the constant current or constant height mode. As the names already reveal, in these two modes either the current or the height is kept fixed. In the constant height mode, this means that while scanning with the tip over the sample surface the tunneling current is recorded. Such an image of the tunneling current can then be related to the surface topography. The advantage of the constant height mode is its fast scan speed. However, on rough surfaces the danger of crashing the tip into the sample is very high. Therefore, the most widely used operational mode is the constant current mode. Here, the tunneling current is set to a fixed value, typically between a few pA up to a few nA. A feedback loop ensures

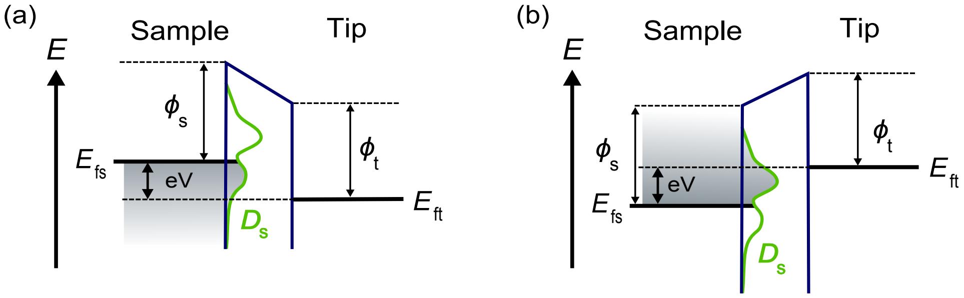

Figure A.2: Visualization of the tunneling process for (a) a negative and (b) a positive bias voltage V. The Fermi energy of the tip (sample) is denoted as E_{ft} (E_{fs}). Φ_t (Φ_s) is the work function of the tip (sample) and D_s is the LDOS of the sample. The LDOS of the tip is assumed to be constant.

that the tips is retracted or lowered in order to keep the tunneling current constant. This concept is also visualized in fig. A.1(a). Subsequently, a height difference can be attributed to every point of the scan from which the topographic image of the surface can be obtained.

The STM operation presented here is obviously limited to imaging conductive or at least semi-conducting samples. Imaging insulating surfaces is not straightforward but possible, for example by using alternating tunneling currents [296].

A.1.2 SCANNING TUNNELING SPECTROSCOPY

Further insight into the electronic structure of the surface can be gained by means of scanning tunneling spectroscopy (STS). The underlying concept is straightforward. A local I_tV curve (tunneling current versus applied bias) is recorded by keeping the tip in a constant distance from the surface while ramping the bias voltage. Any feedback loop in use for normal scanning operation therefore needs to be turned of. The information content of such a measurement becomes directly clear from eq. A.4. Under the assumption that the DOS of the tip as well as the matrix element is constant, the tunneling current reads

$$I_t \sim \int_0^{eV} D_s(E_{fs} - eV + E)dE \, . \tag{A.6}$$

A constant DOS of the tip is a reasonable assumption and can be realized by choosing a proper tip material or using a blunt and disordered tip. However, a constant matrix element might be possible at low temperature and bias voltage, but at real experimental conditions matrix element effects cannot be ruled out. Nevertheless, the first derivative of eq. A.6 with respect to the bias voltage yields

$$\frac{dI_t}{dV} \sim D_s(E_{fs} - eV) \, . \tag{A.7}$$

Hence, it is proportional to the LDOS of the sample at the tip position.

The derivative can be obtained numerically from the measured I_tV spectra. A higher accuracy can be reached by measuring the dI_t/dV signal directly by means of a lock-in amplifier. Here, a small high-frequency sinusoidal signal is superimposed to the bias voltage. This modulation causes a sinusoidal modulation of the tunneling current as well. Expanding the modulated tunneling current in a Taylor series leads to

$$I_t(V+V_{mod}\sin(\omega t)) \sim I_t(V) + \frac{dI_t(V)}{dV}V_{mod}\sin(\omega t) + \frac{d^2I_t(V)}{dV^2}V_{mod}^2\sin^2(\omega t) + \ldots \quad (A.8)$$

where $V_{mod}\sin(\omega t)$ is the modulation signal. The lock-in amplifier allows to extract the first harmonic frequency which is obviously proportional to the dI_t/dV signal.

So far, effects due to finite temperature have been completely neglected. For non zero temperatures and sample and tip in thermal equilibrium, the following relation for the dI_t/dV can be found [297]

$$\frac{dI_t}{dV} \sim \int_{-\infty}^{\infty} D_s(eV+E)\mathrm{sech}^2\left(\frac{E}{k_{BT}}\right)dE\,. \quad (A.9)$$

This implies that an infinitely sharp signal in the LDOS is thermally broadened by $3.2\,k_BT$. Hence, for high-resolution spectroscopy low temperatures are inevitable.

Besides varying the bias voltage it is also advantageous to locally record the tunneling current with respect to the tip sample separation. The tunneling current decays exponentially with the tip sample distance d [298]

$$I_t \sim e^{-2\kappa d} \quad (A.10)$$

where the decay constant is given by

$$\kappa = \frac{\sqrt{2m_e\phi}}{\hbar} \quad (A.11)$$

with ϕ being the average work function of tip and sample $\phi = (\phi_t + \phi_s)/2$. Hence, measuring the tunneling current with respect to d allows to extract the work functions of tip and sample. For the determination of the absolute values of the work function, it is necessary to work with reference samples of known work functions because only the average work function of tip and sample can be measured.

A.2 ATOMIC FORCE MICROSCOPY

The atomic force microscopy (AFM) is based on the interaction of a scanning probe with the sample surface. In principle, it measures the forces between tip and sample. Similar to a STM, with an AFM up to atomic resolution can be achieved. However, in contrast to the STM, an AFM can be used on conducting and insulating samples with the same accuracy because the measurement principle does only rely on the

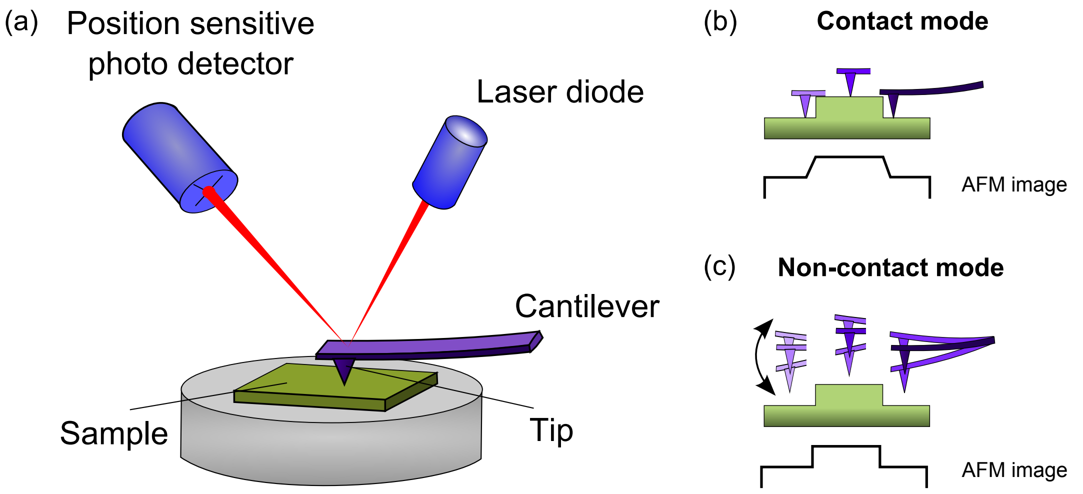

Figure A.3: (a) Schematic setup of an AFM. (b) AFM operating in contact mode. (c) AFM operating in non-contact mode.

atomic forces which are present between a mechanical tip and the sample surface. The typical setup of an AFM is shown in fig. A.3(a). It consists of an atomically sharp tip attached to a much larger cantilever. The length and width of the cantilevers is typically in the range from 20 µm to 300 µm. Widely used materials are silicon or silicon nitride. Based on Hooke's Law atomic forces between tip and sample cause a deflection of the cantilever. The spring constants of the cantilevers are typically in the range of N/m, consequently, forces in the range of a few pN can be measured. The deflection of the cantilever is detected by means of a laser beam which is focused onto the top side of the cantilever and reflected into an array of position-sensitive photodiodes. The tip is scanned over the sample surface using piezo motors and the atomic forces at every scanning point are recorded. This results in a topographic image of the sample surface.

A.2.1 IMAGING MODES

Like in a STM, several imaging modes can be used when operating an AFM. They are exploiting different kinds of tip-sample forces. In general, long and short range forces can be distinguished. The long range forces are dominated by the van der Waals force. It includes forces between permanent dipoles (Keesom force), between a permanent and an induced dipole (Debye force) and between instantaneously induced dipoles (London force). The van der Waals forces are strongest in the range of 1 nm to 10 nm above the surface. Furthermore, also magnetic as well as electrostatic forces are present in the long range regime.

On the other hand, the short range forces originate from the overlap of the electronic orbitals of tip and sample. If they are very close to each other, strong repulsive forces arise due to the Coulomb interaction and the Pauli exclusion principle. The short range forces can be best described with the Morse potential accounting for re-

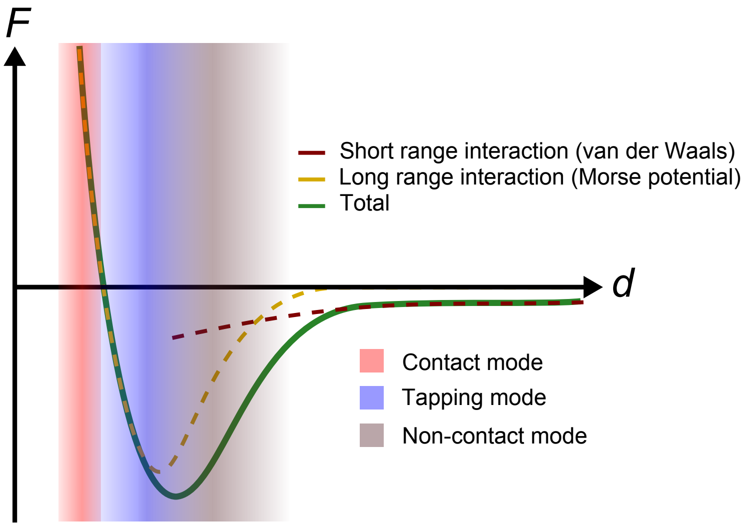

Figure A.4: Forces between tip and sample as a function of tip sample preparation d. Adapted from [299].

pulsive as well as attractive forces [299]. In fig. A.4 the forces between tip and sample are plotted as a function of tip-sample distance. The shaded areas mark the operation ranges of different measurement modes.

The most simple imaging mode is the contact mode (see also fig. A.3(a)) which operates in the range of short range repulsive forces. Tip and sample are in hard contact while the tip is scanning over the sample surface. Due to the large force gradient, the contact mode is very sensitive to height changes. The contact mode can be operated by either keeping a constant height or a constant force similar to the constant current and constant height modes in a STM (cf. section A.1.1). The advantage of the constant height mode is its large scan speed because no feedback loop is needed. Due to the danger of a tip crash, the constant height mode is only an option for very smooth sample surfaces.

In non-contact mode, the tip does not contact the sample (cf. fig. A.3(b)). The cantilever is kept oscillating at its resonance frequency with an oscillation amplitude of typically a few nm. Forces on the tip cause a shift in the resonance frequency [299] which can be detected by measuring either the phase or the amplitude shift. A feedback loop maintains a constant oscillation amplitude or frequency by adjusting the tip-sample distance accordingly. Since the tip is held in a larger height compared to the contact mode, the danger of a tip crash and hence of compromising the sample surface is minimized.

The tapping mode is very similar to the non-contact mode. The cantilever is driven to oscillate at its resonant frequency but with amplitudes typically 10 to 100 times higher than in the non contact mode. Therefore, the tip is occasionally very close to the surface. Hence short range forces become detectable.

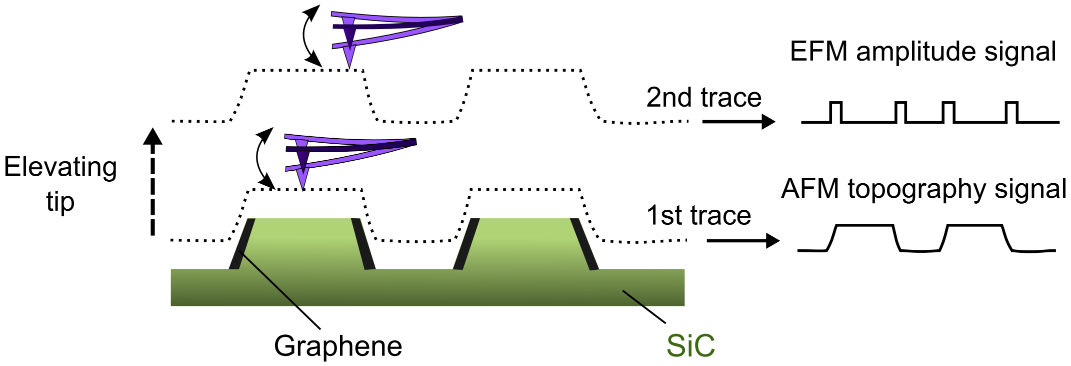

Figure A.5: Illustration of image acquisition with EFM via 2nd trace operation. The example surface is graphene on SiC.

A.2.2 ELECTROSTATIC FORCE MICROSCOPY

A variety of specialized measurement techniques can be operated based on the AFM principle. One of them is the electrostatic force microscopy (EFM). Its purpose is to measure the long range electrostatic forces between tip and sample. It allows to gain insight into local work function differences present on the sample surface. Important for EFM imaging is a conductive tip and the possibility to apply a bias voltage between tip and sample. In the following the detection of electrostatic forces by means of the so called 2nd trace method will be shortly discussed.

In 2nd trace operation, first a standard non-contact topographic image is obtained. Subsequently, a voltage V is applied between tip and sample and the tip is lifted about several nm in height to reduce the interaction with van der Waals forces. Then, the tip scans the sample again, following the height profile previously obtained in the AFM imaging mode. Ideally, the lifted tip does not interact with the sample via other forces than the electrostatic ones. Hence, modulations of the oscillation amplitude of the tip can be directly attributed to these electrostatic forces. The vertical (z) component of the force can be expressed in a simple parallel plate capacitor model as

$$F_{\text{el.static}} = -\frac{1}{2}\frac{dC}{dz}\Delta V^2 \tag{A.12}$$

where C denotes the capacitance and ΔV the potential difference between tip and sample. If tip and sample are made of different materials and have hence different work functions, the potential difference is given by the $\Delta V = V - V_{CPD}$ where V is the applied bias voltage and $V_{CPD} = 1/e(\Phi_t - \Phi_s)$ is the contact potential difference which is simply the difference of the work functions of tip Φ_t and sample Φ_s [300]. The EFM hence allows to identify different material compositions or charge distributions on a sample surface.

The measurement setup is depicted in fig. A.5. Typically, not a complete AFM image is recorded before switching to EFM mode but the EFM image is recorded line-wise directly after every AFM image line. Critical for the EFM measurements is the choice of the lifting height. It needs to be ensured that it is high enough that

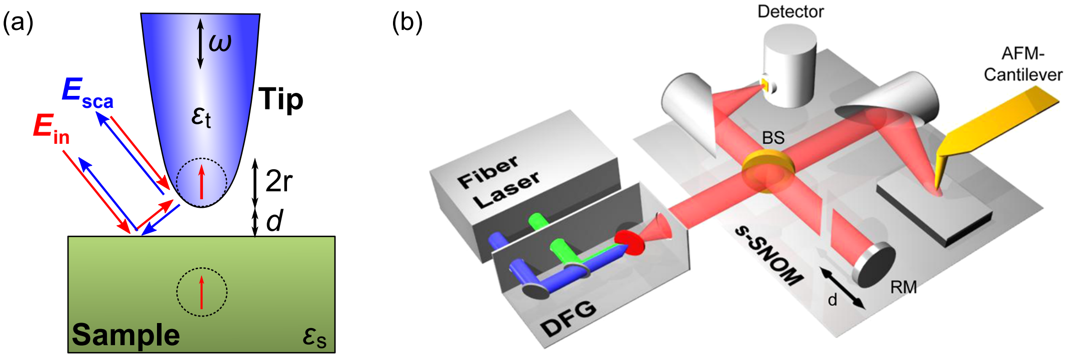

Figure A.6: (a) Principle of a s-SNOM. A focused light beam illuminates the tip of an AFM. The AFM is operated in the tapping mode and the scattered light is recorded. (b) Experimental setup of a s-SNOM [301]. The laser system provides a mid-infrared continuum beam by using a difference frequency generator (DFG). A Michelson interferometer consisting of a beam splitter (BS) and a reference mirror (RM) is used to analyze the backscattered light.

the topography of the sample is not imaged, but still low enough to ensure a strong electrostatic signal.

A.2.3 SCATTERING-TYPE NEAR FIELD OPTICAL MICROSCOPY

Despite using an AFM for simple imaging it can also serve as base instrument for scattering-type scanning near field optical microscopy (s-SNOM). In general, s-SNOM is designed to break the far field resolution limit of roughly $\lambda/2$ by making use of the properties of evanescent waves. A typical setup is shown in fig. A.6(a). The AFM tip is illuminated by a focused laser beam and the backscattered light is recorded. The AFM itself is operated in tapping mode.

The generation of a near field image can be rationalized in a simple dipole model. The AFM tip is assumed to be a polarizable sphere with permittivity ϵ_t and radius r. The polarizability α of the sphere is hence given by [302]

$$\alpha = 4\pi r^3 \frac{\epsilon_t - 1}{\epsilon_t + 1} \, . \tag{A.13}$$

Assuming that the sample is polarizable only indirectly by the dipolar field of the tip and not by the incident electric field (which is much smaller than the tip enhanced near field), the effective polarizability α_{eff} combining the effect of tip and sample can be written as [302]

$$\alpha_{eff} = \frac{\alpha}{1 - \frac{\alpha\beta}{16\pi(d+r^3)}} \, . \tag{A.14}$$

Here, d is the distance between tip and sample and β is the dielectric surface response function

$$\beta = \frac{\epsilon_s - 1}{\epsilon_s + 1} \tag{A.15}$$

with the the sample permittivity ϵ_s. It is clear that the backscattered field is related to the incoming field via $E_{sca} \propto \alpha_{eff} E_{in}$. Since α, β and ϵ are complex, it is intuitively clear that also E_{sca} has to have a complex value

$$E_{sca} = S\, e^{i\Theta} \; . \tag{A.16}$$

The amplitude S and the phase shift Θ are the quantities measured in a s-SNOM setup. The sample itself is only contributing to the signal with ϵ_s. Hence s-SNOM is a tool to measure the local dielectric function of the sample surface.

A major problem which needs to be overcome in order to detect sample properties with s-SNOM is the large background signal due to unwanted scattering from tip or sample outside the gap region. The key to overcome this obstacle is the demodulation of the detector signal at higher harmonics of the tip tapping frequency ω [302]. The tip sample distance then varies according to $d = d_0 + \Delta d \, \sin(\omega t)$ which results in a time dependency of α_{eff}

$$\alpha_{eff} = \sum_n \alpha_{eff,n} \cos(n\omega t) \; . \tag{A.17}$$

Consequently, after harmonic demodulation the s-SNOM measures also the higher harmonic amplitudes S_n and phase shifts Θ_n which suffer much less from background signals.

The resolution of the s-SNOM is no longer limited by the wavelength of the incident light like in conventional optical microscopy. The spatial resolution is only determined by the tip geometry and can reach down to a few nm.

A.3 ELECTRON MICROSCOPY

Since an optical microscope is not suitable for investigating objects on the nanoscale due to its diffraction limited resolution, electron microscopy is a widely used technique for this purpose. The wavelength λ of an electron accelerated by a voltage V is given by

$$\lambda = \frac{h}{\sqrt{2 m_e e V \left(1 + \frac{eV}{2 m e c^2}\right)}} \; . \tag{A.18}$$

Hence, the wavelength of an electron accelerated by a voltage of 15 kV (as in typical SEM operation) is smaller than 10 pm. Thus, the wavelength is no limitation for the resolution of an electron microscope.

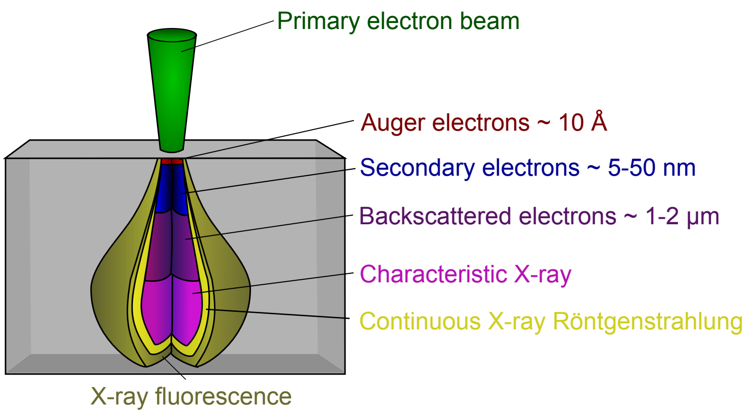

Figure A.7: Schematic of electronic interactions with the sample surface causing detectable signals.

A.3.1 INTERACTION OF ELECTRONS WITH THE SURFACE

In electron microscopy, basically all processes which occur when an electron beam of a few kV hits the sample surface can be used for imaging. Fig. A.7 provides an overview of these processes. Most commonly used for imaging are the secondary electrons which are emitted from the sample by inelastic collisions with the primary beam electrons. The secondary electrons have energies of only a couple eV. Hence, they are stemming from a region up to several nm below the surface. Thus, imaging the secondary electrons is a surface sensitive technique. Furthermore, the backscattered electrons are electrons from the primary beam which leave the sample again after undergoing elastic collisions with sample atoms. Their energies can be up to a few kV, hence, they can originate from up to 2 µm below the sample surface. The backscattering of primary electrons is of course dependent on the atomic number of the element under investigation, and consequently an image of the backscattered electrons provides a strong material contrast. A material contrast can also be obtained by the detection of the characteristic X-rays. This technique is known as energy-dispersive X-ray spectroscopy (EDX) and is a very powerful and fast technique to identify the material composition of the sample surface.

A.3.2 SCANNING ELECTRON MICROSCOPY

The scanning electron microscopy (SEM) makes use of the interactions presented in the previous section and uses them to provide an image of the sample surface. Basically, a scanning electron microscope needs an electron source, a series of magnetic lenses to focus the electron beam, scan coils which allow to scan the electron beam over the sample and detectors for any kind of signal which shall be detected. The setup of the SEM used in this thesis is shown in fig. 4.2(a) in chapter 4 and its special properties are discussed there. Hence, it shall not be reviewed here again.

Electromagnetic lenses work on the basis of the Lorentz force. They are formed by two circularly symmetric pole pieces and a copper winding in between as shown

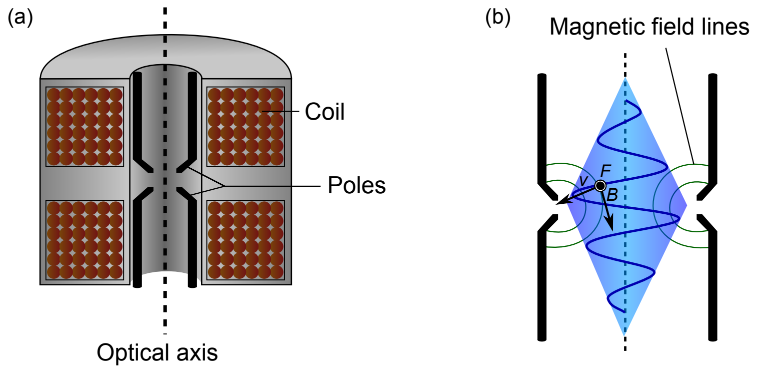

Figure A.8: (a) Section view and (b) working principle of a magnetic lens.

in fig A.8(a). The magnetic field will force any electron passing through the pole pieces into the direction of the optical axis. Furthermore, the electrons are forced into a spiral rotation around the optical axis. The combination of these two force components yields a focusing effect as shown in fig. A.8(b).

The focused electron beam is then scanned over the sample surface by means of the scan coils to obtain a complete image of the sample surface. For example by detecting the secondary electrons, the surface morphology can be recorded because the intensity of secondary electron emission is highly dependent on the surface morphology, e.g. tilted surface areas yield a higher intensity than flat areas.

A.3.3 ABERRATION AND CHARACTERISTIC PARAMETERS

Typical aberrations found in electron microscopy can be defined in analogy with optical systems. A major parameter which has strong influence on the imaging capabilities is the working distance which is defined as the distance between the final

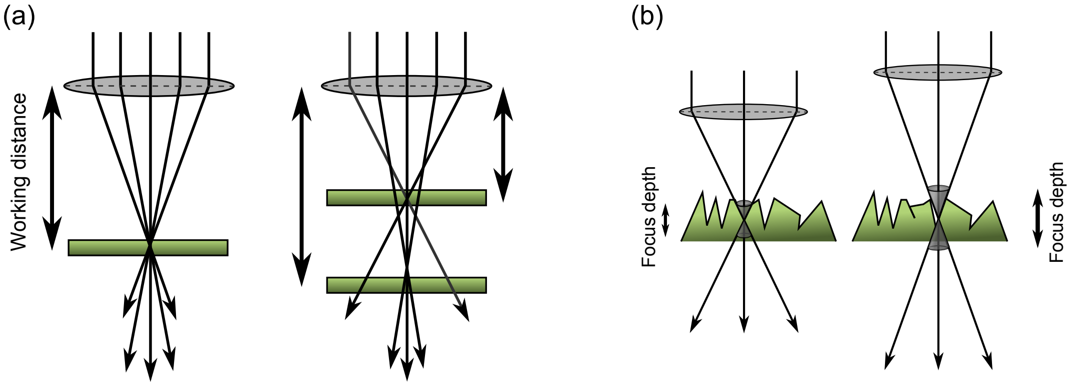

Figure A.9: (a) Illustration of the influence of the working distance on the spot size with and without spherical aberration. (b) Illustration of the influence of the working distance on the depth of focus.

lens and the sample. Its influence on the spherical aberration is shown in fig. A.9(a). Electrons passing an electromagnetic lens along the axis of the electron beam refract less than those passing it in the periphery of the electron beam. If no spherical aberration is present, the electrons focus in one point. Hence, the working distance has no influence. If spherical aberration is present more than one focal point is created and the beam spot is smeared out. Therefore, in the presence of spherical aberration a smaller working distance leads to a smaller spot size and in further consequence a better resolution. The working distance also has an influence on the depth of focus as shown in fig. A.9(b). At a larger working distance the cone of the electron beam has a smaller angle and thus the depth of focus is larger. Hence, on a sample with large height variations a larger working distance can be advantageous in order to gain a sharp image of all height levels.

A.4 LOW ENERGY ELECTRON DIFFRACTION

Low energy electron diffraction (LEED) is a widely used technique for the determination of the crystal structure of surfaces. For this purpose, an electron beam containing low energy electrons of 20 eV up to 200 eV is directed onto the sample and the diffraction pattern is recorded. The mean free path of such low energy electrons is below 1 nm [303] making LEED an extremely surface sensitive technique. The corresponding electron wavelength is comparable to the inter atomic distances making the atomic arrangement in the surface unit cell accessible. LEED is a non-destructive method for most surfaces due to the use of small beam energies.

A.4.1 KINEMATIC APPROACH

The origin of the spots in the diffraction pattern can be described within kinematic theory in which the electrons are assumed to elastically scatter only once with the surface. The Laue condition relates the wave vector of an incident electron $\vec{k}_i$ and a scattered one $\vec{k}_f$

$$\vec{K} = \vec{k}_i - \vec{k}_f = \vec{G}_{hkl} \tag{A.19}$$

where $\vec{G}$ is a reciprocal lattice vector. Due to the small penetration depth of the low energy electrons, no scattering potential is present in perpendicular direction to the surface. Hence, the perpendicular component of $\vec{K}$ obeys no selection rule and eq. A.19 can be rewritten containing only the parallel components

$$\vec{K}_{||} = \vec{k}_{i,||} - \vec{k}_{f,||} = \vec{G}_{hk} \ . \tag{A.20}$$

This means, that the reciprocal lattice of the surface consists of periodic lattice rods. In a conventional LEED the angle of the incident electrons (and therefore $\vec{k}_{i,||}$) stays constant. By detecting the diffracted electrons on a phosphor screen, diffraction spots can be seen at positions where $\vec{k}_{f,||}$ obeys eq. A.20.

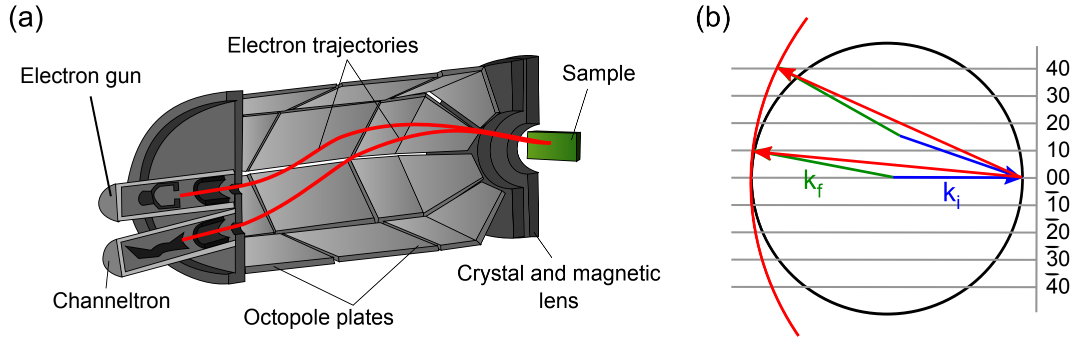

Figure A.10: (a) Schematic of the setup of a SPA-LEED. (b) Standard (indicated in black) and modified Ewald sphere for SPA-LEED (indicated in red).

A.4.2 SPA-LEED

The measurement of the reciprocal surface lattice can be done with extremely high resolution by means of spot profile analyzing LEED (SPA-LEED). In contrast to a conventional LEED the diffracted electrons are not detected with a phosphor screen but a channeltron detector. For this purpose the electron beam is not focused on the sample but onto the detector. The electrons which are diffracted from the surface are guided into the channeltron by means of an electrostatic field generated by octopole plates. As shown in fig. A.10(a) the detector is located very close to the electron gun and the diffracted electron beam follows almost the same path as the incident one. The angle between the incident and the diffracted wave vector is very small (a few degrees) and is kept constant. Hence, changing $\vec{k}_{i,||}$ (the incident angle) changes $\vec{k}_{f,||}$ accordingly.

Eq. A.20 can be visualized nicely with an Ewald construction as shown in fig. A.10(b). To find the wave vectors at which the Laue condition is fulfilled, a circle with radius $|\vec{k}_{i,||}| = |\vec{k}_{f,||}|$ is drawn around the origin of $\vec{k}_{i,||}$. If a lattice rods intersects the Ewald sphere eq. A.20 is fulfilled. In the case of the SPA-LEED the Ewald construction needs to be modified. Since $\vec{k}_{i,||}$ and $\vec{k}_{f,||}$ are altered simultaneously, the standard Ewald sphere is rotating around the origin of reciprocal space. As a consequence, the diameter of the modified Ewald sphere is twice that of the standard one which allows to measure a larger area in reciprocal space. The detection of the electron beam with a channeltron makes it fairly easy to obtain intensity profiles of individual diffraction spots or to record LEED images with high resolution. A detailed review of SPA-LEED can be found in [304].

A.5 RAMAN SPECTROSCOPY

If a sample surface is hit by a focused light beam, the photons can either be reflected, absorbed or scattered. The scattered light is of specific interest if informations regarding the rotational or vibrational modes are needed. In a Raman spectrometer the sample is illuminated with a focused laser beam. The electromagnetic radiation orig-

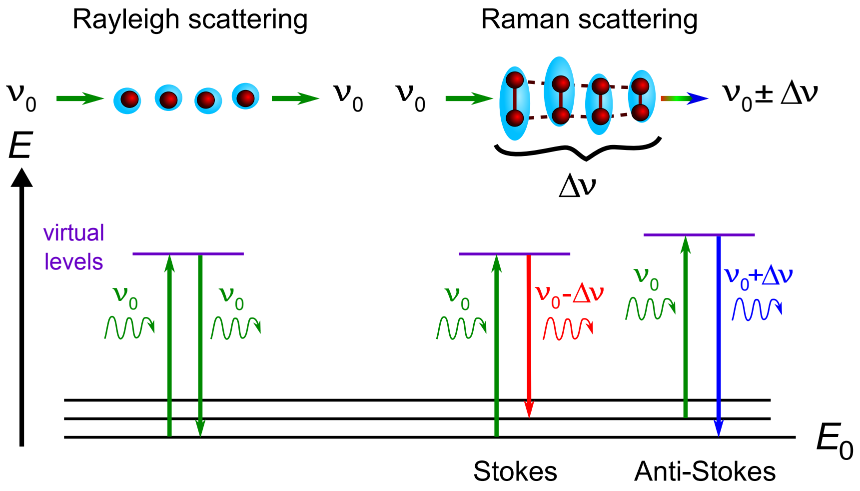

Figure A.11: Illustration of Raman and Rayleigh scattering.

inating from the illuminated spot is collected into a monochromator. The light can either be scattered elastically or inelastically. The elastic scattering is called Rayleigh scattering. The molecule is excited into a virtual energy level and falls back into its original vibrational state as shown in fig. A.11. The Rayleigh scattered light is not of interest since it does not contain informations about the vibrational modes.

The term Raman scattering refers to the inelastically scattered light. It can be distinguished by whether the frequency of the incident light is shifted to a higher or lower frequency. If the incident light is shifted to a lower frequency, the scattering is called Stokes scattering. The molecule is excited to a virtual level and returns to a vibrational mode of higher energy. The scattering is called Anti-Stokes, if the molecule returns into a vibrational mode of lower energy. The frequency of the scattered light is blue shifted. The plot of the intensity of the scattered light with respect to its frequency shift is a Raman spectrum. Typically much of the molecules are in the vibrational ground state. This implies that the Stokes lines in the spectrum are much more intense than the Anti-Stokes lines.

A.5.1 CLASSICAL THEORY OF RAMAN SCATTERING

Deriving the Raman effect can be easily done by considering a simple diatomic molecule with masses m_1 and m_2 connected by a spring with constant Π. By using the reduced mass $m_r = m_1 m_1 / m_1 + m_2$ the differential equation

$$m_r \frac{d^2 x}{dx^2} = -\Pi x \tag{A.21}$$

can be obtained, where x denotes the total displacement of the molecule. The result for this equation can be written as

$$x = x_0 \cos(2\pi \nu_n t) \tag{A.22}$$

where the frequency of molecular vibration is defined as

$$\nu_n = \frac{1}{2\pi}\sqrt{\frac{\Pi}{m_r}}\,. \tag{A.23}$$

If now light is focused onto the molecule the corresponding electric field is given by

$$E = E_0\,\cos(2\pi\nu_0 t) \tag{A.24}$$

with intensity E_0 and frequency ν_0. The interaction of light with the molecule induces a dipole moment $\hat{P} = \alpha\,E$ with α being the polarizability of the molecule. The polarizability can be easily expressed in terms of the displacement x as

$$\alpha = \alpha_0 + x\left(\frac{\delta\alpha}{\delta t}\right)_0 + \ldots\,. \tag{A.25}$$

Hence, an expression for the dipole moment can be found

$$\hat{P} = \alpha\,E = \underbrace{\alpha_0\,E_0\cos(2\pi\nu_0 t)}_{\text{Rayleigh}} + \frac{1}{2}E_0\,x_0\left(\frac{\delta\alpha}{\delta t}\right)_0\Big(\underbrace{\cos(2\pi(\nu_0+\nu_n)t)}_{\text{Anti}-\text{Stokes}} + \underbrace{\cos(2\pi(\nu_0-\nu_n)t)}_{\text{Stokes}}\Big)\,. \tag{A.26}$$

As indicated, the three terms refer to Rayleigh, Stokes and Anti-Stokes scattering.

The classical theory presented here, correctly describes that Raman scattering is weaker than Rayleigh scattering. However, it does not take into account that excited vibrational states are only thermally populated following the Boltzmann distribution. Consequently, the intensity ratio of Stokes/Anti-Stokes will be underestimated in classical theory.

A.5.2 RAMAN SPECTROSCOPY ON GRAPHENE

Raman spectroscopy is a highly efficient tool to gain informations about a graphene sample concerning for example the determination of the number of graphene layers or the defect concentration. The Raman processes which can be observed in Raman spectroscopy can involve up to four phonons [305]. However, most research focuses only on one- and two-phonon processes and the following discussion will be also limited to one- and two-phonon processes.

An overview over the relevant processes which lead to peaks in the Raman spectrum is given in fig. A.12. The three most prominent ones are referred to as G, D and 2D peak. The G peak originates from a one-phonon process. It is an intravalley transition and the corresponding phonon is the E_{2g} mode [306] schematically shown in fig. A.13(a). The G peak can be found at a Raman shift of $1580\,\text{cm}^{-1}$ [118]. The G peak experiences a small red shift (up to $6\,\text{cm}^{-1}$) for an increased number of layers [307].

A further one-phonon process gives rise to the D peak. However, since this process involves intervalley transitions, defect scattering is needed to return into the initial

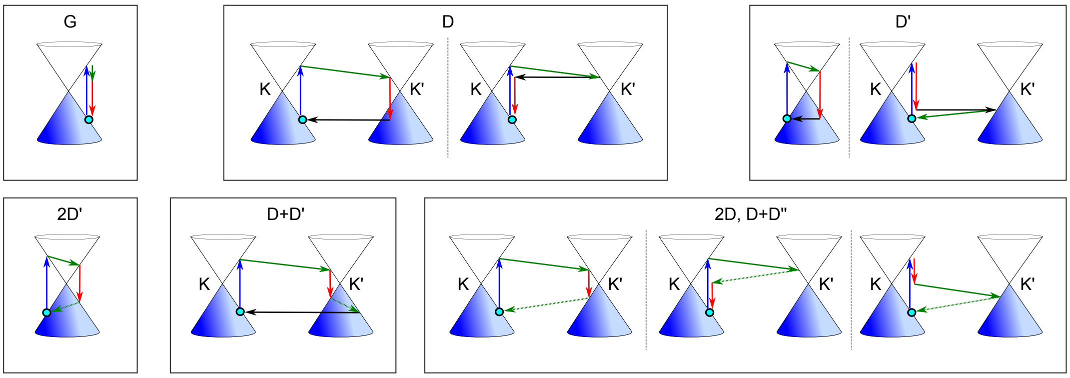

Figure A.12: Overview of possible Raman processes in graphene. The processes involve photon absorption (blue arrows), photon emission (red arrows), phonon emission (green arrows) and defect scattering (black arrows). The photon momentum is neglected in this illustration.

valley. The involvement of defect scattering makes the D peak highly sensitive to the defect concentration in the graphene layer. The corresponding phonon is the A_{1g} breathing mode shown in fig. A.13(b). The D peak is dispersive, hence its Raman shift is dependent on the excitation energy of the laser [308]. It is located at a Raman shift of $1350\,\mathrm{cm}^{-1}$ for a laser wavelength of 532 nm [118].

The 2D peak arises from a two-phonon process and it is the D peak overtone. In contrast to the D peak, no defect is needed to provide the necessary intervalley transition. Like the D peak, the 2D peak is dispersive and for a laser wavelength of 532 nm it can be found at a Raman shift of $2690\,\mathrm{cm}^{-1}$. The 2D peak is highly sensitive to the number of graphene layers. In the case of bilayer graphene, the π bands split into four different band, giving rise to a splitting of the 2D peak into four components [309]. The role of further contributions to the 2D peak of bilayer graphene, such as the splitting of the transversal optical phonon branch, are still under discussion [310]. Nevertheless, it is a strong fingerprint of single layer graphene, if the 2D peak in a Raman spectrum can be fitted with a single Lorentzian. Additionally, an increased number of layers leads to a significant red shift of the 2D peak [309].

Further defect involving Raman processes are the D′, with its overtone the two-phonon 2D′ and the $D + D'$. Finally, the $D + D''$ is an additional two-phonon process. Since these processes show up in the Raman spectra of graphene but are usually not analyzed in detail they shall not be discussed her further.

A complete Raman spectrum of a defective graphene sample is shown in fig. A.13(c). All peaks mentioned in this section show up in the spectrum. In case of a perfect graphene sample all defect associated peaks (D, D′, $D + D'$) will vanish.

The defect sensitivity of the D peak can be also exploited in a quantitative manner. The intensity ratio of the D and G peak I(D)/I(G) is directly related to the mean distance between Raman active defects L_D by the expression [186]

$$L_D^2(\mathrm{nm}^2) = (1.8 \pm 0.5) \times 10^{-9}\,\lambda_L^4 \left(\frac{I_D}{I_G}\right)^{-1} \tag{A.27}$$

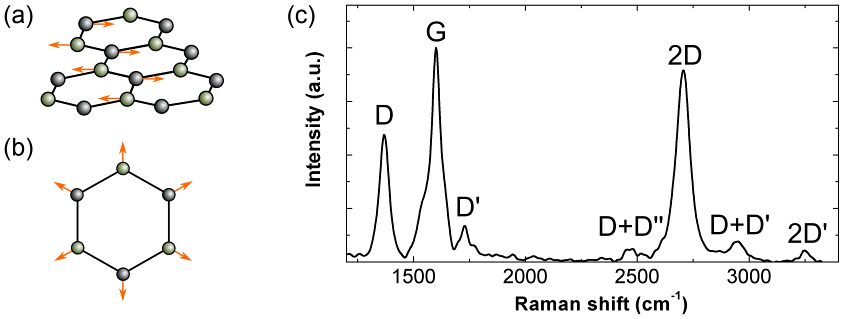

Figure A.13: (a) Atom displacement at the Γ point for the E_{2g} phonon mode in graphene which corresponds to the G peak. (b) Atom displacement at the K point for the A_{1g} phonon mode (breathing mode) in graphene which corresponds to the D peak. (c) Example Raman spectrum of defective graphene.

where λ_L is the excitation laser wavelength in nm. This expression of course only accounts for Raman active defects. This is especially important considering the edges of a graphene sheet. Since an edge is in principle a lattice defect, it should give rise to an enhanced D peak. Interestingly this depends on the edge orientation. Since the D peak involves intervalley scattering, it can only occur if an electron backscattered from the edge gets a momentum transfer equal to the momentum needed to change from K to K′. Along the edge direction momentum is conserved and backscattering can only proceed in a direction perpendicular to the edge [191]. For obvious geometric reasons a momentum transfer perpendicular to an armchair edge allows the electron to change its valley while at a zigzag edge it does not. Consequently, an armchair edge does contribute to the D peak in contrast to the zigzag edge [190].

A last remark concerns the Raman spectrum of epitaxial graphene on SiC. Interfering signals from the SiC substrate as well as charge transfer and strain have been shown to give rise to additional shifts of the characteristic Raman peaks [115, 117, 311]. This makes it somewhat difficult to compare Raman shifts measured on epitaxial graphene with the theoretical values given above. Hence, to discuss Raman shifts with respect to, for example, the number of graphene layers, additional shifts arising from the substrate interaction need to be considered. Furthermore, the FWHM of the 2D peak is broadened for ML graphene on SiC compared to exfoliated graphene. In exfoliated graphene samples the FWHM of the 2D peak is typically $< 30\,\text{cm}^{-1}$ [309] while for epitaxial ML graphene it is enhanced to about $40\,\text{cm}^{-1}$ [117, 146]. This broadening has also been found for epitaxial graphene flakes transfered to SiO_2 substrates and hence it was suggested to originate from structural properties of the graphene, e.g. curvature effects [117].

A.6 LITHOGRAPHY

The structural modification of micro- and nanosystems is a common task in semiconductor research and industry. A standard lithography process using reactive ion etching (RIE) and UV light exposure is shown in fig. A.14. In the first step, the sample

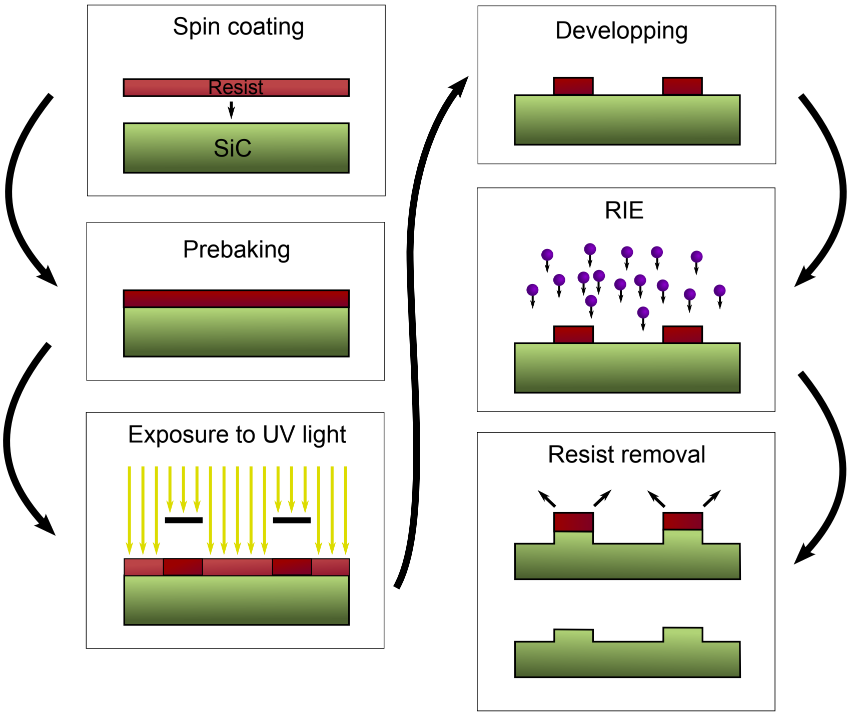

Figure A.14: Illustration of a etching process using positive photoresist, UV light and RIE.

is homogeneously spin coated with photoresist. The following baking step removes solvents and hardens the photoresist. The sample is then exposed to UV light through an optical mask. Subsequently, the exposed photoresist is developed. In case of a positive photoresist, the parts of the resist which were covered by the mask and not exposed to the UV light are removed. Etching via reactive ion etching transfers the structure defined by the mask into the sample surface. In the last step, the resist is removed from the surface.

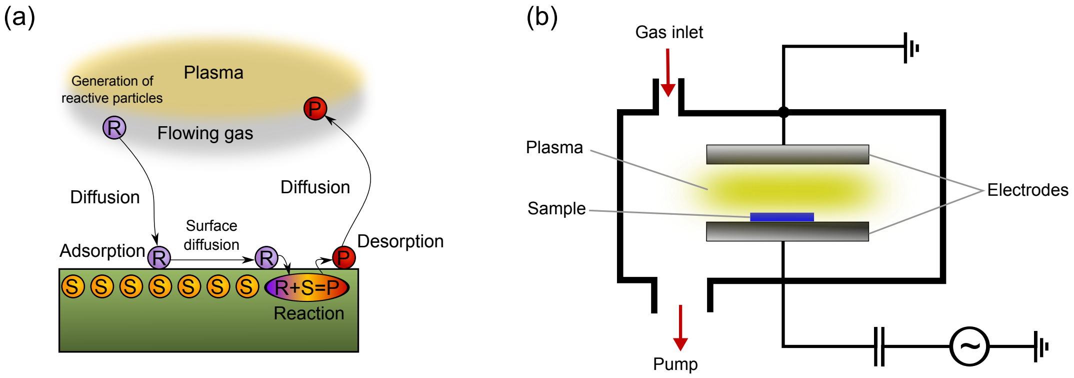

Figure A.15: (a) Schematic of a plasma etching process showing reactive particles (R) diffusing to the surface and reacting with a surface atom (S) to a volatile product (P). (b) Setup of a RIE chamber.

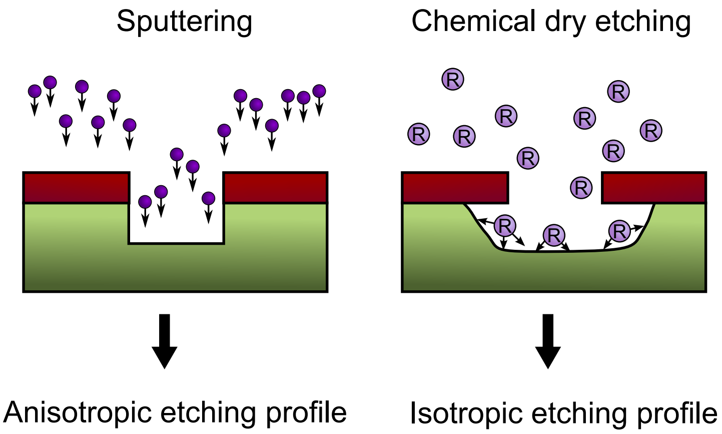

Figure A.16: Comparison of sputtering and chemical dry etching with respect to their etching profile.

For the etching process itself, RIE is a widely used technique. It is a combination of sputter etching and plasma etching. Plasma etching makes use of the chemical reaction between surface atoms with the reactive particles within a plasma. The process is depicted in fig. A.15(a). It is carried out inside a vacuum chamber. A plasma is ignited via a strong radiofrequency field producing reactive particles which diffuse to the sample surface where they react with surface atoms. The plasma contents are chosen such that the reaction products are volatile. Thus, they will be removed out of the system by the vacuum pump. In addition to this chemical dry etching process, RIE also makes use of a sputter process. The general setup of a RIE chamber is shown in fig. A.15(b). The bottom electrode on which the sample is resting, is coupled to the RF source. This causes a directed stream of plasma ions onto the sample leading to material removal from the sample surface.

In fig. A.16 plasma etching and sputtering are compared with respect to the isotropy of the etching profile. As directly obvious, plasma etching will lead to a very isotropic etching while sputtering is highly anisotropic. It depends on the sample material which of the processes is dominating. The SiC substrates which were used in this thesis exhibit a very anisotropic etching profile in RIE. Due to the strong Si-C bonds the chemical etching is very slow. The bonds need to be broken first by the sputtering process to allow for the chemical etching to take place [312]. Hence only very small undercuts are observed on SiC substrates.

BIBLIOGRAPHY

[1] M. Stoneham. Electrons in carbon country. *Nat Mater*, 3(1):3, jan 2004. doi: 10.1038/nmat1042.

[2] A. M. Song, A. Lorke, A. Kriele, J. P. Kotthaus, W. Wegscheider, and M. Bichler. Nonlinear electron transport in an asymmetric microjunction: A ballistic rectifier. *Phys. Rev. Lett.*, 80(17):3831, apr 1998. doi: 10.1103/physrevlett.80.3831.

[3] T. Palm and L. Thylen. Analysis of an electron-wave y-branch switch. *Applied Physics Letters*, 60(2):237, jan 1992. doi: 10.1063/1.106975.

[4] E. Forsberg. Reversible logic based on electron waveguide y-branch switches. *Nanotechnology*, 15(4):S298, mar 2004. doi: 10.1088/0957-4484/15/4/034.

[5] G. R. Facer, B. E. Kane, A. S. Dzurak, R. J. Heron, N. E. Lumpkin, R. G. Clark, L. N. Pfeiffer, and K. W. West. Evidence for ballistic electron transport exceeding 160 μm in an undoped GaAs/AlxGa1-xAs field-effect transistor. *Physical Review B*, 59(7):4622, feb 1999. doi: 10.1103/physrevb.59.4622.

[6] Y. Hirayama and S. Tarucha. High temperature ballistic transport observed in AlGaAs/InGaAs/GaAs small four-terminal structures. *Applied Physics Letters*, 63(17):2366, jun 1993. doi: 10.1063/1.110799.

[7] P. Avouris, Z. Chen, and V. Perebeinos. Carbon-based electronics. *Nature Nanotech*, 2(10):605, sep 2007. doi: 10.1038/nnano.2007.300.

[8] S. Iijima. Helical microtubules of graphitic carbon. *Nature*, 354(6348):56, nov 1991. doi: 10.1038/354056a0.

[9] T. Ando and T. Nakanishi. Impurity scattering in carbon nanotubes – absence of back scattering –. *Journal of the Physical Society of Japan*, 67(5):1704, may 1998. doi: 10.1143/jpsj.67.1704.

[10] C. T. White and T. N. Todorov. Carbon nanotubes as long ballistic conductors. *Nature*, 393(6682):240, may 1998. doi: 10.1038/30420.

[11] S. Frank, P. Poncharal, Z. L. Wang, and W. A. de Heer. Carbon nanotube quantum resistors. *Science*, 280(5370):1744, jun 1998. doi: 10.1126/science.280.5370.1744.

[12] P. Poncharal, C. Berger, Y. Yi, Z. L. Wang, and W. A. de Heer. Room temperature ballistic conduction in carbon nanotubes. *J. Phys. Chem. B*, 106(47):12104, nov 2002. doi: 10.1021/jp021271u.

[13] M. P. Anantram and F. Léonard. Physics of carbon nanotube electronic devices. *Rep. Prog. Phys.*, 69(3):507, feb 2006. doi: 10.1088/0034-4885/69/3/r01.

[14] J.-C. Charlier, X. Blase, and S. Roche. Electronic and transport properties of nanotubes. *Reviews of Modern Physics*, 79(2):677, may 2007. doi: 10.1103/revmodphys.79.677.

[15] C. Dekker, S. J. Tans, and A. R. M. Verschueren. Room-temperature transistor based on a single carbon nanotube. *Nature*, 393(6680):49, may 1998. doi: 10.1038/29954.

[16] P. Wallace. The band theory of graphite. *Physical Review*, 71(9):622, may 1947. doi: 10.1103/physrev.71.622.

[17] C. Berger, Z. Song, T. Li, X. Li, A. Y. Ogbazghi, R. Feng, Z. Dai, A. N. Marchenkov, E. H. Conrad, P. N. First, and W. A. de Heer. Ultrathin epitaxial graphite: 2d electron gas properties and a route toward graphene-based nanoelectronics. *J. Phys. Chem. B*, 108(52):19912, dec 2004. doi: 10.1021/jp040650f.

[18] K. S. Novoselov, A. K. Geim, S. V. Morozov, D. Jiang, Y. Zhang, S. V. Dubonos, I. V. Grigorieva, and A. A. Firsov. Electric field effect in atomically thin carbon films. *Science*, 306(5696):666, oct 2004. doi: 10.1126/science.1102896.

[19] Y. Zhang, Y.-W. Tan, H. L. Stormer, and P. Kim. Experimental observation of the quantum Hall effect and Berry's phase in graphene. *Nature*, 438(7065):201, nov 2005. doi: 10.1038/nature04235.

[20] K. S. Novoselov, Z. Jiang, Y. Zhang, S. V. Morozov, H. L. Stormer, U. Zeitler, J. C. Maan, G. S. Boebinger, P. Kim, and A. K. Geim. Room-Temperature Quantum Hall Effect in Graphene. *Science*, 315(5817):1379, mar 2007. doi: 10.1126/science.1137201.

[21] K. I. Bolotin, K. J. Sikes, Z. Jiang, M. Klima, G. Fudenberg, J. Hone, P. Kim, and H. Stormer. Ultrahigh electron mobility in suspended graphene. *Solid State Communications*, 146(9-10):351, jun 2008. doi: 10.1016/j.ssc.2008.02.024.

[22] O. Klein. Die Reflexion von Elektronen an einem Potentialsprung nach der relativistischen Dynamik von Dirac. *Z. Physik*, 53(3-4):157, mar 1929. doi: 10.1007/bf01339716.

[23] M. I. Katsnelson, K. S. Novoselov, and A. K. Geim. Chiral tunnelling and the Klein paradox in graphene. *Nature Physics*, 2(9):620, aug 2006. doi: 10.1038/nphys384.

[24] V. V. Cheianov and V. I. Fal'ko. Selective transmission of Dirac electrons and ballistic magnetoresistance of n-p junctions in graphene. *Phys. Rev. B*, 74(4):041403, jul 2006. doi: 10.1103/PhysRevB.74.041403.

[25] R. V. Gorbachev, A. S. Mayorov, A. K. Savchenko, D. W. Horsell, and F. Guinea. Conductance of p-n-p graphene structures with "air-bridge" top gates. *Nano Letters*, 8(7):1995, jun 2008. doi: 10.1021/nl801059v.

[26] N. Stander, B. Huard, and D. Goldhaber-Gordon. Evidence for Klein Tunneling in Graphene p-n Junctions. *Phys. Rev. Lett.*, 102(2):026807, jan 2009. doi: 10.1103/PhysRevLett.102.026807.

[27] K. Nakada, M. Fujita, G. Dresselhaus, and M. Dresselhaus. Edge state in graphene ribbons: Nanometer size effect and edge shape dependence. *Physical Review B*, 54(24):17954, dec 1996. doi: 10.1103/physrevb.54.17954.

[28] K. Wakabayashi, M. Fujita, H. Ajiki, and M. Sigrist. Electronic and magnetic properties of nanographite ribbons. *Physical Review B*, 59(12):8271, mar 1999. doi: 10.1103/physrevb.59.8271.

[29] K. Wakabayashi. Electronic transport properties of nanographite ribbon junctions. *Physical Review B*, 64(12):125428, sep 2001. doi: 10.1103/physrevb.64.125428.

[30] K. Wakabayashi, Y. Takane, M. Yamamoto, and M. Sigrist. Electronic transport properties of graphene nanoribbons. *New J. Phys.*, 11(9):095016, sep 2009. doi: 10.1088/1367-2630/11/9/095016.

[31] M. Y. Han, B. Özyilmaz, Y. Zhang, and P. Kim. Energy band-gap engineering of graphene nanoribbons. *Phys. Rev. Lett.*, 98(20):206805, may 2007. doi: 10.1103/PhysRevLett.98.206805.

[32] M. Y. Han, J. C. Brant, and P. Kim. Electron transport in disordered graphene nanoribbons. *Phys. Rev. Lett.*, 104(5):056801, feb 2010. doi: 10.1103/PhysRevLett.104.056801.

[33] J.-H. Chen, C. Jang, S. Xiao, M. Ishigami, and M. S. Fuhrer. Intrinsic and extrinsic performance limits of graphene devices on SiO2. *Nature Nanotech*, 3(4):206, mar 2008. doi: 10.1038/nnano.2008.58.

[34] K. Todd, H.-T. Chou, S. Amasha, and D. Goldhaber-Gordon. Quantum dot behavior in graphene nanoconstrictions. *Nano Letters*, 9(1):416, jan 2009. doi: 10.1021/nl803291b.

[35] L. C. Campos, V. R. Manfrinato, J. D. Sanchez-Yamagishi, J. Kong, and P. Jarillo-Herrero. Anisotropic etching and nanoribbon formation in single-layer graphene. *Nano Letters*, 9(7):2600, jul 2009. doi: 10.1021/nl900811r.

[36] L. Tapaszto, G. Dobrik, P. Lambin, and L. P. Biro. Tailoring the atomic structure of graphene nanoribbons by scanning tunnelling microscope lithography. *Nature Nanotech*, 3(7):397, jun 2008. doi: 10.1038/nnano.2008.149.

[37] G. Z. Magda, X. Jin, I. Hagymási, P. Vancsó, Z. Osváth, P. Nemes-Incze, C. Hwang, L. P. Biró, and L. Tapasztó. Room-temperature magnetic order on zigzag edges of narrow graphene nanoribbons. *Nature*, 514(7524):608, oct 2014. doi: 10.1038/nature13831.

[38] Y. Y. Li, M. X. Chen, M. Weinert, and L. Li. Direct experimental determination of onset of electron–electron interactions in gap opening of zigzag graphene nanoribbons. *Nat Comms*, 5:4311, jul 2014. doi: 10.1038/ncomms5311.

[39] A. J. Van Bommel, J. E. Crombeen, and A. Van Tooren. LEED and Auger electron observations of the SiC(0001) surface. *Surface Science*, 48(2):463, mar 1975. doi: 10.1016/0039-6028(75)90419-7.

[40] K. V. Emtsev, A. Bostwick, K. Horn, J. Jobst, G. L. Kellogg, L. Ley, J. L. McChesney, T. Ohta, S. A. Reshanov, J. Röhrl, E. Rotenberg, A. K. Schmid, D. Waldmann, H. B. Weber, and T. Seyller. Towards wafer-size graphene layers by atmospheric pressure graphitization of silicon carbide. *Nat Mater*, 8(3):203, feb 2009. doi: 10.1038/nmat2382.

[41] W. A. de Heer, C. Berger, M. Ruan, M. Sprinkle, X. Li, Y. Hu, B. Zhang, J. Hankinson, and E. Conrad. Large area and structured epitaxial graphene produced by confinement controlled sublimation of silicon carbide. *Proceedings of the National Academy of Sciences*, 108(41):16900, sep 2011. doi: 10.1073/pnas.1105113108.

[42] A. K. Geim and K. S. Novoselov. The rise of graphene. *Nat Mater*, 6(3):183, mar 2007. doi: 10.1038/nmat1849.

[43] M. Rubio-Roy, F. Zaman, Y. Hu, C. Berger, M. W. Moseley, J. D. Meindl, and W. A. de Heer. Structured epitaxial graphene growth on SiC by selective graphitization using a patterned AlN cap. *Applied Physics Letters*, 96(8):082112, feb 2010. doi: 10.1063/1.3334683.

[44] M. Sprinkle, M. Ruan, Y. Hu, J. Hankinson, M. Rubio-Roy, B. Zhang, X. Wu, C. Berger, and W. A. de Heer. Scalable templated growth of graphene nanoribbons on SiC. *Nature Nanotech*, 5(10):727, oct 2010. doi: 10.1038/nnano.2010.192.

[45] C. Riedl, C. Coletti, T. Iwasaki, A. A. Zakharov, and U. Starke. Quasi-free-standing epitaxial graphene on SiC obtained by hydrogen intercalation. *Phys. Rev. Lett.*, 103(24):246804, dec 2009. doi: 10.1103/physrevlett.103.246804.

[46] I. Gierz, T. Suzuki, R. T. Weitz, D. S. Lee, B. Krauss, C. Riedl, U. Starke, H. Höchst, J. H. Smet, C. R. Ast, and K. Kern. Electronic decoupling of an epitaxial graphene monolayer by gold intercalation. *Physical Review B*, 81(23):235408, jun 2010. doi: 10.1103/physrevb.81.235408.

[47] A. L. Walter, K.-J. Jeon, A. Bostwick, F. Speck, M. Ostler, T. Seyller, L. Moreschini, Y. S. Kim, Y. J. Chang, K. Horn, and E. Rotenberg. Highly p-doped epitaxial graphene obtained by fluorine intercalation. *Applied Physics Letters*, 98(18):184102, may 2011. doi: 10.1063/1.3586256.

[48] D. B. Farmer, R. Golizadeh-Mojarad, V. Perebeinos, Y.-M. Lin, G. S. Tulevski, J. C. Tsang, and P. Avouris. Chemical doping and electron-hole conduction asymmetry in graphene devices. *Nano Letters*, 9(1):388, jan 2009. doi: 10.1021/nl803214a.

[49] M. Ishigami, J. H. Chen, W. G. Cullen, M. S. Fuhrer, and E. D. Williams. Atomic structure of graphene on SiO2. *Nano Letters*, 7(6):1643, jun 2007. doi: 10.1021/nl070613a.

[50] A. Pirkle, J. Chan, A. Venugopal, D. Hinojos, C. W. Magnuson, S. McDonnell, L. Colombo, E. M. Vogel, R. S. Ruoff, and R. M. Wallace. The effect of chemical residues on the physical and electrical properties of chemical vapor deposited graphene transferred to SiO2. *Applied Physics Letters*, 99(12):122108, sep 2011. doi: 10.1063/1.3643444.

[51] S.-H. Ji, J. B. Hannon, R. M. Tromp, V. Perebeinos, J. Tersoff, and F. M. Ross. Atomic-scale transport in epitaxial graphene. *Nat Mater*, 11(2):114, nov 2011. doi: 10.1038/nmat3170.

[52] R. Hobara, S. Yoshimoto, T. Ikuno, M. Katayama, N. Yamauchi, W. Wongwiriyapan, S. ichi Honda, I. Matsuda, S. Hasegawa, and K. Oura. Electronic transport in multiwalled carbon nanotubes contacted with patterned electrodes. *Japanese Journal of Applied Physics*, 43(No. 8B):L1081, jul 2004. doi: 10.1143/jjap.43.l1081.

[53] H. Okino, I. Matsuda, R. Hobara, Y. Hosomura, S. Hasegawa, and P. A. Bennett. In situ resistance measurements of epitaxial cobalt silicide nanowires on Si(110). *Applied Physics Letters*, 86(23):233108, jun 2005. doi: 10.1063/1.1948519.

[54] T. Tono, T. Hirahara, and S. Hasegawa. In situ transport measurements on ultrathin Bi(111) films using a magnetic tip: possible detection of current-induced spin polarization in the surface states. *New J. Phys.*, 15(10):105018, oct 2013. doi: 10.1088/1367-2630/15/10/105018.

[55] N. W. Ashcroft and N. D. Mermin. *Solid State Physics*. Cengage Learning Emea, 1976.

[56] S. Datta. *Electronic Transport in Mesoscopic Systems*. Cambridge University Press, 1995. doi: 10.1017/cbo9780511805776.

[57] D. K. Schroder. *Semiconductor material and device characterization*. Wiley-Interscience, 2006.

[58] S. Yoshimoto, Y. Murata, K. Kubo, K. Tomita, K. Motoyoshi, T. Kimura, H. Okino, R. Hobara, I. Matsuda, S. ichi Honda, M. Katayama, and S. Hasegawa. Four-point probe resistance measurements using PtIr-coated carbon nanotube tips. *Nano Letters*, 7(4):956, apr 2007. doi: 10.1021/nl0630182.

[59] F. Wang, D. H. Petersen, T. M. Hansen, T. R. Henriksen, P. Boggild, and O. Hansen. Sensitivity study of micro four-point probe measurements on small samples. *Journal of Vacuum Science & Technology B: Microelectronics and Nanometer Structures*, 28(1):C1C34, mar 2010. doi: 10.1116/1.3224889.

[60] J. D. Buron, D. H. Petersen, P. Bøggild, D. G. Cooke, M. Hilke, J. Sun, E. Whiteway, P. F. Nielsen, O. Hansen, A. Yurgens, and P. U. Jepsen. Graphene

conductance uniformity mapping. *Nano Letters*, 12(10):5074, oct 2012. doi: 10.1021/nl301551a.

[61] S. Hasegawa. Multi-probe scanning tunneling microscopy. In *Scanning Probe Microscopy*, pages 480–505. Springer New York, 2007. doi: 10.1007/978-0-387-28668-6_18.

[62] T. Kanagawa, R. Hobara, I. Matsuda, T. Tanikawa, A. Natori, and S. Hasegawa. Anisotropy in conductance of a quasi-one-dimensional metallic surface state measured by a square micro-four-point probe method. *Phys. Rev. Lett.*, 91(3):036805, jul 2003. doi: 10.1103/physrevlett.91.036805.

[63] J. W. Wells, J. F. Kallehauge, and P. Hofmann. Surface-sensitive conductance measurements on clean and stepped semiconductor surfaces: Numerical simulations of four point probe measurements. *Surface Science*, 602(10):1742, may 2008. doi: 10.1016/j.susc.2008.02.041.

[64] P. Anderson, D. Thouless, E. Abrahams, and D. Fisher. New method for a scaling theory of localization. *Physical Review B*, 22(8):3519, oct 1980. doi: 10.1103/physrevb.22.3519.

[65] R. Landauer. Electrical resistance of disordered one-dimensional lattices. *Philosophical Magazine*, 21(172):863, apr 1970. doi: 10.1080/14786437008238472.

[66] P. A. Lee. Disordered electronic systems. *Reviews of Modern Physics*, 57(2):287, apr 1985. doi: 10.1103/revmodphys.57.287.

[67] N. F. Mott. Conduction in non-crystalline materials. *Philosophical Magazine*, 19(160):835, apr 1969. doi: 10.1080/14786436908216338.

[68] B. I. Shklovskii and A. L. Efros. *Electronic Properties of Doped Semiconductors*. Springer Series in Solid-State Sciences, 1984.

[69] M. Büttiker. Symmetry of electrical conduction. *IBM Journal of Research and Development*, 32(3):317, may 1988. doi: 10.1147/rd.323.0317.

[70] M. Büttiker. Four-terminal phase-coherent conductance. *Phys. Rev. Lett.*, 57(14):1761, oct 1986. doi: 10.1103/physrevlett.57.1761.

[71] M. Büttiker. Role of quantum coherence in series resistors. *Physical Review B*, 33(5):3020, mar 1986. doi: 10.1103/physrevb.33.3020.

[72] P. Brouwer and C. Beenakker. Effect of a voltage probe on the phase-coherent conductance of a ballistic chaotic cavity. *Physical Review B*, 51(12):7739, mar 1995. doi: 10.1103/physrevb.51.7739.

[73] T. Ihn. *Semiconductor Nanostructures*. Oxford University Press, 2010.

[74] R. de Picciotto, H. L. Stormer, L. N. Pfeiffer, K. W. Baldwin, and K. W. West. Four-terminal resistance of a ballistic quantum wire. *Nature*, 411(6833):51, may 2001. doi: 10.1038/35075009.

[75] K. S. Novoselov, D. Jiang, F. Schedin, T. J. Booth, V. V. Khotkevich, S. V. Morozov, and A. K. Geim. Two-dimensional atomic crystals. *Proceedings of the National Academy of Sciences*, 102(30):10451, jul 2005. doi: 10.1073/pnas.0502848102.

[76] A. H. C. Neto, N. M. R. Peres, K. S. Novoselov, and A. K. Geim. The electronic properties of graphene. *Reviews of Modern Physics*, 81(1):109, jan 2009. doi: 10.1103/revmodphys.81.109.

[77] T. Fang, A. Konar, H. Xing, and D. Jena. Carrier statistics and quantum capacitance of graphene sheets and ribbons. *Applied Physics Letters*, 91(9):092109, aug 2007. doi: 10.1063/1.2776887.

[78] S. Adam, E. H. Hwang, V. M. Galitski, and S. D. Sarma. A self-consistent theory for graphene transport. *Proceedings of the National Academy of Sciences*, 104(47): 18392, nov 2007. doi: 10.1073/pnas.0704772104.

[79] A. Ludwig, M. Fisher, R. Shankar, and G. Grinstein. Integer quantum hall transition: An alternative approach and exact results. *Physical Review B*, 50(11): 7526, sep 1994. doi: 10.1103/physrevb.50.7526.

[80] K. S. Novoselov, A. K. Geim, S. V. Morozov, D. Jiang, M. I. Katsnelson, I. V. Grigorieva, S. V. Dubonos, and A. A. Firsov. Two-dimensional gas of massless Dirac fermions in graphene. *Nature*, 438(7065):197, nov 2005. doi: 10.1038/nature04233.

[81] F. Miao, S. Wijeratne, Y. Zhang, U. C. Coskun, W. Bao, and C. N. Lau. Phase-coherent transport in graphene quantum billiards. *Science*, 317(5844):1530, sep 2007. doi: 10.1126/science.1144359.

[82] P. E. Allain and J. N. Fuchs. Klein tunneling in graphene: optics with massless electrons. *Eur. Phys. J. B.*, 83(3):301, oct 2011. doi: 10.1140/epjb/e2011-20351-3.

[83] M. M. Fogler, D. S. Novikov, L. I. Glazman, and B. I. Shklovskii. Effect of disorder on a graphene p-n junction. *Physical Review B*, 77(7):075420, feb 2008. doi: 10.1103/physrevb.77.075420.

[84] S. K. Lilov. Study of the equilibrium processes in the gas phase during silicon carbide sublimation. *Materials Science and Engineering: B*, 21(1):65, sep 1993. doi: 10.1016/0921-5107(93)90267-q.

[85] J. Hass, R. Feng, T. Li, X. Li, Z. Zong, W. A. de Heer, P. N. First, E. H. Conrad, C. A. Jeffrey, and C. Berger. Highly ordered graphene for two dimensional electronics. *Applied Physics Letters*, 89(14):143106, oct 2006. doi: 10.1063/1.2358299.

[86] T. Ohta, F. E. Gabaly, A. Bostwick, J. L. McChesney, K. V. Emtsev, A. K. Schmid, T. Seyller, K. Horn, and E. Rotenberg. Morphology of graphene thin film growth on SiC(0001). *New J. Phys.*, 10(2):023034, feb 2008. doi: 10.1088/1367-2630/10/2/023034.

[87] R. Kaplan. Surface structure and composition of beta- and 6H-SiC. *Surface Science*, 215(1-2):111, may 1989. doi: 10.1016/0039-6028(89)90704-8.

[88] I. Forbeaux, J.-M. Themlin, A. Charrier, F. Thibaudau, and J.-M. Debever. Solid-state graphitization mechanisms of silicon carbide 6H–SiC polar faces. *Applied Surface Science*, 162-163:406, aug 2000. doi: 10.1016/s0169-4332(00)00224-5.

[89] F. Owman, C. Hallin, P. Mårtensson, and E. Janzén. Removal of polishing-induced damage from 6H-SiC(0001) substrates by hydrogen etching. *Journal of Crystal Growth*, 167(1-2):391, sep 1996. doi: 10.1016/0022-0248(96)00296-5.

[90] V. Ramachandran, M. F. Brady, A. R. Smith, R. M. Feenstra, and D. W. Greve. Preparation of atomically flat surfaces on silicon carbide using hydrogen etching. *Journal of Electronic Materials*, 27(4):308, apr 1998. doi: 10.1007/s11664-998-0406-7.

[91] M. Ostler, F. Speck, M. Gick, and T. Seyller. Automated preparation of high-quality epitaxial graphene on 6H-SiC(0001). *physica status solidi (b)*, 247(11-12): 2924, sep 2010. doi: 10.1002/pssb.201000220.

[92] W. A. de Heer, C. Berger, X. Wu, P. N. First, E. H. Conrad, X. Li, T. Li, M. Sprinkle, J. Hass, M. L. Sadowski, M. Potemski, and G. Martinez. Epitaxial graphene. *Solid State Communications*, 143(1-2):92, jul 2007. doi: 10.1016/j.ssc.2007.04.023.

[93] J. Hass, F. Varchon, J. Millán-Otoya, M. Sprinkle, N. Sharma, W. de Heer, C. Berger, P. First, L. Magaud, and E. Conrad. Why Multilayer Graphene on 4H-SiC($000\bar{1}$) Behaves Like a Single Sheet of Graphene. *Phys. Rev. Lett.*, 100(12): 125504, mar 2008. doi: 10.1103/physrevlett.100.125504.

[94] M. Sprinkle, D. Siegel, Y. Hu, J. Hicks, A. Tejeda, A. Taleb-Ibrahimi, P. Le Fèvre, F. Bertran, S. Vizzini, H. Enriquez, S. Chiang, P. Soukiassian, C. Berger, W. A. de Heer, A. Lanzara, and E. H. Conrad. First direct observation of a nearly ideal graphene band structure. *Phys. Rev. Lett.*, 103(22):226803, nov 2009. doi: 10.1103/PhysRevLett.103.226803.

[95] C. Riedl and U. Starke. Structural properties of the graphene-SiC(0001) interface as a key for the preparation of homogeneous large-terrace graphene surfaces. *Physical Review B*, 76(24):245406, dec 2007. doi: 10.1103/physrevb.76.245406.

[96] K. V. Emtsev, F. Speck, T. Seyller, and L. Ley. Interaction, growth, and ordering of epitaxial graphene on SiC{0001} surfaces: A comparative photoelectron spectroscopy study. *Physical Review B*, 77(15):155303, apr 2008. doi: 10.1103/physrevb.77.155303.

[97] S. Forti, K. V. Emtsev, C. Coletti, A. A. Zakharov, C. Riedl, and U. Starke. Large-area homogeneous quasifree standing epitaxial graphene on SiC(0001): Electronic and structural characterization. *Physical Review B*, 84(12):125449, sep 2011. doi: 10.1103/physrevb.84.125449.

[98] J. Ristein, S. Mammadov, and T. Seyller. Origin of doping in quasi-free-standing graphene on silicon carbide. *Phys. Rev. Lett.*, 108(24):246104, jun 2012. doi: 10.1103/physrevlett.108.246104.

[99] J. Hass, W. A. de Heer, and E. H. Conrad. The growth and morphology of epitaxial multilayer graphene. *Journal of Physics: Condensed Matter*, 20(32):323202, jul 2008. doi: 10.1088/0953-8984/20/32/323202.

[100] R. Tromp and J. Hannon. Thermodynamics and kinetics of graphene growth on SiC(0001). *Phys. Rev. Lett.*, 102(10):106104, mar 2009. doi: 10.1103/physrevlett.102.106104.

[101] X. Yu, C. Hwang, C. Jozwiak, A. Köhl, A. Schmid, and A. Lanzara. New synthesis method for the growth of epitaxial graphene. *Journal of Electron Spectroscopy and Related Phenomena*, 184(3-6):100, apr 2011. doi: 10.1016/j.elspec.2010.12.034.

[102] E. Rauls, Z. Hajnal, P. Deák, and T. Frauenheim. Theoretical study of the nonpolar surfaces and their oxygen passivation in 4H- and 6H-SiC. *Physical Review B*, 64(24):245323, dec 2001. doi: 10.1103/physrevb.64.245323.

[103] M. Ostler, I. Deretzis, S. Mammadov, F. Giannazzo, G. Nicotra, C. Spinella, T. Seyller, and A. L. Magna. Direct growth of quasi-free-standing epitaxial graphene on nonpolar SiC surfaces. *Physical Review B*, 88(8):085408, aug 2013. doi: 10.1103/physrevb.88.085408.

[104] K. Wakabayashi, K. ichi Sasaki, T. Nakanishi, and T. Enoki. Electronic states of graphene nanoribbons and analytical solutions. *Science and Technology of Advanced Materials*, 11(5):054504, oct 2010. doi: 10.1088/1468-6996/11/5/054504.

[105] Y.-W. Son, M. L. Cohen, and S. G. Louie. Energy gaps in graphene nanoribbons. *Phys. Rev. Lett.*, 97(21):216803, nov 2006. doi: 10.1103/PhysRevLett.97.216803.

[106] S. Dutta and S. K. Pati. Novel properties of graphene nanoribbons: a review. *Journal of Materials Chemistry*, 20(38):8207, jun 2010. doi: 10.1039/c0jm00261e.

[107] Y.-W. Son, M. L. Cohen, and S. G. Louie. Half-metallic graphene nanoribbons. *Nature*, 444(7117):347, nov 2006. doi: 10.1038/nature05180.

[108] L. Pisani, J. Chan, B. Montanari, and N. Harrison. Electronic structure and magnetic properties of graphitic ribbons. *Physical Review B*, 75(6):064418, feb 2007. doi: 10.1103/physrevb.75.064418.

[109] J. Slater. Magnetic effects and the hartree-fock equation. *Physical Review*, 82(4): 538, may 1951. doi: 10.1103/physrev.82.538.

[110] L. F. Huang, G. R. Zhang, X. H. Zheng, P. L. Gong, T. F. Cao, and Z. Zeng. Understanding and tuning the quantum-confinement effect and edge magnetism in zigzag graphene nanoribbon. *Journal of Physics: Condensed Matter*, 25(5): 055304, jan 2013. doi: 10.1088/0953-8984/25/5/055304.

[111] F. Muñoz-Rojas, J. Fernández-Rossier, and J. Palacios. Giant magnetoresistance in ultrasmall graphene based devices. *Phys. Rev. Lett.*, 102(13):136810, apr 2009. doi: 10.1103/physrevlett.102.136810.

[112] K. Wakabayashi, Y. Takane, and M. Sigrist. Perfectly conducting channel and universality crossover in disordered graphene nanoribbons. *Phys. Rev. Lett.*, 99 (3):036601, Jul 2007. doi: 10.1103/PhysRevLett.99.036601.

[113] H. Jaksch and J.-P. Vermeulen. New developments in gemini fesem technology. Technical report, Carl Zeiss SMT Oberkochen, Germany.

[114] J. Baringhaus, F. Edler, C. Neumann, C. Stampfer, S. Forti, U. Starke, and C. Tegenkamp. Local transport measurements on epitaxial graphene. *Applied Physics Letters*, 103(11):111604, sep 2013. doi: 10.1063/1.4821364.

[115] J. Röhrl, M. Hundhausen, K. V. Emtsev, T. Seyller, R. Graupner, and L. Ley. Raman spectra of epitaxial graphene on SiC(0001). *Applied Physics Letters*, 92 (20):201918, may 2008. doi: 10.1063/1.2929746.

[116] D. Graf, F. Molitor, K. Ensslin, C. Stampfer, A. Jungen, C. Hierold, and L. Wirtz. Spatially Resolved Raman Spectroscopy of Single- and Few-Layer Graphene. *Nano Letters*, 7(2):238, feb 2007. doi: 10.1021/nl061702a.

[117] D. S. Lee, C. Riedl, B. Krauss, K. von Klitzing, U. Starke, and J. H. Smet. Raman spectra of epitaxial graphene on SiC and of epitaxial graphene transferred to SiO2. *Nano Letters*, 8(12):4320, dec 2008. doi: 10.1021/nl802156w.

[118] A. C. Ferrari. Raman spectroscopy of graphene and graphite: Disorder, electron–phonon coupling, doping and nonadiabatic effects. *Solid State Communications*, 143(1-2):47, jul 2007. doi: 10.1016/j.ssc.2007.03.052.

[119] F. Fromm, M. H. O. Jr, A. Molina-Sánchez, M. Hundhausen, J. M. J. Lopes, H. Riechert, L. Wirtz, and T. Seyller. Contribution of the buffer layer to the Raman spectrum of epitaxial graphene on SiC(0001). *New J. Phys.*, 15(4):043031, apr 2013. doi: 10.1088/1367-2630/15/4/043031.

[120] Y. Zhang, V. W. Brar, F. Wang, C. Girit, Y. Yayon, M. Panlasigui, A. Zettl, and M. F. Crommie. Giant phonon-induced conductance in scanning tunnelling spectroscopy of gate-tunable graphene. *Nature Physics*, 4(8):627, jul 2008. doi: 10.1038/nphys1022.

[121] M. Ridene, T. Wassmann, E. Pallecchi, G. Rodary, J. C. Girard, and A. Ouerghi. Epitaxial graphene on step bunching of a 6H-SiC(0001) substrate: Aromatic ring pattern and Van Hove singularities. *Applied Physics Letters*, 102(11):111610, mar 2013. doi: 10.1063/1.4796170.

[122] V. W. Brar, S. Wickenburg, M. Panlasigui, C.-H. Park, T. O. Wehling, Y. Zhang, R. Decker, Ç. Girit, A. V. Balatsky, S. G. Louie, A. Zettl, and M. F. Crommie. Observation of carrier-density-dependent many-body effects in graphene via

tunneling spectroscopy. *Phys. Rev. Lett.*, 104(3):036805, jan 2010. doi: 10.1103/physrevlett.104.036805.

[123] M. Z. Hossain, M. A. Walsh, and M. C. Hersam. Scanning tunneling microscopy, spectroscopy, and nanolithography of epitaxial graphene chemically modified with aryl moieties. *J. Am. Chem. Soc.*, 132(43):15399, nov 2010. doi: 10.1021/ja107085n.

[124] G. Li, A. Luican, and E. Y. Andrei. Scanning tunneling spectroscopy of graphene on graphite. *Phys. Rev. Lett.*, 102(17):176804, apr 2009. doi: 10.1103/physrevlett.102.176804.

[125] S. Y. Zhou, G.-H. Gweon, A. V. Fedorov, P. N. First, W. A. de Heer, D.-H. Lee, F. Guinea, A. H. C. Neto, and A. Lanzara. Substrate-induced bandgap opening in epitaxial graphene. *Nat Mater*, 6(11):916, nov 2007. doi: 10.1038/nmat2056.

[126] G. M. Rutter, N. P. Guisinger, J. N. Crain, E. A. A. Jarvis, M. D. Stiles, T. Li, P. N. First, and J. A. Stroscio. Imaging the interface of epitaxial graphene with silicon carbide via scanning tunneling microscopy. *Physical Review B*, 76(23):235416, dec 2007. doi: 10.1103/physrevb.76.235416.

[127] P. Lauffer, K. V. Emtsev, R. Graupner, T. Seyller, and L. Ley. Atomic and electronic structure of few-layer graphene on SiC(0001) studied with scanning tunneling microscopy and spectroscopy. *Physical Review B*, 77(15):155426, apr 2008. doi: 10.1103/physrevb.77.155426.

[128] V. W. Brar, Y. Zhang, Y. Yayon, T. Ohta, J. L. McChesney, A. Bostwick, E. Rotenberg, K. Horn, and M. F. Crommie. Scanning tunneling spectroscopy of inhomogeneous electronic structure in monolayer and bilayer graphene on SiC. *Applied Physics Letters*, 91(12):122102, 2007. doi: 10.1063/1.2771084.

[129] T. Wehling, I. Grigorenko, A. Lichtenstein, and A. Balatsky. Phonon-mediated tunneling into graphene. *Phys. Rev. Lett.*, 101(21):216803, nov 2008. doi: 10.1103/physrevlett.101.216803.

[130] B. C. Stipe, M. A. Rezaei, and W. Ho. Single-molecule vibrational spectroscopy and microscopy. *Science*, 280(5370):1732, 1998. doi: 10.1126/science.280.5370.1732.

[131] M. Mohr, J. Maultzsch, E. Dobardžić, S. Reich, I. Milošević, M. Damnjanović, A. Bosak, M. Krisch, and C. Thomsen. Phonon dispersion of graphite by inelastic x-ray scattering. *Physical Review B*, 76(3):035439, jul 2007. doi: 10.1103/physrevb.76.035439.

[132] J. Cervenka, K. van de Ruit, and C. F. J. Flipse. Local enhancement of inelastic tunnelling in epitaxial graphene on SiC(0001). *physica status solidi (b)*, 247(11-12):2992, oct 2010. doi: 10.1002/pssb.201000167.

[133] J. Cervenka, K. van de Ruit, and C. F. J. Flipse. Giant inelastic tunneling in epitaxial graphene mediated by localized states. *Physical Review B*, 81(20):205403, may 2010. doi: 10.1103/physrevb.81.205403.

[134] R. Dombrowski, C. Steinebach, C. Wittneven, M. Morgenstern, and R. Wiesendanger. Tip-induced band bending by scanning tunneling spectroscopy of the states of the tip-induced quantum dot on InAs(110). *Physical Review B*, 59(12): 8043, mar 1999. doi: 10.1103/physrevb.59.8043.

[135] R. M. Feenstra. Tunneling spectroscopy of the GaAs(110) surface. *Journal of Vacuum Science & Technology B: Microelectronics and Nanometer Structures*, 5(4): 923, jul 1987. doi: 10.1116/1.583691.

[136] J. Jobst, D. Waldmann, F. Speck, R. Hirner, D. K. Maude, T. Seyller, and H. B. Weber. Transport properties of high-quality epitaxial graphene on 6H-SiC(0001). *Solid State Communications*, 151(16):1061, aug 2011. doi: 10.1016/j.ssc.2011.05.015.

[137] F. Speck, J. Jobst, F. Fromm, M. Ostler, D. Waldmann, M. Hundhausen, H. B. Weber, and T. Seyller. The quasi-free-standing nature of graphene on H-saturated SiC(0001). *Applied Physics Letters*, 99(12):122106, sep 2011. doi: 10.1063/1.3643034.

[138] A. J. M. Giesbers, P. Procházka, and C. F. J. Flipse. Surface phonon scattering in epitaxial graphene on 6H-SiC. *Physical Review B*, 87(19):195405, may 2013. doi: 10.1103/physrevb.87.195405.

[139] V. Perebeinos and P. Avouris. Inelastic scattering and current saturation in graphene. *Physical Review B*, 81(19):195442, may 2010. doi: 10.1103/physrevb.81.195442.

[140] K. Zou, X. Hong, D. Keefer, and J. Zhu. Deposition of High-Quality HfO2 on Graphene and the Effect of Remote Oxide Phonon Scattering. *Phys. Rev. Lett.*, 105(12):126601, sep 2010. doi: 10.1103/physrevlett.105.126601.

[141] S. Tanabe, Y. Sekine, H. Kageshima, M. Nagase, and H. Hibino. Carrier transport mechanism in graphene on SiC(0001). *Physical Review B*, 84(11):115458, sep 2011. doi: 10.1103/physrevb.84.115458.

[142] L. Vitali, M. Schneider, K. Kern, L. Wirtz, and A. Rubio. Phonon and plasmon excitation in inelastic electron tunneling spectroscopy of graphite. *Physical Review B*, 69(12):121414, mar 2004. doi: 10.1103/physrevb.69.121414.

[143] E. Hwang and S. D. Sarma. Acoustic phonon scattering limited carrier mobility in two-dimensional extrinsic graphene. *Physical Review B*, 77(11):115449, mar 2008. doi: 10.1103/physrevb.77.115449.

[144] H. Suzuura and T. Ando. Phonons and electron-phonon scattering in carbon nanotubes. *Physical Review B*, 65(23):235412, may 2002. doi: 10.1103/physrevb.65.235412.

[145] L. Woods and G. Mahan. Electron-phonon effects in graphene and armchair (10, 10) single-wall carbon nanotubes. *Physical Review B*, 61(16):10651, apr 2000. doi: 10.1103/physrevb.61.10651.

[146] M. Kruskopf, K. Pierz, S. Wundrack, R. Stosch, T. Dziomba, C.-C. Kalmbach, A. Müller, J. Baringhaus, C. Tegenkamp, F. J. Ahlers, and H. W. Schumacher. Epitaxial graphene on SiC: modification of structural and electron transport properties by substrate pretreatment. *Journal of Physics: Condensed Matter*, 27 (18):185303, apr 2015. doi: 10.1088/0953-8984/27/18/185303.

[147] P. J. James, M. Antognozzi, J. Tamayo, T. J. McMaster, J. M. Newton, and M. J. Miles. Interpretation of Contrast in Tapping Mode AFM and Shear Force Microscopy. *Langmuir*, 17(2):349, jan 2001. doi: 10.1021/la000332h.

[148] C. Dimitrakopoulos, Y.-M. Lin, A. Grill, D. B. Farmer, M. Freitag, Y. Sun, S.-J. Han, Z. Chen, K. A. Jenkins, Y. Zhu, Z. Liu, T. J. McArdle, J. A. Ott, R. Wisnieff, and P. Avouris. Wafer-scale epitaxial graphene growth on the Si-face of hexagonal SiC(0001) for high frequency transistors. *Journal of Vacuum Science & Technology B: Microelectronics and Nanometer Structures*, 28(5):985, sep 2010. doi: 10.1116/1.3480961.

[149] S. Goler, C. Coletti, V. Piazza, P. Pingue, F. Colangelo, V. Pellegrini, K. V. Emtsev, S. Forti, U. Starke, F. Beltram, and S. Heun. Revealing the atomic structure of the buffer layer between SiC(0001) and epitaxial graphene. *Carbon*, 51:249, jan 2013. doi: 10.1016/j.carbon.2012.08.050.

[150] I. Iezhokin, P. Offermans, S. H. Brongersma, A. J. M. Giesbers, and C. F. J. Flipse. High sensitive quasi freestanding epitaxial graphene gas sensor on 6H-SiC. *Applied Physics Letters*, 103(5):053514, aug 2013. doi: 10.1063/1.4816762.

[151] J. B. Hannon and R. M. Tromp. Pit formation during graphene synthesis on SiC(0001): In situ electron microscopy. *Physical Review B*, 77(24):241404, jun 2008. doi: 10.1103/physrevb.77.241404.

[152] A. Ruammaitree, H. Nakahara, K. Akimoto, K. Soda, and Y. Saito. Determination of non-uniform graphene thickness on SiC(0001) by x-ray diffraction. *Applied Surface Science*, 282:297, oct 2013. doi: 10.1016/j.apsusc.2013.05.122.

[153] N. Camara, G. Rius, J.-R. Huntzinger, A. Tiberj, L. Magaud, N. Mestres, P. Godignon, and J. Camassel. Early stage formation of graphene on the C-face of 6H-SiC. *Applied Physics Letters*, 93(26):263102, dec 2008. doi: 10.1063/1.3056655.

[154] W. Zhu, C. Dimitrakopoulos, M. Freitag, and P. Avouris. Layer number determination and thickness-dependent properties of graphene grown on SiC. *IEEE Trans. Nanotechnology*, 10(5):1196, sep 2011. doi: 10.1109/tnano.2011.2130536.

[155] H. Hiura, H. Miyazaki, and K. Tsukagoshi. Determination of the number of graphene layers: Discrete distribution of the secondary electron intensity stemming from individual graphene layers. *Appl. Phys. Express*, 3(9):095101, aug 2010. doi: 10.1143/apex.3.095101.

[156] H. Hibino, H. Kageshima, M. Kotsugi, F. Maeda, F.-Z. Guo, and Y. Watanabe. Dependence of electronic properties of epitaxial few-layer graphene on the number of layers investigated by photoelectron emission microscopy. *Physical Review B*, 79(12):125437, mar 2009. doi: 10.1103/physrevb.79.125437.

[157] G. F. Dionne. Origin of secondary-electron-emission yield-curve parameters. *J. Appl. Phys.*, 46(8):3347, 1975. doi: 10.1063/1.322061.

[158] C. Riedl, C. Coletti, and U. Starke. Structural and electronic properties of epitaxial graphene on SiC(0001): a review of growth, characterization, transfer doping and hydrogen intercalation. *Journal of Physics D: Applied Physics*, 43(37):374009, sep 2010. doi: 10.1088/0022-3727/43/37/374009.

[159] T. Ohta. Controlling the electronic structure of bilayer graphene. *Science*, 313 (5789):951, aug 2006. doi: 10.1126/science.1130681.

[160] T. Ohta, A. Bostwick, J. McChesney, T. Seyller, K. Horn, and E. Rotenberg. Interlayer interaction and electronic screening in multilayer graphene investigated with angle-resolved photoemission spectroscopy. *Phys. Rev. Lett.*, 98(20):206802, may 2007. doi: 10.1103/physrevlett.98.206802.

[161] E. C. Peters, A. J. M. Giesbers, and M. Burghard. Variable range hopping in graphene antidot lattices. *Phys. Status Solidi B*, 249(12):2522, nov 2012. doi: 10.1002/pssb.201200177.

[162] H. Zhang, J. Lu, W. Shi, Z. Wang, T. Zhang, M. Sun, Y. Zheng, Q. Chen, N. Wang, J.-J. Lin, and P. Sheng. Large-scale mesoscopic transport in nanostructured graphene. *Phys. Rev. Lett.*, 110(6):066805, feb 2013. doi: 10.1103/physrevlett.110.066805.

[163] M. K. Yakes, D. Gunlycke, J. L. Tedesco, P. M. Campbell, R. L. Myers-Ward, C. R. Eddy, D. K. Gaskill, P. E. Sheehan, and A. R. Laracuente. Conductance anisotropy in epitaxial graphene sheets generated by substrate interactions. *Nano Letters*, 10(5):1559, may 2010. doi: 10.1021/nl9035302.

[164] J. A. Robinson, M. Wetherington, J. L. Tedesco, P. M. Campbell, X. Weng, J. Stitt, M. A. Fanton, E. Frantz, D. Snyder, B. L. VanMil, G. G. Jernigan, R. L. Myers-Ward, C. R. Eddy, and D. K. Gaskill. Correlating Raman Spectral Signatures with Carrier Mobility in Epitaxial Graphene: A Guide to Achieving High Mobility on the Wafer Scale. *Nano Letters*, 9(8):2873, aug 2009. doi: 10.1021/nl901073g.

[165] V. Pereira, A. C. Neto, and N. Peres. Tight-binding approach to uniaxial strain in graphene. *Physical Review B*, 80(4):045401, jul 2009. doi: 10.1103/physrevb.80.045401.

[166] T. Low, V. Perebeinos, J. Tersoff, and P. Avouris. Deformation and scattering in graphene over substrate steps. *Phys. Rev. Lett.*, 108(9):096601, mar 2012. doi: 10.1103/physrevlett.108.096601.

[167] T. Ciuk, S. Cakmakyapan, E. Ozbay, P. Caban, K. Grodecki, A. Krajewska, I. Pasternak, J. Szmidt, and W. Strupinski. Step-edge-induced resistance anisotropy in quasi-free-standing bilayer chemical vapor deposition graphene on SiC. *J. Appl. Phys.*, 116(12):123708, sep 2014. doi: 10.1063/1.4896581.

[168] F. Giannazzo, I. Deretzis, A. L. Magna, F. Roccaforte, and R. Yakimova. Electronic transport at monolayer-bilayer junctions in epitaxial graphene on SiC. *Physical Review B*, 86(23):235422, dec 2012. doi: 10.1103/physrevb.86.235422.

[169] T. Yager, A. Lartsev, R. Yakimova, S. Lara-Avila, and S. Kubatkin. The effect of bilayer domains on electronic transport properties of epitaxial graphene on SiC. arXiv:1502.02013, 2015.

[170] M. Ezawa. Peculiar width dependence of the electronic properties of carbon nanoribbons. *Phys. Rev. B*, 73(4):045432, jan 2006. doi: 10.1103/PhysRevB.73.045432.

[171] V. Barone, O. Hod, and G. E. Scuseria. Electronic structure and stability of semiconducting graphene nanoribbons. *Nano Letters*, 6(12):2748, dec 2006. doi: 10.1021/nl0617033.

[172] L. Wang, I. Meric, P. Y. Huang, Q. Gao, Y. Gao, H. Tran, T. Taniguchi, K. Watanabe, L. M. Campos, D. A. Muller, J. Guo, P. Kim, J. Hone, K. L. Shepard, and C. R. Dean. One-dimensional electrical contact to a two-dimensional material. *Science*, 342(6158):614, oct 2013. doi: 10.1126/science.1244358.

[173] J. Baringhaus, F. Edler, and C. Tegenkamp. Edge-states in graphene nanoribbons: a combined spectroscopy and transport study. *Journal of Physics: Condensed Matter*, 25(39):392001, aug 2013. doi: 10.1088/0953-8984/25/39/392001.

[174] J. Baringhaus, M. Ruan, F. Edler, A. Tejeda, M. Sicot, A. Taleb-Ibrahimi, A.-P. Li, Z. Jiang, E. H. Conrad, C. Berger, C. Tegenkamp, and W. A. de Heer. Exceptional ballistic transport in epitaxial graphene nanoribbons. *Nature*, 506(7488):349, feb 2014. doi: 10.1038/nature12952.

[175] J. Baringhaus, J. Aprojanz, J. Wiegand, D. Laube, M. Halbauer, J. Hübner, M. Oestreich, and C. Tegenkamp. Growth and characterization of sidewall graphene nanoribbons. *Applied Physics Letters*, 106(4):043109, jan 2015. doi: 10.1063/1.4907041.

[176] S. Tanaka, K. Morita, and H. Hibino. Anisotropic layer-by-layer growth of graphene on vicinal SiC(0001) surfaces. *Physical Review B*, 81(4):041406, jan 2010. doi: 10.1103/physrevb.81.041406.

[177] J. Robinson, X. Weng, K. Trumbull, R. Cavalero, M. Wetherington, E. Frantz, M. LaBella, Z. Hughes, M. Fanton, and D. Snyder. Nucleation of epitaxial graphene on SiC(0001). *ACS Nano*, 4(1):153, jan 2010. doi: 10.1021/nn901248j.

[178] A. Nakajima, H. Yokoya, Y. Furukawa, and H. Yonezu. Step control of vicinal 6H-SiC(0001) surface by H2 etching. *J. Appl. Phys.*, 97(10):104919, may 2005. doi: 10.1063/1.1901838.

[179] S. Nie, C. Lee, R. Feenstra, Y. Ke, R. Devaty, W. Choyke, C. Inoki, T. Kuan, and G. Gu. Step formation on hydrogen-etched 6H-SiC(0001) surfaces. *Surface Science*, 602(17):2936, sep 2008. doi: 10.1016/j.susc.2008.07.021.

[180] H. Nakagawa, S. Tanaka, and I. Suemune. Self-ordering of nanofacets on vicinal SiC surfaces. *Phys. Rev. Lett.*, 91(22):226107, nov 2003. doi: 10.1103/physrevlett.91.226107.

[181] M. Ruan, Y. Hu, Z. Guo, R. Dong, J. Palmer, J. Hankinson, C. Berger, and W. A. de Heer. Epitaxial graphene on silicon carbide: Introduction to structured graphene. *MRS Bull.*, 37(12):1138, nov 2012. doi: 10.1557/mrs.2012.231.

[182] W. Norimatsu and M. Kusunoki. Formation process of graphene on SiC(0001). *Physica E: Low-dimensional Systems and Nanostructures*, 42(4):691, feb 2010. doi: 10.1016/j.physe.2009.11.151.

[183] W. Norimatsu and M. Kusunoki. Growth of graphene from SiC(0001) surfaces and its mechanisms. *Semicond. Sci. Technol.*, 29(6):064009, may 2014. doi: 10.1088/0268-1242/29/6/064009.

[184] G. Nicotra, Q. M. Ramasse, I. Deretzis, A. L. Magna, C. Spinella, and F. Giannazzo. Delaminated graphene at silicon carbide facets: Atomic scale imaging and spectroscopy. *ACS Nano*, 7(4):3045, apr 2013. doi: 10.1021/nn305922u.

[185] I. Palacio, A. Celis, M. N. Nair, A. Gloter, A. Zobelli, M. Sicot, D. Malterre, M. S. Nevius, W. A. de Heer, C. Berger, E. H. Conrad, A. Taleb-Ibrahimi, and A. Tejeda. Atomic structure of epitaxial graphene sidewall nanoribbons: Flat graphene, miniribbons, and the confinement gap. *Nano Letters*, 15(1):182, jan 2015. doi: 10.1021/nl503352v.

[186] L. G. Cançado, A. Jorio, E. H. M. Ferreira, F. Stavale, C. A. Achete, R. B. Capaz, M. V. O. Moutinho, A. Lombardo, T. S. Kulmala, and A. C. Ferrari. Quantifying defects in graphene via Raman spectroscopy at different excitation energies. *Nano Letters*, 11(8):3190, aug 2011. doi: 10.1021/nl201432g.

[187] D. Bischoff, J. Güttinger, S. Dröscher, T. Ihn, K. Ensslin, and C. Stampfer. Raman spectroscopy on etched graphene nanoribbons. *J. Appl. Phys.*, 109(7):073710, apr 2011. doi: 10.1063/1.3561838.

[188] A. Grüneis, R. Saito, G. Samsonidze, T. Kimura, M. Pimenta, A. Jorio, A. Filho, G. Dresselhaus, and M. Dresselhaus. Inhomogeneous optical absorption

around the k point in graphite and carbon nanotubes. *Physical Review B*, 67 (16):165402, apr 2003. doi: 10.1103/physrevb.67.165402.

[189] L. Cançado, M. Pimenta, B. Neves, G. Medeiros-Ribeiro, T. Enoki, Y. Kobayashi, K. Takai, K. ichi Fukui, M. Dresselhaus, R. Saito, and A. Jorio. Anisotropy of the Raman Spectra of Nanographite Ribbons. *Phys. Rev. Lett.*, 93(4):047403, jul 2004. doi: 10.1103/physrevlett.93.047403.

[190] C. Casiraghi, A. Hartschuh, H. Qian, S. Piscanec, C. Georgi, A. Fasoli, K. S. Novoselov, D. M. Basko, and A. C. Ferrari. Raman spectroscopy of graphene edges. *Nano Letters*, 9(4):1433, apr 2009. doi: 10.1021/nl8032697.

[191] B. Krauss, P. Nemes-Incze, V. Skakalova, L. P. Biro, K. von Klitzing, and J. H. Smet. Raman scattering at pure graphene zigzag edges. *Nano Letters*, 10(11): 4544, nov 2010. doi: 10.1021/nl102526s.

[192] U. Starke, J. Schardt, J. Bernhardt, M. Franke, and K. Heinz. Stacking transformation from hexagonal to cubic SiC induced by surface reconstruction: A seed for heterostructure growth. *Phys. Rev. Lett.*, 82(10):2107, mar 1999. doi: 10.1103/physrevlett.82.2107.

[193] M. S. Nevius, F. Wang, C. Mathieu, N. Barrett, A. Sala, T. O. Menteş, A. Locatelli, and E. H. Conrad. The bottom-up growth of edge specific graphene nanoribbons. *Nano Letters*, 14(11):6080, nov 2014. doi: 10.1021/nl502942z.

[194] J. Hicks, A. Tejeda, A. Taleb-Ibrahimi, M. S. Nevius, F. Wang, K. Shepperd, J. Palmer, F. Bertran, P. L. Fèvre, J. Kunc, W. A. de Heer, C. Berger, and E. H. Conrad. A wide-bandgap metal–semiconductor–metal nanostructure made entirely from graphene. *Nature Physics*, 9(1):49, nov 2012. doi: 10.1038/nphys2487.

[195] J. Cervenka, K. van der Ruit, and K. Flipse. Effect of local doping on the electronic properties of epitaxial graphene on SiC. *physica status solidi (a)*, 207(3): 595, mar 2010. doi: 10.1002/pssa.200982767.

[196] F. Giannazzo, I. Deretzis, G. Nicotra, G. Fisichella, C. Spinella, F. Roccaforte, and A. L. Magna. Electronic properties of epitaxial graphene residing on SiC facets probed by conductive atomic force microscopy. *Applied Surface Science*, 291:53, feb 2014. doi: 10.1016/j.apsusc.2013.10.041.

[197] F. Besenbacher. Scanning tunnelling microscopy studies of metal surfaces. *Rep. Prog. Phys.*, 59(12):1737, dec 1996. doi: 10.1088/0034-4885/59/12/004.

[198] R. M. Feenstra, J. A. Stroscio, and A. Fein. Tunneling spectroscopy of the Si(111) 2 × 1 surface. *Surface Science*, 181(1-2):295, mar 1987. doi: 10.1016/0039-6028(87) 90170-1.

[199] A. Chaika, S. Bozhko, and I. Shvets. Imaging atomic orbitals with scanning tunneling microscopy. In *Fundamentals of Picoscience*, pages 319–350. Informa UK Limited, sep 2013. doi: 10.1201/b15523-24.

[200] A. V. de Parga, O. Hernan, R. Miranda, A. L. Yeyati, N. Mingo, A. Martin-Rodero, and F. Flores. Electron resonances in sharp tips and their role in tunneling spectroscopy. *Phys. Rev. Lett.*, 80(2):357, jan 1998. doi: 10.1103/physrevlett.80.357.

[201] C. Tao, L. Jiao, O. V. Yazyev, Y.-C. Chen, J. Feng, X. Zhang, R. B. Capaz, J. M. Tour, A. Zettl, S. G. Louie, H. Dai, and M. F. Crommie. Spatially resolving edge states of chiral graphene nanoribbons. *Nature Physics*, 7(8):616, may 2011. doi: 10.1038/nphys1991.

[202] Z. Klusek, Z. Waqar, E. Denisov, T. Kompaniets, I. Makarenko, A. Titkov, and A. Bhatti. Observations of local electron states on the edges of the circular pits on hydrogen-etched graphite surface by scanning tunneling spectroscopy. *Applied Surface Science*, 161(3-4):508, jul 2000. doi: 10.1016/s0169-4332(00)00374-3.

[203] Y. Kobayashi, K. ichi Fukui, T. Enoki, K. Kusakabe, and Y. Kaburagi. Observation of zigzag and armchair edges of graphite using scanning tunneling microscopy and spectroscopy. *Physical Review B*, 71(19):193406, may 2005. doi: 10.1103/physrevb.71.193406.

[204] Y. Niimi, T. Matsui, H. Kambara, K. Tagami, M. Tsukada, and H. Fukuyama. Scanning tunneling microscopy and spectroscopy of the electronic local density of states of graphite surfaces near monoatomic step edges. *Physical Review B*, 73(8):085421, feb 2006. doi: 10.1103/physrevb.73.085421.

[205] Y. Sugiyama, O. Kubo, R. Omura, M. Shigehara, H. Tabata, N. Mori, and M. Katayama. Spectroscopic study of graphene nanoribbons formed by crystallographic etching of highly oriented pyrolytic graphite. *Applied Physics Letters*, 105(12):123116, sep 2014. doi: 10.1063/1.4896594.

[206] K. A. Ritter and J. W. Lyding. The influence of edge structure on the electronic properties of graphene quantum dots and nanoribbons. *Nat Mater*, 8(3):235, feb 2009. doi: 10.1038/nmat2378.

[207] M. Pan, E. C. Girão, X. Jia, S. Bhaviripudi, Q. Li, J. Kong, V. Meunier, and M. S. Dresselhaus. Topographic and spectroscopic characterization of electronic edge states in CVD grown graphene nanoribbons. *Nano Letters*, 12(4):1928, apr 2012. doi: 10.1021/nl204392s.

[208] Y. Lu and J. Guo. Band gap of strained graphene nanoribbons. *Nano Research*, 3(3):189, mar 2010. doi: 10.1007/s12274-010-1022-4.

[209] C. Chen, J. Z. Wu, K. T. Lam, G. Hong, M. Gong, B. Zhang, Y. Lu, A. L. Antaris, S. Diao, J. Guo, and H. Dai. Graphene nanoribbons under mechanical strain. *Adv. Mater.*, 27(2):303, oct 2014. doi: 10.1002/adma.201403750.

[210] Y. Li, W. Zhang, M. Morgenstern, and R. Mazzarello. Electronic and magnetic properties of zigzag graphene nanoribbons on the (111) surface of Cu, Ag, and Au. *Phys. Rev. Lett.*, 110(21):216804, may 2013. doi: 10.1103/physrevlett.110.216804.

[211] D. Gunlycke, H. Lawler, and C. White. Room-temperature ballistic transport in narrow graphene strips. *Physical Review B*, 75(8):085418, feb 2007. doi: 10.1103/physrevb.75.085418.

[212] C. Berger, Y. Yi, Z. L. Wang, and W. A. de Heer. Multiwalled carbon nanotubes are ballistic conductors at room temperature. *Applied Physics A: Materials Science & Processing*, 74(3):363, mar 2002. doi: 10.1007/s003390201279.

[213] A. S. Mayorov, R. V. Gorbachev, S. V. Morozov, L. Britnell, R. Jalil, L. A. Ponomarenko, P. Blake, K. S. Novoselov, K. Watanabe, T. Taniguchi, and A. K. Geim. Micrometer-scale ballistic transport in encapsulated graphene at room temperature. *Nano Letters*, 11(6):2396, may 2011. doi: 10.1021/nl200758b.

[214] T. Filleter, K. V. Emtsev, T. Seyller, and R. Bennewitz. Local work function measurements of epitaxial graphene. *Applied Physics Letters*, 93(13):133117, oct 2008. doi: 10.1063/1.2993341.

[215] A. J. Huber, A. Ziegler, T. Köck, and R. Hillenbrand. Infrared nanoscopy of strained semiconductors. *Nature Nanotech*, 4(3):153, jan 2009. doi: 10.1038/nnano.2008.399.

[216] P. Hermann, A. Hoehl, P. Patoka, F. Huth, E. Rühl, and G. Ulm. Near-field imaging and nano-fourier-transform infrared spectroscopy using broadband synchrotron radiation. *Opt. Express*, 21(3):2913, feb 2013. doi: 10.1364/oe.21.002913.

[217] J. L. Lado, N. Garcia-Martinez, and J. Fernandez-Rossier. Edge states in graphene-like systems. arXiv:1502.07112, 2015.

[218] O. Yazyev and M. Katsnelson. Magnetic correlations at graphene edges: Basis for novel spintronics devices. *Phys. Rev. Lett.*, 100(4):047209, jan 2008. doi: 10.1103/physrevlett.100.047209.

[219] W.-Y. He and L. He. Coupled spin and pseudomagnetic field in graphene nanoribbons. *Phys. Rev. B*, 88(8):085411, aug 2013. doi: 10.1103/PhysRevB.88.085411.

[220] H. Santos, M. C. Muñoz, M. P. López-Sancho, and L. Chico. Interplay between symmetry and spin-orbit coupling on graphene nanoribbons. *Physical Review B*, 87(23):235402, jun 2013. doi: 10.1103/physrevb.87.235402.

[221] G. P. Tang, Z. H. Zhang, X. Q. Deng, Z. Q. Fan, and H. L. Zhu. Tuning spin polarization and spin transport of zigzag graphene nanoribbons by line defects. *Phys. Chem. Chem. Phys.*, 17(1):638, oct 2014. doi: 10.1039/c4cp03837a.

[222] G. Lippert, J. Dabrowski, Y. Yamamoto, F. Herziger, J. Maultzsch, J. Baringhaus, C. Tegenkamp, M. C. Lemme, W. Mehr, and G. Lupina. Molecular beam epitaxy of graphene on mica. *Phys. Status Solidi B*, 249(12):2507, oct 2012. doi: 10.1002/pssb.201200104.

[223] Y.-M. Lin, V. Perebeinos, Z. Chen, and P. Avouris. Electrical observation of subband formation in graphene nanoribbons. *Phys. Rev. B*, 78(16):161409, Oct 2008. doi: 10.1103/PhysRevB.78.161409.

[224] C. L. Kane and E. J. Mele. Z2 Topological Order and the Quantum Spin Hall Effect. *Phys. Rev. Lett.*, 95(14):146802, sep 2005. doi: 10.1103/physrevlett.95.146802.

[225] C. L. Kane and E. J. Mele. Quantum Spin Hall Effect in Graphene. *Phys. Rev. Lett.*, 95(22):226801, nov 2005. doi: 10.1103/physrevlett.95.226801.

[226] H. Min, J. E. Hill, N. A. Sinitsyn, B. R. Sahu, L. Kleinman, and A. H. MacDonald. Intrinsic and Rashba spin-orbit interactions in graphene sheets. *Physical Review B*, 74(16):165310, oct 2006. doi: 10.1103/physrevb.74.165310.

[227] Y. Yao, F. Ye, X.-L. Qi, S.-C. Zhang, and Z. Fang. Spin-orbit gap of graphene: First-principles calculations. *Physical Review B*, 75(4):041401, jan 2007. doi: 10.1103/physrevb.75.041401.

[228] J. C. Boettger and S. B. Trickey. First-principles calculation of the spin-orbit splitting in graphene. *Physical Review B*, 75(12):121402, mar 2007. doi: 10.1103/physrevb.75.121402.

[229] D. Huertas-Hernando, F. Guinea, and A. Brataas. Spin-orbit coupling in curved graphene, fullerenes, nanotubes, and nanotube caps. *Physical Review B*, 74(15):155426, oct 2006. doi: 10.1103/physrevb.74.155426.

[230] J.-S. Jeong, J. Shin, and H.-W. Lee. Curvature-induced spin-orbit coupling and spin relaxation in a chemically clean single-layer graphene. *Physical Review B*, 84(19):195457, nov 2011. doi: 10.1103/physrevb.84.195457.

[231] Z.-D. Chu and L. He. Crossover from room-temperature double-channel ballistic transport to single-channel ballistic transport in zigzag graphene nanoribbons. arXiv:1408.0327, 2015.

[232] A. C. Neto and F. Guinea. Impurity-induced spin-orbit coupling in graphene. *Phys. Rev. Lett.*, 103(2):026804, jul 2009. doi: 10.1103/physrevlett.103.026804.

[233] F. Muñoz-Rojas, D. Jacob, J. Fernández-Rossier, and J. J. Palacios. Coherent transport in graphene nanoconstrictions. *Physical Review B*, 74(19):195417, nov 2006. doi: 10.1103/physrevb.74.195417.

[234] F. Muñoz-Rojas, J. Fernández-Rossier, L. Brey, and J. J. Palacios. Performance limits of graphene-ribbon field-effect transistors. *Physical Review B*, 77(4):045301, jan 2008. doi: 10.1103/physrevb.77.045301.

[235] A. Rycerz, J. Tworzydło, and C. W. J. Beenakker. Valley filter and valley valve in graphene. *Nature Physics*, 3(3):172, feb 2007. doi: 10.1038/nphys547.

[236] F. Molitor, C. Stampfer, J. Güttinger, A. Jaobsen, T. Ihn, and K. Ensslin. Energy and transport gaps in etched graphene nanoribbons. *Semicond. Sci. Technol.*, 25 (3):1, feb 2010. doi: 10.1088/0268-1242/25/3/034002.

[237] P. Darancet, V. Olevano, and D. Mayou. Coherent electronic transport through graphene constrictions: Subwavelength regime and optical analogy. *Phys. Rev. Lett.*, 102(13):136803, mar 2009. doi: 10.1103/physrevlett.102.136803.

[238] S. Ihnatsenka and G. Kirczenow. Conductance quantization in graphene nanoconstrictions with mesoscopically smooth but atomically stepped boundaries. *Physical Review B*, 85(12):121407, mar 2012. doi: 10.1103/physrevb.85.121407.

[239] T. Gunst, J.-T. Lü, P. Hedegård, and M. Brandbyge. Phonon excitation and instabilities in biased graphene nanoconstrictions. *Physical Review B*, 88(16): 161401, oct 2013. doi: 10.1103/physrevb.88.161401.

[240] D.-H. Kim, J.-Y. Koo, and J.-J. Kim. Cutting of multiwalled carbon nanotubes by a negative voltage tip of an atomic force microscope: A possible mechanism. *Physical Review B*, 68(11):113406, sep 2003. doi: 10.1103/physrevb.68.113406.

[241] A. Kaiser and Y. Park. Current-voltage characteristics of conducting polymers and carbon nanotubes. *Synthetic Metals*, 152(1-3):181, sep 2005. doi: 10.1016/j.synthmet.2005.07.245.

[242] C. Stampfer, J. Güttinger, S. Hellmüller, F. Molitor, K. Ensslin, and T. Ihn. Energy gaps in etched graphene nanoribbons. *Phys. Rev. Lett.*, 102(5):056403, feb 2009. doi: 10.1103/physrevlett.102.056403.

[243] F. Molitor, A. Jacobsen, C. Stampfer, J. Güttinger, T. Ihn, and K. Ensslin. Transport gap in side-gated graphene constrictions. *Physical Review B*, 79(7):075426, feb 2009. doi: 10.1103/physrevb.79.075426.

[244] F. Sols, F. Guinea, and A. H. C. Neto. Coulomb blockade in graphene nanoribbons. *Phys. Rev. Lett.*, 99(16):166803, oct 2007. doi: 10.1103/PhysRevLett.99.166803.

[245] D. Querlioz, Y. Apertet, A. Valentin, K. Huet, A. Bournel, S. Galdin-Retailleau, and P. Dollfus. Suppression of the orientation effects on bandgap in graphene nanoribbons in the presence of edge disorder. *Applied Physics Letters*, 92(4): 042108, jan 2008. doi: 10.1063/1.2838354.

[246] D. Gunlycke, D. A. Areshkin, and C. T. White. Semiconducting graphene nanostrips with edge disorder. *Applied Physics Letters*, 90(14):142104, apr 2007. doi: 10.1063/1.2718515.

[247] J. Bai, R. Cheng, F. Xiu, L. Liao, M. Wang, A. Shailos, K. L. Wang, Y. Huang, and X. Duan. Very large magnetoresistance in graphene nanoribbons. *Nature Nanotech*, 5(9):655, aug 2010. doi: 10.1038/nnano.2010.154.

[248] J. Velasco, L. Jing, W. Bao, Y. Lee, P. Kratz, V. Aji, M. Bockrath, C. N. Lau, C. Varma, R. Stillwell, D. Smirnov, F. Zhang, J. Jung, and A. H. MacDonald. Transport spectroscopy of symmetry-broken insulating states in bilayer graphene. *Nature Nanotech*, 7(3):156, jan 2012. doi: 10.1038/nnano.2011.251.

[249] F. Freitag, M. Weiss, R. Maurand, J. Trbovic, and C. Schönenberger. Spin symmetry of the bilayer graphene ground state. *Physical Review B*, 87(16):161402, apr 2013. doi: 10.1103/physrevb.87.161402.

[250] F. Freitag, J. Trbovic, M. Weiss, and C. Schönenberger. Spontaneously gapped ground state in suspended bilayer graphene. *Phys. Rev. Lett.*, 108(7):076602, feb 2012. doi: 10.1103/physrevlett.108.076602.

[251] F. Freitag, M. Weiss, R. Maurand, J. Trbovic, and C. Schönenberger. Homogeneity of bilayer graphene. *Solid State Communications*, 152(22):2053, nov 2012. doi: 10.1016/j.ssc.2012.09.001.

[252] B. Roy. Classification of massive and gapless phases in bilayer graphene. *Physical Review B*, 88(7):075415, aug 2013. doi: 10.1103/physrevb.88.075415.

[253] F. Giubileo, D. Roditchev, W. Sacks, R. Lamy, and J. Klein. Strong coupling and double-gap density of states in superconducting MgB 2. *Europhys. Lett.*, 58(5): 764, jun 2002. doi: 10.1209/epl/i2002-00415-5.

[254] P. J. Lowell, G. C. O'Neil, J. M. Underwood, and J. N. Ullom. Andreev reflections in micrometer-scale normal metal-insulator-superconductor tunnel junctions. *Journal of Low Temperature Physics*, 167(3-4):392, nov 2011. doi: 10.1007/s10909-011-0425-2.

[255] A. F. Young and P. Kim. Quantum interference and Klein tunnelling in graphene heterojunctions. *Nature Physics*, 5(3):222, feb 2009. doi: 10.1038/nphys1198.

[256] J. R. Williams, L. DiCarlo, and C. M. Marcus. Quantum hall effect in a gate-controlled p-n junction of graphene. *Science*, 317(5838):638, aug 2007. doi: 10.1126/science.1144657.

[257] B. Huard, J. A. Sulpizio, N. Stander, K. Todd, B. Yang, and D. Goldhaber-Gordon. Transport measurements across a tunable potential barrier in graphene. *Phys. Rev. Lett.*, 98(23):236803, jun 2007. doi: 10.1103/PhysRevLett.98.236803.

[258] I. Gierz, C. Riedl, U. Starke, C. R. Ast, and K. Kern. Atomic hole doping of graphene. *Nano Letters*, 8(12):4603, dec 2008. doi: 10.1021/nl802996s.

[259] W. Chen, S. Chen, D. C. Qi, X. Y. Gao, and A. T. S. Wee. Surface transfer p-type doping of epitaxial graphene. *J. Am. Chem. Soc.*, 129(34):10418, aug 2007. doi: 10.1021/ja071658g.

[260] C. Coletti, C. Riedl, D. S. Lee, B. Krauss, L. Patthey, K. von Klitzing, J. H. Smet, and U. Starke. Charge neutrality and band-gap tuning of epitaxial graphene on SiC by molecular doping. *Physical Review B*, 81(23):235401, jun 2010. doi: 10.1103/physrevb.81.235401.

[261] M. Petrović, I. Š. Rakić, S. Runte, C. Busse, J. T. Sadowski, P. Lazić, I. Pletikosić, Z.-H. Pan, M. Milun, P. Pervan, N. Atodiresei, R. Brako, D. Šokčević, T. Valla, T. Michely, and M. Kralj. The mechanism of caesium intercalation of graphene. *Nat Comms*, 4:2772, nov 2013. doi: 10.1038/ncomms3772.

[262] P. Sutter, J. T. Sadowski, and E. A. Sutter. Chemistry under cover: Tuning metal-graphene interaction by reactive intercalation. *J. Am. Chem. Soc.*, 132(23):8175, jun 2010. doi: 10.1021/ja102398n.

[263] C. Virojanadara, S. Watcharinyanon, A. A. Zakharov, and L. I. Johansson. Epitaxial graphene on 6H-SiC and Li intercalation. *Physical Review B*, 82(20):205402, nov 2010. doi: 10.1103/physrevb.82.205402.

[264] L. Kubler, K. Ait-Mansour, M. Diani, D. Dentel, J.-L. Bischoff, and M. Derivaz. Bidimensional intercalation of ge between SiC(0001) and a heteroepitaxial graphite top layer. *Physical Review B*, 72(11):115319, sep 2005. doi: 10.1103/physrevb.72.115319.

[265] K. V. Emtsev, A. A. Zakharov, C. Coletti, S. Forti, and U. Starke. Ambipolar doping in quasifree epitaxial graphene on SiC(0001) controlled by ge intercalation. *Physical Review B*, 84(12):125423, sep 2011. doi: 10.1103/physrevb.84.125423.

[266] J. Baringhaus, A. Stöhr, S. Forti, S. A. Krasnikov, A. A. Zakharov, U. Starke, and C. Tegenkamp. Bipolar gating of epitaxial graphene by intercalation of Ge. *Applied Physics Letters*, 104(26):261602, jul 2014. doi: http://dx.doi.org/10.1063/1.4886411.

[267] I. Deretzis and A. L. Magna. Ab Initio Study of Ge Intercalation in Epitaxial Graphene on SiC(0001) . *Appl. Phys. Express*, 4(12):125101, nov 2011. doi: 10.1143/apex.4.125101.

[268] T. P. Kaloni, M. U. Kahaly, Y. C. Cheng, and U. Schwingenschlögl. Ge-intercalated graphene: The origin of the p-type to n-type transition. *EPL*, 99(5):57002, sep 2012. doi: 10.1209/0295-5075/99/57002.

[269] B. Premlal, M. Cranney, F. Vonau, D. Aubel, D. Casterman, M. M. D. Souza, and L. Simon. Surface intercalation of gold underneath a graphene monolayer on SiC(0001) studied by scanning tunneling microscopy and spectroscopy. *Applied Physics Letters*, 94(26):263115, 2009. doi: 10.1063/1.3168502.

[270] S. K. Sharma. *Atomic and Nuclear Physics*. Pearson Education India, 2008.

[271] D. Wei, Y. Liu, Y. Wang, H. Zhang, L. Huang, and G. Yu. Synthesis of n-doped graphene by chemical vapor deposition and its electrical properties. *Nano Letters*, 9(5):1752, may 2009. doi: 10.1021/nl803279t.

[272] J. Baringhaus, A. Stöhr, S. Forti, U. Starke, and C. Tegenkamp. Ballistic bipolar junctions in chemically gated graphene ribbons. *Scientific Reports*, 5:9955, apr 2015. doi: 10.1038/srep09955.

[273] P. Rickhaus, R. Maurand, M.-H. Liu, M. Weiss, K. Richter, and C. Schönenberger. Ballistic interferences in suspended graphene. *Nat Comms*, 4:2342, aug 2013. doi: 10.1038/ncomms3342.

[274] A. L. Grushina, D.-K. Ki, and A. F. Morpurgo. A ballistic pn junction in suspended graphene with split bottom gates. *Applied Physics Letters*, 102(22):223102, jun 2013. doi: 10.1063/1.4807888.

[275] P. Rickhaus, P. Makk, M.-H. Liu, E. Tóvári, M. Weiss, R. Maurand, K. Richter, and C. Schönenberger. Snake trajectories in ultraclean graphene p–n junctions. *Nat Comms*, 6:6470, mar 2015. doi: 10.1038/ncomms7470.

[276] V. V. Cheianov, V. Falko, and B. L. Altshuler. The focusing of electron flow and a veselago lens in graphene p-n junctions. *Science*, 315(5816):1252, mar 2007. doi: 10.1126/science.1138020.

[277] A. Rahman, J. W. Guikema, N. M. Hassan, and N. Marković. Angle-dependent transmission in graphene heterojunctions. *Applied Physics Letters*, 106(1):013112, jan 2015. doi: 10.1063/1.4905566.

[278] S. Sutar, E. S. Comfort, J. Liu, T. Taniguchi, K. Watanabe, and J. U. Lee. Angle-dependent carrier transmission in graphene p–n junctions. *Nano Letters*, 12(9): 4460, sep 2012. doi: 10.1021/nl3011897.

[279] R. N. Sajjad, S. Sutar, J. U. Lee, and A. W. Ghosh. Manifestation of chiral tunneling at a tilted graphene p-n junction. *Phys. Rev. B*, 86(15):155412, oct 2012. doi: 10.1103/PhysRevB.86.155412.

[280] C. Cocchi, D. Prezzi, A. Calzolari, and E. Molinari. Spin-transport selectivity upon Co adsorption on antiferromagnetic graphene nanoribbons. *J. Chem. Phys.*, 133(12):124703, 2010. doi: 10.1063/1.3478317.

[281] M. Gmitra, D. Kochan, and J. Fabian. Spin-orbit coupling in hydrogenated graphene. *Phys. Rev. Lett.*, 110(24):246602, jun 2013. doi: 10.1103/physrevlett.110.246602.

[282] N. Tombros, C. Jozsa, M. Popinciuc, H. T. Jonkman, and B. J. van Wees. Electronic spin transport and spin precession in single graphene layers at room temperature. *Nature*, 448(7153):571, jul 2007. doi: 10.1038/nature06037.

[283] W. Han, K. McCreary, K. Pi, W. Wang, Y. Li, H. Wen, J. Chen, and R. Kawakami. Spin transport and relaxation in graphene. *Journal of Magnetism and Magnetic Materials*, 324(4):369, feb 2012. doi: 10.1016/j.jmmm.2011.08.001.

[284] J. Avila, I. Razado-Colambo, S. Lorcy, B. Lagarde, J.-L. Giorgetta, F. Polack, and M. C. Asensio. ANTARES, a scanning photoemission microscopy beamline at

SOLEIL. *J. Phys.: Conf. Ser.*, 425(19):192023, mar 2013. doi: 10.1088/1742-6596/425/19/192023.

[285] G. Lippert, J. Dabrowski, M. Lemme, C. Marcus, O. Seifarth, and G. Lupina. Direct graphene growth on insulator. *Phys. Status Solidi B*, 248(11):2619, aug 2011. doi: 10.1002/pssb.201100052.

[286] G. Wang, M. Zhang, Y. Zhu, G. Ding, D. Jiang, Q. Guo, S. Liu, X. Xie, P. K. Chu, Z. Di, and X. Wang. Direct growth of graphene film on germanium substrate. *Scientific Reports*, 3:2465, aug 2013. doi: 10.1038/srep02465.

[287] J.-H. Lee, E. K. Lee, W.-J. Joo, Y. Jang, B.-S. Kim, J. Y. Lim, S.-H. Choi, S. J. Ahn, J. R. Ahn, M.-H. Park, C.-W. Yang, B. L. Choi, S.-W. Hwang, and D. Whang. Wafer-scale growth of single-crystal monolayer graphene on reusable hydrogen-terminated germanium. *Science*, 344(6181):286, apr 2014. doi: 10.1126/science.1252268.

[288] G. Lippert, J. Dąbrowski, T. Schroeder, M. A. Schubert, Y. Yamamoto, F. Herziger, J. Maultzsch, J. Baringhaus, C. Tegenkamp, M. C. Asensio, J. Avila, and G. Lupina. Graphene grown on Ge(001) from atomic source. *Carbon*, 75:104, aug 2014. doi: 10.1016/j.carbon.2014.03.042.

[289] H. Fukidome, Y. Miyamoto, H. Handa, E. Saito, and M. Suemitsu. Epitaxial growth processes of graphene on silicon substrates. *Japanese Journal of Applied Physics*, 49(1):01AH03, jan 2010. doi: 10.1143/jjap.49.01ah03.

[290] M. Suemitsu and H. Fukidome. Epitaxial graphene on silicon substrates. *Journal of Physics D: Applied Physics*, 43(37):374012, sep 2010. doi: 10.1088/0022-3727/43/37/374012.

[291] R. Szoszkiewicz, T. Okada, S. C. Jones, T.-D. Li, W. P. King, S. R. Marder, and E. Riedo. High-speed, sub-15 nm feature size thermochemical nanolithography. *Nano Letters*, 7(4):1064, apr 2007. doi: 10.1021/nl070300f.

[292] F. Schwabl. *Quantenmechanik I*. Springer, 2007.

[293] J. Bardeen. Tunnelling from a many-particle point of view. *Phys. Rev. Lett.*, 6(2):57, jan 1961. doi: 10.1103/PhysRevLett.6.57.

[294] N. Boulanger-Lewandowski and A. Rochefort. Intrusive STM imaging. *Phys. Rev. B*, 83(11):115430, Mar 2011. doi: 10.1103/PhysRevB.83.115430.

[295] J. Tersoff and D. R. Hamann. Theory of the scanning tunneling microscope. *Phys. Rev. B*, 31(2):805, jan 1985. doi: 10.1103/PhysRevB.31.805.

[296] G. P. Kochanski. Nonlinear alternating-current tunneling microscopy. *Phys. Rev. Lett.*, 62(19):2285, may 1989. doi: 10.1103/PhysRevLett.62.2285.

[297] M. Ternes. *Scanning tunneling spectroscopy at the single atom scale*. PhD thesis, Ecole polytechnique federale de Lausanne, 2006.

[298] L. E. C. van de Leemput and H. van Kempen. Scanning tunnelling microscopy. *Rep. Prog. Phys.*, 55(8):1165, aug 1992. doi: 10.1088/0034-4885/55/8/002.

[299] F. J. Giessibl. Advances in atomic force microscopy. *Reviews of Modern Physics*, 75(3):949, jul 2003. doi: 10.1103/revmodphys.75.949.

[300] M. Nonnenmacher, M. P. O'Boyle, and H. K. Wickramasinghe. Kelvin probe force microscopy. *Applied Physics Letters*, 58(25):2921, jun 1991. doi: 10.1063/1.105227.

[301] F. Huth, A. Govyadinov, S. Amarie, W. Nuansing, F. Keilmann, and R. Hillenbrand. Nano-FTIR absorption spectroscopy of molecular fingerprints at 20 nm spatial resolution. *Nano Letters*, 12(8):3973, aug 2012. doi: 10.1021/nl301159v.

[302] F. Keilmann and R. Hillenbrand. Near-field microscopy by elastic light scattering from a tip. *Philosophical Transactions of the Royal Society A: Mathematical, Physical and Engineering Sciences*, 362(1817):787, apr 2004. doi: 10.1098/rsta.2003.1347.

[303] M. P. Seah and W. A. Dench. Quantitative electron spectroscopy of surfaces: A standard data base for electron inelastic mean free paths in solids. *Surf. Interface Anal.*, 1(1):2, feb 1979. doi: 10.1002/sia.740010103.

[304] M. H. Hoegen. Growth of semiconductor layers studied by spot profile analysing low energy electron diffraction. *Zeitschrift für Kristallographie*, 214 (10):591, jan 1999. doi: 10.1524/zkri.1999.214.10.591.

[305] R. Rao, D. Tishler, J. Katoch, and M. Ishigami. Multiphonon Raman scattering in graphene. *Physical Review B*, 84(11):113406, sep 2011. doi: 10.1103/physrevb.84.113406.

[306] F. Tuinstra. Raman spectrum of graphite. *J. Chem. Phys.*, 53(3):1126, aug 1970. doi: 10.1063/1.1674108.

[307] A. Gupta, G. Chen, P. Joshi, S. Tadigadapa, and Eklund. Raman Scattering from High-Frequency Phonons in Supported n-Graphene Layer Films. *Nano Letters*, 6(12):2667, dec 2006. doi: 10.1021/nl061420a.

[308] R. Saito, M. Hofmann, G. Dresselhaus, A. Jorio, and M. S. Dresselhaus. Raman spectroscopy of graphene and carbon nanotubes. *Advances in Physics*, 60(3):413, jun 2011. doi: 10.1080/00018732.2011.582251.

[309] A. C. Ferrari, J. C. Meyer, V. Scardaci, C. Casiraghi, M. Lazzeri, F. Mauri, S. Piscanec, D. Jiang, K. S. Novoselov, S. Roth, and A. K. Geim. Raman spectrum of graphene and graphene layers. *Phys. Rev. Lett.*, 97(18):187401, oct 2006. doi: 10.1103/physrevlett.97.187401.

[310] F. Herziger, M. Calandra, P. Gava, P. May, M. Lazzeri, F. Mauri, and J. Maultzsch. Two-Dimensional Analysis of the Double-Resonant 2D Raman Mode in Bilayer Graphene. *Phys. Rev. Lett.*, 113(18):187401, oct 2014. doi: 10.1103/physrevlett.113.187401.

[311] R. Yang, Q. S. Huang, X. L. Chen, G. Y. Zhang, and H.-J. Gao. Substrate doping effects on Raman spectrum of epitaxial graphene on SiC. *J. Appl. Phys.*, 107(3): 034305, feb 2010. doi: 10.1063/1.3283922.

[312] P. Yih, V. Saxena, and A. Steckl. A review of SiC reactive ion etching in fluorinated plasmas. *physica status solidi (b)*, 202(1):605, jul 1997. doi: 10.1002/1521-3951(199707)202:1<605::aid-pssb605>3.0.co;2-y.

CURRICULUM VITAE

PERSONAL INFORMATION

NAME	Jens Baringhaus
DATE OF BIRTH	14.06.1987 in Hannover

EDUCATION

1999-2005	Gymnasium, St.-Ursula-Schule in Hannover
2006-2009	Bachelor studies, Physics, Gottfried Wilhelm Leibniz Universität Hannover Thesis: *Plasmonische Anregungen in epitaktischen Graphenschichten*
2009-2011	Master studies, Physics, Gottfried Wilhelm Leibniz Universität Hannover Thesis: *Wachstum und Charakterisierung von Graphen-Nanostrukturen*
2011-2015	Doctoral studies at Institut für Festkörperphysik, Gottfried Wilhelm Leibniz Universität Hannover Thesis: *Mesoscopic transport phenomena in epitaxial graphene nanostructures: A surface science approach*

CIVILIAN SERVICE

2005-2006	Landesbildungszentrum für Blinde in Hannover

PUBLICATIONS

PRINTED

1. M. Kruskopf, K. Pierz, S. Wundrack, R. Stosch, T. Dziomba, C.-C. Kalmbach, A. Müller, J. Baringhaus, C. Tegenkamp, F. J. Ahlers, and Hans W. Schumacher. Epitaxial graphene on SiC: modification of structural and electron transport properties by substrate pretreatment. *Journal of Physics: Condensed Matter*, 27(18):185303, apr 2015.

2. J. Baringhaus, A. Stöhr, S. Forti, U. Starke, and C. Tegenkamp. Ballistic bipolar junctions in chemically gated graphene ribbons. *Scientific Reports*, 5:9955, apr 2015.

3. J. Baringhaus, J. Aprojanz, J. Wiegand, D. Laube, M. Halbauer, J. Hübner, M. Oestreich, and C. Tegenkamp. Growth and characterization of sidewall graphene nanoribbons. *Applied Physics Letters*, 106(4):043109, jan 2015.

4. G. Lippert, J. Dabrowski, T. Schroeder, Y. Yamamoto, F. Herziger, J. Maultzsch, J. Baringhaus, C. Tegenkamp, M. C. Sansio, J. Avila, and G. Lupina. Graphene Grown on Ge(001) from Atomic Source. *CARBON*, 74:104, aug 2014.

5. J. Baringhaus, A. Stöhr, S. Forti, S. A. Krasnikov, A. A. Zakharov, U. Starke, and C. Tegenkamp. Bipolar gating of epitaxial graphene by intercalation of Ge. *Applied Physics Letters*, 104(26):261602, jul 2014.

6. J. Baringhaus, M. Ruan, F. Edler, A. Tejeda, M. Sicot, A. Taleb-Ibrahimi, A.-P. Li, Z. Jiang, E. H. Conrad, C. Berger, C. Tegenkamp, and W. A. de Heer. Exceptional ballistic transport in epitaxial graphene nanoribbons. *Nature*, 506(7488):349, feb 2014.

7. J. Baringhaus, F. Edler, C. Neumann, C. Stampfer, U. Starke, and C. Tegenkamp. Local transport measurements on epitaxial graphene. *Applied Physics Letters*, 103(11):111604, sep 2013.

8. J. Baringhaus, F. Edler, and C. Tegenkamp. A combined spectroscopy and transport study: edge-states in graphene nanoribbons. *Journal of Physics: Condensed Matter*, 103(39):111604, aug 2013.

9. G. Lippert, J. Dabrowski, Y. Yamamoto, F. Herziger, J. Maultzsch, J. Baringhaus, C. Tegenkamp, M. Lemme, W. Mehr, and G. Lupina. Molecular Beam Epitaxy of Graphene on Mica. *physisca status solidi b*, 249(12):2507 oct 2012.

10. T. Block, C. Tegenkamp, J. Baringhaus, T. Inaoka, and H. Pfnür. Plasmons in Pb nanowire arrays on Si(557): Between one and two dimensions. *Physical Review B*, 84(20):205402, nov 2011.

11. H. Pfnür, T. Langer, J. Baringhaus, and C. Tegenkamp. Multiple plasmon excitations in adsorbed two-dimensional systems. *Journal of Physics: Condensed Matter*, 23(11):112204, mar 2011
12. C. Tegenkamp, H. Pfnür, T. Langer, J. Baringhaus, and H. W. Schumacher. Plasmon electron-hole resonance in epitaxial graphene. *Journal of Physics: Condensed Matter*, 23(1):012001, nov 2010
13. T. Langer, J. Baringhaus, H. Pfnür, H. W. Schumacher, and C. Tegenkamp. Plasmon damping below the Landau regime: the role of defects in epitaxial graphene. *New Journal of Physics*, 12(3):033017, mar 2010

ACKNOWLEDGMENTS

An dieser Stelle möchte ich mich bei all denjenigen bedanken, die mich in den vergangenen Jahren bei der Fertigstellung dieser Arbeit, wissenschaftlich wie auch privat, unterstützt haben.

Ein besonderer Dank gebührt Prof. Christoph Tegenkamp für die intensive Betreuung, die vielen wissenschaftlichen Diskussionen sowie sein immer offenes Ohr für alle Fragen und Probleme. Seine Anregungen waren immer wieder die Triebfeder zu neuen Erkenntnissen und weiterem Fortschritt.

I want to thank Prof. Walter de Heer and Claire Berger from Georgia Tech for all their scientific input regarding the graphene nanoribbon project. Their expertise was a key factor for the understanding of the exceptional transport properties of graphene nanoribbons.

Prof. Ulrich Starke vom MPI Stuttgart möchte ich für die erfolgreiche Zusammenarbeit danken. Seine Erfahrung insbesondere bei der Herstellung und Interkalation von Graphenschichten haben Teile dieser Arbeit erst ermöglicht. Auch seinen Mitarbeitern Stiven Forti und Alexander Stöhr danke ich für ihr Engagement in diesem Projekt.

Des Weiteren möchte ich mich bei Prof. Thomas Seyller und Prof. Walter de Heer für die Übernahme des Korreferats meiner Dissertation bedanken.

Auch den weiteren Kooperationspartnern, die zu dieser Arbeit beigetragen haben und mit denen gemeinsame Veröffentlichungen realisiert wurden, möchte ich an dieser Stelle für die gute Zusammenarbeit danken. Hier zu nennen sind insbesondere Prof. Christoph Stampfer und Christoph Neumann von der RWTH Aachen für die Durchführung und Interpretation von Raman Messungen, Gunther Lippert vom IHP Frankfurt/Oder für die Kooperation zum Thema Graphen auf Isolatoren und Germanium sowie PD Hans Werner Schumacher, Klaus Pierz und Mattias Kruskopf von der PTB Braunschweig für die Zusammenarbeit beim Wachstum und der Charakterisierung von epitaktischen Graphenschichten. Des Weiteren möchte ich mich bei Andreas Huber von der Neaspec GmbH für die Charakterisierung von Proben mit s-SNOM bedanken. Ausdrücklich möchte ich auch den theoretischen Beitrag von Mikkel Settnes von der DTU Nanotech zur Interpretation der Ergebnisse an Graphen Nanoconstrictions hervorheben.

Allen Bachelor- und Masterstudenten, die ich während ihrer Abschlussarbeiten betreuen durfte, danke ich für ihre Mitarbeit und ihren Einsatz. Ich danke Frederik Edler, Malte Halbauer, Dennis Laube, Maren Wehr und Johannes Aprojanz. Meinem Nachfolger Johannes Aprojanz wünsche ich zudem weiterhin viel Erfolg mit dem Graphenprojekt.

Thomas Langer, der mich während meiner eigenen Bachelor- und Masterarbeit betreut hat, danke ich besonders für die Einführung in das Thema Graphen und alle

Tricks und Kniffe, die er mir in dieser Zeit vermittelt hat und die mir die Laborarbeit oft erleichtert haben.

Prof. Pfnür danke ich für den Antrieb, die eigenen Messergebnisse immer kritisch zu hinterfragen und die vielen wissenschaftlichen Diskussionen.

Die Abteilung ATMOS des Instituts für Festkörperphysik hat sich immer durch eine exzellente Arbeitsatmosphäre und ein stets freundliches Miteinander ausgezeichnet. Hier möchte ich namentlich Thomas Langer, Daniel Lükermann, Ulrich Krieg, Tammo Block, Timo Lichtenstein und Philipp Kröger erwähnen, aber auch allen aktuellen und ehemaligen Mitarbeitern der Abteilung meinen Dank aussprechen.

Für die Unterstützung während meiner Promotions- und Studienzeit möchte ich meinen Eltern danken und des Weiteren auch meiner Partnerin für ihre Liebe und den Rückhalt, den sie mir gegeben hat.